

**ROTATIONAL AND VIBRATIONAL ACTION
SPECTROSCOPIC STUDIES ON COLD MOLECULAR
IONS**

**ROTATIONAL AND VIBRATIONAL ACTION
SPECTROSCOPIC STUDIES ON COLD MOLECULAR
IONS**

Proefschrift

ter verkrijging van de graad van doctor
aan de Radboud Universiteit Nijmegen
op gezag van de rector magnificus prof. dr. J.H.J.M. van Krieken,
volgens besluit van het college voor promoties
in het openbaar te verdedigen op

by

Aravindh Nivas MARIMUTHU

geboren op 28 mei, 1995
te Tamil Nadu, India

This dissertation has been approved by the promotor.

Composition of the doctoral committee:

Prof. dr. Britta Redlich, Radboud Universiteit, *promotor*
Dr. Sandra Brünken, Radboud Universiteit, *copromotor*

Manuscript committee:

dr. Oskar Asvany Universität zu Köln
prof. dr. Jana Roithova Universität zu Köln
prof. dr. Melanie Schnell Universität zu Kiel and DESY

Other members:



Keywords: ...

Printed by:

Cover by: Beautiful cover art that captures the entire content of this thesis in a single illustration.

Copyright © 2023 by A.N. Marimuthu

ISBN 000-00-0000-000-0

An electronic copy of this dissertation is available at
<https://repository.ru.nl/?>.

Einstiens work is to make physics more philosophical (in a good sense).

Hendrik Antoon Lorentz

CONTENTS

I. INTRODUCTION AND METHODS	1
1. Introduction	3
1.1. Measurements: A historical perspective	4
1.1.1. Measuring stars	4
1.1.2. Beyond stars	5
1.2. Molecules in space	6
1.2.1. Optical observation	7
1.2.2. Radio observation	7
1.2.3. Infrared observation	8
1.2.4. Current status	9
1.3. Spectroscopy	9
1.4. Cryogenic ion trap	13
1.4.1. 22-pole cryogenic ion trap	14
1.5. Action spectroscopy	15
1.5.1. Vibrational action spectroscopy	15
1.5.1.1. Tagging photodissociation ion spectroscopy	16
1.5.1.2. IR multi-photon dissociation (IRMPD)	17
1.5.1.3. Laser induced reactions (LIR)	19
1.5.1.4. Laser induced inhibition of He attachment (LIICG) .	20
1.5.2. Rotational action spectroscopy	20
1.5.2.1. Rotational LIR	21
1.5.2.2. Double resonance methods	21
1.5.2.3. ROSAA	22
1.6. This thesis	24
2. Experimental and theoretical methods	27
2.1. FELion instrument	28
2.1.1. Ion source	29
2.1.2. Ion trap and detector	31
2.2. Vibrational spectroscopy	32
2.2.1. Experimental method	32

2.2.2. IR radiation source	33
2.2.2.1. FELIX	33
2.2.2.2. OPO/A	36
2.2.3. Data analysis	36
2.3. Rotational spectroscopy	38
2.3.1. Experimental method	38
2.3.2. THz radiation source	39
2.3.3. Determining the radiation power at the trap region	42
2.3.4. Determining the collisional ion temperature	44
2.3.5. Numerical simulation	46
2.3.5.1. Collisional process (R)	46
2.3.5.2. Spontaneous emission (A)	48
2.3.5.3. Radiative process (R_B)	49
2.3.5.4. Attachment and dissociation process (R_3 and R_{CID})	50
2.3.5.5. Solving rate equations	51
2.4. Theoretical methods	51
2.4.1. Molecular vibration	52
2.4.1.1. Diatomic molecules	53
2.4.1.2. Polyatomic molecules	55
2.4.1.3. Selection rules	55
2.4.2. Molecular rotation	56
2.4.2.1. Linear molecules	57
2.4.2.2. Non-linear molecules	58
2.4.2.3. Selection rules	60
2.4.3. Quantum chemical calculations	60
2.5. Technical details	61
2.5.1. Determining number density	61
2.5.2. Calibration of the hot-cathode ionization gauge (HIG) to SRG	64
 II. VIBRATIONAL SPECTROSCOPY	 69
3. Laboratory gas-phase vibrational spectra of $[C_3H_3]^+$ isomers and iso-topologues by IRPD spectroscopy	71
3.1. Introduction	73
3.2. Methods	75
3.2.1. Experimental details	75
3.2.2. Computational details	78
3.3. Results and discussions	79
3.3.1. Cyclic isomer	82
3.3.2. Linear isomer	83

3.3.3. Ne-effect	84
3.3.4. Deuterated species	86
3.3.5. Isomer quantification	93
3.4. Conclusion	97
4. Infrared predissociation spectroscopy of protonated methyl cyanide, CH_3CNH^+	99
4.1. Introduction	101
4.2. Methods	102
4.2.1. Experimental details	102
4.2.2. Computational details	104
4.3. Results and discussions	105
4.3.1. Vibrational spectroscopy of CH_3CNH^+	105
4.3.2. Prediction of rotational spectroscopic parameters	111
4.3.3. Influence of the neon atom on vibrational band positions . .	112
4.4. Conclusions	115
5. A vibrational action spectroscopic study of the Renner-Teller and spin-orbit affected cyanoacetylene radical cation HC_3N^+	117
5.1. Introduction	119
5.2. Methods	120
5.2.1. Experimental methods	120
5.2.2. Theoretical approach	122
5.2.2.1. Ab Initio	122
5.2.2.2. Effective Hamiltonian	122
5.2.2.3. The HC_3N^+ ion	125
5.3. Results and Discussion	125
5.3.1. Stretching modes	126
5.3.2. Vibronic coupling effects	129
5.3.3. Influence of the rare-gas tag	132
5.4. Conclusions	134
III. ROTATIONAL SPECTROSCOPY	137
6. Kinetics of CD^+ ion with He buffer gas	139
6.1. Motivation	140
6.2. Kinetic measurement	140
6.3. Theory of association reactions	141
6.4. Rate equations	143
6.5. Rate loss channels	144

6.6. Deriving rate constants	146
6.7. Influence of radiation	149
6.7.1. CD ⁺ rotational transition ($J = 0 - 1$)	149
6.7.2. Determining ion temperature	150
6.7.3. Kinetics	152
6.8. ROSAA Numerical simulation	153
6.8.1. Collisional process	153
6.8.2. Radiative processes	154
6.8.3. Attachment processes	155
6.8.4. Analysing numerical results	158
6.9. Temperature dependence of rate coefficients	162
6.10. Conclusion	165
7. The Zeeman effect in CO⁺ observed with rotational action spectroscopy	167
7.1. Introduction	169
7.2. Experiment	170
7.3. Results and discussions	174
7.4. Conclusions	180
APPENDICES	181
A. Chapter 3	183
A.1. Internal coordinates of c-C ₃ H ₃ ⁺	184
A.1.1. fc-CCSD(T)/ANO0	184
A.1.2. fc-CCSD(T)/ANO1	184
A.1.3. fc-CCSD(T)/ANO2	184
A.2. Internal coordinates of H ₂ C ₃ H ⁺	185
A.2.1. fc-CCSD(T)/ANO0	185
A.2.2. fc-CCSD(T)/ANO1	185
A.2.3. fc-CCSD(T)/ANO2	186
B. Chapter 4	193
B.1. Internal coordinates of CH ₃ CNH ⁺	194
B.1.1. fc-CCSD(T)/ANO0	194
B.1.2. fc-CCSD(T)/ANO1	194
B.1.3. fc-CCSD(T)/ANO2	195
B.1.4. fc-CCSD(T)/cc-pVDZ	195
B.1.5. fc-CCSD(T)/cc-pVTZ	196
B.1.6. ae-CCSD(T)/cc-pwCV5Z	197

B.2. Internal coordinates of CH ₃ CNH ⁺ -Ne	197
B.2.1. fc-CCSD(T)/ANO0	197
B.2.2. fc-CCSD(T)/cc-pVDZ	198
C. Chapter 5	207
D. Chapter 6	219
D.1. CD ⁺ + He rate coefficients	220
E. Chapter 7	223
Bibliography	227
Summary and outlook	249
1. Summary	249
2. Outlook	251
Samenvatting	253
1. Summary	253
Acknowledgements	255
List of Publications	257
Curriculum Vitæ	259

LIST OF FIGURES

1.1. The optical spectrum of the sunlight. (a) is the original recorded spectrum (Credit: Fraunhofer [1]) while (b) is the same visible spectrum but coloured, from 380 nm to 710 nm (Credit: Wikimedia Commons).	5
1.2. The Astronomer's Periodic Table, as it is referred to. This figure represents the elements by boxes with areas corresponding to their cosmic abundances. Figure adapted from McCall [2].	6
1.3. James Webb Space Telescope - An infrared-optimized astronomical observatory (Credit: NASA)	8
1.4. Percentage of different classes of known interstellar molecules. Many molecules fall into more than one of these categories e.g. most radical species have a net neutral charge. Data is computed using <i>astromol - A Database of Molecules Detected in Space</i> python library [41]	10
1.5. Schematic diagram of the electromagnetic spectrum, the rainbow-coloured inset shows the visible spectrum. The vertical dashed line indicates a corresponding comparison to the different unit systems as labelled on the left, and “x3” indicates that the scale value is multiplied by factor 3.	10
1.6. The triangular approach of observations, models, and laboratory studies is necessary to address astrochemistry questions. Examples for every category are provided in smaller fonts with respective boxes. “Laboratory” implies both experimental and theoretical work. The blue coloured box indicates the area focused on in this thesis.	12
1.7. Schematic diagram to describe the principle of absorption spectroscopy.	12
1.8. Schematic diagram of a quadrupole mass filter. Ions enter and move along the z-axis as they oscillate in the x-y plane. The oscillation is regulated by applying DC (U) and radio frequency (RF) (V) potentials to each set of rods. Only ions with stable paths at the chosen U and V values will pass through the quadrupole mass filter.	13

1.9. (a) Schematic drawing of the 22-pole cryogenic ion trap (grey) in copper housing (orange) mounted onto cryogenic coldhead. (b) A photograph of the 22-pole ion trap mounted inside copper housing.	15
1.10. Schematic drawing of the IRPD method. He-A ⁺ represents the weakly bound helium complex of molecular ion A ⁺ , and D ₀ indicates the complex dissociation limit.	16
1.11. Simulated IRPD spectrum measuring complex counts as a function of frequency. N ₀ indicates the initial background counts, while the counts drop due to the dissociation of the complex at the resonance frequency.	17
1.12. Schematic drawing of the Infrared multi-photon dissociation (IRMPD) spectroscopy. AB ⁺ represents molecular ion consisting of A and B chemical fragments. Figure adapted from [84].	18
1.13. Schematic description of (a) bimolecular reaction initiated by laser excitation suitable for LIR spectroscopy, (b) LIR signal as a function of frequency detected by monitoring the product counts.	19
1.14. Schematic diagrams of rotational action spectroscopic methods. The captions indicate the corresponding name of the method. DR stands for double resonance. “predis.” and “det.” in (c) and (d) correspond to “predissociation” and “detachment”, respectively. The symbol A and B indicates molecular species while superscript (such as A ⁺) indicates molecular cations. He indicates a helium atom while He-A ⁺ indicates a weakly bound helium-ion complex.	23
2.1. Schematic drawing of the FELion ion trap setup. The 22-pole ion trap is coupled in-between two quadrupole mass filters (Q1 and Q2). The ions are guided into the trap from Q1 via quadrupole bender (labelled BENDER). The trap contents are extracted after irradiation from the radiation source into Q2 to filter desired product molecular ions and then guided into a Daly type detector to be counted.	28
2.2. Schematic drawing of the ion sources. The various components are labelled, and the corresponding connections are indicated by solid lines for (a) storage source and (b) non-storage (S1, S2 and S3 are grounded base plates for support). The pink circles represent ruby balls for insulation between connected electrodes. The labelled Macor sealing ring on top of the B0 electrode is placed to seal the ion source chamber and prevent any accidental contact between B0 and the Q1 rods.	29

2.3. Cool-down behaviour of the 22-pole cryogenic ion trap from room temperature using a He cryostat. The inset shows a detailed view of temperatures below 5 K.	31
2.4. Schematic drawing of FELIX and OPO/A system interfaced with FE-Lion user-station. The blue and green coloured lines represent the FELIX and OPO/A output laser beam paths, respectively. Only one system, FELIX or OPO/A, is operated at a given time.	34
2.5. Schematic diagram of the FELIX laser micro and macro pulse structure.	35
2.6. Data processing (for Ne-HC ₃ N ⁺ IRPD spectrum using FELIX): (a) is the raw data obtained by directly measuring the depletion counts of formed complex ions in IRPD schemes at varying frequencies. The blue line corresponds to a possible baseline to account for ion count fluctuation. (b) is the first processed spectrum with baseline correction from (a). (c) is the final normalised spectrum (see text) and the solid line corresponds to fitting the spectrum with a multi-component Gaussian function.	37
2.7. Power curves measured with Virginia Diodes, Inc. (VDI) WR9.0 Modular SGX Modules in (a) WR9.0 and (b) WR2.2 configuration as described in Table 2.1.	40
2.8. Power curves measured with Virginia Diodes, Inc. (VDI) WR9.0 Modular SGX Modules in WR9.0 configuration, for the frequency ranges (a) 117.68 – 117.70 GHz and (b) 118.09 – 118.11 GHz. (c) shows the user-controlled attenuation power output for (a) and (b) as labelled 117 and 118 GHz, respectively.	41
2.9. Schematics of the nominal feed horn antenna are shown. Z _A is defined as the location of the beam waist radius (w_0) with respect to the horn aperture. The upward arrow (orange solid line) indicates the polarisation direction of the electric field.	42
2.10. Gaussian beam (for a frequency of $\nu = 453$ GHz) propagation from a beam waist radius of 0.15 cm produced from diagonal feed horn antenna. The solid lines - orange and green indicates the position of FELion instrument entrance window (CVD diamond window, 3 cm from antenna, 2 cm aperture radius) and bender (10.4 cm from window, 0.43 cm aperture radius), 22-pole ion-trap (14 cm from window, 0.3 cm aperture radius). respectively.	43

2.11. The radiation intensity profile distribution is shown in the blue line. The shaded orange region indicates the fraction of output power at a 3 cm beam radius, i.e., inside trap region as shown in Figure 2.10. The position of the orange region <i>w.r.t</i> the x-axis represents the part of the propagating Gaussian beam reaching the trap region when (a): aligned and (b): 1.5 cm offset <i>w.r.t</i> beam centre.	44
2.12. Schematic kinetic model of the ROSAA action spectroscopic technique. The coloured labels and arrows indicate several competing processes for the reaction between the molecular ion M^+ and the neutral He atom. The typical rates for collisional (blue) and radiative process (red) are in the range of $10^4 - 10^5 \text{ s}^{-1}$, effective binary complex formation (orange) is $> 0.01 \text{ s}^{-1}$ and the collision-induced dissociation (violet) is $> 0.1 \text{ s}^{-1}$ at a given number density of $> 1 \cdot 10^{14} \text{ cm}^{-3}$. The spontaneous emission is labelled A_{10} , and rates are typically in order of $> 10^{-4} \text{ s}^{-1}$. Figure adapted from Brünken <i>et al.</i> [3].	47
2.13. Heteronuclear diatomic molecule (solid circles at the bottom) vibrating at energy level $\nu = 3$. The black and red curve represent harmonic and anharmonic (Morse) potential energy curves, respectively. r_e is the equilibrium bond length, D_0 and D_e correspond to dissociation energy with and without ZPE (zero-point energy) correction, respectively.	53
2.14. Triatomic molecule (H_2O) ball-spring representation. The blue and grey circle represents oxygen and hydrogen, respectively.	55
2.15. Rotation of linear molecule (heteronuclear diatomic) <i>w.r.t</i> principal rotational axis a, b and c , with corresponding moment of inertia I_a, I_b and I_c , respectively ($I_a=0, I_b=I_c$ for linear and diatomic molecules). m and r represent the mass of the atom and the distance to the rotating axis, respectively. The centre of mass lies at the origin.	57
2.16. Comparing number density, n_{trap} , with and without thermal transpiration. The figure shows pressure measured using SRG vs n_{trap} (Thermal transpiration / low-pressure approximation) ratio. The marked box region indicates the pressure range used in this study.	63
2.17. Schematic diagram on the relation of ion-trap, spinning rotor gauge (SRG) and the main chamber. The orange and green coloured region represents the connecting tube for SRG to trap and trap to the chamber, respectively, with the corresponding aperture of diameter d and A	65

2.18. Pressure measured with SRG and HIG are plotted at 5 K trap nominal temperature. The derived calibration factor is $C = 179(4)$	66
3.1. Molecular structures of c-C ₃ H ₃ ⁺ (left) and H ₂ C ₃ H ⁺ (right) isomers.	75
3.2. Mass spectra of ions produced from electron impact ionization (20 eV) of allene (left, in storage EI source) and propargyl chloride (right, in direct EI source) precursors (upper panel), and of mass filtered [C ₃ H ₃] ⁺ ($m = 39$ u) together with tagged Ne-[C ₃ H ₃] ⁺ ($m = 59$ u) species produced in the cryogenic ion trap (lower panel).	76
3.3. The experimental and fitted FELIX IRPD spectrum of Ne-[C ₃ H ₃] ⁺ (upper panel) compared to computed frequencies (lower panel) at CCSD(T)/ANO2 combined with the anharmonic correction from CCSD(T)/ANO1 (H ₂ C ₃ H ⁺) and CCSD(T)/ANO0 (c-C ₃ H ₃ ⁺). Only fundamental (solid line), combination (dashed line) and overtone (dotted line) infrared bands with intensity $> \sim 1$ km/mol were included. The theoretical spectrum was folded with a Gaussian corresponding to the FEL linewidth. Peaks marked with :n indicate that the depicted peak intensity is scaled down by a factor n, for better visualization.	80
3.4. Comparing Ne-[C ₃ H ₃] ⁺ (upper panel) and H ₂ -[C ₃ H ₃] ⁺ (lower panel) IRPD spectra produced from allene precursor in the storage ion source recorded with FELIX laser and OPO.	85
3.5. The experimental and fitted FELIX IRPD spectrum of Ne-[C ₃ D ₃] ⁺ (upper panel) compared to computed frequencies (lower panel) at CCSD(T)/ANO2 combined with the anharmonic correction from CCSD(T)/ANO1 (c-C ₃ D ₃ ⁺) and CCSD(T)/ANO0 (D ₂ C ₃ D ⁺). Only fundamental (solid line) combination (dashed line) and overtone (dotted line) infrared bands with intensity $> \sim 1$ km/mol were included. The theoretical spectrum was folded with a Gaussian corresponding to the FEL linewidth. Peaks marked with :n indicate that the depicted peak intensity is scaled down by a factor n, for better visualization.	88
3.6. Isomer variation depending on ion production conditions. Upper panel: Experimental IRPD spectrum of Ne-[C ₃ H ₃] ⁺ produced from propargyl chloride in the EI source. Lower panel: Same as above but using an allene precursor and the storage ion source.	94

3.7. Saturation depletion measurements on the ν_5 band of c-C ₃ H ₃ ⁺ , produced from propargyl chloride in the direct EI ion source with 16.5 eV electrons. Top: On-resonance (blue, at 1293 cm ⁻¹ , ν_5) and off-resonance (orange, at 1150 cm ⁻¹) depletion measurement. Bottom: Relative depletion $D(E)$ as a function of deposited energy E , showing saturation at $A = 84\%$	95
4.1. Upper panel: Mass spectra of ions produced from electron impact ionization (~30eV) in a storage ion source. See text for discussion of the main peaks Lower panel: Mass filtered CH ₃ CNH ⁺ ($m/z = 42$, < 10 % contribution at $m/z = 41$ and 43) together with tagged CH ₃ CNH ⁺ -Ne ($m/z = 62$, also CH ₃ CNH ⁺ - ²² Ne at $m/z = 64$) species produced in the cryogenic ion trap. Additional weaker contributions at $m/z = 60$, 70, and 74 stem from tagging with residual H ₂ O, N ₂ , and O ₂ , respectively.	102
4.2. Computed equilibrium geometry (C _{3v} symmetry) for CH ₃ CNH ⁺ based on (fc-CCSD(T)/ANO2, <i>ae-CCSD(T)/cc-pwCV5Z</i>) level of theory. Bond lengths and angles are in Å and deg° respectively.	104
4.3. The experimental and fitted FELIX IRPD spectrum of CH ₃ CNH ⁺ -Ne (upper panel) compared to the computed anharmonic (VPT2) frequency values (lower panel) of CH ₃ CNH ⁺ at the fc-CCSD(T)/ANO2 level of theory showing fundamental (orange, solid line), combination and overtone (orange, dashed line) bands. NOTE: /n and *n indicates that the computed intensities are divided or multiplied, respectively, by a factor n for better visualisation	106
4.4. The experimental and fitted FELIX IRPD spectrum of CH ₃ CNH ⁺ -Ne (upper panel) but using FELIX in 3 rd harmonic mode, compared to the computed anharmonic (VPT2) frequency values (lower panel) of CH ₃ CNH ⁺ at the (fc)-CCSD(T)/ANO2 level of theory.	107
4.5. Computed potential energy surface as a function of H-Ne distance R for the minimum energy C _{3v} structure of the CH ₃ CNH ⁺ -Ne complex at various levels of theory.	113

- 5.1. (a) Mass spectrum of ions produced from electron impact ionization (~ 28 eV) of acrylonitrile (blue). (b) Mass-selected (orange) HC_3N^+ (m/z 51) together with tagged (green) $\text{Ne}-\text{HC}_3\text{N}^+$ (m/z 71) complexes produced in the cryogenic ion trap at temperature $8.5(2)$ K and He:Ne gas mixture number density of $9(1)\cdot 10^{14}$ cm $^{-3}$. The attachment of isotopic ^{22}Ne can also be seen in panel (b). A small contamination from C_3N^+ (m/z 50) can be seen in the mass-selected spectrum, resulting from insufficient mass-filtering of the primary ions. 121
- 5.2. Measured IRPD spectrum of the HC_3N^+ ion in the range 130 - 270 cm $^{-1}$ (FEL1) 310 - 2500 cm $^{-1}$ (FEL2), and 3110 - 3270 cm $^{-1}$ (OPO) using Ne as a messenger atom. The ν_1 - ν_4 labels represent the four stretching modes of HC_3N^+ and ν_5 - ν_7 the RT-affected bending modes. A full list of the obtained frequencies, relative intensities and their uncertainties is given in Appendix Table C.1. 127
- 5.3. Bending region of the IRPD spectrum of $\text{Ne}-\text{HC}_3\text{N}^+$ (black) overlaid with the bands predicted from the fitted spectroscopic parameters (orange). For the assignment of weaker features please see Table 5.3. A zoom of the 900 – 1600 cm $^{-1}$ region is presented to show the large density of transitions of weak intensity. 133
- 5.4. Calculated interaction energy as a function of the Ne angle with respect to the molecular axis. A' represents the symmetric electronic wavefunction, where the Π_x orbitals are partially filled. A'' represents the antisymmetric electronic wavefunction, where the Π_x orbitals are completely filled 135
- 6.1. Measured mass spectrum after storing CD^+ ions (m/z 14) for ~ 600 ms in the cryogenic ion trap using He buffer gas (a): $1.97(7)\cdot 10^{14}$ cm $^{-3}$; (b): $3.07(12)\cdot 10^{14}$ cm $^{-3}$ number density at $T=4.8(3)$ K, showing the CD^+ ion and the subsequent formation of ion-He complexes with up to (a): four; (b): five He atoms attached. 141
- 6.2. Comparing loss channels additions: (a) is with both R_{loss} and R_{loss30} channels included while (b) is only with R_{loss30} . The (c) and (d) are zoomed-in regions for (a) and (b), respectively. The measurements were carried out at $6.9(3)$ K and $1.770(45)\cdot 10^{14}$ cm $^{-3}$ helium number density. No higher order complexes were formed other than mass 30, which most probably could be DCO^+ as described in Eq. 6.22 and 6.23 145

- 6.3. (a) and (b) shows the counts of primary and complex ions monitored as a function of trap time at $1.16(2) \cdot 10^{14} \text{ cm}^{-3}$ and $6.0(2) \cdot 10^{14} \text{ cm}^{-3}$ respectively at 4.8(3) K. The circle marker and the solid line represent measured and numerically fitted data, respectively. 147
- 6.4. The effective binary rate constant (k_e), the ternary association (k_{3_1}) and collision-induced dissociation (k_{CID_1}) rate constants are plotted as a function of helium number density. (a) The effective binary rate constant (k_e) is plotted as a function of number density to derive k_{3_1} (ternary association) and k_r (radiative) rate constants. The solid line indicates the linear fit where the slope and intercept correspond to k_3 and k_r , respectively. (b) shows the k_{3_1} as a function of number density under $k_3[\text{He}] \gg k_r$ assumption (see text). The weighted average values are shown in the legend box. 147
- 6.5. The numerically derived formation and dissociation rate constants for higher order of complexes ($n > 1$) plotted as a function of number density at 4.8(3) K temperature. 148
- 6.6. CD⁺ measured $J = 0 - 1$ rotational transition using ROSAA technique (see Section 2.3.1). The coloured solid lines indicate the fitted line profile as labelled. The experiment performed at 35(12) ~ μW power - (a) with He tag, $T_{trap} = 4.7(3)$ K [$2.7(4) \cdot 10^{14} \text{ cm}^{-3}$] with He tag and derived $T_{ion} = 14(5)$ K and $T_{coll} = 7(1)$ K; (b): with Ne tag, $T_{trap} = 8.7(3)$ K [$1.8(2) \cdot 10^{14} \text{ cm}^{-3}$] and derived $T_{ion} = 23(5)$ K and $T_{coll} = 19(3)$ K. 150
- 6.7. Comparing nominal trap temperature (T_{trap}) and derived ion temperature (T_{ion}) from rotational spectrum. The solid (black) line corresponds to Ref. [116], and the solid (blue) represents derived data in this work (see text). 152
- 6.8. Deriving rate coefficients in the presence of radiation resonant with $J = 0 - 1$ transition of CD⁺. (a) The effective binary rate constant (k_e) is plotted as a function of number density to derive k_{3_1} (ternary association) and k_r (radiative) rate constants. The solid line indicates the linear fit where the slope and intercept correspond to k_3 and k_r , respectively. While (b) shows the ternary association (k_{3_1}) and collision-induced dissociation (k_{CID_1}) rate constants are plotted as a function of helium number density under the assumption: $k_3[\text{He}] \gg k_r$ (see text). The weighted average values are shown in the legend box. 153

- 6.9. (a) Collisional process for CD^+ ion up to $J = 5$ with He buffer gas ($2.2 \cdot 10^{14} \text{ cm}^{-3}$). The coloured label indicates the corresponding CD^+ (J) state. At $t = 0$, $T_{coll} = 300 \text{ K}$, at which the relative population corresponds to Boltzmann distribution at 300 K. The relative population evolves as collisions with He with rate constants for $T_{coll} = 7 \text{ K}$ (derived from [304]), subsequently reaching equilibrium at $< 0.5 \text{ ms}$. (b) Comparison of the Boltzmann distribution at 7 K with the relative population involving only collisional process (Coll.) at $t = 1 \text{ ms}$ 154
- 6.10.(a) Simulated relative rotational level populations for CD^+ as labelled in parenthesis. The population evolves from $t = 0$ ($T_{coll} = 300 \text{ K}$) to reach equilibrium at $t < 0.5 \text{ ms}$. The solid and dashed lineshapes correspond with (ON) and without (OFF) the presence of radiation for $\text{CD}^+ J = 0 - 1$ transition. The radiation power is $35 \mu \text{W}$. (b) Compares the Boltzmann distribution at 7 K with the relative population involving only collisional process (Coll.) and, collision and radiative process (Coll. + Rad.) at $t = 1 \text{ ms}$ 155
- 6.11.(a) Simulated relative rotational level populations for CD^+ and corresponding number J levels as labelled in parenthesis. The population evolves from $t = 0$ ($T_{coll} = 300 \text{ K}$) to reach equilibrium at $t < 0.5 \text{ ms}$. The solid and dashed lineshapes correspond with (ON) and without (OFF) the presence of radiation for $\text{CD}^+ J = 0 - 1$ transition. The radiation power is 3.5 W . (b) Compares the Boltzmann distribution at 7 K with the relative population involving only collisional process (Coll.) and, collision and radiative process for power $3.5 \mu\text{W}$ (Coll. + Rad.), collision and radiative process for power 3.5 W (Coll. \ll Rad.), at $t = 1 \text{ ms}$ 156
- 6.12.(a) Simulated relative rotational level populations for CD^+ and corresponding number of He_nCD^+ clusters ($n=1, 2$) where CD^+ (J) indicates CD^+ in J rotational state. The simulation conditions are as follows: k_3 ratio, $a = 0.5$, collisional rates for $T_{coll} = 7 \text{ K}$ (at $t = 0$, $T_{coll} = 300 \text{ K}$), Helium number density $2.2 \cdot 10^{14} \text{ cm}^{-3}$ and radiation power $3.5 \cdot 10^{-5} \text{ W}$. The solid and dashed lines correspond to, with (-ON) and without (-OFF), the presence of radiation on the $\text{CD}^+ J = 0 - 1$ transition frequency. The simulation duration for (a) 1 ms, (b) 600 ms and (d) 100 s. Figures (c) and (e) correspond to signal intensity, i.e., HeCD^+ depletion % as a function of time for (b) and (d), respectively. 159

6.13. Numerical simulation of ROSAA process with computed signal intensities as a function of radiation power, 10^{-7} – 10^{-2} W, He number density, 10^{12} – 10^{16} cm $^{-3}$, and function of k_{3_1} ratio, 0.3–1, at 600 ms trap duration and $T_{coll} = 7(1)$ K temperature. The captions of subplots (a)-(e) indicate the respective k_{3_1} ratio value. (f) as captioned, shows the combined plots of (a)-(e).	161
6.14. HeCD $^+$ The formation (k_{3_1}) and dissociation (k_{CID_1}) rate constants (weighted) are plotted as a function of nominal trap temperature (T_{trap}) and ion temperature (T_{ion}). The x-axis error bar corresponds to T_{trap}	163
6.15. HeN $^+$ formation (k_{3_1}) and dissociation (k_{CID_1}) rate constants (weighted) are plotted as a function of nominal trap temperature	164
7.1. (a): Measured mass spectrum after storing CO $^+$ ions (m/z 28) for ~600 ms in the cryogenic ion trap using He buffer gas (~ $4 \cdot 10^{14}$ cm $^{-3}$ number density, T=4.7(3) K), showing the CO $^+$ ion and the subsequent formation of ion-He complexes with up to three He atoms attached. A small contamination from HCO $^+$ can be seen, resulting from insufficient mass-filtering of the primary ions. (b): The counts of primary and complex ions are monitored as a function of trap time (~ $1.5 \cdot 10^{14}$ cm $^{-3}$, T=4.7(3) K). The formation (k_{3_1}) and dissociation rate (k_{CID_1}) constants as described in Eq. 7.1 are derived by numerical fitting.	171
7.2. CO $^+$ ($X^2\Sigma^+, v = 0$): Numerical simulation of rotational population distribution of N_J states with (-ON) and without (-OFF) radiation for the $N_J = 0_{1/2} - 1_{1/2}$ transition. At t=0, the initial population is given by a Boltzmann distribution (at collisional temperature T=6(1) K) and the collisional rates (with He number density [He]= $4 \cdot 10^{14}$ cm $^{-3}$) are derived from He-CO $^+$ collisional rate constants values [328]. The radiation rates (Einstein B coefficients for stimulated emission and absorption) are derived from Einstein A coefficients for spontaneous emission (PGOPHER simulation [122]).	172
7.3. Simulated population ratio (N_J : up/down) of the CO $^+$ $N_J = 0_{1/2} - 1_{1/2}$ transition as a function of excitation power, at different He number densities, after storing for 600 ms in the trap. Lower He number densities lead to saturation of the transition at lower excitation power.	173

7.4. Rotational energy level diagram for CO ⁺ ($X^2\Sigma^+$, $v = 0$) showing fine-structure and Zeeman splittings (not to scale). The dashed arrow lines show the expected Zeeman components of the $N_J = 0_{1/2} - 1_{1/2}$ transition. ΔE_J , the magnetic interaction energy is given by Equation 7.2.	175
7.5. Measured rotational transitions of the CO ⁺ molecular ion in the presence of Earth magnetic field causing anomalous Zeeman splitting. The σ and π correspond to perpendicular ($\Delta M = \pm 1$) and parallel ($\Delta M = 0$) magnetic field, respectively, w.r.t electric field.	176
A.1. Potential energy pathway for c-C ₃ H ₃ ⁺ and H ₂ C ₃ H ⁺ formation from ionization of propargyl chloride (ClCH ₂ CCH). The calculations are done at the CCSD(T)/cc-pVTZ level with zero-point energy corrections from MP2/cc-pVTZ level. The ClCH ₂ CCH ⁺ ion (propargyl chloride cation, relative energy arbitrarily set to 0 ~kJ/mol) can undergo hydrogen migration to the linear ClCHCHCH ⁺ ion ($E_{\text{rel}} = -46.56 \sim \text{kJ/mol}$) via transition state TS1 ($E_{\text{rel}} = 53.45 \sim \text{kJ/mol}$). This isomer can then convert to ClCHCHCH ⁺ (iso) ($E_{\text{rel}} = -30.98 \sim \text{kJ/mol}$) via TS4 ($E_{\text{rel}} = -39.45 \sim \text{kJ/mol}$). The latter species can subsequently cyclise via a submerged transition state TS2 ($E_{\text{rel}} = -5.79 \sim \text{kJ/mol}$) to the cyclic c-ClCHCHCH ⁺ ($E_{\text{rel}} = -21.40 \sim \text{kJ/mol}$). This means that the highest barrier for the isomerisation of ClCH ₂ CCH ⁺ to c-ClCHCHCH ⁺ is 53.45~kJ/mol, i.e. only 0.55~eV. Also the dissociation energy barrier to c-C ₃ H ₃ ⁺ and Cl ($E_{\text{rel}} = -29.99 \sim \text{kJ/mol}$) is only at 13.19~kJ/mol (TS3).	191
B.1. Computed potential energy surface as a function of Ne distance R for CH ₃ CNH ⁺ -Ne from various sites neon atom placed.	203
B.2. Vibrational displacement vectors for CH ₃ modes.	204
C.1. IRPD spectrum of the HC ₃ N ⁺ ion tagged with Ne in the range 3120-3260 cm ⁻¹ recorded with an OPO (red) overlayed with a prediction of the ν_1 ro-vibrational structure using the PGOPHER program package [122] (black, $T=20$ K and $B = 0.033 \text{ cm}^{-1}$, calculated at RCCSD(T)/cc-pVTZ level of theory).	210

- D.1. $\text{N}^+ + \text{He}$ reaction rate constants at (a)&(b) $\Rightarrow 4.8(3)$ K, (c)&(d) $\Rightarrow 6.5(3)$ K, (e)&(f) $\Rightarrow 8.4(3)$ K and (g)&(h) $\Rightarrow 10.0(4)$ K: The ternary association (k_{3_1}) and collision-induced dissociation (k_{CID_1}) rate constants are plotted as a function of helium number density. (a, c, e, g) - represents: Effective binary rate constants are plotted as a function of number density to derive k_{3_1} (ternary association) and k_r (radiative) rate coefficients. The solid line indicates the linear fit where the slope and intercept correspond to k_3 and k_r , respectively. (b, d, f, h) corresponds to formation rate without k_r , the weighted average values are shown in the legend box (see Section 6.6). 222
- E.1. Numerical simulations of the rotational state population distribution of N_J states with (solid line) and without (dashed line) radiation upon excitation of the transitions indicated in the title of each figure. The color code represents N_J states as follows: CO^+ ($0_{0.5}$), CO^+ ($1_{0.5}$), CO^+ ($1_{1.5}$), CO^+ ($2_{1.5}$) and CO^+ ($2_{2.5}$). At t=0, the initial population is given by the Boltzmann distribution at T=300 K which undergoes collisional cooling to reach collisional temperature T=6(1)K. The collisional rates are computed from collisional rate constants and He number density $[\text{He}] \sim 4 \cdot 10^{14} \text{ cm}^{-3}$. The radiative rates (Einstein B coefficients for stimulated emission and absorption) are derived from Einstein A coefficients for spontaneous emission (PGOPHER simulation) with radiation power for (a) & (b) $25\mu\text{W}$ and (c) & (d) $20\mu\text{W}$ 224
- E.2. Simulated population ratio (N_J : up/down) of CO^+ fine-structure transitions as a function of continuous excitation power on the respective transition after storing for 600ms in the trap with a constant He number density of $[\text{He}] \sim 4 \cdot 10^{14} \text{ cm}^{-3}$ 225
- E.3. Comparison of the normalized simulated population ratio (N_J : up/down) of the respective CO^+ fine-structure transitions as a function of continuous excitation power on the respective transition after storing for 600ms in a trap with a constant He number density of $[\text{He}] \sim 4 \cdot 10^{14} \text{ cm}^{-3}$. Transitions with higher transition strength reach saturation at lower excitation power. 226

LIST OF TABLES

1.1.	Dominant types of molecular transitions in each region of the electromagnetic spectrum	11
2.1.	WR9.0M-SGX configuration details at standard RF input mode.	40
3.1.	Summary of IRPD experimental vibrational band position of Ne-[C ₃ H ₃] ⁺ compared to computed fundamental, overtone and combination band frequencies at the CCSD(T)/ANO2 level of theory combined with anharmonic corrections from CCSD(T)/ANO1 (for H ₂ C ₃ H ⁺) and CCSD(T)/ANO0 (for c-C ₃ H ₃ ⁺).	81
3.2.	Comparing H ₂ C ₃ H ⁺ Ne-IRPD band positions with available computational studies based on coupled cluster methods. All frequencies are in cm ⁻¹ units	86
3.3.	Summary of IRPD experimental vibrational band position of Ne-[C ₃ D ₃] ⁺ compared to computed fundamental, overtone and combination band frequencies at the CCSD(T)/ANO2 level of theory combined with anharmonic corrections from CCSD(T)/ANO1 (for c-C ₃ D ₃ ⁺) and CCSD(T)/ANO0 (for D ₂ C ₃ D ⁺).	89
4.1.	Summary of IRPD experimental vibrational band position of CH ₃ CNH ⁺ -Ne and comparison to computed values. Vibrational frequencies are in cm ⁻¹ [calc. intensities in km/mol]	109
4.2.	Comparison of calculated (all using CCSD(T)) and experimental spectroscopic constants for the vibrational ground state of CH ₃ CNH ⁺ , with relative deviations to the experimental values [244] given in parentheses (in %). The last two columns give scaled spectroscopic constants for the two lowest vibrational state	112
4.3.	Computed binding energies E_{int} or D_e , respectively, for the lowest energy CH ₃ CNH ⁺ -Ne complex (C_{3v} structure) using different BSSE corrections methods. All values are in cm ⁻¹	112
5.1.	Calculated equilibrium bond lengths (in Å) of the bare ion for linear geometry.	126

5.2. Comparison of experimental and calculated harmonic frequencies (in cm^{-1}). If the bands are split due to vibronic interaction the lowest and highest observed components are given.	128
5.3. Observed and calculated transition frequencies in wavenumbers together with their normalized calculated intensity.	131
5.4. <i>Ab initio</i> and fitted spectroscopic parameters. The fitted parameters are determined based on the bands marked with a * in Appendix Table C.4	132
5.5. Harmonic vibrational frequencies of HC_3N^+ and $\text{Ne}-\text{HC}_3\text{N}^+$ calculated on RCCSD(T)-F12a/cc-pVTZ-F12 level of theory.	135
6.1. Comparing derived k_{3n} rate coefficients [in cm^6s^{-1}] in this work to previous results from Brünken <i>et al.</i> [3]	147
6.2. Comparing derived k_{CID_n} rate constants [in cm^3s^{-1}] in this work to previous results from Brünken <i>et al.</i> [3]	148
6.3. Pure-rotational $J = 0-1$ transition frequency of CD^+ ion using ROSAA action spectroscopy with He tag at 4.5(3) and 5.6(2) K temperature, and $35 \sim \mu\text{W}$ power.	150
6.4. Pure-rotational $J = 0-1$ transition frequency of CD^+ ion using ROSAA action spectroscopy with Ne tag for temperature range 5-14 K, and $35 \sim \mu\text{W}$ power.	151
6.5. Formation (k_{31}) and dissociation (k_{CID_1}) rate constants for N^+ and CD^+ reactions with helium at different nominal trap temperature .	165
7.1. Resolved Zeeman splitting for $N_J = 0_{1/2} - 1_{1/2}$ transition	177
7.2. Rotational transition frequencies of CO^+ ($X^2\Sigma^+$)	178
7.3. Derived molecular constants	179
A.1. Vibrational wavenumbers and IR intensities of $\text{c-C}_3\text{H}_3^+$ (cm^{-1} and km/mol, respectively).	187
A.2. Vibrational wavenumbers and IR intensities of $\text{c-C}_3\text{D}_3^+$ (cm^{-1} and km/mol, respectively); CCSD(T)/ANO1 anharmonic force field. .	187
A.3. Vibrational wavenumbers and IR intensities of $\text{c-C}_3\text{D}_3^+$ (cm^{-1} and km/mol, respectively); CCSD(T)/ANO0 anharmonic force field. .	188
A.4. Vibrational wavenumbers and IR intensities of $\text{H}_2\text{C}_3\text{H}^+$ (cm^{-1} and km/mol, respectively); CCSD(T)/ANO1 anharmonic force field. .	188
A.5. Vibrational wavenumbers and IR intensities of $\text{H}_2\text{C}_3\text{H}^+$ (cm^{-1} and km/mol, respectively); CCSD(T)/ANO0 anharmonic force field. .	189
A.6. Vibrational wavenumbers and IR intensities of $\text{D}_2\text{C}_3\text{D}^+$ (cm^{-1} and km/mol, respectively).	190

B.1. Computed fc-CCSD(T) vibrational frequencies (in cm^{-1}) using ANO basis sets for CH_3CNH^+	200
B.2. Computed harmonic CCSD(T) vibrational frequencies (in cm^{-1}) using Dunning's basis sets for CH_3CNH^+	201
B.3. Computed harmonic CCSD(T) vibrational frequencies (in cm^{-1}) comparing both CH_3CNH^+ (bare ion) and CH_3CNH^+ -Ne (complex) using ANO0 and cc-pVDZ basis sets.	202
B.4. Calculated spectroscopic parameters of CH_3CNH^+ at the CCSD(T)/ANO2 level of theory. Rotational constants B_e , B_0 , $\Delta B_0 = 1/2\sum\alpha_i^B$ (ΔA_0 analogous), and α_i^A and α_i^B . All values are in MHz.	205
C.1. Observed band centers and intensities in the IRPD spectrum of HC_3N^+ tagged with Ne obtained from fitting Gaussian functions to the experimental data in both relative depletion and power normalized intensity units (see main text). The frequency error is dominated by the calibration method using either a grating spectrometer (FEL) or a wavemeter (OPO).	208
C.2. Calculated frequencies and intensities based on <i>ab initio</i> parameters of Dai <i>et al.</i> [4] together with the assigned P and K quantum numbers and the population in the v_5 , v_6 and v_7 bending modes	210
C.3. Same as Table C.2, but calculated based on fitted spectroscopic parameters of the IRPD spectrum, all given in cm^{-1} : $\omega_5 = 699$, $g_{55} = 115$, $g_{56} = -50$, $\omega_6 = 455$, $g_{66} = -23$, $g_{57} = -34.72$, $\omega_7 = 198$, $g_{77} = -14$, $g_{67} = 15$, $A_{SO} = -44$	214
C.4. Comparison between the derived band center frequencies of the PFI-ZEKE work [4] and those obtained in our work.	218
D.1. Derived attachment and dissociation rate coefficients (k_3 & k_{CID}) and rates(R_3 & R_{CID}), for CD^+ molecular ion collision with helium buffer gas at $2.2 \cdot 10^{14} \text{ cm}^{-3}$ number density. The rates are given for up to two complexes, i.e., HeCD^+ and He_2CD^+	220
D.2. Derived collisional rates at $T = 7 \text{ K}$ (derived from [304]), CD^+ collision with He [$2.2 \cdot 10^{14} \text{ cm}^{-3}$ number density] for an initial $ i\rangle$ state transitions into final $ j\rangle$ state via k_{ij} rate coefficients [in cm^3/s] and R_{ij} rate [in s^{-1}].	220

- D.3. Derived radiative rates at $P=3.5 \cdot 10^{-5}$ W, for an initial $|i\rangle$ state transitions into final $|j\rangle$ state with A_{ij} spontaneous emission, B_{ij} stimulated absorption and B_{ji} stimulated emission. The spontaneous emission rates are derived from the effective Hamiltonian fitting of CD^+ ion using the Pgopher program [122]. Subsequently, the stimulated emissions are computed from spontaneous emission rates (see Section 2.3.5.3). All A_{ij} , B_{ij} and B_{ji} are in units of s^{-1} 221

I

INTRODUCTION AND METHODS

1

INTRODUCTION

1.1. MEASUREMENTS: A HISTORICAL PERSPECTIVE

No science attains maturity until it acquires methods of measurement

Logan Clendening

Science depends on measurement, and it lets us compare, for example, a foot and a mile or a gram and a pound. Our modern society's technological and scientific development is a direct consequence of the evolution of scientific measurement methods.

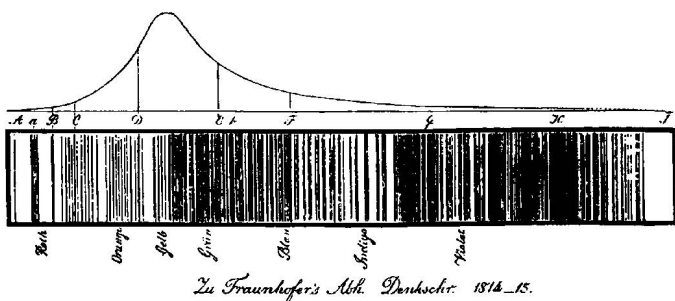
1.1.1. MEASURING STARS

ASTRONOMICAL observatories developed into significant resources during the nineteenth century and enabled astronomers to work on massive projects such as star catalogues. In the late 1830s, Bessel [5], Henderson [6], and Struve [7] were the first three people to perform parallax measurements, which provided the first direct evidence of the enormous distances to even the nearest stars [8]. Many believed that the star's composition would remain a mystery since humankind's travel to the stars was and is impossible with currently available technology (not yet!). Nevertheless, the composition of the stars and the interstellar medium and also (exo-)planetary atmospheres is now well-researched (see Section 1.2). How did this circumstance arise?

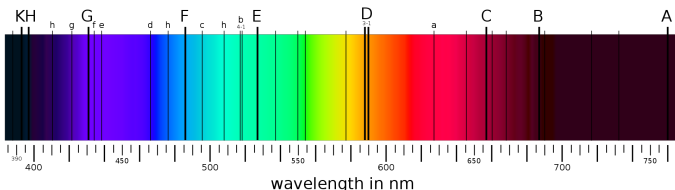
Fraunhofer [1] used one of the first optics (the same optics that made parallax measurements possible, see above) built in 1814 to reflect a ray of sunshine from a slit into a shutter onto a whitewashed wall. As shown in Figure 1.1, in addition to the rainbow's distinctive colours, which have been observed since Newton [9], he noticed numerous dark lines. He meticulously recorded the precise wavelength of each dark line, now referred to as Fraunhofer lines, and assigned letters to the strongest ones. As a result, Fraunhofer recorded the first-ever high-resolution astronomical spectrum.

However, he could not determine the origin of the dark patterns he saw. When he conducted a similar experiment using light from the nearby red star Betelgeuse, he discovered that the dark lines he had observed before had significantly altered. Fraunhofer arrived at the correct conclusion that most of those characteristics were somehow connected to the nature of the object he was examining.

Nearly 45 years later, Gustav Kirchhoff and Robert Bunsen's [10] (1860) experiments helped to understand Fraunhofer's observations. They investigated the colour of the light emitted as metals burned. In certain conditions, they discovered, the wavelength of the produced light matched the Fraunhofer lines. These



(a)



(b)

Figure 1.1.: The optical spectrum of the sunlight. (a) is the original recorded spectrum (Credit: Fraunhofer [1]) while (b) is the same visible spectrum but coloured, from 380 nm to 710 nm (Credit: Wikimedia Commons).

experiments demonstrated that the atomic constitution of the Sun is the origin of the observation of the Fraunhofer lines.

1.1.2. BEYOND STARS

Until the mid-20th century, in the interstellar medium (ISM) the formation and stability of molecules and the efficiency of chemical reactions were assumed to be impossible. Because of the intense radiation and high-energy particles present in space, as well as extremely low densities (at maximum reaching $10^6 - 10^7 \text{ cm}^{-3}$) and temperatures ($< 10 \text{ K}$) [11], were believed to prevent the formation and survival of molecules. For comparison, on Earth global average temperature is around $\sim 298 \text{ K}$ and number density (atmosphere) amounts to $\sim 10^{19} \text{ cm}^{-3}$. Therefore, it was generally believed that most matter in space would appear in the form of atoms or amorphous dust grains rather than individual molecules.

Most astrophysical environments possess very low densities of gases. However, even if densities are high, H and He are the primary elements accessible for chemistry (see Figure 1.2), which was thought to significantly limit the complexity of potential chemical reactions. Fortunately, the emergence of telescopes,

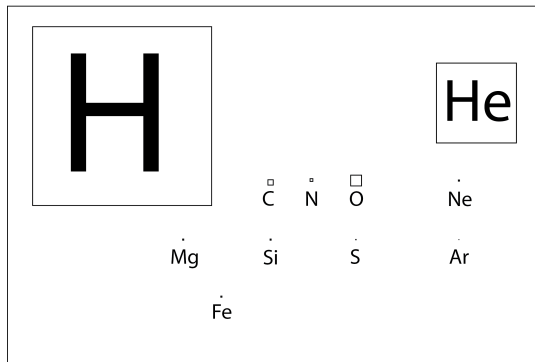


Figure 1.2.: The Astronomer's Periodic Table, as it is referred to. This figure represents the elements by boxes with areas corresponding to their cosmic abundances. Figure adapted from McCall [2].

detectors, and spectrometers operating in the radio, infrared (IR), and ultraviolet (UV)/visible regions of the electromagnetic spectrum proved this consideration incorrect. Indeed, low densities and extreme temperatures (both high and low) in space frequently constrain chemistry, but the vast quantities of matter and time availability compensate for it. Interstellar space represents a unique laboratory in which fundamental molecular processes can be investigated under conditions distinct from Earth's.

In the following sections, a brief introduction is given to the discovery of molecules in space and the laboratory spectroscopic techniques that allow us to study molecular ions under interstellar conditions.

1.2. MOLECULES IN SPACE

Somewhere, something incredible is waiting to be known

Carl Sagan

Sir Arthur Stanley Eddington's Bakerian Lecture on “*Diffuse matter in interstellar space*” [12] of 1926 may be a natural starting point for the discussion of molecules in the interstellar medium. The sharp calcium spectral line observed by Hartmann [13] in 1904 and the subsequent discovery of D-lines of sodium (Heger [14] in 1919) and H and K lines of calcium (Plaskett [15] in 1923) were the premises of Eddington's discussion. These lines were not arising from absorption in either

the stellar atmosphere or Earth's atmosphere. Since they were also unaffected by stellar motion, they were known as *fixed* or *stationary* lines. These lines were assumed to originate from interstellar space. Eddington pointed out in his lecture that "...it is difficult to admit the existence of molecules in interstellar space because when once a molecule becomes dissociated, there seems no chance of the atoms joining up again".

1.2.1. OPTICAL OBSERVATION

In the early 1930s, Merrill [16] identified several interstellar lines (much wider than interstellar atomic lines) of unknown origin, and Russell [17] conjectured that the origin of these lines was molecular rather than atomic. Merrill [18] noted that "the chemical identification of these lines had not been made yet", and remarkably, the chemical identity is unknown even today for these *diffuse interstellar bands* (DIBs). An exception is C_{60}^+ which is the only species identified as the carrier of two DIBs by Campbell *et al.* [19] only recently in 2015 based on laboratory action spectroscopic methods similar to the ones described in this thesis. However, hundreds of DIBs remain to be identified. Hence, it remains the oldest unsolved problem in astronomical spectroscopy. Nevertheless, it became clear that the interstellar absorption lines could not all be due to neutral or ionized atoms.

Later, in the late 1930s, Adams, Dunham and McKellar established the presence of CH, CN and CH^+ molecular species in the interstellar medium based on four sharp absorption lines seen in the optical spectra of several distant stars using Mount Wilson Observatory (Dunham [20] 1937, Adams [21] 1937, McKellar [22, 23] 1940) and laboratory data (Jenkins and Wooldridge [24] and Douglas and Herzberg [25, 26]). Three interstellar molecules were identified in four years, one of which was a positively charged ion. Detailed quantitative studies by Bates and Spitzer [27] in 1951, and its extension by Solomon and Klemperer [28] in 1972 and Herbst and Klemperer [29] in 1973, to understand the formation of these interstellar molecular species showed the crucial role of ion-molecule reactions.

1.2.2. RADIO OBSERVATION

The hydroxyl radical (OH) is a molecule with a ground state of ${}^2\Pi$ resembling CH. However, its optical resonance lines lie in the 3060 Å region, close to the atmosphere's edge of transmission. Due to interference from our own atmosphere's ozone absorption bands, it is challenging to observe these lines. Weinreb *et al.* [30] (1963) observed the first lines of OH near radio frequency 1665 MHz, which represents a transition between the Λ doublet components of the lowest rotational level $J = 3/2$ of ${}^2\Pi_{3/2}$ (hyperfine structure). The radio detection of OH

inspired many radio astronomers to consider the possibilities of detecting polyatomic molecule lines in the radio frequency range. Cheung *et al.* [31] succeeded in 1968 with NH₃ and shortly after with H₂O [32], both in emission. Snyder *et al.* [33] soon discovered formaldehyde (H₂CO) in absorption; numerous new compounds have been discovered annually, a trend that has continued at a nearly linear rate ever since [34].

1.2.3. INFRARED OBSERVATION

Gillett *et al.* [35] using ground observations, discovered three distinct emission bands in the 8 - 13 μm spectra of two planetary nebulae (NGC 7027 and 6572), ushering in a new era in astrochemistry in the early 1970s. Merrill *et al.* [36] reported the detection of a broad emission band in NGC 7027 two years later. Airborne observations also became feasible during that period for the first time. This allowed the Kuiper Airborne Observatory (KAO) to find two new, unreachable from the ground, powerful emission bands in NGC 7027 and an external galaxy (M82) [37, 38]. These characteristics were subsequently discovered to be widespread throughout the cosmos and closely related, forming the PAH family (PAH=Polycyclic Aromatic Hydrocarbons). Although the precise nature of the carriers of these features is still unknown, they have been collectively referred to as unidentified infrared emission (UIE) features. However, the hypothesis that PAH molecules serve as carriers has received significant support [39, 40].

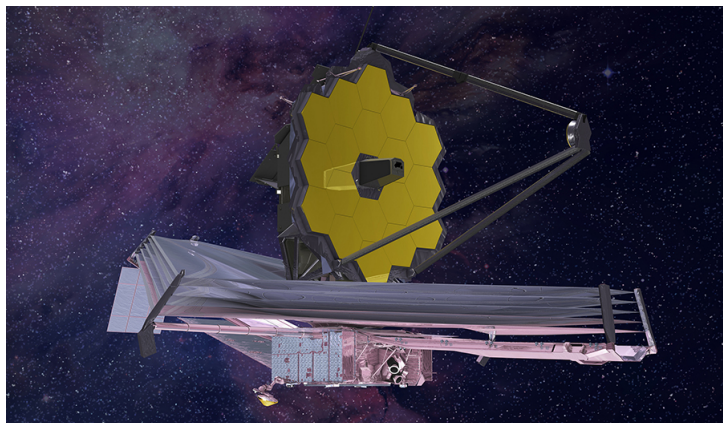


Figure 1.3.: James Webb Space Telescope - An infrared-optimized astronomical observatory (Credit: NASA)

Recently, the James Webb Space Telescope (JWST), as shown in Figure 1.3 was launched in late 2021. It is an infrared-optimized astronomical observatory which

will operate in near- ($0.6 - 5 \mu\text{m}$) and mid- ($5 - 28 \mu\text{m}$) infrared regions ¹ to address a range of astrophysical and cosmological questions, including the role of PAHs.

1.2.4. CURRENT STATUS

Astronomers are now aware of many additional diatomic and polyatomic molecules in the ISM. Furthermore, a large number of unknown species await their identification, such as the UIEs and DIBs. As of late May 2022, about 270 molecules have been detected in the ISM or circumstellar shells (CDMS database²), and $\sim 12\%$ of them are cationic species [34] see Figure 1.4. Interstellar molecules can be identified through their electronic (optical), vibrational (infrared), and rotational (radio) spectra as shown in Sections 1.2.1 through 1.2.3. However, most ($\sim 80\%$) of interstellar species are identified via their rotational transition [34] because of their low excitation temperature and distinct spectroscopic fingerprint. In conclusion, one can say that laboratory spectroscopic data are indeed vital in identifying these molecular species. However, it is difficult for highly reactive molecular ions, but their laboratory characterization and subsequent astronomical detection are important to understand the ion-molecule chemistry of ISM. Therefore, in the next section, a brief introduction to spectroscopy followed by a detailed review of spectroscopic methods especially for studying molecular ions are discussed.

1.3. SPECTROSCOPY

The Light of Knowledge is a common expression, but it fits especially in the spectroscopy context. Spectroscopy is the broad field of study that measures and interprets the electromagnetic spectra produced by the interaction of light, i.e., electromagnetic radiation, with matter as a function of wavelength or frequency. Most of what we know about atoms and molecules comes from examining their interactions with electromagnetic radiation; as a result of such interactions, various parts of the electromagnetic spectrum supply different types of information (see Figure 1.5). The molecular transitions such as rotational, vibrational and electronic excitation are characterized via interactions in different regions of the electromagnetic spectrum as shown in Table 1.1. Spectroscopic characteristics are like molecular fingerprints.

Spectrochemical analysis was invented in 1860 by Kirchhoff and Bunsen [10], but it saw limited use until the 1930s. Since the discovery of the first molecules in space by their optical spectra, i.e., CN and CH [20, 21, 22, 23], spectroscopy

¹<https://www.jwst.nasa.gov/content/observatory/instruments/index.html>

²<https://cdms.astro.uni-koeln.de/classic/molecules>

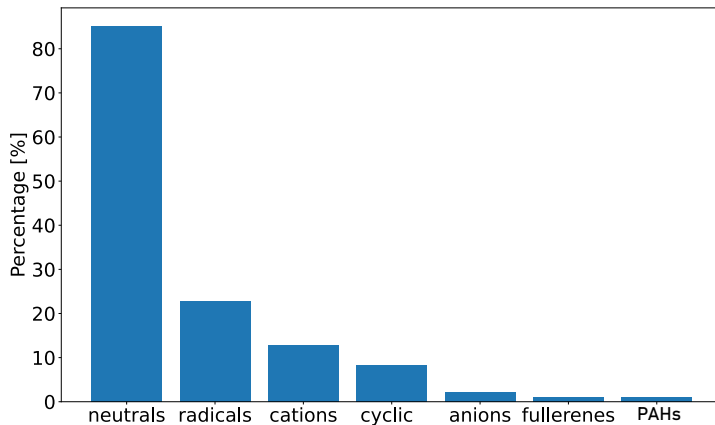


Figure 1.4.: Percentage of different classes of known interstellar molecules. Many molecules fall into more than one of these categories e.g. most radical species have a net neutral charge. Data is computed using *astromol - A Database of Molecules Detected in Space* python library [41]

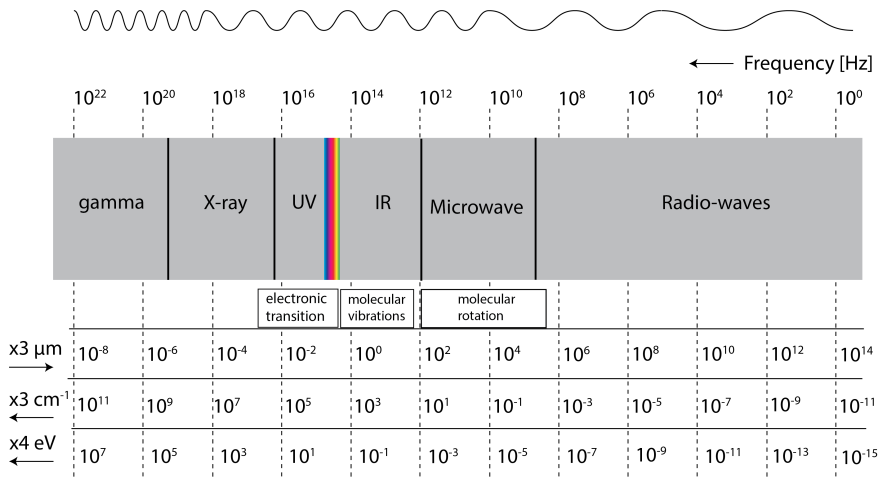


Figure 1.5.: Schematic diagram of the electromagnetic spectrum, the rainbow-coloured inset shows the visible spectrum. The vertical dashed line indicates a corresponding comparison to the different unit systems as labelled on the left, and “x3” indicates that the scale value is multiplied by factor 3.

has been successfully used in astronomy to identify new molecular species and determine physical and chemical conditions such as gas excitation temperatures

Table 1.1.: Dominant types of molecular transitions in each region of the electromagnetic spectrum

Region of Spectrum	Energy [cm ⁻¹]	Molecular transitions
<i>Ultraviolet (UV)</i>		
far	10 ⁶ – 50,000	Electronic
near	50,000 – 26,300	
<i>Visible (Vis)</i>	26,300 – 12,800	
<i>Infrared (IR)</i>		
near	12,800 – 4000	Vibrational
mid	4000 – 200	
far	200 – 10	
<i>Microwave (THz)</i>	10 – 0.01	Rotational

and chemical abundances. Over the past two decades, there has been a significant increase in the amount of accurate spectral data from astronomical observations over the accessible frequency range (from the UV-vis to the millimetre and centimetre wavelength region). A direct comparison with astronomical data is made possible by laboratory spectroscopic investigations of gas-phase molecules, which has significantly aided the interpretation of astrophysical findings (see Figure 1.6).

Traditionally spectroscopic measurements of vibrational and rotational transitions for molecules are recorded via direct absorption techniques to detect radiation absorption as a function of frequency or wavelength due to its interaction with the molecule sample. Since all of the atoms and molecules have distinct and distinguishable energy levels, a measurement of the absorption lines from incident radiation permits the identification of the absorbing species. The absorption spectrum is the variation in absorption intensity as a function of frequency (see Figure 1.7).

However, these conventional absorption techniques are very challenging to record spectra of gas-phase molecular ions, especially of highly reactive, open-shell species, since it is difficult to produce them with in sufficient number density. Another complication arises from background contamination from other species during the formation process. Oka's [42] search for the infrared spectrum of CH₅⁺ using a discharge through a CH₄–H₂–He mixture is a well-known illus-

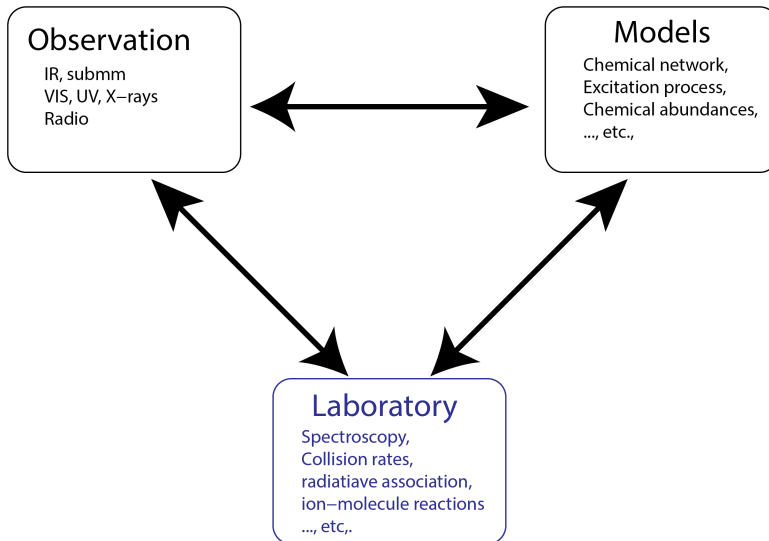


Figure 1.6.: The triangular approach of observations, models, and laboratory studies is necessary to address astrochemistry questions. Examples for every category are provided in smaller fonts with respective boxes. “Laboratory” implies both experimental and theoretical work. The blue coloured box indicates the area focused on in this thesis.

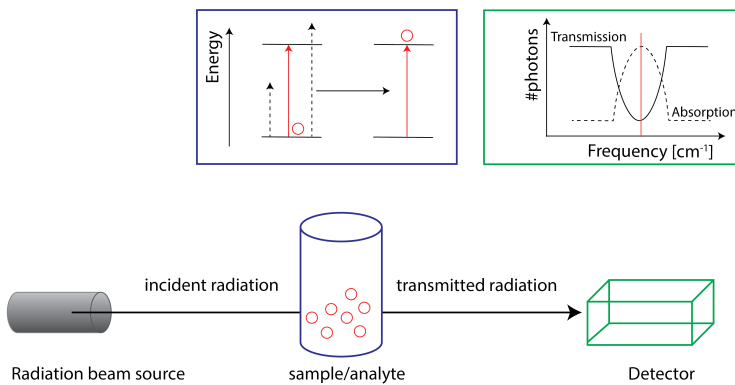


Figure 1.7.: Schematic diagram to describe the principle of absorption spectroscopy.

tration of this challenge. However, these limitations can be overcome by employing action spectroscopic methods based on sensitive mass-spectrometric tech-

niques, which measure the change in the chemical composition of ions when they interact with resonant radiation light instead of the absorption of photons by the molecular ions. Asvany *et al.* [43] successfully employed one such technique in a cryogenic ion trap to record the infrared spectrum of the elusive CH_5^+ molecular ion (see Section 1.5.1.3 and 1.5.1.4).

Action spectroscopy can offer several advantages, such as mass selection and storage in a cold ion trap, leading to uncontaminated spectra and narrow line widths. In the next section, we shall discuss the cryogenic ion trap techniques to isolate and confine molecular ions before continuing to action spectroscopy techniques.

1.4. CRYOGENIC ION TRAP

An electric field exerts a force on a charged particle, such as an atomic or molecular ion. Earnshaw's theorem states that it is impossible to maintain stable confinement (i.e., trapping) of charged particles by static electric fields. However, it is possible to trap ions in stable confinement using time-varying (rf - radiofrequency) electric fields due to an average confining force in all three directions. Since the ions are confined in a fast oscillating rf electric field, it is also known as radiofrequency ion trapping.

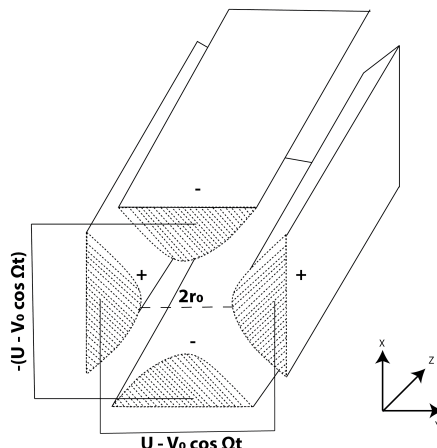


Figure 1.8.: Schematic diagram of a quadrupole mass filter. Ions enter and move along the z-axis as they oscillate in the x-y plane. The oscillation is regulated by applying DC (U) and radio frequency (RF) (V) potentials to each set of rods. Only ions with stable paths at the chosen U and V values will pass through the quadrupole mass filter.

Paul *et al.* [44] had developed the quadrupole ion trap, also known as the Paul trap, which is the most basic electric field geometry. He also developed the quadrupole mass filter technique [45] (see Figure 1.8). Using the combination of mass filter and ion trap, one can isolate and trap desired molecular ions with a specific mass-over-charge ratio (m/z). As a result, molecular spectroscopy in ions trap is routinely employed using action spectroscopic techniques [46, 47, 48], as discussed in more detail in Section 1.5.

The trapped ions are usually cryogenically cooled to allow low temperatures experiments. Ion spectroscopic techniques typically employ collisional cooling with neutral buffer gas [49, 50]. In the next section, we shall discuss the advantage of using a higher-multipole order ion trap, the 22-pole ion trap developed by Gerlich [51], and further improved by Asvany and Schlemmer [52] for low-temperature experiments under interstellar conditions.

1.4.1. 22-POLE CRYOGENIC ION TRAP

As discussed in Section 1.2.1, since the 1950s, ion chemistry under interstellar medium conditions has gained interest in exploring ion-molecule reactions at low temperatures and low-density [53, 54]. Cryogenic ion trap experiments are commonly used to investigate laboratory ion-molecule reactions relevant to astrochemistry, and many astronomical objects have temperatures as low as 6 K [11]. However, in quadrupole traps, it is difficult to achieve low temperatures (kinetic and internal ion temperature) below < 10 K [55]. Therefore, higher-order multipole traps with large field-free zones are required for low-temperature astrochemical experiments.

In a seminal review by Gerlich [55] titled *Inhomogeneous rf fields: a versatile tool for the study of processes with slow ions*, the ideas of ion guiding and trapping using multipole fields have been described in great detail. Most notably, Gerlich [51] also pioneered the development of the 22-pole ion trap (see Figure 1.9a) for studies of ion-molecular reactions. The sensitivity and efficiency at low density and low temperature in 22-pole ion trap experiments is a major advantage over ion-molecule reaction studies at 300 K using other well-established techniques such as flowing afterglow (FA) [56], ion cyclotron resonance (ICR) ion traps [57], and selected ion flow tube experiments (SIFT) [58]. With the development of the cryogenic 22-pole ion traps, significant advancements have occurred in studying low-temperature processes such as radiative association and three-body collisional processes in molecular complex formation [54, 59, 60].

The 22-pole cryogenic ion trap is also employed for high-resolution molecular spectroscopy of electronic [61, 19], vibrational [43] and rotational [3] transitions (see Section 1.5.1 and 1.5.2), including the first laboratory confirmation of C_{60}^+ as

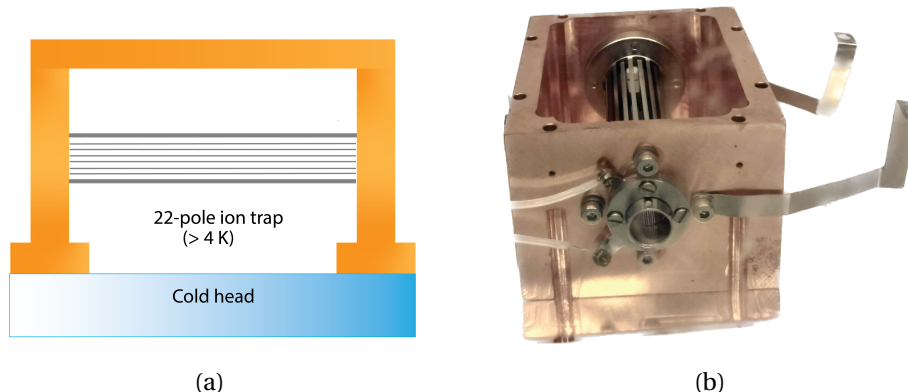


Figure 1.9.: (a) Schematic drawing of the 22-pole cryogenic ion trap (grey) in copper housing (orange) mounted onto cryogenic coldhead. (b) A photograph of the 22-pole ion trap mounted inside copper housing.

the carrier of two DIBs by Campbell *et al.* [19], using a 22-pole ion trap. It has gained even more popularity during the past two decades as a tool for researching ion-molecule interactions, and molecular ion spectroscopy [62, 63, 64, 65, 66].

In the next section, the action spectroscopic techniques developed in cryogenic ion traps for high-resolution molecular ion spectroscopy will be discussed.

1.5. ACTION SPECTROSCOPY

As discussed in Section 1.3, in contrast to absorption spectroscopy, which detects the effect molecules have on light, action spectroscopy measures effect of light on molecules. Ions are the optimum choice for action spectroscopy methods because of their charge, which makes it easy to guide, mass select and trap them efficiently. This section will focus only on vibrational and rotational “gas-phase action ion spectroscopy”.

1.5.1. VIBRATIONAL ACTION SPECTROSCOPY

Photodissociation of isolated ions after light absorption (as long as the energy of the absorbed photons is higher than the bond dissociation threshold) is likely one of the most straightforward experimental techniques. So, most gas-phase action ion spectroscopy methods rely on the detection of charged products of dissociation or the loss of the parent ion signal after one or more photons are absorbed. In 1973, Dunbar [67] first investigated photodissociation in the visible

spectral range. Soon after, Okumura *et al.* [68] studied photodissociation in the infrared region yielding the vibrational spectra.

In general, a single IR photon's absorption is insufficient to promote the breakdown of covalent bonds. However, several ways to circumvent this constraint are described in the following sections.

1.5.1.1. TAGGING PHOTODISSOCIATION ION SPECTROSCOPY

The most straightforward technique to overcome the limitation is to utilise a loosely bound “tag” to the molecular ion that detaches upon absorption of a single IR photon. The tags are chosen to have minimal effect on the structure of the ion core, i.e., they should be very weakly bound. Therefore, rare gas atoms such as He, Ne or Ar are preferred tagging agents.

The formed weakly bound complexes are dissociated as a result of resonance photon absorption as shown in Figure 1.10 and the vibrational spectra are recorded as a function of IR frequency as shown in Figure 1.11. This process is known as “photo-dissociation” or “pre-dissociation”. The very well-known technique using this approach for measuring vibrational transitions is called “InfraRed Photo-Dissociation” (IRPD) spectroscopy.

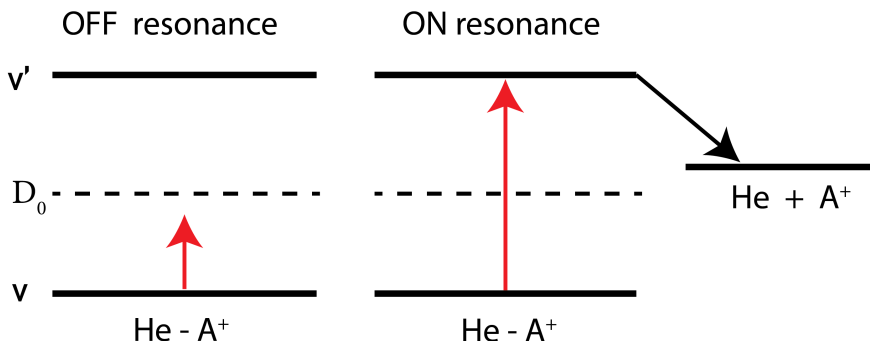


Figure 1.10.: Schematic drawing of the IRPD method. $\text{He}-\text{A}^+$ represents the weakly bound helium complex of molecular ion A^+ , and D_0 indicates the complex dissociation limit.

Yuan T. Lee demonstrated the first IRPD action spectroscopy technique [68] for hydrogen cluster ion, which several groups further developed [69, 70, 71] using molecular beam experiments. However, in the molecular ion beam, the small interaction time between the ion and tag and ion and photons ($\sim \mu\text{s}$ range, flight time of ions) is a disadvantage for efficient complex formation and dissociation, respectively.

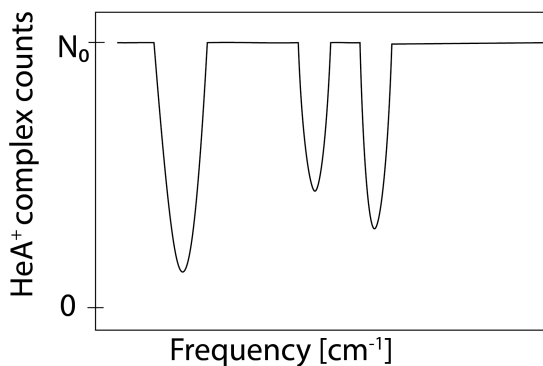


Figure 1.11.: Simulated IRPD spectrum measuring complex counts as a function of frequency. N_0 indicates the initial background counts, while the counts drop due to the dissociation of the complex at the resonance frequency.

Cryogenic ion trap experiments overcome these restrictions [72, 73, 65, 74, 75] by storing for longer duration ($\geq 1\text{s}$) and by using cryogenic cooling to relax the molecular ion to its vibrational and electronic ground state. The low temperatures in the ion trap ($> 4\text{ K}$) also result in a high tagging efficiency even for weakly bound complexes [76, 77], which is an important factor since the tagging method is predicated on the notion that the binding of the tag does not significantly alter the structure of the original ion. Consequently, the spectra produced from tagging spectroscopy can be correlated with the structure of "bare" ions.

The IRPD technique is employed in this thesis to characterize vibrational transitions of the molecular ion. Section 2.2 discusses the integration of this technique into our 22-pole cryogenic ion trap instrument (Section 2.1). The following sections discuss several other methods developed for vibrational action spectroscopy in cryogenic ion traps.

1.5.1.2. IR MULTI-PHOTON DISSOCIATION (IRMPD)

As discussed above, the energy of a single infrared (IR) photon is insufficient to cause dissociation in the majority of untagged ions. However, numerous photons can be absorbed when employing high-power light sources. The combined sum of the absorbed energy thus overcomes the dissociation energy limit, as shown in Figure 1.12.

In 1973, Isenor and coworkers [78] were the first to notice this IRMPD effect

when they exposed SiF_4 vapour to powerful CO_2 laser pulses. This study was quickly replicated in laboratories worldwide, and it was later shown that many different types of molecules could undergo infrared multiple-photon dissociation or isomerization [79, 80, 81]. However, it was not until the 1990's that widely tunable free electron IR laser sources with adequate pulse energies became available, launching a new infrared ion spectroscopy area. Oomens *et al.* [82] and Lemaire *et al.* [83] demonstrated the potential of a widely tunable infrared free-electron laser (FEL) in the study of the IR spectroscopy of mass-selected ions in an ion trap.

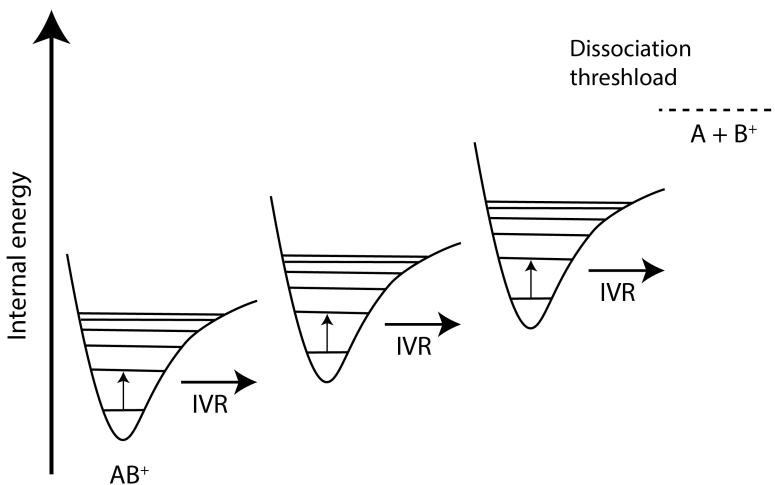


Figure 1.12.: Schematic drawing of the Infrared multi-photon dissociation (IRMPD) spectroscopy. AB^+ represents molecular ion consisting of A and B chemical fragments. Figure adapted from [84].

Extensive experimental and theoretical research investigated the fundamentals of IR multiple-photon excitation in polyatomic molecules [85, 86, 87, 88]. IRMPD is a low-energy fragmentation method that requires absorbing many photons of IR radiation before dissociation occurs. Vibrational potentials are inherently anharmonic, and absorption of tens to hundreds of photons occurs in a non-coherent manner. This effect is often referred to as the anharmonicity bottleneck [89]. Before the subsequent photon is absorbed, intramolecular vibrational redistribution (IVR) swiftly spreads the energy stored in the excited vibrational coordinate over all other vibrational degrees of freedom. The molecule is slowly heated, and dissociation typically follows the lowest-energy fragmentation pathway.

However, this poses a difficult challenge to investigate small molecular ions using IRMPD because the method requires a high density of vibrational states, which guarantees that there are always a lot of vibrational eigenstates such that the IVR is feasible. Therefore IRMPD is typically well-suited for larger molecular ions. In this thesis, only smaller molecular ions (≤ 7 atoms) are investigated; hence IRPD is employed, as mentioned in the previous section.

1.5.1.3. LASER INDUCED REACTIONS (LIR)

LIR combines the benefits of trapping molecular ions in a cryogenic ion trap with the idea of using a chemical reaction to determine the ion's internal state. In the late 1990s, Schlemmer *et al.* [90] developed LIR for spectroscopy by measuring the vibronic N_2^+ ($\text{A}^2\Pi_u \leftarrow \text{X}^2\Sigma_g$) spectrum by excitation with visible laser photons to overcome the endothermic energy of a charge-transfer (CT) reaction as shown in equation 1.1. Counting the laser-induced product ions as a function of laser frequency yields the spectroscopic signal (see Figure 1.13).

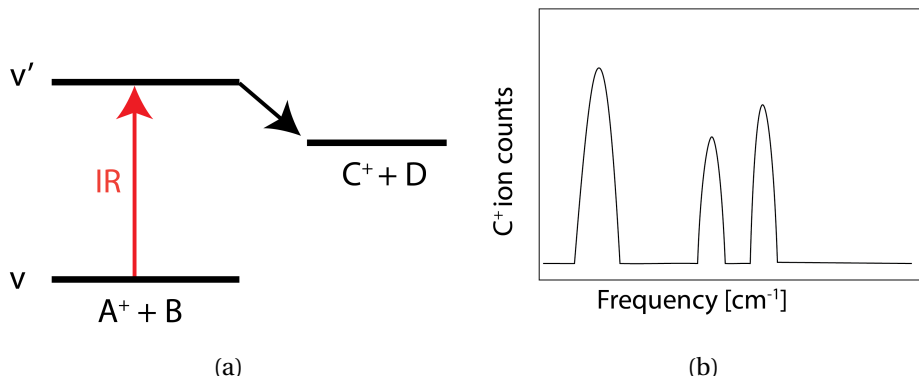
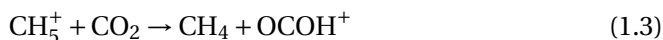


Figure 1.13.: Schematic description of (a) bimolecular reaction initiated by laser excitation suitable for LIR spectroscopy, (b) LIR signal as a function of frequency detected by monitoring the product counts.

Several endothermic reaction systems have been studied with the LIR method for bimolecular reactions, such as hydrogen abstraction and proton transfer (see

Eq. 1.2 and 1.3), to record vibrational transitions of reactant C_2H_2^+ [91, 92, 93] and CH_5^+ [43], respectively, by detecting the laser-induced products C_2H_3^+ and OCOH_2^+ , respectively.

1.5.1.4. LASER INDUCED INHIBITION OF HE ATTACHMENT (LIICG)

The requirement for an endothermic chemical reaction with a neutral reaction partner is an obvious limitation of the LIR method. Acquiring endothermic energy for chemical reactions is challenging, especially for highly reactive molecular ions. Also, the endothermicity cannot be too high since it needs to be overcome by the absorption of a single infrared photon. Another limitation is that since the cryogenic trap has very low temperatures, the neutral reaction partner should not condense in the trap. These conditions limit the use of LIR.

LIICG takes advantage of the fact that the excitation of molecular ions can inhibit the ternary attachment of He atoms. Maier and Gerlich [61] pioneered this method by measuring the electronic transition of N_2^+ ($\text{A} \ ^2\Pi_u \leftarrow \text{X} \ ^2\Sigma_g$) using a 22-pole cryogenic ion trap.

First vibrational LIICG was demonstrated for rovibrational transitions in the floppy CH_5^+ molecular ion by Asvany *et al.* [63] by forming $\text{CH}_5^+ - \text{He}$ complexes and observing an on-resonance decrease in the number of $\text{CH}_5^+ - \text{He}$ due to laser-induced inhibition of helium attaching to CH_5^+ (not via destruction of $\text{CH}_5^+ - \text{He}$ as in IRPD). The vibrational LIICG has been employed to record many other molecular ions such as O_2H^+ [73], CH^+ [94], H_3^+ , H_2D^+ and D_2H^+ [95], CD_2H^+ [96], CH_2NH_2^+ [97], CN^+ [98]; HHe_2^+ and HHe_3^+ [74].

Interestingly, the ternary rate coefficient for He attachment can be affected by rotational excitation, even though rotational photons only carry a fraction of energy compared to vibrational photons. Section 1.5.2.3 describes how to use this phenomenon to our advantage to measure high-resolution molecular ions' rotational spectra.

1.5.2. ROTATIONAL ACTION SPECTROSCOPY

Action spectroscopy for measuring rotational transitions is very challenging since the rotational transition energies are much lower than vibrational or electronic states (see Table 1.1). While vibrational and electronic action spectroscopic methods have been available for trapped ions and ionic clusters since the 1980s, the first rotational action spectroscopic methods appeared only a decade ago from Schlemmer's group [99].

This section provides a brief summary of the detailed review by Asvany and Schlemmer [48] but focuses only on rotational action spectroscopic methods. Figure 1.14 shows the summary of rotational action spectroscopic methods schematic

diagrams.

1.5.2.1. ROTATIONAL LIR

Schlemmer and coworkers showed the first realization of pure rotational action spectroscopy in a cryogenic trap using a direct-LIR method (as discussed in Section 1.5.1.3) [100]. Using this approach, they measured the lowest-lying rotational transitions *para*-H₂D⁺ and *ortho*-D₂H⁺, two astronomically important molecular ions that exhibit large rotational energy spacing (1.37 THz and 1.48 THz for the ground state transitions, respectively). The on-resonance laser-induced reactions of H₂D⁺ and D₂H⁺ held in a cold ion trap increases the reactivity (producing H₃⁺ and H₂D⁺, respectively) with a neutral H₂ reaction partner. Therefore the rotational transitions of the investigated ions are reflected in the yield of the reaction products as shown in Figure 1.14a.

1.5.2.2. DOUBLE RESONANCE METHODS

As discussed in Section 1.5.1.4 there are limitations to the direct-LIR technique. Therefore further rotational action spectroscopic techniques were later developed to generalise the scheme for a wide range of molecular ions, such as using a double resonance approach. A vibrational action spectroscopy scheme can be used to perform high-resolution rotational spectroscopy by double resonance. In other words, if a molecule has a vibrational action spectroscopy scheme with a rotational resolution, the spectroscopy can easily be extended into the rotational domain by a double resonance approach; the possibilities are as follows:

via LIR: As shown in Figure 1.14b, this method uses a combination of infrared (IR) and Terahertz (THz) radiation to irradiate ions. The frequency of the IR photon is kept fixed on a rovibrational transition. The signal is monitored by counting the number of the product ions produced as a function of the THz frequency [101, 102]. The signal can be depletion or gain depending on whether the IR is fixed at a rotational ground or excited state.

via predissociation: Predissociation is another effective vibrational action spectroscopic technique (see Section 1.5.1.1). Based on prior IR predissociation work by Dopfer and collaborators [103], the vibrational-rotational predissociation via double resonance approach (see Figure 1.14c) has been shown for the first time for the He–CH₃⁺ complex [104].

via electron detachment: This high-resolution rotational action spectroscopy via double resonance schemes method is suitable for molecular anions. Wester and coworkers [105] devised an action scheme using state-selective electron photodetachment via fixed “visible” (vis) frequency radiation (see Figure 1.14d), and demonstrated it by measuring the two lowest rotational transitions of OD[−]. The

molecular anion counts are monitored as a function of frequency (rotational photon). On rotational resonance, the radiation populates the initial state probed by a fixed-vis laser which subsequently increases the electron photo-detachment, thereby decreasing molecular ion counts (depletion signal).

via LIICG: In LIICG, excitation of the bare cation can inhibit He-attachment in a ternary collision process at 4 K (see Section 1.5.1.4), and this is utilised in this method. The IR laser is fixed at a rovibrational transition; the He-cation molecular ion complexes are monitored as a function of THz frequency (see Figure 1.14e). The depletion in complex counts on the rotational transition resonance frequency of the bare cation is the signal. It has been demonstrated for protonated methenamine, CH_2NH_2^+ [97].

1.5.2.3. ROSAA

The rotational high-resolution rotational action spectroscopy technique employed in this thesis is ROSAA which is an abbreviation of to ROTational State-dependent Attachment of rare gas Atoms. This method exploits that the ternary attachment of neutral atoms (typically He) depends on their rotational quantum state since the ternary attachment of He is only hindered (or changed, see Figure 1.14f) instead of inhibited as discussed in LIICG (see Section 1.5.1.4). Brünken *et al.* [99] demonstrated it by measuring four pure high-resolution rotational transitions for $\text{C}_3\text{H}^+ ({}^2\Sigma)$.

The fact that helium atoms can theoretically be attached to any cation at low temperatures (< 15 K) is a significant advantage of this approach. Several molecular cations have been studied in the laboratory for the first time with the state-dependent He attachment approach. High-resolution pure rotational transition frequencies have been measured using this technique for $\text{l-C}_3\text{H}^+$ [99], CF^+ [106], SiH^+ [107], HCO^+ [108], CD^+ [3], CH^+ and ${}^{13}\text{CH}^+$ [94], NH_3D^+ [106, 109], NH_2D_2^+ and NHD_3^+ [109], CN^+ [110], CH_2NH_2^+ [97], CH_3NH_3^+ [111], NO^+ [112], CCl^+ [113] and CO^+ with resolved Zeeman components from earth magnetic field [114, 3] (see Chapter 7).

As mentioned above, the ROSAA technique is employed in this thesis for characterising the rotational transition of molecular cations. More detail and in-depth analysis of ROSAA action spectroscopic schemes are explored using numerical simulations (Section 2.3.1 and 2.3.5) for CD^+ (see Section 6.7 and 6.8) and CO^+ (see Chapter 7) ions.

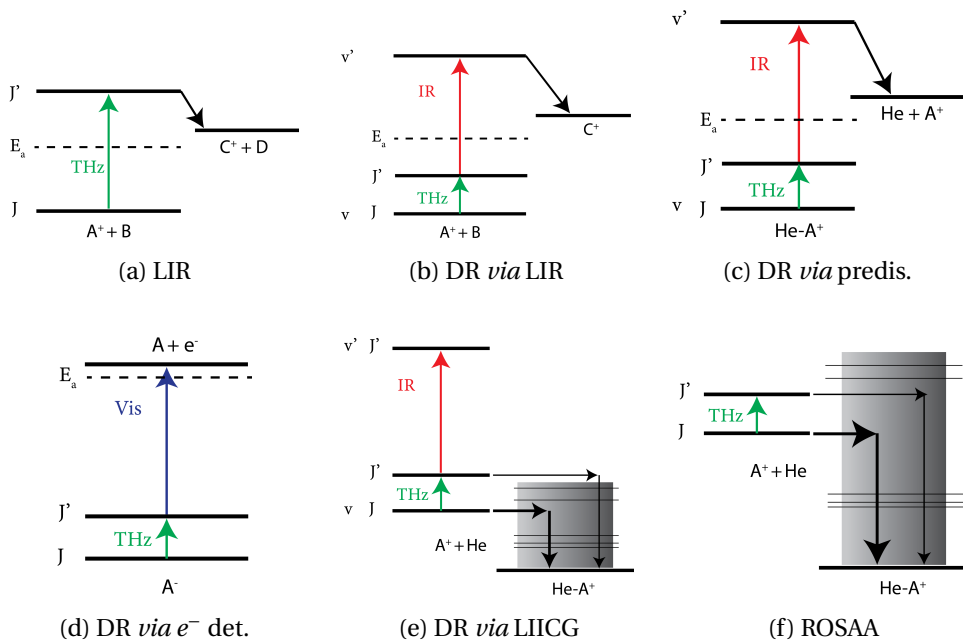


Figure 1.14.: Schematic diagrams of rotational action spectroscopic methods. The captions indicate the corresponding name of the method. DR stands for double resonance. “predis.” and “det.” in (c) and (d) correspond to “predissociation” and “detachment”, respectively. The symbol A and B indicates molecular species while superscript (such as A^+) indicates molecular cations. He indicates a helium atom while $He-A^+$ indicates a weakly bound helium-ion complex.

1.6. THIS THESIS

This thesis titled “Rotational and vibrational action spectroscopic studies on cold molecular ions” discusses action spectroscopic techniques employed to characterise molecular ions in a cryogenic ion trap spectroscopically. Molecular ions relevant to astrochemistry, especially in the interstellar medium and planetary atmospheres, are mainly focused on and are discussed in respective chapters.

Chapter 2 “*Experimental and theoretical methods*”: gives an overview of the experimental setup used in this study, including the ion source, cryogenic trap and detector. A detailed description of the action spectroscopic methods employed in this thesis to characterize molecular ions’ rotational and vibrational transitions is discussed. Technical details such as determining number density with uncertainty, calibration of instruments and instrument setup are discussed in detail.

Chapter 3 “*Laboratory gas-phase vibrational spectra of $[C_3H_3]^+$ isomers and isotopologues by IRPD spectroscopy*”: In this chapter, we investigated broadband gas-phase Ne-IRPD spectra of both linear and cyclic forms of $[C_3H_3]^+$ and reported the first gas-phase IR spectra of the corresponding $[C_3D_3]^+$ isomers. Various high-level coupled-cluster methods are benchmarked. WE also investigated the isomeric ratio quantification of $[C_3D_3]^+$ produced with different ion source conditions and precursors.

Chapter 4 “*Infrared predissociation spectroscopy of protonated methyl cyanide, CH_3CNH^+* ”: In this chapter we present a comprehensive experimental and quantum-chemical study of the vibrational spectrum of Ne- CH_3CNH^+ . A focus is on the influence of the weakly-bound neon atom on the infrared pre-dissociation experiments. We also demonstrated an efficient computational approach to provide accurate estimates of anharmonic vibrational frequencies of the bare ion and complex.

Chapter 5 “*A vibrational action spectroscopic study of the Renner-Teller and spin-orbit affected cyanoacetylene radical cation HC_3N^+* ”: In this chapter, we present the investigation of the vibrational transitions of HC_3N^+ , an open shell linear molecular ion. The breakdown of the Born-Oppenheimer approximation due to the Renner-Teller (RT) effect (vibrational coupling) is analysed using an effective Hamiltonian approach. The influence of the tag in IRPD, especially on the bending modes of RT-affected open-shell, is discussed in detail.

In these first chapters, the vibrations transitions on the potential candidates of interstellar molecular ions are experimentally and theoretically investigated

in detail, and discussed from various perspectives, such as isomer quantification, the influence of tag on smaller molecular ions and RT-affected open-shell species. In the following chapters, the investigation focuses on high-resolution pure-rotational action spectroscopy. Rotational transitions provide distinct molecular fingerprints, and importantly, due to their low excitation temperature, most interstellar species are identified through their rotational transitions. The molecular ions discussed above are potential interstellar and also (exo-)planetary candidates. On the basis of their vibrational characterisation, rotational characterisation will be followed in future. Therefore, the following two chapters discuss the implementation and investigation of a novel rotational action spectroscopic technique (ROSAA), which utilises a change in rare-gas atoms attachment rates for measuring pure rotational transitions of bare ions. The method is illustrated for a closed and for the first time, an open-shell molecular ion.

Chapter 6 “*Kinetics of CD⁺ ion with He buffer gas*”: In this chapter, we report a systematic study and detailed analysis of the CD⁺ reaction with helium buffer gas atoms with and without the presence of radiation resonant with the $J = 0 - 1$ rotational transition of CD⁺ ion. This is important in investigating the ROSAA signal intensity (i.e., measured rotational transition intensity) processes using numerical simulation. Consequently, a robust numerical simulation model was developed to predict the intensity of the rotation transition of the molecular ions of interest.

Chapter 7 “*The Zeeman effect in CO⁺ observed with rotational action spectroscopy*”: In this chapter, the high-resolution rotational transition of CO⁺, an open-shell molecular ionic species, is investigated using the ROSAA technique. In addition to an unpaired electron fine structure splitting, a (partly) resolved hyperfine Zeeman splitting is observed due to Earth’s magnetic field. The measured signal intensity is investigated using the developed numerical simulation model.

2

EXPERIMENTAL AND THEORETICAL METHODS

2.1. FELION INSTRUMENT

The various spectroscopic and kinetics experimental studies reported in this thesis have been performed using the 22-pole cryogenic ion trap instrument (referred to as FELion), which has been built in the Cologne Laboratory Astrophysics group and installed permanently at the widely tunable “Free Electron Lasers for Infrared eXperiments” (FELIX) [115] in Nijmegen, The Netherlands. As shown in the schematic diagram (Figure 2.1), the FELion instrument consists of an ion source, quadrupole mass filters, an ion trap and a detector. A detailed description of the FELion instrument has been given by Asvany *et al.* [63], Kluge [116] and Jusko *et al.* [65]. This section will provide a brief discussion focusing on the

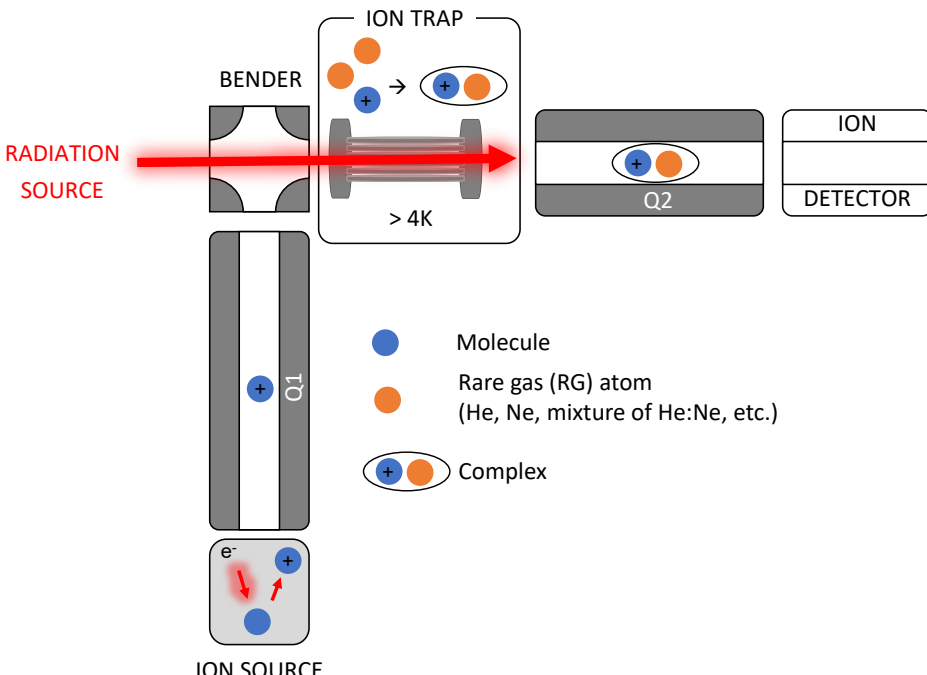


Figure 2.1.: Schematic drawing of the FELion ion trap setup. The 22-pole ion trap is coupled in-between two quadrupole mass filters (Q1 and Q2). The ions are guided into the trap from Q1 via quadrupole bender (labelled BENDER). The trap contents are extracted after irradiation from the radiation source into Q2 to filter desired product molecular ions and then guided into a Daly type detector to be counted.

FELion instrumental apparatus used in this study.

2.1.1. ION SOURCE

One of the main challenges when studying highly reactive molecular ions is their production. The primary molecular ions are produced in the ion source using electron ionisation (EI), where an energetic electron (typical 20 – 70 eV) interacts with molecules. Dempster [117] first demonstrated this process for the solid phase and later Bleakney [118] for the gas phase molecules. The ionisation process produces dissociative and non-dissociative products, i.e., ionised fragments and ionised parent molecules, respectively. A short pulse of produced ions is then extracted into the first quadrupole (Q1) by applying an adjustable pulse on the exit electrode (referred to as B0, see Figure 2.2). This section will discuss the types of ion sources coupled to the FELion instrument.

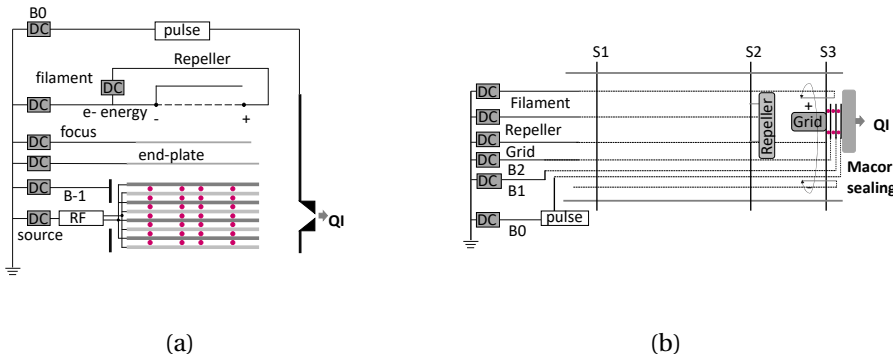


Figure 2.2.: Schematic drawing of the ion sources. The various components are labelled, and the corresponding connections are indicated by solid lines for (a) storage source and (b) non-storage (S1, S2 and S3 are grounded base plates for support). The pink circles represent ruby balls for insulation between connected electrodes. The labelled Macor sealing ring on top of the B0 electrode is placed to seal the ion source chamber and prevent any accidental contact between B0 and the Q1 rods.

Storage source: One type of ion source is a radiofrequency storage source, developed by Gerlich and Horning [54]. The primary ions are generated and stored (\sim s) in this source using an in-homogeneous RF field and DC potentials. The benefit of storing the ions in the source is that the produced molecular ions can undergo collisions with the background neutral gas or gas mixtures (typically at

pressures of $10^{-6} - 10^{-5}$ mbar and a temperature of ~ 400 K), leading to the production of secondary ions via chemical reactions and de-excitation and thermalization of the ions.

2

As depicted in the schematic diagram (Figure 2.2a), the storage ion source consists of a stack of eight “double H-shaped” molybdenum plates (1 mm thickness), which are connected and electrically insulated by ruby balls (1 mm diameter). Four of the eight plates are connected alternately, and a typical 50 – 280 V RF voltage is applied. The filament wire (rhenium 99.97%, 0.2 mm diameter) is covered by the “repeller” and the “focus”, which are made up of 0.5 mm thick molybdenum plates. The filament typically operates around ~ 5 V and 2.8 A and is held on a negative potential corresponding to the electron energy. The repeller is connected to the negative end of the corresponding filament. The DC voltages applied to the “focus” and “repeller” help to focus and accelerate electrons into the source. The B0 and B-1 are mounted at the front and back of the source apertures, respectively. This combination helps to confine the ions in the axial direction of the source by applying corresponding DC-potentials. The B0 can be pulsed to generate a short pulse (typically 10–100 ms) of ions for the experiments.

Direct EI source: The other type of ion source is called “direct EI”, which produces primary ions by “direct electron ionisation” but they are not stored. This source is a simple combination of repeller, grid, filament and lens, as shown in Figure 2.2b. The filament wire is made up of a 0.25 mm Rhenium wire mounted in a circular arrangement around the grid covering 270 deg arc length. The filament’s power supply (~ 5 V / 2.8 A) is floated to 10 – 70 eV and, together with the grid voltage (1 – 4 V), acts as an electron gun which accelerates the electrons to provide the necessary energy to ionise molecules in the grid region. The repeller (typically operated around -5 to -15 V) is mounted on a grounded base plate with ceramic insulators and helps to focus and accelerate electrons into the grid region. The einzel lens (electrodes) set up towards the end consists of B0, B1 and B2 electrodes (insulated by ruby balls) to confine the ions in the axial direction of the source by applying corresponding DC-potentials.

Depending on the nature of the study, storage and direct EI sources can be used accordingly. The storage ion source provides the benefit of storing the formed ion for a few seconds, thereby often quenching ions to the most stable isomeric form and the electronic ground state by undergoing (reactive) collision with the background gas. Additionally, the storage source can produce secondary ions via reactions with the background gas, e.g., protonation reactions. An efficient protonation process is, for example, discussed in more detail in chapter 4. On the other hand, the direct EI source allows us to produce also energetically higher-lying isomeric forms of ions and to characterise, for example, their formation routes via dissociative ionization. In Chapter 3, a detailed investigation of two

different isomers (cyclic and linear form) are discussed using both direct EI and storage ion source.

Once the ions are formed in the source, a short pulse of ions is extracted into the first quadrupole mass filter (Q1). Adjusting the RF and DC potential voltages can further isolate and guide the molecular ion of interest into the trap, as will be discussed in the following section.

2.1.2. ION TRAP AND DETECTOR

The heart of the FELion instrument is a 4 K cryogenic 22-pole ion trap coupled in-between two quadrupole mass filters (Q1 and Q2). The Q1 and Q2 are perpendicularly angled. Therefore, the produced mass-filtered target ions from Q1 are guided into the trap by passing via a quadrupole bender, as shown in Figure 2.1. The 22-pole ions trap's design details are described by Asvany *et al.* [52]. The trap RF is generated using amplified output (10 W amplifier) of a direct digital synthesizer (DDS) and operated at the trap resonance of around ~ 18.3 MHz.

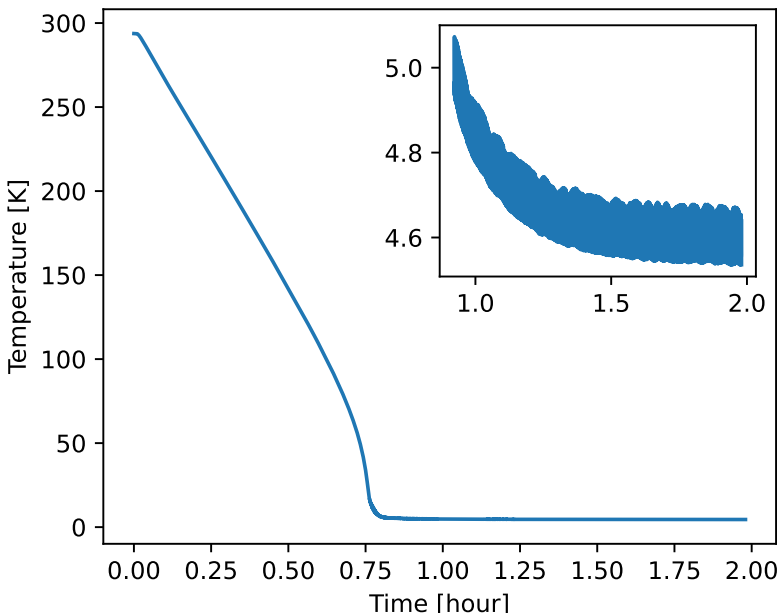


Figure 2.3.: Cool-down behaviour of the 22-pole cryogenic ion trap from room temperature using a He cryostat. The inset shows a detailed view of temperatures below 5 K.

The ion trap is mounted inside a copper housing and directly onto a cold head (Sumitomo RDK-408D2), allowing to cool it down to a minimum temperature of around 4 K using a He cryostat (see Figure 2.3). The FELion instrument's 1 Hz machine cycle is synchronised with the cold head and FELIX laser (see Section 2.2.2) for infrared experiments. The temperature can be varied between 4 – 40 K using a thermo-strip (Kapton material, providing up to 40 W heating power) and monitored using an attached Si diode (Lakeshore DT-470-CU-13). The ions are kinetically and internally cooled by collisions with buffer gas atoms such as He or He:Ne mixture. However, it should be noted that the ion temperature is typically higher than the nominal trap temperature [119] (see Section 2.3.4). The buffer gas is admitted directly into the trap region at high number densities (10^{14} – 10^{15} cm⁻³, see Section 2.5.1 for number density measurements inside trap) either continuously or via a pulsed piezo valve depending on the experimental methods.

The ions can be stored in the trap for up to 10 s (depending on the experiment) and then extracted from the trap. Subsequently the parent or possible product ions are mass-selected with a second quadrupole mass filter (Q2) into a single-ion counting Daly type detector [120] for analysis. The pulses generated by the detector are amplified and discriminated (Phillips Scientific model 6906, 300 MHz) and counted with a gated 100 MHz counter (Ortec model 996).

In the next section, we shall discuss the spectroscopic methods employed in the 22-pole cryogenic ion trap (FELion instrument) for vibrational and rotational transition measurements of molecular ions.

2.2. VIBRATIONAL SPECTROSCOPY

2.2.1. EXPERIMENTAL METHOD

The action spectroscopic method employed to record the vibrational transitions of the molecular ions in this study is the well-known “infrared predissociation (IRPD)” spectroscopy, as introduced in Section 1.5.1.1.

In our IRPD experiment, the primary target ions are formed in the ion source and mass filtered into the 22-pole ion trap. A short He or He:Ne mixture pulse (50-100 ms) is introduced into the trap (typically at 4-9 K range). The molecular ion can form a weakly bound complex at low temperatures (< 10 K) and high number density (10^{15} cm⁻³) via three-body collisions, as discussed in more detail in Section 6.7.3. The tagging efficiency in forming the complex depends on the interaction strength between the molecular ion and the tag (He or Ne). This study typically obtains > 10% tagging yield; more details on different molecular ions are described in their respective chapters. For tagging partners, the neon atom is often preferred, although the helium is better suited for IRPD studies

due to its lower polarizability, lower binding energy, and thus minimal perturbation on the ionic vibrational frequencies. However, for the same reason, since the He-complex is very weakly bound, it dissociates due to trap heating from a high-power radiation source, such as the free-electron laser employed in this study. The influence of the Ne tag on bare ion vibrational modes is discussed in corresponding chapters.

The trap contents are stored in the ion trap for about 1-2 s while being irradiated with pulsed IR radiation as a function of frequency, and the formed complexes are then mass filtered and counted. The dissociation of the complex at resonance transition yields the signal, thereby characterising the vibrational mode of the ionic complex. The IR radiation source and data normalising procedures are described in the following sections.

2.2.2. IR RADIATION SOURCE

The IRPD measurements for characterising the infrared signature of ionic complexes in this study are performed with two types of infrared (IR) radiation sources, the free-electron lasers FELIX and an optical parametric oscillator/amplifier (OPO/A) system. In this section, we shall briefly describe the interface of the FELion ion-trap instrument with these IR radiation sources.

2.2.2.1. FELIX

FELIX stands for “Free Electron Lasers for Infrared eXperiment”; as the name suggests, it is a free-electron laser (FEL) facility, and the FELion instrument is located as one of its user-stations [65]. This section briefly introduces the operating principles of FEL, followed by a detailed description of the FELIX laser system coupled to the FELion instrument used in this study for infrared experiments.

Operating principles: In a conventional laser device, the laser light is generated/emitted through optical amplification based on the stimulated emission of electromagnetic radiation from e.g. an atom or a molecular excitation. A free-electron laser system however employs relativistic electrons as a gain medium. As shown in Figure 2.4, an electron accelerator provides a beam of relativistic electrons followed by an undulator (periodic arrangement of magnets with alternating poles) in which the electrons perform a transverse oscillation and travel along the axis of the undulator. Two highly reflective mirrors form an optical laser resonator in which the radiation is amplified. By adjusting the electron beam’s energy or the magnetic field strength of the undulator, the wavelength of the radiation emitted, λ_r , can be easily tuned and given by [115]:

2

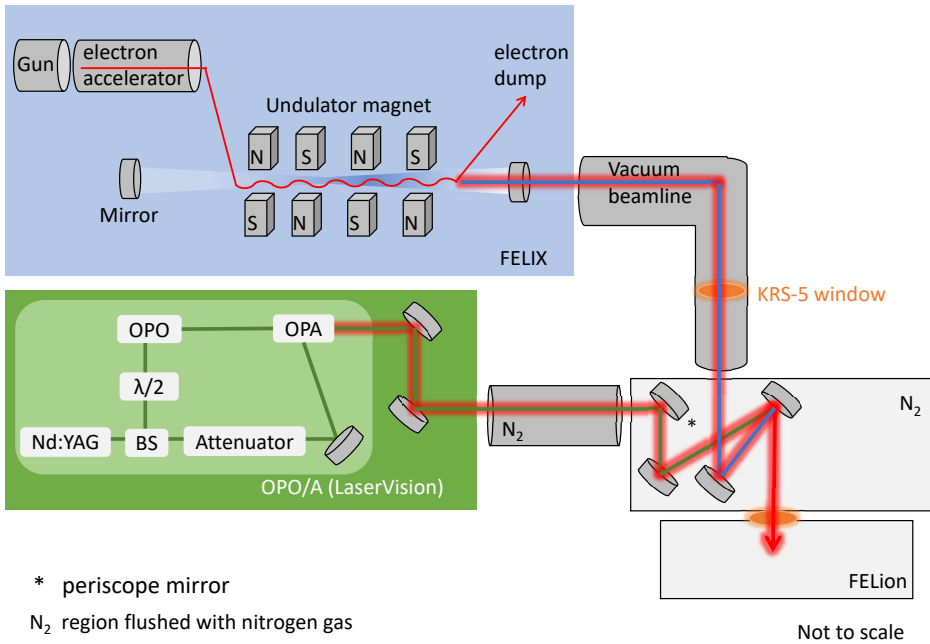


Figure 2.4.: Schematic drawing of FELIX and OPO/A system interfaced with FE-Lion user-station. The blue and green coloured lines represent the FELIX and OPO/A output laser beam paths, respectively. Only one system, FELIX or OPO/A, is operated at a given time.

$$\lambda_r = \frac{\lambda_u}{2\gamma^2} \left(1 + \frac{K^2}{2} \right)$$

where λ_u is the undulator wavelength (spatial period of the magnetic field), γ is the relativistic Lorentz factor, and K is the dimensionless parameter describing undulator magnetic strength.

The γ and K are defined as:

$$\gamma = \frac{1}{\sqrt{1 - (v_z/c)^2}}$$

$$K = \frac{eB_u\lambda_u}{2\pi m_e c}$$

where v_z is the velocity of the electron in the direction of the undulator, c is the speed of light, m_e is the mass of the electron, e is the elementary charge, and B_u

is the applied magnetic field strength.

FELIX laser system: Currently, the FELIX laboratory consists of four laser systems, FEL-1, FEL-2, FELICE, and FLARE, each producing their range of wavelengths, and together, they provide a tuning range of 3-1500 μm . The FELion instrument is interfaced with FEL-1 and FEL-2 pulsed IR laser system via an evacuated beamline with a wide tunable frequency range of 30-150 μm ($330\text{-}66 \text{ cm}^{-1}$) and 3-45 μm ($3330\text{-}220 \text{ cm}^{-1}$), respectively. FEL-2 delivers $> 2000 \text{ cm}^{-1}$ in 3rd harmonic operation mode (FEL-2 was updated in 2022 after the experiments reported in this thesis have been concluded). The IR pulsed FELIX laser has a repetition rate of 10 Hz with a typical macropulse length of $\sim 10 \mu\text{s}$ and for the experiments reported here a 1 GHz micro-pulse structure (see Figure 2.5) has been used.

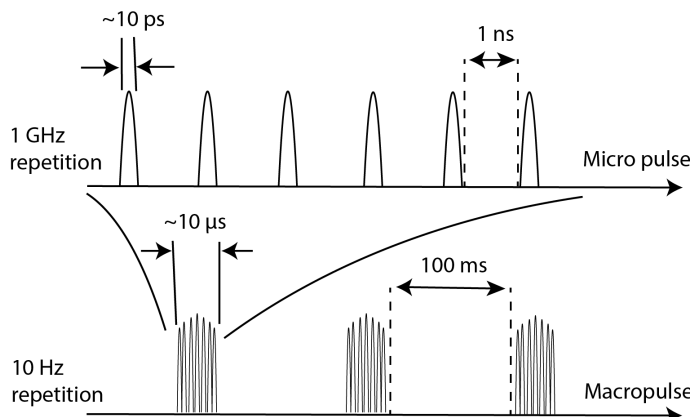


Figure 2.5.: Schematic diagram of the FELIX laser micro and macro pulse structure.

The maximum macropulse output power reaching the user station is $> 50 \text{ mJ}$. The full-width half maxima (FWHM) of radiation is Fourier-transform limited and on the order of $\Delta\nu = 5 \text{ cm}^{-1}$ at 1000 cm^{-1} . The schematic drawing of the free-electron laser (FELIX) interfaced with the FELion user station is shown in Figure 2.4. At the FELion user station, the IR radiation from FEL-2 is coupled into the FELion via two mirrors (one of them focuses the laser beam into the trap region) and two vacuum windows KRS-5 which permit photons down to 250 cm^{-1} with 75% transmission. The KRS-5 windows are replaced with a CVD diamond window when FEL-1 is used. The region between the FELIX beamline and FELion is flushed with N_2 gas to avoid absorption.

2.2.2.2. OPO/A

In addition to the FELIX laser system, the FELion instrument is coupled to a tunable OPO/A system (LaserVision, Narrowband OPO/A model).

2

Operating principles:

The OPO/A system uses an optical parametric oscillator (OPO) and amplifier (OPA) instead of stimulated emission for optical gain. Hence, it consists of an optical resonator and non-linear crystals. It relies on two non-linear optical processes: second harmonic generation (SHG) and difference frequency generation (DFG).

The 1064 nm laser source (pump) input is split using a beam splitter, and one part is directed to the OPO stage and the other to the OPA stage. Before entering the OPO stage, the 1064 nm input is frequency doubled via SHG to provide 532 nm input for OPO. In OPO, the input laser beam of frequency w_p is split into two new lower energy photons via DFG using KTP crystals, called signal and idler, with frequency w_s and w_i , respectively, such that $w_p = w_s + w_i$. The wavelengths of w_s and w_i can be tuned by phase-matching conditions (i.e., by changing the angle between the incident pump laser and optical axes of crystals). While in OPA (KTA crystals), in addition to the initial 1064 nm input, the idler output from OPO acts as a signal input for OPA, resulting in tunable intermediate/mid-infrared output in the $3 \mu\text{m}$ range using DFG.

Setup:

The OPO/A system coupled to the FELion instrument is shown as a schematic diagram in Figure 2.4. This is a multi-stage nonlinear device designed to convert the fixed-frequency output of a seeded 1064 nm Nd:YAG pump laser (operated at 10Hz) into tunable radiation in the intermediate and mid-infrared, using the combination of a 532 nm pumped OPO followed by a 1064 nm pumped OPA. The system produces a tunable output (Mid-IR Idler) from $2.218\text{-}5 \mu\text{m}$, i.e., $2000\text{-}4500 \text{ cm}^{-1}$ frequency range with a maximum pulse energy of up to 25 mJ and line bandwidth of $\sim 0.1 \text{ cm}^{-1}$ (seeded).

2.2.3. DATA ANALYSIS

This section will discuss the data processing, including calibration, normalization, and averaging process of the obtained spectra from the FELion instrument combined with FELIX. During the PhD work, an analysis software package based

on Python 3 was developed¹.

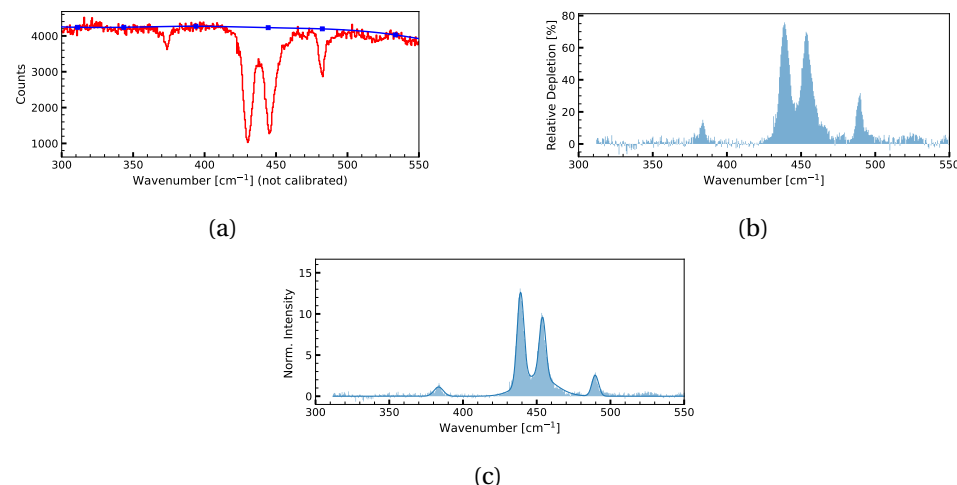


Figure 2.6.: Data processing (for $\text{Ne}-\text{HC}_3\text{N}^+$ IRPD spectrum using FELIX): (a) is the raw data obtained by directly measuring the depletion counts of formed complex ions in IRPD schemes at varying frequencies. The blue line corresponds to a possible baseline to account for ion count fluctuation. (b) is the first processed spectrum with baseline correction from (a). (c) is the final normalised spectrum (see text) and the solid line corresponds to fitting the spectrum with a multi-component Gaussian function.

Baseline correction: The formed ion complex is monitored and counted in the IRPD experiments reported in this thesis. Figure 2.6a shows the measured raw data. Each data point is typically an average of 4 iterations. This spectrum should be baseline corrected for ion count fluctuation. Since even slight changes in the experimental condition, such as temperature, number density, and change in tagging efficiency due to laser heating, etc., can induce a non-linear shift in an otherwise constant background signal. As shown in Figure 2.6a, the solid blue line is the constructed baseline via a cubic spline interpolation and can be manually adjusted. In addition to baseline correction, the raw spectrum needs to be frequency calibrated against the actual frequency output from the radiation source, i.e., using a grating spectrum analyser (FELIX) and manual wavenumber corrections based on a wavemeter (HighFinesse WS - Series) reading (OPO/A

¹<https://felion-docs.vercel.app/>

system).

Normalisation and fitting: Initially, baseline corrected data is a relative depletion (D) of complex ions and is given by:

$$D = 1 - \frac{N_{ON}(\nu)}{N_{OFF}}$$

where N_{OFF} is the baseline value and $N_{ON}(\nu)$ is the depleted value of the number of complex ions that are observed upon resonant vibrational excitation as shown in Figure 2.6b.

To account for variations of the laser pulse energy E , pulse number n , and for saturation effects, the signal is normalised (I) as given below:

$$I[\text{per J}] = \frac{-\ln(N_{ON}(\nu)/N_{OFF})}{E[\text{in J}]}$$

where I is the intensity in units of relative cross-section per Joule.

One can obtain a relative cross-section per photon by multiplying I with the wavenumber. Figure 2.6c shows the final normalised spectrum. The measurements are repeated in the same frequency range for averaging, i.e., the final spectrum is obtained by averaging using statistical binning with a typical bin size of 1.5-2 cm⁻¹ of all normalised data. Line parameters such as band positions, intensities, and line widths (fwhm) are then obtained with statistical errors by fitting a multi-component Gaussian function to the experimental data. Figure 2.6c shows the final normalised spectrum.

2.3. ROTATIONAL SPECTROSCOPY

2.3.1. EXPERIMENTAL METHOD

The ROSAA action spectroscopic technique is employed in this work to record pure rotational transitions. In this section, we shall discuss this technique in detail.

Initially, the primary target molecular ions are produced from an ion source (see Section 2.1.1) by electron ionization from a neutral precursor using either storage or non-storage ion sources. A short pulse of the isolated molecular ion of interest is injected into the trap and stored for a specified time, typically ~ 600 ms for rotational action spectroscopic experiments, with continuous inflow of either pure He or He:Ne mixture buffer gas for collisional cooling and complex formation. At low temperatures (around 5-6 K and 6-15 K trap ambient temperature for helium and neon tag, respectively) and high number density ~ 10¹⁴ cm⁻³

of gas inflow, the buffer gas atoms will readily attach to the target ion by ternary association and can dissociate by collision-induced dissociation.

The ROSAA technique utilises the change in the rare gas atoms' attachment rate to a molecular ion (M^+) depending on its internal excitation, i.e., ions with a specific rotational quantum number J have different attachment rate coefficients for forming $\text{He}M^+$ clusters with Helium (see Section 2.3.5). The ternary association and collision-induced dissociation rate coefficients can be experimentally measured by following corresponding reactants and products ion counts as a function of trap time. These rate coefficients are a weighted averaged rate coefficient over the thermal population of rotational levels, i.e., the Boltzmann distribution close to the nominal trap temperature, reached by He collisional excitation rates of the order of $\sim 10^4 \text{ s}^{-1}$ at the typical number densities ($\sim 10^{14} \text{ cm}^{-3}$) used in these experiments. Upon resonant excitation, the thermal equilibrium distribution is disturbed by competing radiative processes (typically with comparable rates of $\sim 10^5 \text{ s}^{-1}$ for the M^+ rotational transitions), leading to a change in the attachment rate and thus the number of formed complexes. Hence, the measured signal intensity (S) is given as the observed change (in %) of the number of $\text{He}-M^+$ complexes formed between the set frequency (I_{ON}) and a fixed reference frequency (I_{OFF} , offset about $3 \sim \text{GHz}$ from scanning range), and scaled by I_{OFF} , i.e., $S = (I_{OFF} - I_{ON}) / I_{OFF}$, after storing for a fixed time of typically $\sim 600 \text{ ms}$ in the trap at each data point (see Sections 2.3.2 and 2.3.3 for radiation source details). The spectra are measured in typically $10 \sim \text{kHz}$ steps.

2.3.2. THz RADIATION SOURCE

A continuous wave Signal Generator Extension (SGX) Module (VDI - Virginia Diode, Inc. WR9.0-SGX) has been used to measure pure rotational transitions of molecular ions. The SGX covers the frequency range from 82.5 - 1100 GHz using different frequency doubler or tripler combinations. Table 2.1 provides the configurations used in this thesis. The microwave signal generator (R&S® SMB100A up to 40 GHz) drives the SGX and is disciplined by an atomic clock (Stanford Research Systems - FS740), such that the intrinsic radiation linewidths are better than 1 kHz, and the relative frequency accuracy is specified to be better than $1 \cdot 10^{-13}$. The WR9.0 SGX was placed directly in front of a $\sim 0.6 \text{ mm}$ thick CVD diamond window (Diamond Materials GmbH) with a conical/diagonal horn antenna and directed into the trap region. Figure 2.7 shows the power output measured using a high sensitivity thermal sensor (3A-P-THz Ophir photonics) for

configuration WR9.0 and WR2.2 SGX.

Table 2.1.: WR9.0M-SGX configuration details at standard RF input mode.

2

Designation	Frequency [GHz]	Configuration	N*
WR9.0	82.5-125	WR9.0SGX	9
WR4.3	170-250	WR9.0SGX + WR4.3X2	18
WR2.2	340-500	WR9.0SGX + WR4.3X2 + WR2.2X2	36

* N indicates the multiplier for signal generator (R&S® SMB100A) frequencies.

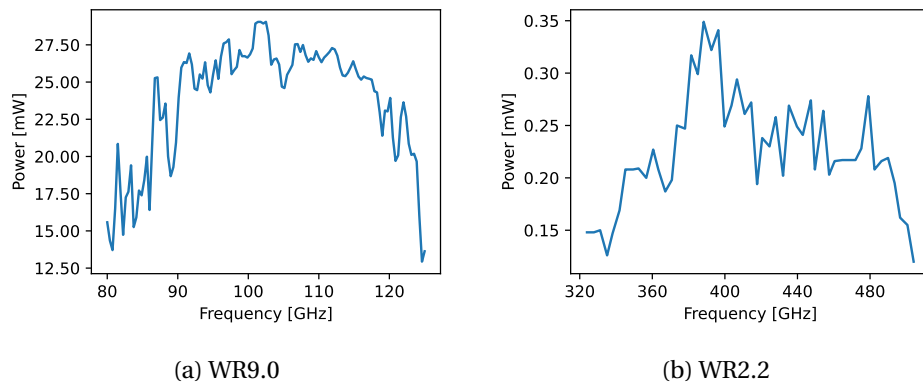


Figure 2.7.: Power curves measured with Virginia Diodes, Inc. (VDI) WR9.0 Modular SGX Modules in (a) WR9.0 and (b) WR2.2 configuration as described in Table 2.1.

The maximum radiation output power can be regulated using “User Controlled Attenuation (UAC)”. The UCA voltage reduces the SGX module’s output power. Figure 2.8 shows the WR9.0 SGX module output power as a function of UAC voltage from 0 – 5 V using a DC power supply (0 V = no attenuation, 5 V = full attenuation). The maximum output power reaching the trap centre region is discussed in the following section 2.3.3.

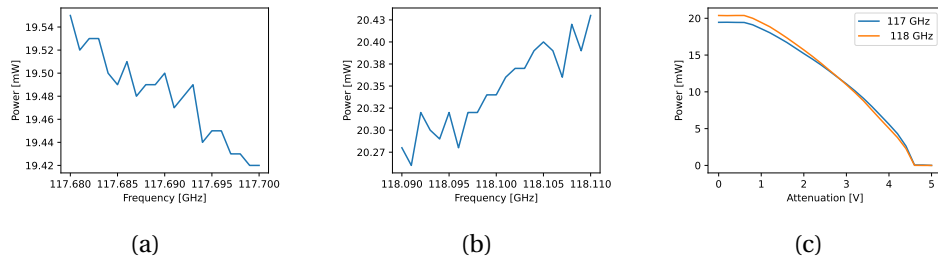


Figure 2.8.: Power curves measured with Virginia Diodes, Inc. (VDI) WR9.0 Modular SGX Modules in WR9.0 configuration, for the frequency ranges (a) 117.68 – 117.70 GHz and (b) 118.09 – 118.11 GHz. (c) shows the user-controlled attenuation power output for (a) and (b) as labelled 117 and 118 GHz, respectively.

2.3.3. DETERMINING THE RADIATION POWER AT THE TRAP REGION

2

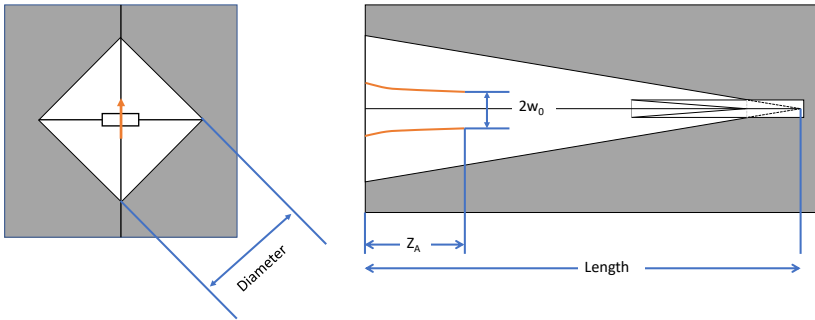


Figure 2.9.: Schematics of the nominal feed horn antenna are shown. Z_A is defined as the location of the beam waist radius (w_0) with respect to the horn aperture. The upward arrow (orange solid line) indicates the polarisation direction of the electric field.

The feed horn antenna's electric field radiation emitted/propagated is shown in Figure 2.9. The propagation of the emitted Gaussian beam radius ($w(z)$) from a horn antenna is given by:

$$w(z) = w_0 * \sqrt{1 + \left(\frac{z}{Z_R}\right)^2} \quad (2.1)$$

where Z_R is the Rayleigh length (or Rayleigh range) for Gaussian beams.

Z_R is determined by the waist radius w_0 and the wavelength (λ) as shown below:

$$Z_R = \frac{\pi \cdot w_0^2}{\lambda}$$

Using a diagonal horn antenna (VDI waveguide band WM-570) of length, aperture diameter and beam waist radius of 36, 3.6 and 1.5 mm, respectively. The Gaussian beam propagation simulation for a frequency $\Delta\nu = 453$ GHz is shown in Figure 2.10.

As the Gaussian laser beam propagates, the waist radius increases in size and the corresponding intensity profile of the electric field is given by:

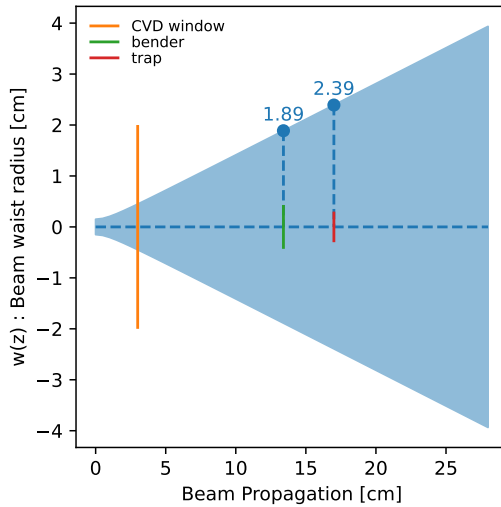


Figure 2.10.: Gaussian beam (for a frequency of $\nu = 453$ GHz) propagation from a beam waist radius of 0.15 cm produced from diagonal feed horn antenna. The solid lines - orange and green indicates the position of FELion instrument entrance window (CVD diamond window, 3 cm from antenna, 2 cm aperture radius) and bender (10.4 cm from window, 0.43 cm aperture radius), 22-pole ion-trap (14 cm from window, 0.3 cm aperture radius). respectively.

$$\begin{aligned} I(r) &= I_0 \cdot \exp \left[-2 \left(\frac{r}{w(z)} \right)^2 \right] \\ &= \frac{2P}{\pi w(z)^2} \cdot \exp \left[-2 \left(\frac{r}{w(z)} \right)^2 \right] \end{aligned} \quad (2.2)$$

where I_0 is the peak irradiance at the centre of the beam, r is the radial distance away from the propagation axis, $w(z)$ is the radius of the laser beam where the irradiance is $1/e^2$ (13.5%) of I_0 , z is the distance propagated from the plane where the wavefront is flat, and P is the total power of the beam.

Figure 2.11 shows the intensity profile using Eq. 2.2, when the beam waist radius, $w(z) = 2.5$ cm, is at the trap entrance (see Figure 2.10). Since the ion-trap aperture diameter is 0.3 cm which is much narrower compared to the incoming beam radius (2.5 cm), one needs to consider an offset for the Gaussian beam centre reaching the trap centre. Therefore, the figure 2.2 also features the or-

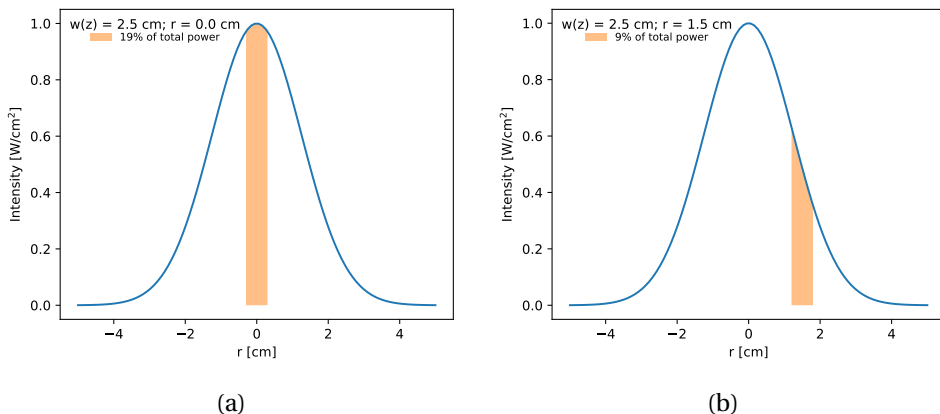


Figure 2.11.: The radiation intensity profile distribution is shown in the blue line. The shaded orange region indicates the fraction of output power at a 3 cm beam radius, i.e., inside trap region as shown in Figure 2.10. The position of the orange region *w.r.t* the x-axis represents the part of the propagating Gaussian beam reaching the trap region when (a): aligned and (b): 1.5 cm offset *w.r.t* beam centre.

ange marked region, which indicates the actual power estimated to reach the trap depending on its alignment, $r(z)$, *w.r.t* the propagating Gaussian beam centre, $r_0(z)$. If we assume that in our experiment, $r(z) = 0 - 1.5$ cm, then the final radiation power reaching the trap, for $\Delta\nu = 453$ GHz frequency is 9-19 % of the peak power (250 μ W), i.e., 35(12) μ W.

2.3.4. DETERMINING THE COLLISIONAL ION TEMPERATURE

In the spectroscopic experiment to investigate pure rotational transitions, the ions are cooled down in the trap by collisions with a buffer gas atom such as He, Ne or He:Ne mixture. The collisional ion temperature (T_{coll}), i.e., translational or kinetic temperature of the ions in the trap, which corresponds to mean collisional energy between the partners, thus the neutral buffer gas and the molecular ion, is an important factor to be determined especially for the models described in Section 2.3.5 . This temperature cannot be measured directly but can be estimated by:

$$T_{\text{coll}} = \frac{m_{\text{He}} \cdot T_{\text{ion}} + m_{\text{ion}} \cdot T_{\text{He}}}{m_{\text{He}} + m_{\text{ion}}} \quad (2.3)$$

where "m" is mass and "T" is temperature, and the subscript "He" and "ion" indicates the corresponding buffer gas atom used (helium in this case) and the

molecular ion of interest, respectively. The nominal trap temperature measured is assumed to be T_{He} . However, it has to be noted that the ion temperature (T_{ion}) is often higher than the nominal trap temperature [119]. Furthermore, T_{ion} can be measured via the Doppler width estimated from the recorded full-width half maxima (FWHM) of a rotational transition at a given power. The measured rotational line profile corresponds to the Voigt profile, which is a convolution of a Gaussian profile (due to the kinetic energy distribution of the ions) and a Lorentzian profile (caused by power broadening). The FWHM of the Gaussian (f_G) and Lorentzian (f_L) profile can be derived as follows:

$$f_G = \nu \cdot \sqrt{\frac{8 \cdot k_b \cdot T_{ion} \cdot \ln(2)}{m_{ion} \cdot c^2}} = C_G \cdot \sqrt{T_{ion}} \quad (2.4)$$

where ν corresponds to the central line frequency of the profile and C_G is the Doppler proportionality constant, and by:

$$f_L = \frac{\sqrt{2}}{2 \cdot \pi} \cdot \Omega_R$$

substituting angular Rabi frequency of the transition, which is defined as, $\Omega_R = \frac{\mu \cdot E}{\hbar}$ ², we get

$$f_L = \frac{\sqrt{2}}{2 \cdot \pi} \cdot \frac{\mu \cdot E}{\hbar}$$

Substituting electric field strength, $E = \sqrt{\frac{2 \cdot I}{c \cdot \epsilon_0}}$ where I is the intrinsic intensity $I = \frac{1}{2} \cdot c \cdot \epsilon_0 \cdot E^2 = \frac{P}{A_{trap}}$, we get the final expression for Lorentzian FWHM, f_L :

$$f_L = \frac{2 \cdot \mu}{h} \sqrt{\frac{P}{A_{trap} \cdot c \cdot \epsilon_0}} = C_P \cdot \sqrt{P} \quad (2.5)$$

where P is the output radiation power in W, $A_{trap} = 5 \cdot 10^{-5} \text{ cm}^2$ is the trap area and C_P is a power-broadening proportionality constant.

The Voigt profile is given by:

$$V(x; \sigma, \gamma) = \frac{Re[w(z)]}{\sigma \sqrt{2\pi}} \quad (2.6)$$

where σ is the standard deviation in Gaussian profile, γ is the half-width half maxima of Lorentzian profile and $Re[w(z)]$ is the real part of the Faddeeva function.

² μ is transition dipole moment, and E is the electric field, hence dividing the energy term ($\mu \cdot E$) by \hbar gives angular frequency

$$\sigma = \frac{f_G}{2\sqrt{2 \cdot \ln(2)}} \quad (2.7)$$

$$\gamma = \frac{f_L}{2} \quad (2.8)$$

$$z = \frac{x + i\gamma}{\sigma\sqrt{2}}$$

The FWHM of Voigt profile can be approximated with an accuracy of 0.02% by [121]:

$$f_V = 0.5346 \cdot f_L + \sqrt{0.2166 \cdot f_L^2 + f_G^2} \quad (2.9)$$

To determine T_{ion} , the experimentally measured rotational spectrum is fitted with the Voigt profile (Eq. 2.6); subsequently, line parameters σ and γ are obtained. Using σ , one can compute f_G using Eq. 2.7 and finally, T_{ion} from f_G using Eq. 2.4.

2.3.5. NUMERICAL SIMULATION

The ROSAA action spectroscopic technique, as described in Section 2.3.1 utilises the change in attachment rate of rotation-specific energy levels to record the pure rotational spectrum. As depicted in Figure 2.12 there are several competing processes involved in affecting the molecular ions population distribution on different rotational levels, and consequently affecting the obtained signal intensity. Therefore, in this section, we discuss a kinetic numerical model approach to understanding the ROSAA signal intensity.

2.3.5.1. COLLISIONAL PROCESS (R)

As hot molecular ions (M^+) enter the trap (typical ambient trap temperature ~ 4.5 K) from the ion source (room temperature, 300 K or higher), they are collisionally cooled down by buffer gas atoms. The population distribution of rotational levels reaches a new equilibrium corresponding to the kinetic/collisional temperature (T_{coll}) of the system, which can be derived from the ion temperature (T_{ion}) as described in Section 2.3.4. The rotational level-specific population ratio is given by:

$$\left(\frac{dM_i^+}{dt} \right)_{coll.} = \sum_{f \neq i} R_{fi} \cdot M_f^+ - R_{if} \cdot M_i^+ \quad (2.10)$$

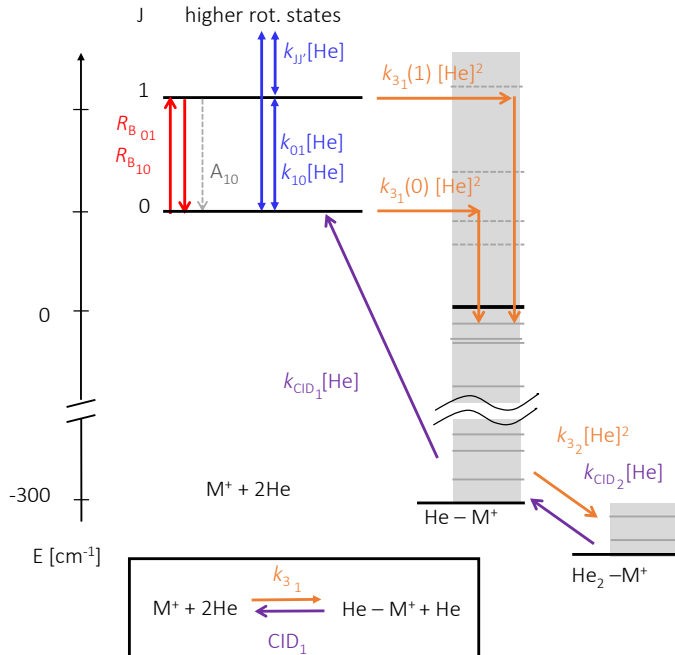


Figure 2.12.: Schematic kinetic model of the ROSAA action spectroscopic technique. The coloured labels and arrows indicate several competing processes for the reaction between the molecular ion M^+ and the neutral He atom. The typical rates for collisional (blue) and radiative process (red) are in the range of $10^4 - 10^5 \text{ s}^{-1}$, effective binary complex formation (orange) is $> 0.01 \text{ s}^{-1}$ and the collision-induced dissociation (violet) is $> 0.1 \text{ s}^{-1}$ at a given number density of $> 1 \cdot 10^{14} \text{ cm}^{-3}$. The spontaneous emission is labelled A_{10} , and rates are typically in order of $> 10^{-4} \text{ s}^{-1}$. Figure adapted from Brünken *et al.* [3].

where i and f represents rotational states with rotational quantum numbers $J = i, f$, $i f$ indicates initial $|i\rangle$ state transitions into final $|f\rangle$ state and R_{if} corresponds to collisional rates [s^{-1}] for $i f$ transition and given by

$$R_{if} = k_{if} \cdot [\text{He}]$$

where k_{if} and $[\text{He}]$ indicate collisional rate coefficients and buffer gas (generally He gas) number density, respectively.

The rate coefficients can be derived from a quantum dynamical investigation using a closed coupling $M^+ - \text{He}$ rotational cross-section calculation method within

a rigid body approach. However, in this study, no such investigations have been undertaken; the rate coefficient values (k_{if}) have been retrieved from the available literature. The fundamental detailed balancing relation is given as:

$$\frac{k_{if}}{k_{fi}} = \frac{G_f}{G_i} e^{\Delta E/(k_B T)} \quad (2.11)$$

where g_i indicates statistical weight of corresponding $|i\rangle$ state ($G_i = 2J+1$), k_B is the Boltzmann constant, T is the temperature of the system, and ΔE is the difference between final state energy (ϵ_f) and initial state (ϵ_i) energy, i.e.:

$$\Delta E = \epsilon_f - \epsilon_i$$

At a given T (actually T_{coll}), if only the collisional process is involved, solving equation 2.10, equilibrium values are reached typically in few $100 \sim \mu\text{s}$ at $[He] \sim 10^{14} \text{ cm}^{-3}$ leading to a distribution equal to the Boltzmann population at T , i.e.:

$$M_i^+ = \frac{G_i \cdot e^{\epsilon_i/(k_B T)}}{\sum_{j=1}^N G_j \cdot e^{\epsilon_j/(k_B T)}} = \frac{G_i \cdot e^{\epsilon_i/(k_B T)}}{Z} \quad (2.12)$$

where N is the given system's total number of accessible rotational quantum levels, and Z is the molecular partition function.

2.3.5.2. SPONTANEOUS EMISSION (A)

It is the process in which a quantum mechanical system transits from an excited energy state to a lower lying energy state (e.g., its ground state) and emits a quantized amount of energy in the form of a photon. An initial state $|i\rangle$ with energy ϵ_i can decay to a final state $|f\rangle$ with energy ϵ_f via spontaneous emission of a photon with frequency ($\Delta\nu$). The Einstein A-coefficient gives the spontaneous emission rate [in photons per s]:

$$A_{fi} = \frac{2\nu^3}{3\epsilon_0 hc^3} \cdot \mu_{fi}$$

where ϵ_0 , h , c and μ_{fi} are vacuum permittivity, Planck's constant, speed of light and transition dipole moment, respectively. Including this emission process into Equation 2.10 gives us the following relations:

$$\left(\frac{dM_i^+}{dt} \right)_{coll.+Spont.} = \left(\frac{dM_i^+}{dt} \right)_{coll} + A_{fi} \quad (2.13)$$

$$\left(\frac{dM_f^+}{dt} \right)_{coll.+Spont.} = \left(\frac{dM_i^+}{dt} \right)_{coll.} - A_{fi} \quad (2.14)$$

The spontaneous rates are derived from the effective Hamiltonian fitting of a given molecular species using a program such as Pgopger [122]. Typically, spontaneous emission rates are in the order of 10^{-4} s^{-1} which are smaller than collisional rates ($10^3 - 10^5 \text{ s}^{-1}$) at high number density ($> 10^{14} \text{ cm}^{-3}$). Since the collisional processes dominate the spontaneous emission rates, for simplicity, the label *coll.* + *Spont.* will just be referred as *coll.*.

2.3.5.3. RADIATIVE PROCESS (R_B)

In the presence of radiation, the population is re-distributed again due to stimulated absorption (B_{if}) and emission (B_{fi}), described by the Einstein-B-coefficients. Both absorption and emission coefficients [$\text{m}^3 \text{J}^{-1} \text{s}^{-2}$] can be derived from corresponding Einstein A-coefficient (A_{fi}):

$$B_{fi} = \frac{c^3}{8\pi h\nu^3} \cdot A_{fi}$$

$$B_{if} = \frac{G_f}{G_i} \cdot B_{fi}$$

The rate of stimulated absorption, $R_{B_{if}}$ [in s^{-1}], is given by:

$$R_{B_{if}} = B_{if} \cdot \frac{P}{A_{trap} \cdot c} \cdot V(x; \sigma, \gamma)$$

where $A_{trap} = 5 \cdot 10^{-5} \text{ m}^2$ indicates the area of 22-pole ion-trap, P corresponds to radiation power [in $\text{J} \cdot \text{s}^{-1}$], and $V(x; \sigma, \gamma)$ corresponds to Voigt profile lineshape (Eq. 2.6) for the rotation transition profile (x) with central frequency $\Delta\nu$.

Including the radiative process in Equation 2.13 gives us the following rate equation:

$$\left(\frac{dM_i^+}{dt} \right)_{coll.+Rad.} = \left(\frac{dM_i^+}{dt} \right)_{coll.} - R_{B_{if}} \cdot M_i^+ + R_{B_{fi}} \cdot M_f^+ \quad (2.15)$$

2.3.5.4. ATTACHMENT AND DISSOCIATION PROCESS (R_3 AND R_{CID})

The ternary association (R_3) and collision-induced dissociation (R_{CID}) rates [s^{-1}] should also be included to complete the kinetic model scheme as shown in Figure 2.12 (read Section 6.3 for more detail on attachment process). The attachment process rates can be experimentally derived but only as a weighted average of all rotational population levels for a given molecular ion of interest (M^+). However, a rotational-specific rate is required for numerical simulation. The ratio of formation rate coefficients for the undergoing transitions is called k_{3_1} ratio and will be referred to as “ a ”:

$$a = \frac{k_{3_1}(f)}{k_{3_1}(i)} \quad (2.16)$$

The final master equation for numerical simulation of ROSAA technique involving *Coll.* + *Rad.* + *Att.* for rotational transition from ground state $|i\rangle$ to excited state $|f\rangle$, and $M + 2\text{He}$ attachment process is given by:

$$\begin{aligned} \left(\frac{dM_i^+}{dt} \right)_{coll.+Att.+Rad.} &= \left(\frac{dM_i^+}{dt} \right)_{coll.+Rad.} - R_{3_1} \cdot M_i^+ + R_{CID_1} \cdot \text{He}M^+ \cdot p \\ \left(\frac{dM_f^+}{dt} \right)_{coll.+Att.+Rad.} &= \left(\frac{dM_f^+}{dt} \right)_{coll.+Rad.} - R'_{3_1} \cdot M_f^+ + R_{CID_1} \cdot \text{He}M^+ \cdot (1-p) \end{aligned}$$

where R_{3_1} and R'_{3_1} correspond to state-dependent first-complex formation rates for ground and excited state, respectively. These rates can be expressed in terms of corresponding rate coefficients (k) (read Section 6.3 for more detail). “ p ” represents the collision-induced dissociation (CID) branching-ratio, *i.e.*, the ratio of population transitions back to ground state from first complex ($\text{He}M^+$) via CID process.

The rate equations for the formation of the first two complex ions are given below (higher-order complexes can be treated accordingly):

$$\begin{aligned} \frac{d\text{He}M^+}{dt} &= +R_{3_1} \cdot M_i^+ - R_{CID_1} \cdot \text{He}M^+ \cdot p \\ &\quad + R'_{3_1} \cdot M_f^+ - R_{CID_1} \cdot \text{He}M^+ \cdot (1-p) \\ &\quad - R_{3_2} \cdot \text{He}M^+ + R_{CID_2} \cdot \text{He}_2M^+ \\ \frac{d\text{He}_2M^+}{dt} &= +R_{3_2} \cdot \text{He}M^+ - R_{CID_2} \cdot \text{He}_2M^+ \end{aligned}$$

2.3.5.5. SOLVING RATE EQUATIONS

The processes involved in these numerical simulations are in widely varying timescales, as will be discussed in the corresponding chapters (see Chapter 6 and 7). These rate equations are known as “stiff equations”. A stiff equation is a differential equation for which specific numerical methods (explicit) for solving the equation are numerically unstable unless the step size is taken to be extremely small [123]. Therefore all of the ODEs discussed in this section are solved using the implicit Runge-Kutta method of the Radau IIA family of order 5 [124] using SciPy library [125].

2.4. THEORETICAL METHODS

In this study, the vibrational and rotational spectroscopic investigations are supported and complemented by quantum chemical calculations. Therefore, this section briefly describes the quantum theory of molecular vibration and rotation using a quantum mechanical approach.

In classical mechanics, the system’s total energy, which includes kinetic (T) and potential (V) energy, is known as the Hamiltonian (H), such that

$$H = T + V \quad (2.17)$$

Schrödinger postulated the form of Hamiltonian (operator) in quantum mechanics, as given below

$$H = -\frac{\hbar^2}{2m} \nabla^2 + V(r) \quad (2.18)$$

where m is mass, r represent the coordinates, ∇^2 is the Laplacian operate, and the corresponding Schrödinger wave equation using ψ , the wavefunction of the quantum state:

$$H\psi(r, t) = i\hbar \frac{\partial\psi(r, t)}{\partial t} \quad (2.19)$$

One can derive a final time-independent Schrödinger equation by substituting Eq. 2.18 in Eq. 2.19

$$H\psi(r) = E\psi(r) \quad (2.20)$$

where E is the eigenvalue of operator H , corresponding to the system’s total energy.

In quantum mechanics, any molecular state can be fully described by a number of different degrees of freedom, each of which has a corresponding coordinate system. In three dimensions, there is the rotational and vibrational motion of the nuclei and the motion of the electrons. Nuclear and electron spin variables could also exist.

A fundamental idea underlying the description of the quantum states of molecules is the Born-Oppenheimer (BO) approximation [126], i.e., the nuclei's (N) motion and electrons' motion can be separated since nuclei are much heavier than the electrons. Under BO approximation, the total wavefunction (ψ) of the molecular system is separable into nuclear (ψ_n) and electronic (ψ_e) parts, that is

$$\psi = \psi_n(R)\psi_e(r, R)$$

where R represents an inter-nuclear separation coordinate for each pair of atoms and r represents the internal coordinates.

The wave function ψ_N can be further factorized into a vibrational (ψ_v) and rotational (ψ_r) part:

$$\psi_n = \psi_v\psi_r$$

so that

$$\psi = \psi_v\psi_r\psi_e$$

The total energy (E) of the system corresponds to the sum of the contributions from vibrational, rotational and electronic parts, as given below:

$$E = E_v + E_r + E_e$$

If the molecule possesses net nuclear or electron spin, it is added and factorised to E and ψ , respectively.

However, the BO approximation does not hold true in all cases. For example, the coupling between electronic and vibrational modes (Renner-Teller effect, vibronic coupling) is observed for open-shell linear molecular systems (see chapter 5 for treatment of this case).

2.4.1. MOLECULAR VIBRATION

A simple ball and spring harmonic oscillator model from classical mechanics can explain molecular vibrations. However, principles from quantum mechanics are required to describe vibrational energy levels and transitions between them.

Atoms are the basic unit of molecules, and covalent bonds hold them together. The distance between atoms or the length of chemical bonds is not fixed. Therefore, molecules can vibrate when excited to a higher energy state by absorbing a resonant photon of electromagnetic radiation in the infrared region.

2

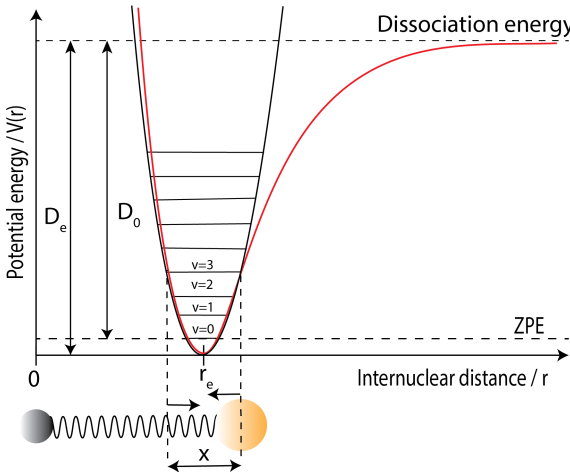


Figure 2.13.: Heteronuclear diatomic molecule (solid circles at the bottom) vibrating at energy level $v = 3$. The black and red curve represent harmonic and anharmonic (Morse) potential energy curves, respectively. r_e is the equilibrium bond length, D_0 and D_e correspond to dissociation energy with and without ZPE (zero-point energy) correction, respectively.

2.4.1.1. DIATOMIC MOLECULES

Assuming a simple ball and spring harmonic oscillator model as shown in Figure 2.13 gives us the potential energy (V) from Hooke's law:

$$\text{Restoring force} = -\frac{dV(x)}{dx} = -kx$$

where $x = r - r_e$ and k is force constant:

$$V(x) = \frac{1}{2}kx^2 \quad (2.21)$$

Substituting, equation 2.21 in equations 2.18 and 2.20, we get the Schrödinger equation for 1D-oscillator:

$$\left(-\frac{\hbar^2}{2\mu} \frac{d}{dx^2} + \frac{1}{2} kx^2 \right) \psi_v(x) = E_v \psi_v(x) \quad (2.22)$$

where μ is the reduced mass.

2

Equation 2.22 can be solved to obtain E_v as given below:

$$E_v = \left(v + \frac{1}{2} \right) h\nu = \left(v + \frac{1}{2} \right) hc\omega \quad (2.23)$$

where ν is classical vibrational frequency, $\nu = \frac{1}{2\pi} \left(\frac{k}{\mu} \right)^{1/2}$, ω is vibrational wavenumber, the vibrational quantum number is $v = 0, 1, 2, \dots$.

Equation 2.23 shows that under the harmonic approximation, the vibrational quantum levels are equally spaced by $\hbar\omega$ and the Zero-point energy (ZPE) i.e., $E_v(v=0) = \frac{1}{2}\hbar\omega$. As shown in Figure 2.13, the ZPE is the minimum energy the molecule may have even at absolute zero temperature because of the uncertainty principle.

The energy terms are usually referred to in wavenumbers [cm^{-1}], so we can write Eq. 2.23 as:

$$\frac{E_v}{hc} = \omega \left(v + \frac{1}{2} \right) = G(v) \quad (2.24)$$

where $G(v)$ is the vibrational term value in dimensions of wavenumber, cm^{-1} .

As shown in Figure 2.13, the Morse $V(r)$ curve, the actual diatomic molecule is not accurately harmonics, especially when $r \gg r_e$. To account for anharmonicity, the harmonic oscillator term value are modified to a power series in $(v + \frac{1}{2})$:

$$G(v) = \omega_e \left(v + \frac{1}{2} \right) - \omega_e x_e \left(v + \frac{1}{2} \right)^2 + \omega_e y_e \left(v + \frac{1}{2} \right)^3 + \dots$$

where ω_e is the vibration wavenumber that a classical oscillator would have for an infinitesimal displacement from equilibrium. $\omega_e x_e, \omega_e y_e, \dots$ are the anharmonic constants.

To determine, say ω_e and $\omega_e x_e$, at least two transition wavenumbers must be obtained such as $G(1) - G(0) = \omega_0$ and $G(2) - G(1) = \omega_1$. The dissociation energy D_e is given approximately (since including only $\omega_e x_e$ anharmonic term) by:

$$D_e \approx \frac{\omega_e^2}{4\omega_e x_e}$$

2.4.1.2. POLYATOMIC MOLECULES

The vibrational modes of an N -atomic molecule are given by $3N - 5$ and $3N - 6$ normal vibration modes for linear and non-linear configuration, respectively.

Polyatomic vibrational modes are much more complicated to treat theoretically than diatomic. As shown in Figure 2.14, a simple ball-spring model with 3-atoms (H_2O), even if one of the nuclei is given a sudden displacement, the whole system undergoes very complicated vibrational motions (bending and stretching); this is known as Lissajous motion. For H_2O , we get $3(3) - 6 = 3$ normal modes of vibrations ($\nu_1 - \nu_3$). In general, a normal vibration mode is one in which all the nuclei undergo in-phase harmonic motion with the same frequency but typically with different amplitude.

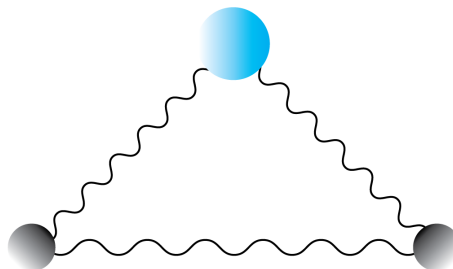


Figure 2.14.: Triatomic molecule (H_2O) ball-spring representation. The blue and grey circle represents oxygen and hydrogen, respectively.

In polyatomic molecules, each vibrational mode can be approximated to a normal vibrational mode. With an analogous approximation from diatomic, the vibrational term value $G(\nu_i)$ associated with each normal vibration i , is given by:

$$G(\nu_i) = \omega_i \left(\nu_i + \frac{d_i}{2} \right)$$

where d_i represents the degree of degeneracy.

2.4.1.3. SELECTION RULES

When two vibrational states undergo absorption or emission transitions, there is usually an interaction between the molecule and the electric component of electromagnetic radiation. Therefore, the electric dipole moment ($\vec{\mu}$) determines the selection rule for vibrational transitions in the infrared spectrum.

The vibrational transition intensity is proportional to $|R_\nu|^2$, the square of the vibrational transition moment R_ν , defined by:

$$R_\nu = \int \psi' \vec{\mu} \psi'' d\tau_\nu \quad (2.25)$$

2

where ψ'' and ψ' are initial and final vibrational wavefunctions, respectively.

A transition is only allowed if the transition dipole integral is non-zero, i.e.:

$R_\nu = 0$ forbidden transition

$R_\nu \neq 0$ allowed transition

For diatomic molecules, within the harmonic approximation, R_ν is non-zero only when $\Delta\nu = \pm 1$. Anharmonicity can lead to $\Delta\nu = \pm 2, \pm 3, \dots$, overtone transitions but they are generally weak.

In general, there are simple requirements for the integral of Eq. 2.25 to be non-zero; they are as follows.

When both ψ'' and ψ' are non-degenerate, the symmetry species of the quantity to be integrated should be totally symmetric; that is:

$$\Gamma(\psi') \otimes \Gamma(\vec{\mu}) \otimes \Gamma(\psi'') = A$$

where A denotes the totally symmetric species of any non-degenerate point group, and Γ stands for symmetry representation.

For degenerate states:

$$\Gamma(\psi') \otimes \Gamma(\vec{\mu}) \otimes \Gamma(\psi'') \supset A$$

A brief overview of molecular vibration for diatomic and polyatomic molecules has been discussed, along with the selection rule for observing IR active vibrational transition modes using quantum mechanics. The following section deals with the quantum mechanical theory of molecular rotation.

2.4.2. MOLECULAR ROTATION

Molecules have electronic and vibrational energy due to the motion of electrons and nuclei, respectively. Furthermore, they have rotational energy due to the overall rotation of the molecule. Like electronic and vibrational, rotational energy is quantized and generally has very small energies compared to the former.

The molecules are classified according to their principal moments of inertia, I_a, I_b and I_c , i.e., the moment of inertia along the principal rotational axis a, b

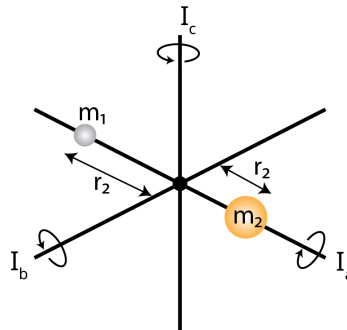


Figure 2.15.: Rotation of linear molecule (heteronuclear diatomic) w.r.t principal rotational axis a, b and c , with corresponding moment of inertia I_a, I_b and I_c , respectively ($I_a=0, I_b=I_c$ for linear and diatomic molecules). m and r represent the mass of the atom and the distance to the rotating axis, respectively. The centre of mass lies at the origin.

and c , respectively. The corresponding rotational constants are denoted as A, B and C , respectively. The principal axes are perpendicular to each other and pass through the molecule's centre of mass (as shown in Figure 2.15). In general, the axes are conventionally defined such that:

$$I_a \leq I_b \leq I_c \quad (2.26)$$

The moment of inertia, I , is defined as

$$I = \sum_i m_i r_i^2 \quad (2.27)$$

where m_i and r_i correspond to mass and distance to the rotating principal axis of atom i , respectively.

The main classifications are linear and non-linear molecules, while the latter is further divided, as will be briefly discussed in the following sections.

2.4.2.1. LINEAR MOLECULES

With a rigid rotor approximation, i.e., the bonds are rigid rods and molecule as a rigid rotor, the angular momentum is given by:

$$P_J = [J(J+1)]^{\frac{1}{2}} \hbar$$

where the rotational number $J = 0, 1, 2, 3, \dots$.

In the presence of an electric or magnetic field,

$$(P_J)_z = M_J \hbar \quad (2.28)$$

2

where, subscript z represent z-axis component and $M_J = J, J-1, \dots, -J$. This indicates that in the absence of an electric or magnetic field, each rotational level has $2J+1$ degenerate states.

The rotational energy (E_r) for a diatomic or linear polyatomic molecule can be solved using Eq. 2.20 and is given by:

$$E_r = \frac{\hbar^2}{8\pi^2 I_b} J(J+1) \quad (2.29)$$

The rotational energy in frequencies [Hz] can be defined using Eq. 2.29:

$$F(J) = \frac{E_r}{\hbar} = \frac{\hbar}{8\pi^2 I_b} J(J+1) = BJ(J+1) \quad (2.30)$$

where $F(J)$ is the rotational term values and B is the rotational constant. Only B rotational constants are involved for linear molecules since as shown in Figure 2.15, $I_a = 0$ and $I_b = I_c$.

The rigid rotor approximation does not hold true, especially in higher J energy levels, because the chemical bonds expand due to centrifugal forces from molecular rotation. The expansion due to centrifugal force is included in equation 2.30 such that

$$F(J) = BJ(J+1) - DJ^2(J+1)^2 + \dots \quad (2.31)$$

where D is the centrifugal distortion constant. Eq. 2.31 also indicates that further higher-order terms may be included.

2.4.2.2. NON-LINEAR MOLECULES

The non-linear molecules are further classified based on the principal moment of inertia. Analogous to B rotational constant for linear molecule (Eq. 2.30), the rotational constants A, B and C are given by:

$$A = \frac{\hbar}{8\pi^2 I_a}; B = \frac{\hbar}{8\pi^2 I_b}; C = \frac{\hbar}{8\pi^2 I_c} \quad (2.32)$$

with units of frequency [Hz].

Symmetric top: It has two equal principal moments of inertia which corresponds to two possibilities: (a) $I_a < I_b = I_c$ and (b) $I_a = I_b < I_c$, these are called prolate and oblate, respectively. In symmetric tops, a second rotational quantum number $K = 0, 1, 2, \dots, J$. is introduced in addition to J ; therefore, Eq. 2.30 becomes

$$F(J, K) = BJ(J+1) + (A - B)K^2 \text{ (prolate)} \quad (2.33)$$

$$F(J, K) = BJ(J+1) + (C - B)K^2 \text{ (oblate)} \quad (2.34)$$

The equations 2.33 and 2.34 indicate that for a particular value of J , the energy levels diverge and converge for a prolate and oblate symmetric tops, respectively. Since from Eq. 2.26 and 2.32, we have $A \geq B \geq C$.

When the effect of centrifugal distortion is included, Eq. 2.31 becomes (for prolate),

$$F(J, K) = BJ(J+1) + (A - B)K^2 - D_J J^2 (J+1)^2 - D_{JK} J(J+1)K^2 - D_K K^4 \quad (2.35)$$

where there are now three centrifugal constants D_J , D_{JK} and D_K .

Spherical top: It has all three principal moments of inertia equal, i.e., $I_a = I_b = I_c$. Therefore, the rotational term value follows the same as the equation for diatomic or linear polyatomic 2.30 and 2.31 (Section 2.4.2.1).

Asymmetric top: It has all three principal moments of inertia unequal, i.e., $I_a \neq I_b \neq I_c$. Generally, the vast majority of molecules are asymmetric tops. But unfortunately, there are no analytical formulae for rotational term values for asymmetric tops molecules. J is still a good quantum number, but K is not, i.e., it does not take integral values. Therefore, only approximate expressions are derived, i.e., to approximate the molecule to either prolate or oblate near-symmetry top, such as:

$$F(J, K) \approx B^* J(J+1) - (A - B^*)K^2 \text{ (near-prolate)}$$

$$F(J, K) \approx B^* J(J+1) - (C - B^*)K^2 \text{ (near-oblate)}$$

where B^* is equal to $\frac{1}{2}(B+C)$ for prolate and $\frac{1}{2}(A+C)$ for oblate rotor.

Since K is not strictly a good quantum number and the $F(J, K)$ is only approximated.

2.4.2.3. SELECTION RULES

Similar to the vibrational selection rule as discussed in Section 2.4.1.3, the rotational selection rule is determined from the rotational transition moment, R_r , defined as:

$$R_r = \int \psi'_r \vec{\mu} \psi''$$

The rotational selection rule constitutes the condition for which R_r is non-zero.

The selection rule:

for linear molecules and spherical top

1. $\Delta J = \pm 1$

for symmetric top

1. $\Delta J = \pm 1$

2. $\Delta K = 0$

for the asymmetric top

1. $\Delta J = 0, \pm 1$

In addition to the above rules, all molecules must have a permanent electric dipole moment ($\vec{\mu} \neq 0$) to observe rotational transition, and in the presence of the electric or magnetic field $\Delta M = 0, \pm 1$ (see Eq. 2.28).

The next section discusses relevant technical details for quantum chemical calculation employed in this thesis work.

2.4.3. QUANTUM CHEMICAL CALCULATIONS

The molecular vibration and rotation laboratory spectroscopic studies reported in this work are supported by quantum chemical calculations as described in Section 2.4.1 and 2.4.2. This section briefly discusses the methods and programs used to employ quantum chemical calculations.

Initially, a potential energy surface is computed to characterise the molecular ion of interest, and energetically stable structures are derived and structurally optimised. These investigations are performed at the coupled-cluster singles

and doubles (CCSD) level augmented by a perturbative treatment of triple excitations, CCSD(T) [127], in combination with atomic natural orbital (ANO0, ANO1, and ANO2) basis sets from Almlöf and Taylor [128, 129] as well as the correlation-consistent valence basis set cc-pVDZ [130] in the frozen core (fc) approximation. The equilibrium geometries have been calculated using analytic gradient techniques [131].

Vibrational modes of molecular ions of interest are further investigated by computing harmonic frequencies using numerical differentiation of gradients [132, 133]. Second-order vibrational perturbation theory (VPT2) [134] has been employed for anharmonic calculations. All CCSD(T) calculations have been carried out using the CFOUR program package [135, 136].

The influence of the rare gas tag on the IRPD spectrum is further investigated by computing interaction energies (using either CFOUR [135] or PSI4 [137] program) as well as harmonic frequencies of the ionic complexes. For the complexes, the Basis Set Superposition Errors (BSSE) [138] are addressed using i) the counter-poise (CP) method introduced by Boys and Bernardi [139], i.e. by calculating CP-corrected CCSD(T) interaction energies at each geometry, and ii) higher-order symmetry-adapted perturbation theory, SAFT2+3 [140, 141].

Measured pure rotational and vibrational transitions (see Chapter 7) are fitted with an effective Hamiltonian approach using the Pgopher program [122] to derive molecular spectroscopic constants. Further computational details specific to certain ionic species are reported in their respective chapters in detail. The next section focuses on experimental technical details such as determining number density.

2.5. TECHNICAL DETAILS

2.5.1. DETERMINING NUMBER DENSITY

Our experiments produce the target molecular ion of interest at room temperature. It enters the trap, which is collisionally cooled by a continuous inflow (for kinetics and ROSAA measurements) of helium buffer gas. This technique could reach the lowest trap nominal temperature of 4.8(3) K (see Figure 2.3). The helium buffer gas pressure is measured inside the trap using a Spinning Rotor Gauge (MKS SRG3-EL). The SRG measuring head (SRG-SH700-V3) is mounted outside at room temperature and connected to the trap via a 3 mm diameter tube. Therefore, thermal transpiration is considered when calculating the helium number density since there is a temperature gradient between the trap and the measuring head.

Reynolds [142] first identified thermal transpiration in 1879. It describes that

when a large temperature difference between the two ends of a pipe connecting two vessels filled with a rarefied (low-pressure) gas, a significant pressure difference will be observed between the two ends. Hence, this phenomenon is known as the *thermo-molecular pressure difference effect*. Knudsen [143] in 1910 derived a low-density approximation for this effect, i.e., if the pressure held in the system is so low that the mean free path of gaseous molecules is several times the diameter of the connecting tube, the ratio of the pressure in the respective vessels is then given as:

$$P_{trap} = P_{SRG} \cdot \sqrt{\frac{T_{trap}}{T_{SRG}}} \quad (2.36)$$

where the subscript *trap* and *SRG* correspond to the cryogenic ion trap (low-temperature) and spinning rotor gauge (high-temperature, i.e., room temperature). They are defined in more detail in the next section. Thus, in this section, a detailed relationship between the two systems will be established.

The number density in the trap (at low-density approximation), n_{trap} , is given by using the ideal gas law:

$$n_{trap} = \frac{1}{k_B} \cdot \frac{P_{trap}}{T_{trap}} \quad (2.37)$$

where k_B is the Boltzmann constant.

Substituting Eq. 2.36 in Eq. 2.37 we get:

$$n_{trap} = \frac{1}{k_B} \cdot \frac{P_{SRG}}{\sqrt{T_{trap} \cdot T_{SRG}}} \quad (2.38)$$

Substituting $T_{SRG} = 300$ K (room temperature) in Eq. 2.38, the number density in cm^{-3} is given by:

$$n_{trap}[\text{cm}^{-3}] = 4.18 \cdot 10^{17} \cdot \frac{P_{SRG}[\text{mbar}]}{\sqrt{T_{trap}[\text{K}]}} \quad (2.39)$$

At higher pressure, thermal transpiration (TT) correction using Takaishi-Sensui [144] equation is used:

$$(P_{trap})_{TT} = P_{SRG} \cdot \left(1 + \frac{\sqrt{\frac{T_{trap}}{T_{SRG}}} - 1}{A \cdot X^2 + B \cdot X + C \cdot \sqrt{X} + 1} \right) \quad (2.40)$$

$$X[\text{mm} \cdot \text{Pa} \cdot \text{K}^{-1}] = \frac{2 \cdot d \cdot P_{SRG}}{T_{trap} + T_{SRG}} \quad (2.41)$$

where d is the connecting tube diameter in mm (3 mm) and pressure is expressed in Pascal (1 mBar = 100 Pa). Sanderson *et al.* [145] empirically fitted and derived the A, B and C constants in Eq. 2.40 for helium gas at low temperature (4.35 K)

2

$$A[K^2 \text{ mm}^{-2} \text{ Pa}^{-2}] = 6.11$$

$$B[K \text{ mm}^{-1} \text{ Pa}^{-1}] = 4.26$$

$$C[K^{\frac{1}{2}} \text{ mm}^{-\frac{1}{2}} \text{ Pa}^{-\frac{1}{2}}] = 0.52$$

The trap number density including thermal transpiration correction, $(n_{trap})_{TT}$, is derived by substituting equation 2.40 in 2.37 and we then get:

$$(n_{trap})_{TT} = \frac{1}{k_B} \cdot \frac{(P_{trap})_{TT}}{T_{trap}} \quad (2.42)$$

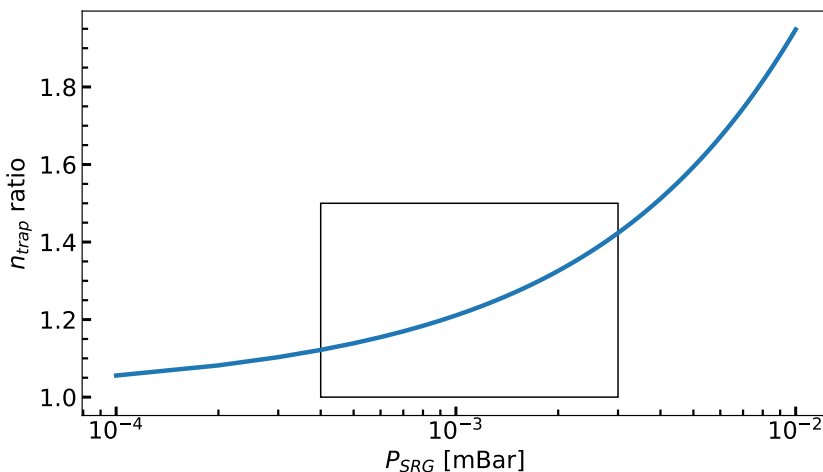


Figure 2.16.: Comparing number density, n_{trap} , with and without thermal transpiration. The figure shows pressure measured using SRG vs n_{trap} (Thermal transpiration / low-pressure approximation) ratio. The marked box region indicates the pressure range used in this study.

Uncertainty considerations: The computed number density ratio, n_{trap} ratio = $\frac{(n_{trap})_{TT}}{n_{trap}}$, is shown in Figure 2.16. In this thesis work, the number density is determined using thermal transpiration corrections. The pressure is measured

using a spinning rotor gauge (SRG), a mean value from 10 iterations per cycle of measurements is taken, and background corrected. When changing the pressure value, a typical wait time of ~ 5 min is considered for the system to reach equilibrium. The SRG determines the pressure by measuring the relative rate of deceleration of a metal sphere freely rotating in a vacuum ambience. Therefore, a measurement uncertainty of up to 10%³ must be considered, caused by an increased heating up of the rotor and gas due to the continuous repetition of the sphere drive. In addition, the room temperature, $T_{SRG} = 300(1)$ K and tube diameter, $d = 3.0(1)$ mm. The number density uncertainty is computed through linear error propagation theory using python *uncertainties package* [146].

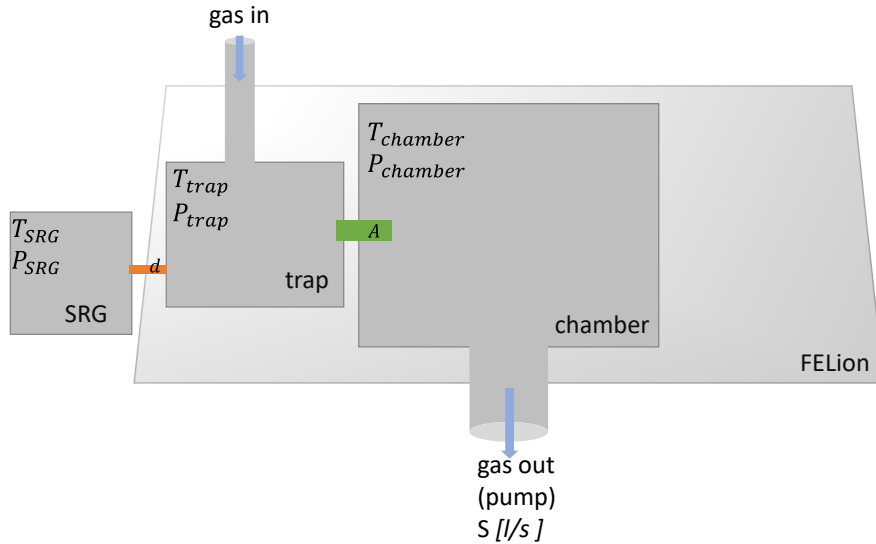
2.5.2. CALIBRATION OF THE HOT-CATHODE IONIZATION GAUGE (HIG) TO SRG

The 22-pole ion trap in the FELion instrument is located at the main chamber where the temperature ($T_{chamber}$) and pressure ($P_{chamber}$) are different from the trap ($T_{trap}, P_{chamber}$), because only the trap is mounted onto the cold head as described in Section 2.1.2, and, more importantly, the gas is admitted into the trap and pumped through the entrance and exit electrodes, leading to a differential pumping. A schematic diagram of this setup is shown in Figure 2.17. As discussed in Section 2.5.1 the pressure in the trap is measured using a spinning rotor gauge (SRG), i.e., P_{SRG} . However, the main chamber is also equipped with a hot-ionisation gauge (Bayard-Alpert gauge, AML AlG17G with NGC2 controller), which is often used to measure the gas pressure let into the trap. Now, to determine the number density from the chamber pressure, a relation between $P_{chamber}$ and P_{SRG} needs to be established and then the number density of gases can be derived as shown in Section 2.5.1.

Hot Ionisation Gauge (HIG) background: In the HIG, electrons are thermionically emitted from a hot cathode filament and are accelerated into an ionization volume (anode) known as the grid (in the main chamber of our instrument). Collisions between free electrons and neutral buffer gas molecules within the volume may result in ionizing the gas molecule (positive ions), which are accelerated into the ion collector (electrode). The generated positive ion collector current (i_c) is directly proportional to the number density of gas, i.e., $P_{chamber}$ as follows

$$i_c = K \cdot i_e \cdot P_{chamber}$$

³<https://www.npl.washington.edu/TRIMS/sites/sand.npl.washington.edu.TRIMS/files/manuals-documentation/MKS-SRG-3-manual.pdf>



2

Figure 2.17.: Schematic diagram on the relation of ion-trap, spinning rotor gauge (SRG) and the main chamber. The orange and green coloured region represents the connecting tube for SRG to trap and trap to the chamber, respectively, with the corresponding aperture of diameter d and A .

where i_e and K are electron emission current and gauge sensitivity, respectively.

Pumping speed (S) and throughput (Q): The throughput of the gas molecule (Q) can be defined in terms of pumping speed, S [liters/s or l/s] and pressure (P) as follows

$$Q = P \text{ [mbar]} \cdot S \text{ [l/s]}$$

As shown in Figure 2.17, the gas is let into the trap (gas in) and flows into the chamber region with an aperture diameter, A , corresponding to the two entrance and exit lenses (6 mm diameter each). The speed at which the gas molecule flows from trap to chamber will depend on the pressure difference between the two regions as well as the geometry of the chamber in-between, i.e., aperture (A). The factor which accounts for this difference is known as "conductance" (C'), which is defined as

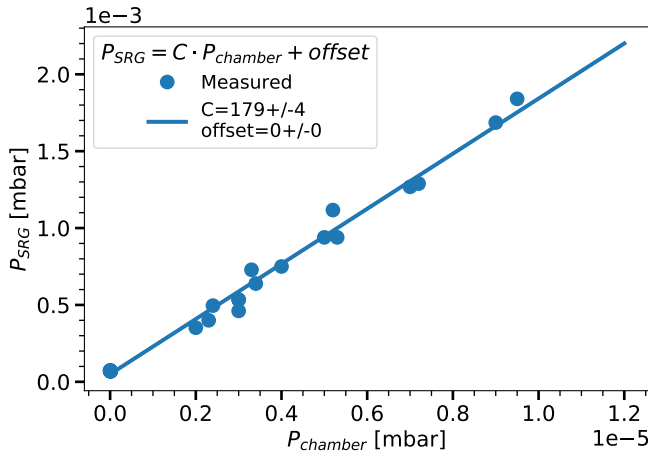


Figure 2.18.: Pressure measured with SRG and HIG are plotted at 5 K trap nominal temperature. The derived calibration factor is $C = 179(4)$.

$$C'_{trap} = \frac{Q_{trap}}{P_{trap} - P_{chamber}}$$

such that,

$$Q_{trap} = C'_{trap} \cdot (P_{trap} - P_{chamber}) \quad (2.43)$$

If we define the pumping speed (S_A) for gas flow from the trap to the chamber via the aperture of diameter A and S for the pumping speed at which the gas molecules leave out off the chamber via a vacuum pump (see Figure 2.17), then at equilibrium, we get

$$Q_{trap} = Q_{pump} \Leftrightarrow P_{trap} \cdot S_A = P_{chamber} \cdot S \quad (2.44)$$

Substituting Eq. 2.43 in 2.44, we get

$$C'_{trap} \cdot (P_{trap} - P_{chamber}) = P_{chamber} \cdot S$$

which becomes,

$$\frac{P_{trap}}{P_{chamber}} = 1 + \frac{S}{C'_{trap}} = C \quad (2.45)$$

where C is the calibration factor for pressure between the trap and the chamber.

Since we are measuring the trap pressure using SRG, i.e., $P_{trap} = P_{SRG}$ and the SRG temperature is the same as the chamber (both at room temperature, RT), i.e., $T_{SRG} = T_{chamber} = RT$, from equation 2.45, we get

$$P_{SRG} = C \cdot P_{chamber} \quad (2.46)$$

The above equation 2.46 provides us with the required relation between SRG and HIG pressure measurement. Figure 2.18 shows the derived calibration value at 5 K trap nominal temperature, i.e., $C = 179(4)$ at 5 K. The C value is also found to be temperature independent but depends only on the settings for HIG (the sensitivity is set to N₂ gas).

III

VIBRATIONAL SPECTROSCOPY

3

LABORATORY GAS-PHASE VIBRATIONAL SPECTRA OF $[C_3H_3]^+$ ISOMERS AND ISOTOPOLOGUES BY IRPD SPECTROSCOPY

This chapter is adapted from: Marimuthu, A. N.; Sundelin, D.; Thorwirth, S.; Redlich, B.; Gepert, W. D.; Brünken, S. Journal of Molecular Spectroscopy 2020, 374, 111377

ABSTRACT

Gas phase vibrational spectra of [C₃H₃]⁺ isomers and their fully deuterated isotopologues measured in a cryogenic 22-pole ion trap are presented. The widely tunable free electron laser for infrared experiments, FELIX, was employed to cover the frequency range 500-2400 cm⁻¹, complemented with an OPO/OPA system covering 2800-3400 cm⁻¹. Spectral assignments for both the linear and cyclic isomeric form (H₂C₃H⁺ and c-C₃H₃⁺, respectively) are made based on various high-level computational studies. The effect of ion source conditions and different precursors (allene and propargyl chloride) for the preferential production of a specific isomer is discussed. The perturbation of the vibrational band position due to complexation with Neon in the recorded infrared-predissociation (IRPD) spectra are also reported in this study.

3.1. INTRODUCTION

Hydrocarbon ions with the chemical composition $[C_3H_3]^+$ are important intermediates in combustion processes, where they initiate soot formation [147, 148, 149], and in various astrochemical environments such as the interstellar medium (ISM) [150, 151, 152, 53], cometary surfaces [153], and planetary atmospheres [154, 155]. The ion has two stable isomers, the cyclic cyclopropenyl cation, $c\text{-}C_3H_3^+$, and the linear propargyl cation, $H_2C_3H^+$, see Figure 3.1. The $c\text{-}C_3H_3^+$ isomer is lower in energy by 28 kcal/mol [156], and a significant activation barrier of about 50 kcal/mol separates the two isomers [157]. $c\text{-}C_3H_3^+$ is the smallest aromatic cation stabilised by two delocalised π electrons; hence it has been observed as a common stable fragment from the electron impact ionization mass spectra of many larger hydrocarbon molecules [158, 159].

In the interstellar medium, $[C_3H_3]^+$ is formed by radiative association addition of H_2 to linear C_3H^+ , a molecular ion recently detected in several astronomical sources [160, 161, 162] based on accurate laboratory spectroscopic determination of its rotational spectrum [99, 163]. Experimental and theoretical studies support the formation of both isomeric variants of $[C_3H_3]^+$ in this process [164, 151, 165]. Both $c\text{-}C_3H_3^+$ and $H_2C_3H^+$ are assumed to be the major precursors (via dissociative recombination) of cyclic and linear forms of $[C_3H_2]$ and $[C_3H]$ [150, 151, 53], which are ubiquitous molecules in the interstellar medium [166, 167, 152, 168, 169, 170, 171]. The observed large variation in the cyclic-to-linear isomeric ratio of both neutrals across different astronomical sources is intricately linked to the formation and destruction of isomeric variants of $[C_3H_3]^+$ [172, 173, 174, 175]. Apart from the main isotopologues, also singly and even doubly deuterated variants of $[C_3H_2]$ were detected [176, 177, 178], and are frequently used to investigate deuterium fractionation via gas-phase processes in cold dark clouds [179, 180, 181]. Although many details about the exact deuteration mechanisms are only partly understood, they all involve deuterated variants of $[C_3H_3]^+$ [182, 177]. It should also be noted that due to its D_{3h} symmetry, the $c\text{-}C_3H_3^+$ isomer has no pure rotational spectrum, thus its direct observation is not possible by radio-astronomy. However, the linear isomer $H_2C_3H^+$ and also singly or doubly D-substituted variants of $c\text{-}C_3H_3^+$ possess a permanent dipole moment, and are therefore good candidates for radio-astronomical detection.

In a recent study of Titan's atmosphere by the Ion and Neutral Mass Spectrometer (INMS) onboard the CASSINI spacecraft, a strong signal at $m/z = 39$ corresponding to the $[C_3H_3]^+$ cation has been recorded [183]. Although these mass spectrometric detections do not allow to identify the isomeric composition, one can assume the presence of both $[C_3H_3]^+$ isomers [155]. Reactions of

H₂C₃H⁺, which was found in experiments to be much more reactive than the aromatic c-C₃H₃⁺ isomer [184, 185, 186], with unsaturated hydrocarbons could be the first elongation steps leading to larger ions, including polycyclic hydrocarbons, in this environment. Upon dissociative and radiative recombination with electrons, heavy neutrals, i.e. tholins, can be formed. Similar processes could happen in other astronomical objects like dark clouds, circumstellar envelopes, star-forming regions, and protoplanetary disks. Model calculations of chemical networks in those environments are dependent on exact data about the reactivity of all isomers of a certain ion. Therefore, it is important to find pathways to produce the isomers selectively to be able to assess their reactive properties in experimental kinetic studies. This has already been done for other ions showing isomers with different reactivity, e.g. for CH₂CN⁺ [187, and references therein]. Although the results are encouraging, the most reliable way to pin down the identities of isomers produced by a certain method is via spectroscopic methods.

Due to their importance in astrochemistry and other fields, numerous experimental and theoretical spectroscopic studies exist on the [C₃H₃]⁺ cations. Breslow and co-workers measured the first infrared spectra of c-C₃H₃⁺, but in acid solutions as a stable salt [188]. Both isomers were later studied in a Neon matrix by electronic and vibrational spectroscopy [189]. Very recently the vibrational spectrum of H₂C₃H⁺ and its fully deuterated form was measured in Argon matrix [190]. The first gas-phase vibrational spectra covering the C-H stretching region of [C₃H₃]⁺ were measured using an infrared-predissociation (IRPD) method [191, 192], and interpreted through high-level quantum-chemical calculations of the ionic structure including the influence of the various tagging agents [193, 194, 195]. The experiments were later extended by Ricks et al., who observed several additional fundamental vibrational bands down to the dissociation limit of the Argon tag that they used in the IRPD experiments (approximately 1000 cm⁻¹) [196]. However, some ambiguity in the assignment of several bands of both isomers remained [156, 157]. Linnartz and co-workers reported the first high-resolution gas-phase IR spectra of the fundamental ν_4 asymmetric C-H stretching band for free (i.e., without ligand tagged) c-C₃H₃⁺ using continuous wave cavity ring-down spectroscopy [197], and found excellent agreement of their results to spectroscopic parameters obtained from high-level ab initio calculations of quartic force fields [156]. Additional information of vibrational band positions of [C₃H₃]⁺ comes from photoelectron studies [198, 199] and electronic spectroscopy [200].

In this study we report the broad range (550-3400 cm⁻¹) vibrational spectra of gas-phase [C₃H₃]⁺ and its fully deuterated variants using different tagging agents

(Ne, H₂), ion-sources, and precursors. We employed IRPD action spectroscopy in a cryogenic ion trap coupled to the powerful and widely tunable FELIX free-electron IR lasers. The aim of this study is manyfold: (i) to unambiguously assign the vibrational bands of both isomers by comparison to quantum-chemical calculations, which then, in turn, can be used to benchmark these calculations; (ii) to investigate isomer-selective formation mechanisms as a prerequisite for isomer-specific kinetic studies; (iii) to obtain reliable IR data that can be used to spectroscopically distinguish the isomeric [C₃H₃]⁺ products of ion-molecule reactions, and (iv) to provide a basis for follow-up high-resolution rotational studies of those isomers and their isotopologues that possess a permanent dipole moment to aid their astronomical detection.

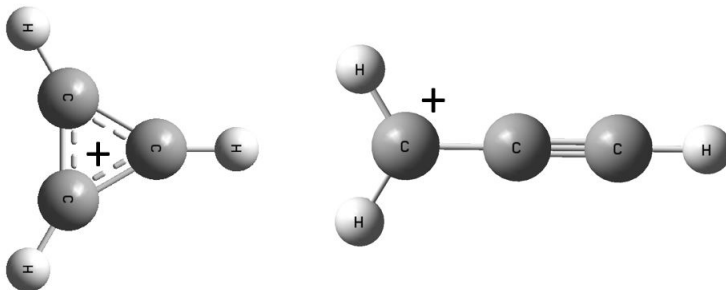


Figure 3.1.: Molecular structures of c-C₃H₃⁺ (left) and H₂C₃H⁺ (right) isomers.

3.2. METHODS

3.2.1. EXPERIMENTAL DETAILS

The vibrational spectra of the [C₃H₃]⁺ isomers and isotopologues were recorded using the FELion cryogenic 22-pole ion trap instrument located at the Free Electron Lasers for Infrared eXperiments (FELIX) Laboratory (see Section 2.2.2.1). A detailed account of the FELion instrument is provided in Section 2.1 and the infrared-predissociation (IRPD) of in-situ rare gas tagged cold molecular ions in Section 1.5.1.1. Here we only give a brief account of details specific to the [C₃H₃]⁺ system.

3

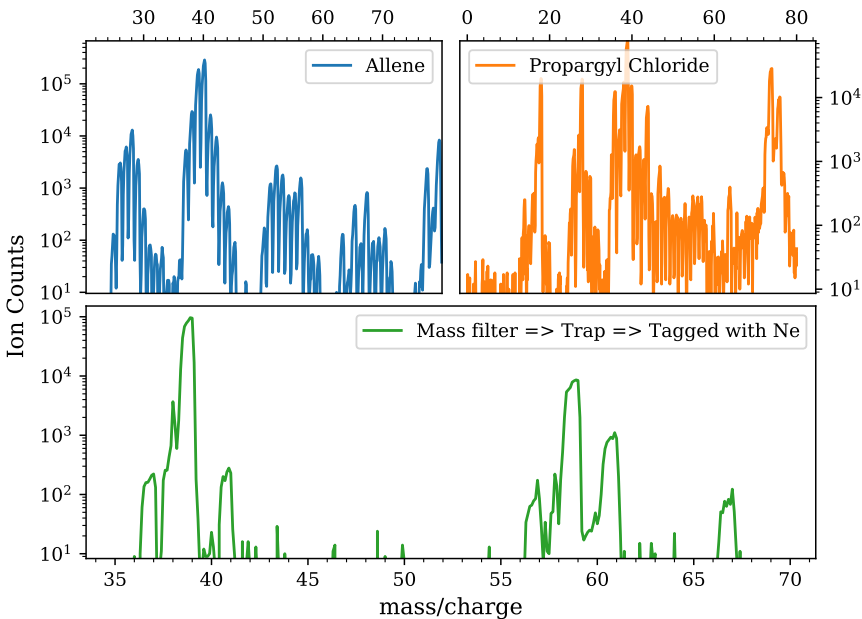


Figure 3.2.: Mass spectra of ions produced from electron impact ionization (20 eV) of allene (left, in storage EI source) and propargyl chloride (right, in direct EI source) precursors (upper panel), and of mass filtered $[C_3H_3]^+$ ($m = 39$ u) together with tagged Ne- $[C_3H_3]^+$ ($m = 59$ u) species produced in the cryogenic ion trap (lower panel).

Isomeric variants of $[C_3H_3]^+$ ($m=39$ u) were produced by electron impact ionization (electron energy 11 – 70 eV) from neutral allene (C_3H_4 , abcr GmbH, 96 %) and propargyl chloride (HC_3H_2Cl , Sigma Aldrich, 98 %). Fully deuterated $[C_3D_3]^+$ was produced from deuterated allene (C_3D_4 , Qmx Laboratories, 98 %). The precursor gases were admitted either pure or diluted with He at a ratio of 1:3 to the ion source chamber at a pressure of $\sim 10^{-5}$ mbar. For most experiments, a simple electron-impact (EI) source was used, and additional measurements were done with a Gerlich-type storage ion source (SIS) [201], where primary ions produced by EI are accumulated for the duration of an experimental cycle (of the order of seconds), thereby allowing further reactions with the present neutral gas (see Figure 3.2).

For spectroscopic experiments a few 10 ms long pulse of ions is extracted from the respective source and filtered for the mass of interest, $m=39$ u in the case of

$[C_3H_3]^+$ and $m=42$ u for $[C_3D_3]^+$, by a quadrupole mass selector before entering the 22-pole ion trap which is held at a fixed temperature in the range 6.1–7 K for experiments using Ne and 11 K for those using H₂ as tagging gasses. Around 10–20 ms before the ions enter the trap, an intense 80–150 ms long Ne:He (or H₂:He) pulse (1:3 mixing ratio and number density of $\sim 10^{15}$ cm⁻³) is admitted to the trap, leading to efficient collisional cooling of the ions to the ambient temperature. Under these conditions, several 10 % of the primary ions form weakly bound complexes with Ne (or H₂), see Figure 3.2. The ions are stored for several seconds in the ion trap and are exposed to several laser pulses before extraction. An IRPD spectrum is recorded by mass-selecting and detecting the $[C_3H_3]^+$ -Ne(H₂) complex ions while tuning the laser frequency ν . A relative depletion $D = 1 - \frac{N_{ON}(\nu)}{N_{OFF}}$ in the number of complex ions $N_{ON}(\nu)$ from the baseline value N_{OFF} is observed upon resonant vibrational excitation. To account for varying laser pulse energy P , pulse number n , and for saturation effects, the signal is normalized prior to averaging using $I = \frac{-\ln(N_{ON}(\nu)/N_{OFF})}{n \cdot P / (\hbar\nu)}$, giving the intensity I in units of relative cross-section per photon¹. After normalizing each measurement in this way, the final spectrum is then obtained by averaging using statistical binning with a typical bin size of 2.5 cm⁻¹. Line parameters such as band positions, intensities, and line widths (fwhm) are then obtained by fitting a multi-component Gaussian function to the experimental data, also providing statistical errors of the line parameters.

Additionally, we performed saturation depletion experiments (see section 3.3.5) to quantify the isomeric ratio of the ionic mixture as described in detail previously [202, 65]. Here we used up to 46 laser pulses, resonant with an isomer-specific vibrational band position, to fully deplete (dissociate) just one isomer complex. The analysis of the depletion signal as a function of laser pulses, corrected for other loss-mechanisms, allows then to derive both the absorption-dissociation cross-section and the isomer abundance.

The vibrational IRPD spectra were recorded using the IR radiation of FEL-2 of the FELIX Laboratory in the frequency region 550–2400 cm⁻¹, also employing the 3rd harmonic mode of the FEL. The laser was operated at 5 or 10 Hz with macro pulse energies in the interaction region between 1.5–60 mJ, and for each data-point $n = 3$ –66 pulses were admitted depending on the signal strength. The FEL was optimized for narrow bandwidth with a full width at half-maximum (fwhm) of 0.3 – 1 % of the center wavelength. Additional spectra were recorded in the C-H-stretching region between 2800–3400 cm⁻¹ using a Laservision OPO/OPA sys-

¹This equation only holds for isomer-pure ionic samples. Saturation effects in isomeric mixtures are underestimated in this way, leading to varying intensity ratios in the presented spectra.

tem ($\sim 3 \text{ cm}^{-1}$ fwhm, 10 Hz, 5 ns pulses) with typical power of $\sim 7\text{-}10 \text{ mJ}$.

3

3.2.2. COMPUTATIONAL DETAILS

The [C₃H₃]⁺ system has previously been studied quantum-chemically on several occasions and at various levels of theory [156, 193, 194, 195]. In the present investigation of the hydrogenated and perdeuterated variants, quantum chemical calculations have been performed at the coupled-cluster singles and doubles (CCSD) level augmented by a perturbative treatment of triple excitations, CCSD(T) [203], together with atomic natural orbital (ANO0, ANO1, and ANO2) basis sets from Almlöf and Taylor [204]. The ANO0, ANO1, and ANO2 basis sets consist of 13s8p6d4f2g to 3s2p1d, 4s3p2d1f, and 5s4p3d2f1fg contractions for C as well as 8s6p4d3f to 2s1p, 4s2p1d, and 4s3p2d1f contractions for H, respectively. Equilibrium geometries have been calculated using analytic gradient techniques [205], while harmonic frequencies have been computed using analytic second-derivative techniques [206, 207]. For anharmonic calculations, second-order vibrational perturbation theory (VPT2) [208] has been employed and additional numerical differentiation of analytic second derivatives has been applied to obtain the third and fourth derivatives required for the application of VPT2 [207, 209]. The frozen core approximation has been used throughout. All calculations (including those employing VPT2) have been carried out using the CFOUR program package [210, 136].

The CCSD(T) method in combination with ANO basis sets has been shown previously to provide vibrational wavenumbers of high quality [211, 212]. In the present investigation, harmonic force fields were calculated at the CCSD(T)/ANO2 level throughout. For the c-C₃D₃⁺ and H₂C₃H⁺ species, best estimates of the fundamental vibrational wavenumbers were then calculated by applying anharmonic vibrational corrections calculated at the CCSD(T)/ANO1 level to the CCSD(T)/ANO2 harmonic wavenumbers. Because of numerical problems in the CCSD(T)/ANO1 VPT2 calculation, for the c-C₃H₃⁺ and D₂C₃D⁺ species, anharmonic corrections were taken from corresponding CCSD(T)/ANO0 calculations. A comparison of the fundamental vibrational frequencies obtained in this fashion using CCSD(T)/ANO1 and CCSD(T)/ANO0 for the c-C₃D₃⁺ and H₂C₃H⁺ species reveals that the differences between the two levels are small, order of a few cm^{-1} only. From the anharmonic force field calculations we also find that in the c-C₃D₃⁺ species, the ν_1 mode is in resonance with the overtone of the ν_5 mode (using thresholds of $\Delta\omega = 50 \text{ cm}^{-1}$ and $\Phi_{ijj} = 80 \text{ cm}^{-1}$). The corresponding VPT2 frequencies were unperturbed by removing the term involving the res-

onance denominators. VPT2 intensities are not unperturbed in the present version of CFOUR and are reported here as provided by the program. To support the spectroscopic assignment of vibrational features other than the fundamentals, overtone and combination modes were also derived from the CCSD(T)/ANO1 (*c*-C₃D₃⁺ and H₂C₃H⁺) and CCSD(T)/ANO0 (*c*-C₃H₃⁺ and D₂C₃D⁺) computations. A summary of the computational results is given as part of the electronic supplementary material.

3.3. RESULTS AND DISCUSSIONS

We measured experimental IRPD spectra of [C₃H₃]⁺ isomers under various conditions such as using different ligands (Ne and H₂), ion sources (storage and direct EI sources, Figure 3.6), and different precursors (propargyl chloride and allene) with ionization energy ranging from (14-70) eV. The presence of both isomers with varying relative abundance in different conditions was observed and is discussed in detail in Section 3.3.5. The IRPD vibrational band frequencies obtained from an average spectrum (Figure 3.3, including data from the propargyl chloride and allene precursors produced in the direct EI source with varying electron impact energies) compared with computed and previous experimental frequencies of both isomers are summarised in Table 3.1. The C-H stretching region was measured with the OPO/OPA system only for the allene precursor produced in the storage source, see Figure 3.4. The vibrational band assignments based on various computational studies using coupled cluster methods will be discussed for the cyclic and linear isomer in detail in Sections 3.3.1 and 3.3.2, respectively, and for the deuterated species in Section 3.3.4. The influence of the tagging agent will be discussed in Section 3.3.3, but was found to be negligible.

3

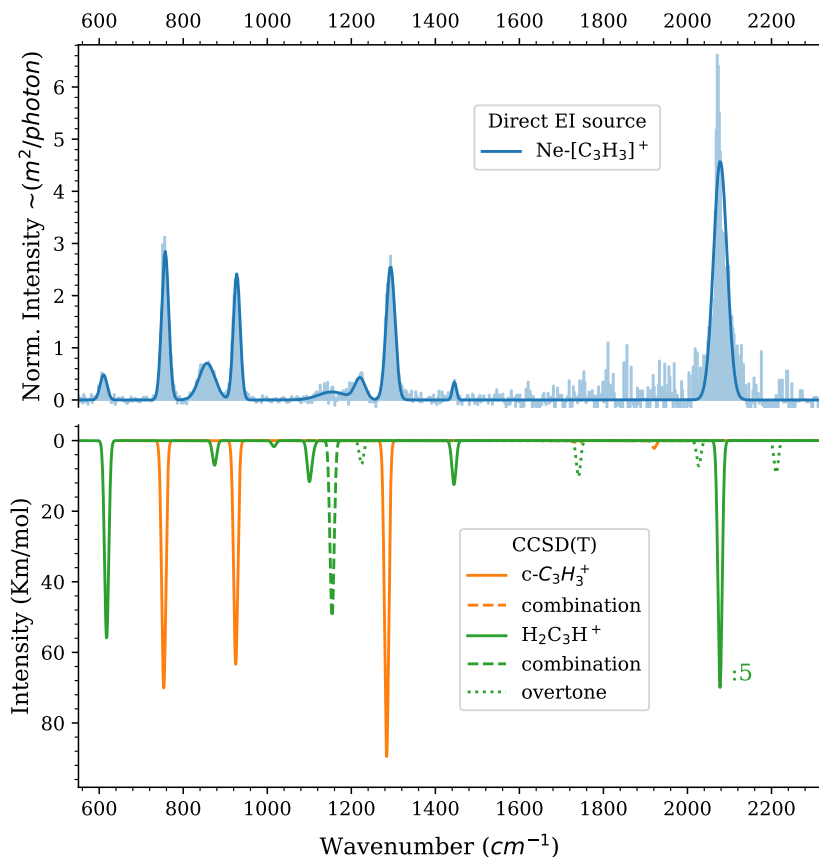


Figure 3.3.: The experimental and fitted FELIX IRPD spectrum of $Ne-[C_3H_3]^+$ (upper panel) compared to computed frequencies (lower panel) at CCSD(T)/ANO2 combined with the anharmonic correction from CCSD(T)/ANO1 ($H_2C_3H^+$) and CCSD(T)/ANO0 (c- $C_3H_3^+$). Only fundamental (solid line), combination (dashed line) and overtone (dotted line) infrared bands with intensity $> \sim 1$ km/mol were included. The theoretical spectrum was folded with a Gaussian corresponding to the FEL linewidth. Peaks marked with :n indicate that the depicted peak intensity is scaled down by a factor n, for better visualization.

Table 3.1.: Summary of IRPD experimental vibrational band position of Ne-[C₃H₃]⁺ compared to computed fundamental, overtone and combination band frequencies at the CCSD(T)/ANO2 level of theory combined with anharmonic corrections from CCSD(T)/ANO1 (for H₂C₃H⁺) and CCSD(T)/ANO0 (for c-C₃H₃⁺).

Mode	Ne-IRPD ^a (this work)	FWHM cm ⁻¹	Calc. [Int.] cm ⁻¹ [Km/mol]	Ar-IRPD cm ⁻¹	VMI-PE ^c cm ⁻¹	Ar-Matrix ^d cm ⁻¹
c-C₃H₃⁺						
$v_1(a'_1)$	-	-	3179 [0]	-	-	
$v_2(a'_1)$	-	-	1610 [0]	-	-	
$v_3(a'_2)$	-	-	1024 [0]	-	-	
$v_4(e')$	3133(1) ^b	14	3127 [189]	3182		
$v_5(e')$	1293(1)	25	1284 [88]	1293		
$v_6(e')$	927(1)	19	925 [60]	nc		
$v_7(a''_2)$	757(1)	20	754 [70]	nc		
$v_8(e'')$	-	-	1000 [0]	-		
$v_7+v_8(e')$	-	-	1739 [1]			
$v_3+v_6(e')$	-	-	1921 [2]			
H₂C₃H⁺						
$v_1(a_1)$	-	-	3230 [102]	3238		3195.3
$v_2(a_1)$	3003(1) ^{b, t}	9	2997 [26]	3004		3000.6
$v_3(a_1)$	2078(1)	32	2078 [346]	2077	2086(15)	2075.2
$v_4(a_1)$	1445(1)	12	1444 [12]	1445		1433.2
$v_5(a_1)$	1138(4)	31	1109 [2]	1222	1120(15)	1140
$v_6(b_1)$	1138(4)	31	1100 [11]	1111		1105.2
$v_7(b_1)$	856(1)	44	875 [7]	nc	858(15)	
$v_8(b_1)$	nc	nc	263 [26]	nc		

^a Frequencies (error in parenthesis). nc indicates not-covered and hyphen – indicates not observed.

^b Measured with OPO/OPA system. The remaining bands are measured with the FELIX free electron laser.

^c Ref. [198] - Velocity-map imaging photo-electron method.

^d Ref. [190] - Direct IR absorption spectra of H₂C₃H⁺ in solid Ar matrix.

^t Tentative assignment.

* Ref. [196].

Table 3.1 – continued on next page

Table 3.1 – continued from previous page

Mode	Ne-IRPD ^a (this work)	FWHM cm ⁻¹	Calc. [Int.] cm ⁻¹ [Km/mol]	Ar-IRPD cm ⁻¹	VMI-PE ^c cm ⁻¹	Ar-Matrix ^d cm ⁻¹
$\nu_9(b_2)$	3041(1) ^{b, t}	9	3087 [37]	3093		3063.4
$\nu_{10}(b_2)$	-	-	1016 [2]	-		
$\nu_{11}(b_2)$	610(1)	12	618 [56]	nc		606.8
$\nu_{12}(b_2)$	nc	nc	299 [15]	nc		
$\nu_3+\nu_5(a_1)$	-	-	3168 [7]			
$\nu_3+\nu_{10}(b_2)$	-	-	3086 [4]			
$\nu_4+\nu_{10}(b_2)$	-	-	2444 [2]			
$\nu_7+\nu_8(a_1)$	1138(4)	31	1154 [50]			
$2\nu_4(a_1)$	-	-	2865 [1]			
$2\nu_5(a_1)$	-	-	2211 [9]		2247(15)	
$2\nu_7(a_1)$	-	-	1741 [10]		1744(15)	
$2\nu_{10}(a_1)$		27	2027 [7]			
$2\nu_{11}(a_1)$	1222(1)	27	1224 [7]			

3.3.1. CYCLIC ISOMER

The planar c-C₃H₃⁺ isomer has D_{3h} symmetry with an A'_1 vibronic ground state. All of the only four IR active fundamental bands (ν_4 , ν_5 , ν_6 and ν_7 , with the former three being doubly-degenerate) of this energetically lowest-lying aromatic isomer are clearly observed (see Figure 3.3 and 3.4, and Table 3.1). The band at 3133 cm⁻¹ is assigned to the ν_4 asymmetric CH stretching mode, with good agreement to the computed value of 3127 cm⁻¹ and to a previous Ne-IRPD experiment by Roth and Dopfer [191], who measured this band at 3130 cm⁻¹. This vibration has also been reported in Ne-matrix at 3130 cm⁻¹ [189]. Duncan and coworkers had originally reported this band around 3182 cm⁻¹ [196], but later revised their assignment [157], in line with other experiments [197, 191] (see Table 3.1), including this work, and previous calculations [193, 156]. Based on their calculations, Botschwina et al. [193] argued that the 3182 cm⁻¹ band from Duncan's work could be the $\nu_3+\nu_5$ combination band of the linear isomeric form and not the ν_4 . The fact that we do not observe a band at 3182 cm⁻¹ under conditions preferentially producing the cyclic isomer (see Section 3.3.5), supports this assignment. Somewhat puzzling is the appearance of two weak features at 3003 and 3041 cm⁻¹ which are only present in the Ne-tagged spectrum in Figure 3.4.

No combination or overtone bands of the cyclic isomer are predicted at these frequencies. We tentatively assigned them to the ν_2 and ν_9 modes of the linear isomer. However, the much stronger ν_1 band, observed at 3238 cm^{-1} in the Ne-IRPD spectrum of Botschwina *et al.* [195], is not detected.

The prominent feature $\nu_5(e')$ corresponding to the asymmetric CCC ring stretching is clearly identified at 1293 cm^{-1} . This band was also reported at 1293 cm^{-1} with Ar-tagging [196]. Whereas our computed anharmonic frequency at CCSD(T) level is lower by 11 cm^{-1} , the comparison to CCSD(T) quartic force field calculations in combination with variational calculation (VCI 5MR) from Huang *et al.* [156] shows good agreement (1296.2 cm^{-1}). The in-plane CH scissoring (927 cm^{-1} , $\nu_6(e')$) and symmetric CH out-of-plane wagging (757 cm^{-1} , $\nu_7(a''_2)$) modes have been measured with an excellent agreement to the computed band positions (see Table 3.1), and gas-phase data of these two bands are reported here for the first time. Previously, they were measured by Craig *et al.* [213] in various different polycrystalline salts of $\text{c-C}_3\text{H}_3^+X^-$ (with $X=\text{SbF}_5$) at 757 cm^{-1} (ν_7) and 925 cm^{-1} (ν_6) which agree well with our measurements.

3

3.3.2. LINEAR ISOMER

The linear propargyl isomer with C_{2v} symmetry and an A_1 vibronic ground state has 12 fundamental bands, which are all IR active. Previous measurements on the gas-phase $\text{H}_2\text{C}_3\text{H}^+$ isomer include Ar-IRPD spectra (at frequencies above the Ar binding energy ($\sim 1000\text{ cm}^{-1}$)) [196] and combined vacuum ultraviolet (VUV) laser - velocity-map imaging photoelectron (VMI-PE) spectra obtained only for the ν_3 , ν_5 and ν_7 modes [198]. Here we report and discuss the spectral characterization of the $\text{H}_2\text{C}_3\text{H}^+$ isomer measured in a wide range from $550\text{-}3400\text{ cm}^{-1}$.

The most prominent $\nu_3(a_1)$ CC triple bond stretching mode at 2078 cm^{-1} is clearly seen with an excellent agreement to the computed value of the bare ion (2078 cm^{-1}) and the experimental value (2077 cm^{-1}) obtained with Ar-tagging IRPD [196]. Similarly, the weak band at 1445 cm^{-1} is assigned to the ν_4 CH_2 scissoring vibration. The broad mode identified at 1222 cm^{-1} can be assigned to $2\nu_{11}(a_1)$ supported by a computed value of the overtone at 1224 cm^{-1} with substantial intensity larger than other overtone and combination bands in that region. This band was originally assigned to the ν_5 band by Ricks *et al.* [196]. The similarly broad band at 1138 cm^{-1} with larger uncertainty of $3\text{-}4\text{ cm}^{-1}$ and FWHM of 31 cm^{-1} is consequently assigned here to a blend of ν_5 , ν_6 , and $\nu_7 + \nu_8$ (intensity of this combination mode might be over-estimated in the calcula-

tion, 50 km/mol, see Figure 3.3), which our anharmonic CCSD(T) calculations predict at 1109, 1100, and 1154 cm⁻¹, respectively. We should, however, note here that our calculated ν_5 and ν_6 band position are not consistent with the earlier coupled cluster calculations from Botschwina and co-workers [195, 193] and Huang et al. [156] (see Table 3.2), who predicted these bands at 1123 cm⁻¹ and 1100 cm⁻¹, respectively, for Ne-tagged H₂C₃H⁺ and around 1130 cm⁻¹ and 1058 cm⁻¹ (depending on the level of theory), respectively, for the bare ion. The discrepancy for the ν_5 band is likely due to varying theoretical treatment of a Fermi resonance with the $\nu_7 + \nu_8$ combination band, which might be further influenced by the (small) perturbation of the Ne-tag. Ricks et al. [196] observed a doublet feature centered at 1111 cm⁻¹ with Ar as tagging agent, and assigned it to the partly resolved P- and R-branch of the perpendicular ν_6 band. The ν_7 CCH out-of-plane bending and ν_{11} CCH in-plane bending bands clearly appear at 856 and 610 cm⁻¹, respectively. However, the former band is extremely broad, as is the equivalent band in the fully deuterated species, and was difficult to distinguish from baseline fluctuations in the experiments. We assume a fast predissociation of the Ne-ion complex upon excitation of this mode, leading to life-time broadening.

3.3.3. NE-EFFECT

We analyzed the effect of Ne complexation on the bare ions' vibrational spectra by comparing them to the computed anharmonic frequencies from various coupled cluster methods of both ligand tagged and untagged species. Botschwina and co-workers [195] had carried out very detailed computational studies on the weak interactions in the ion-ligand complexes of $[C_3H_3]^+$ by analyzing the potential energy profile of the complexes while migrating the ligand around the ion-molecule. They have found two C_s and one C_{2v} (highest energy) structures for Ne-c-C₃H₃⁺ and three C_s minima for Ne-H₂C₃H⁺ complex ion. They found negligible shifts of order < 3 cm⁻¹ for the vibrational band positions for both $[C_3H_3]^+$ isomers and all ligand-ion isomers. A detailed comparison of ligand-induced band shifts in the spectrum of the H₂C₃H⁺ isomer is provided in Table 3.2, where we report only values for the lowest energy C_s structure from Botschwina *et al.* [195]. The prominent features ν_3 and ν_4 appear to have no perturbation within 1 cm⁻¹ uncertainty and this is supported by both our Ne-IRPD experiment and calculations on Ne-H₂C₃H⁺. The larger discrepancy in the ν_7 band could be reasonably explained by other effects as discussed in section 3.3.2 and 3.3.4. The four IR active fundamental band of the cyclic isomer of both $[C_3H_3]^+$ (except ν_5 , see section 3.3.1) and $[C_3D_3]^+$ (section 3.3.4) also show excellent agreement with

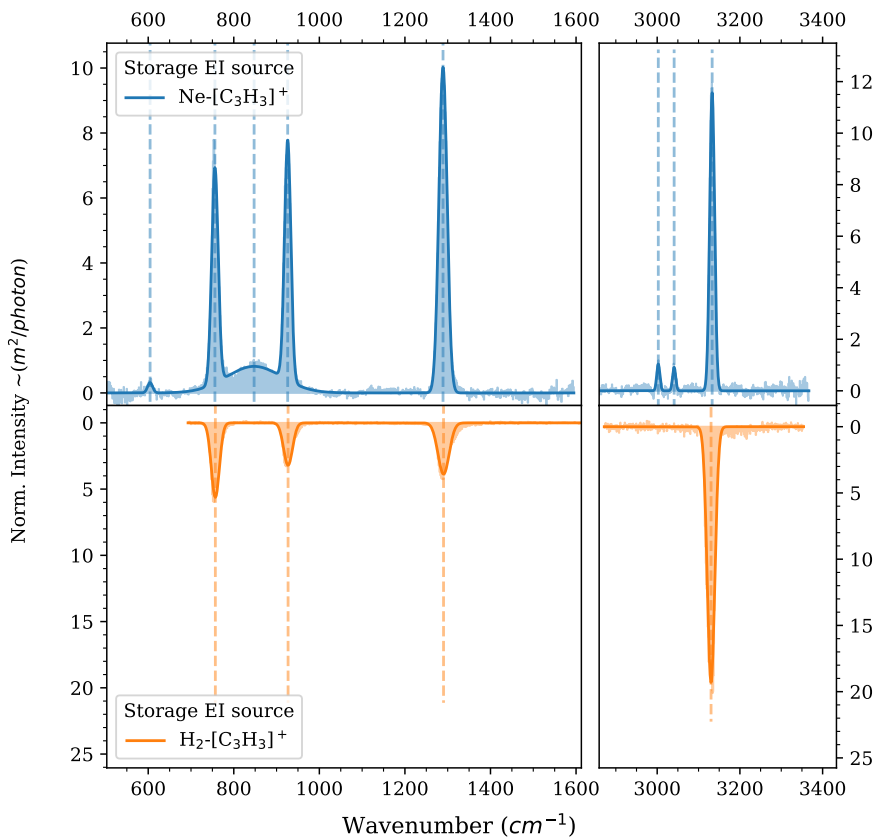


Figure 3.4.: Comparing $\text{Ne}-[\text{C}_3\text{H}_3]^+$ (upper panel) and $\text{H}_2-[\text{C}_3\text{H}_3]^+$ (lower panel) IRPD spectra produced from allene precursor in the storage ion source recorded with FELIX laser and OPO.

the computed fundamental band positions.

We can therefore take the IRPD spectra of the Ne-tagged species as an excellent proxy for those of the bare ion, with predicted vibrational shifts much smaller than those for the corresponding Ar-tagged species. Surprisingly, even the use of H_2 , which has much higher polarizability than Ne (4.5 a.u. [214] vs. 2.66 a.u. [215], respectively) as the tagging agent does not lead to significant shifts, as the comparison in Figure 3.4 shows, taken under conditions favoring the formation of the c- C_3H_3^+ isomer. The predicted small ($\sim 1 \text{ cm}^{-1}$) splitting of the degener-

Table 3.2.: Comparing $H_2C_3H^+$ Ne-IRPD band positions with available computational studies based on coupled cluster methods. All frequencies are in cm^{-1} units

Mode	Ne-IRPD (this work)	$H_2C_3H^+$ (this work) ^a	Ne- $H_2C_3H^+$ Botschwina <i>et al.</i> [195] ^b	Ar- $H_2C_3H^+$ Huang <i>et al.</i> [156] ^c	$H_2C_3H^+$
$v_1(a_1)$		3230	3237(+1)	3241(+5)	3239.0
$v_2(a_1)$	3003 ^t	2997	2992(+2)	2996(+6)	2998.7
$v_3(a_1)$	2078	2078	2080(0)	2081(+1)	2082.2
$v_4(a_1)$	1445	1444	1446(0)	1446(0)	1434.4
$v_5(a_1)$	1138	1109	1123(0)	1119(-4)	1131.8
$v_6(b_1)$		1100	1100(+1)	1097(-2)	1058.1
$v_7(b_1)$	856	875	873(+1)	867(-5)	861.9
$v_8(b_1)$		263	264(0)	281(+17)	251.7
$v_9(b_2)$	3041 ^t	3087	3082(+2)	3086(+6)	3071.0
$v_{10}(b_2)$		1016	1017(0)	1017(0)	1000.6
$v_{11}(b_2)$	610	618	615(0)	618(+3)	607.7
$v_{12}(b_2)$		299	301(+3)	302(+4)	294.8

^a Computed at CCSD(T)/ANO2 combined with anharmonic correction from ANO1

^b C_s min1 structure computed at CCSD(T)-F12/VTZ-F12. Harmonic shift arising from complex formation is given in parentheses.

^c Computed at CCSD(T) QFF with VCI 5MR method. Note that the symmetry labelling of b1 of [156] is b2 in this paper.

^t Tentative assignment.

ate e' modes (v_4 , v_5 , and v_6) of c- $C_3H_3^+$ caused by symmetry-breaking due to the ligand could not be resolved with the given laser linewidth in these experiments.

3.3.4. DEUTERATED SPECIES

Figure 3.5 shows the IRPD spectra of Ne-tagged $[C_3D_3]^+$, produced in the direct EI source from fully deuterated allene (C_3D_4) as a precursor. We covered the range 400-2600 cm^{-1} ; using the FEL in its 3rd harmonic mode in the range (1800-2600 cm^{-1}), where the substantially shifted C-D stretching bands are expected. The first comprehensive spectral characterization of c- $C_3D_3^+$ was reported by

Craig *et al.* [213] using poly-crystalline salts. For the linear form D₂C₃D⁺, the C≡C stretching ν_3 band in Ne-matrix [189] and the ν_1 - ν_6 , ν_9 bands from a recent study of direct absorption of IR bands using isolated solid Ar matrix techniques [190] were previously reported. However, to the best of our knowledge, there are no reports available on gas-phase data. Hence, here we report the first gas-phase data for [C₃D₃]⁺ isomers.

3

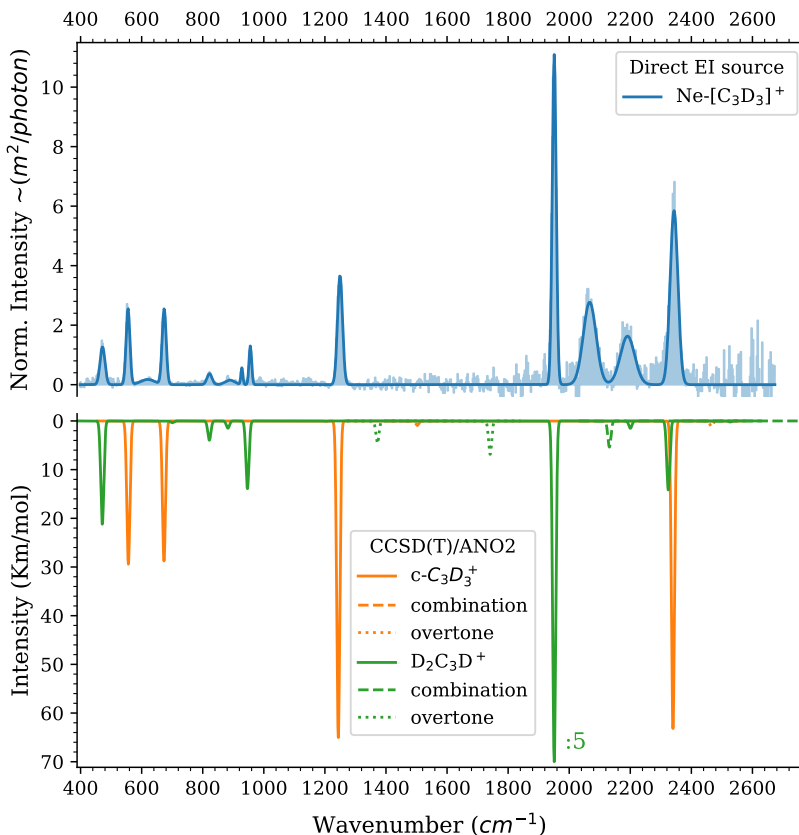


Figure 3.5.: The experimental and fitted FELIX IRPD spectrum of $Ne-[C_3D_3]^+$ (upper panel) compared to computed frequencies (lower panel) at CCSD(T)/ANO2 combined with the anharmonic correction from CCSD(T)/ANO1 ($c\text{-}C_3D_3^+$) and CCSD(T)/ANO0 ($D_2C_3D^+$). Only fundamental (solid line) combination (dashed line) and overtone (dotted line) infrared bands with intensity $> \sim 1$ km/mol were included. The theoretical spectrum was folded with a Gaussian corresponding to the FEL linewidth. Peaks marked with $:n$ indicate that the depicted peak intensity is scaled down by a factor n, for better visualization.

Table 3.3.: Summary of IRPD experimental vibrational band position of Ne-[C₃D₃]⁺ compared to computed fundamental, overtone and combination band frequencies at the CCSD(T)/ANO2 level of theory combined with anharmonic corrections from CCSD(T)/ANO1 (for c-C₃D₃⁺) and CCSD(T)/ANO0 (for D₂C₃D⁺).

Mode	Assignment	Ne-IRPD (this work) ^a	FWHM cm ⁻¹	Calc. [Int.] cm ⁻¹ [Km/mol]	Prev. Exp. cm ⁻¹
c-C₃D₃⁺					
$\nu_1(a'_1)$	sym. CD str.	-	-	2474 [0]	
$\nu_2(a'_1)$	sym. CCC str.	-	-	1478 [0]	
$\nu_3(a'_2)$	in-plane internal torsion	-	-	838 [0]	
$\nu_4(e')$	asym. CD str	2343(1)	30	2340 [64]	2348 ^c , 2344.1(1.0) ^d , 2327 ^e
$\nu_5(e')$	asym. CCC ring str.	1249(1)	25	1244 [65]	1250 ^c , 1239 ^e
$\nu_6(e')$	in-plane CD scissoring	674(1)	19	673 [28]	670 ^c , 665 ^e
$\nu_7(a''_2)$	sym. CD bending \oplus	556(1)	15	556 [27]	542 ^c , 542 ^e

^a Frequencies (error in parenthesis), nc indicates not-covered and hyphen – indicates not observed. \oplus indicates out-of-plane

^b Blended with the ν_4 band of c-C₃D₃⁺ at 2343 cm⁻¹.

^c Craig *et al.* [213], Infrared spectra with polycrystalline salts ([C₃H₃]⁺BF₄⁻).

^d Wyss *et al.* [189], Infrared spectra in Neon matrix.

^e Breslow and Groves [188], Infrared spectra from salts of deuterated cyclopropenyl cation.

^f Chin *et al.* [190], Infrared spectra of H₂C₃H⁺ in solid Ar matrix

Table 3.3 – continued on next page

Table 3.3 - continued from previous page

Mode	Assignment	Ne-IRPD (this work) ^a	FWHM cm ⁻¹	Calc. [Int.] cm ⁻¹ [Km/mol]	Prev. Exp. cm ⁻¹
$\nu_8(e'')$	asym. CD bending \oplus	-	-	817 [0]	
$\nu_3+\nu_5(e')$		2067(1)	49	2061[0.02]	
$2\nu_5(e')$		-	-	2466 [1]	
<hr/>					
D₂C₃D⁺					
$\nu_1(a_1)$	CD str.	-	-	2527 [0.2]	2487.3 ^f
$\nu_2(a_1)$	CD ₂ sym str.	2193(1)	55	2200 [1.5]	2201.0 ^f
$\nu_3(a_1)$	C≡C str.	1951(1)	32	1951[350]	1955.2(1.0) ^d , 1942.1 ^f
$\nu_4(a_1)$	CD ₂ scissoring	-	-	1201 [0.09]	1191.7 ^f

^a Frequencies (error in parenthesis), nc indicates not-covered and hyphen – indicates not observed. \oplus indicates out-of-plane

^b Blended with the ν_4 band of c-C₃D₃⁺ at 2343 cm⁻¹.

^c Craig *et al.* [213], Infrared spectra with polycrystalline salts ([C₃H₃]⁺ BF₄⁻).

^d Wyss *et al.* [189], Infrared spectra in Neon matrix.

^e Breslow and Groves [188], Infrared spectra from salts of deuterated cyclopropenyl cation.

^f Chin *et al.* [190], Infrared spectra of H₂C₃H⁺ in solid Ar matrix

Table 3.3 – continued on next page

Table 3.3 – continued from previous page

Mode	Assignment	Ne-IRPD (this work) ^a	FWHM cm ⁻¹	Calc. [Int.] cm ⁻¹ [Km/mol]	Prev. Exp. cm ⁻¹
$\nu_5(a_1)$	C-C str.	956(1)	10	946 [14]	938,7 ^f
$\nu_6(b_1)$	CD ₂ wag \oplus	883(3)	16	882 [1.5]	891,3 ^f
$\nu_7(b_1)$	CCD bend \oplus	619(5)	54	700 [0.3]	
$\nu_8(b_1)$	CCC bend \oplus	nc		233 [16]	
$\nu_9(b_2)$	CD ₂ asym str.	not resol. ^b		2324 [14]	2301.9 ^f
$\nu_{10}(b_2)$	CD ₂ wag \oplus	822(2)	20	822 [4]	
$\nu_{11}(b_2)$	CCD bend in-plane	472(1)	19	471 [21]	
$\nu_{12}(b_2)$	CCC bend in-plane	nc		262 [10]	
$\nu_1+\nu_7(b_1)$		-	-	3206 [1]	
$\nu_4+\nu_5(a_1)$		-	-	2132 [5]	
$\nu_7+\nu_8(a_1)$		928(1)	7.7	914 [0.6]	

^a Frequencies (error in parenthesis), nc indicates not-covered and hyphen – indicates not observed. \oplus indicates out-of-plane

^b Blended with the ν_4 band of c-C₃D₃⁺ at 2343 cm⁻¹.

^c Craig *et al.* [213], Infrared spectra with polycrystalline salts [(C₃H₃)⁺BF₄⁻].

^d Wyss *et al.* [189], Infrared spectra in Neon matrix.

^e Breslow and Groves [188], Infrared spectra from salts of deuterated cyclopropenyl cation.

^f Chin *et al.* [190], Infrared spectra of H₂C₃H⁺ in solid Ar matrix

Table 3.3 – continued on next page

Table 3.3 - continued from previous page

Mode	Assignment	Ne-IRPD (this work) ^a	FWHM cm ⁻¹	Calc. [Int.] cm ⁻¹ [Km/mol]	Prev. Exp. cm ⁻¹
2ν ₆ (a ₁)	-	-	-	1741 [7]	
2ν ₇ (a ₁)	-	-	-	1372 [5]	

We clearly identify the four IR active fundamental bands of the cyclic isomer (ν_4 , ν_5 , ν_6 and ν_7) with excellent agreement to computed fundamental band positions of the untagged species (see Table 3.3). This again demonstrates that the perturbation due to Ne attachment is very small. We also notice an additional feature, with a larger FWHM of 49 cm^{-1} , at 2067 cm^{-1} . This band can be assigned to the (weak) predicted combination band $\nu_3 + \nu_5$ at 2061 cm^{-1} . For the $\text{D}_2\text{C}_3\text{D}^+$ isomer, the ν_2 , ν_3 , ν_5 , ν_6 , ν_7 , ν_{10} , and ν_{11} vibrational modes are clearly identified. The most prominent feature is the $\text{C}\equiv\text{C}$ stretching (ν_3) band observed at 1951 cm^{-1} . This band was reported at 1955.2 cm^{-1} in Neon matrix [189]. Most bands are in good agreement with theory (see Table 3.3). The ν_7 is assigned to the broad feature centered at 619 cm^{-1} and shows a large deviation to the calculated band position. Interestingly, a similar situation was observed for the corresponding band in the undeuterated species (see Table 3.1). An additional band observed at 928 cm^{-1} is assigned to the $\nu_7 + \nu_8$ combination band predicted at 914 cm^{-1} .

3

3.3.5. ISOMER QUANTIFICATION

One of the goals of this study was to find ion production methods that preferentially form one of the two $[\text{C}_3\text{H}_3]^+$ isomers, in order to perform subsequent ion-molecule reaction kinetic studies starting with an isomer-pure ionic sample. For this purpose, we used two different neutral precursors, allene and propargyl-chloride, two different ion sources, and a range of electron impact energies.

As was described previously [65, 202], it is possible to quantify the percentage of a specific isomer in an isomeric mixture by a saturation depletion method. For this the cluster is resonantly excited at a frequency where only one of the two isomers is active, i.e. absorbs a photon. By increasing the trapping time, thereby increasing the total energy ($E = n \cdot P$) deposited, only the active isomer cluster is depleted until it saturates, and the number of clusters is recorded as a function of deposited energy ($N_{ON}(E)$). To account for additional loss mechanisms from the trap, a second measurement is done with the laser tuned to an off-resonance position, resulting in $N_{OFF}(E)$. From this we can quantify the relative depletion of the particular isomer $D(E) = 1 - \frac{N_{ON}(E)}{N_{OFF}(E)}$. Assuming an exponential decay of the

3

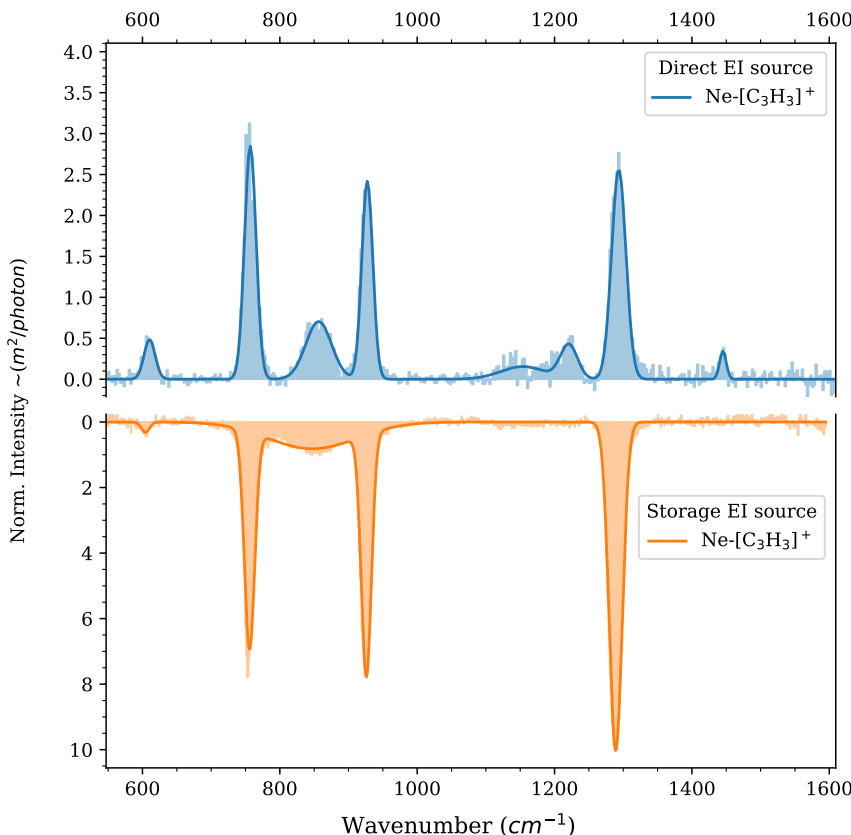


Figure 3.6.: Isomer variation depending on ion production conditions. Upper panel: Experimental IRPD spectrum of $Ne-[C_3H_3]^+$ produced from propargyl chloride in the EI source. Lower panel: Same as above but using an allene precursor and the storage ion source.

clusters with rate coefficients K_{ON} and K_{OFF} , respectively, we can write:

$$\begin{aligned}
 N_{OFF}(E) &= N \cdot e^{-K_{OFF} \cdot E} \\
 N_{ON}(E) &= N_a \cdot e^{-(K_{OFF} + K_{ON}) \cdot E} + N_n \cdot e^{-K_{OFF} \cdot E} \\
 D(E) &= 1 - \frac{N_{ON}}{N_{OFF}} = A \cdot (1 - e^{-K_{ON} \cdot E}),
 \end{aligned}$$

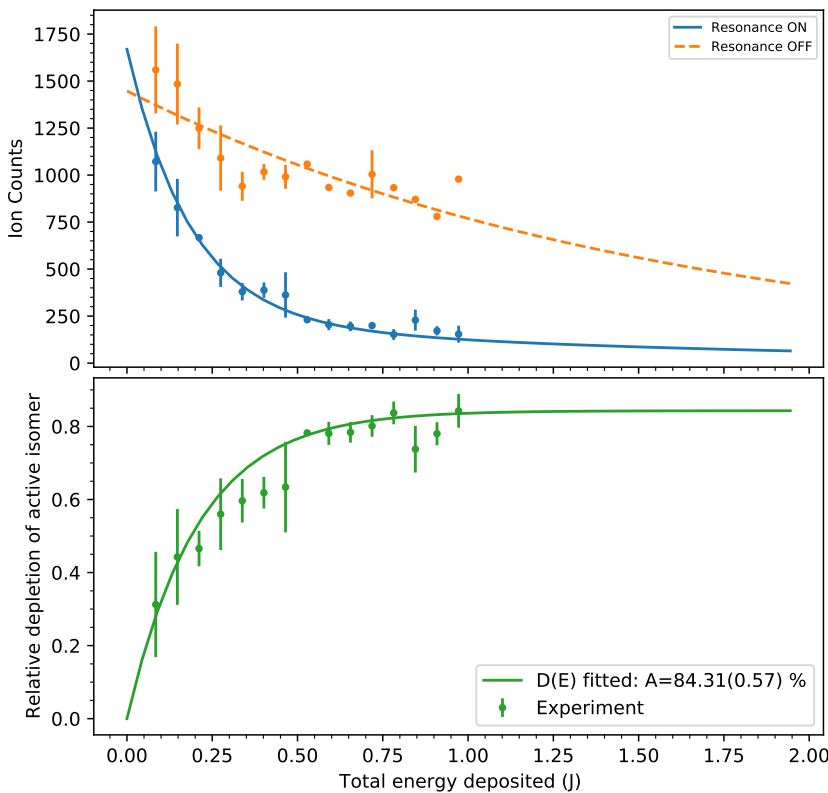


Figure 3.7.: Saturation depletion measurements on the ν_5 band of $c\text{-C}_3\text{H}_3^+$, produced from propargyl chloride in the direct EI ion source with 16.5 eV electrons. Top: On-resonance (blue, at 1293 cm^{-1} , ν_5) and off-resonance (orange, at 1150 cm^{-1}) depletion measurement. Bottom: Relative depletion $D(E)$ as a function of deposited energy E , showing saturation at $A = 84\%$.

where $N (= N_a + N_n)$, N_a and N_n are total cluster, active and non-active isomeric cluster counts respectively, and $A = \frac{N_a}{N_a + N_n}$ is the relative abundance of the active isomer. By fitting the experimental data to the corresponding exponentials, we can derive the respective rate coefficients, and, more importantly, the relative abundance of the targeted active isomer, A . Such an exemplary fit is shown in Figure 3.7. We should note that this method assumes an equal probability for

forming Ne complexes for different isomers. This can be safely assumed, since the binding energies for both Ne- $[C_3H_3]^+$ isomers was calculated to be very similar [195].

3

Although for the $[C_3H_3]^+$ ions the cyclic c- $C_3H_3^+$ is substantially lower in energy than the linear $H_2C_3H^+$ form (28 kcal/mol, [156]), both isomers were regularly observed in various experiments [196, 189, 192], including this work. Presumably, due to the high isomerization barrier between the two isomers (50 kcal/mol), both isomers can be formed in the dissociative ionization of the used precursor gases. Theoretical studies have for example shown that the allene and propyne cations, with a linear carbon backbone, can undergo isomerization and ring closure before hydrogen loss, forming dominantly the c- $C_3H_3^+$ isomer upon dissociation [216, 217]. We indeed observed the cyclic isomer with an abundance of ~81 % (and the linear form with ~19 %) upon electron impact ionization of allene in a direct electron impact ionization source, independent of the chosen electron energy in the range (14 – 70) eV, indicating a constant isomeric branching ratio once the dissociation threshold in the ionization process is reached (allene ionization potential 9.7 eV [218], $[C_3H_3]^+$ appearance energy 11.4 eV [219], below 14 eV we could not produce a high enough $[C_3H_3]^+$ ion number to perform spectroscopic measurements). When using an ion storage source instead, where the primary ions can undergo subsequent reactions with the neutral gas, we predominantly produced the cyclic form (~90–95 %), indicative of the higher reactivity of the linear isomer $H_2C_3H^+$, as discussed previously [184, 185].

In order to increase the formation yield of the propargyl cation $H_2C_3H^+$, we also used propargyl chloride (ionization energy 10.68(3) eV, [220]) as a precursor for direct electron impact ionization. The reasoning here was that the chlorine is expected to be an efficient leaving group after ionization and that thus the propargyl structure is retained in the $[C_3H_3]^+$ ionic fragment, as has been proposed in photodissociation studies of the propargyl chloride ion [221]. A comparison between spectra taken under different conditions is given in Figure 3.6. However, the isomeric ratio shifted only marginally towards the linear isomer, reaching ~22 % at 60 eV electron impact energy, and being lower (~16 %) than for allene ionization at 16.5 eV.

To elucidate the formation of the different isomers upon ionization of propargyl chloride, we performed calculations on the potential energy surface of the $[ClC_3H_3]^+$ system, which are detailed in the Supplementary Information (Figure A.1). Our results agree well with earlier calculations at a lower level of theory by Won *et al.* [222]. They indicate that the dissociation to c- $C_3H_3^+$ and Cl via

an isomerization to a cyclic form of $[\text{ClC}_3\text{H}_3]^+$ is thermodynamically favoured (with a maximum barrier of 53.4 kJ/mol, i.e. 0.55 eV) over the barrier-free dissociation channel to $\text{H}_2\text{C}_3\text{H}^+$ and Cl, which has a relative energy of 81.1 kJ/mol (0.84 eV). Our experimental results indicate that the branching ratio into the two channels stays relatively constant at electron impact ionization energies above 16.5 eV, i.e. 5 eV higher than the $\text{H}_2\text{C}_3\text{H}^+$ appearance energy. This result seems to be contradicting Duncan and co-workers' [196, 157] argument that they were predominantly producing the linear isomeric variant using propargyl bromide as a precursor in a discharge coupled to a supersonic expansion. However, for the propargyl bromide cation, the barrier to isomerization to the cyclic variant is slightly higher in energy than the dissociative channel to $\text{H}_2\text{C}_3\text{H}^+$ and Br [223], which likely alters the branching ratio in favour of $\text{H}_2\text{C}_3\text{H}^+$ over $\text{c-C}_3\text{H}_3^+$. The fact that they were only able to observe a significant signal of the $\text{c-C}_3\text{H}_3^+$ isomer when running the discharge "hot", i.e. with higher voltages, supports this scenario. In addition, the high inert gas pressure in the nozzle orifice in these experiments might lead to efficient quenching of the isomerization before dissociation. A similar argument might hold for the experiments done by Dopfer and co-workers [192], who used electron impact ionization of allene, propyne, 3-chloro-1-propyne, and benzene in a supersonic expansion and identified both $[\text{C}_3\text{H}_3]^+$ isomers with a qualitatively constant ratio of 2:1 ($\text{c-C}_3\text{H}_3^+ : \text{H}_2\text{C}_3\text{H}^+$) in their spectra. However, earlier reactivity studies pointed towards a higher abundance (approaching 60 %) of the linear isomer when producing $[\text{C}_3\text{H}_3]^+$ via low energy electron impact ionization of propyne [185]. We can therefore not exclude that in our experiments the $\text{H}_2\text{C}_3\text{H}^+$ isomer is chemically quenched in the electron impact ion source, where the ions reside for several μs at neutral gas pressures of 10^{-5} mbar. A more effective way to dominantly produce the propargyl cation could be ionization of propargyl iodide [224].

3.4. CONCLUSION

We investigated broadband gas-phase Ne-IRPD spectra of both linear and cyclic forms of $[\text{C}_3\text{H}_3]^+$ and reported the first gas-phase IR spectra of the corresponding $[\text{C}_3\text{D}_3]^+$ isomers. Comparison of this new experimental data with theoretical predictions of the vibrational spectra allowed us to benchmark various high-level coupled-cluster methods. All four IR active fundamental bands of cyclic isomer ν_4 , ν_5 , ν_6 and ν_7 for both $[\text{C}_3\text{H}_3]^+$ and $[\text{C}_3\text{D}_3]^+$ were reported with very good agreement with computed anharmonic frequencies. The ν_6 and ν_7 gas-phase IR spectra were reported for the first time. We, therefore, can confidently resolve

the issues regarding ν_4 assignment for c- $C_3H_3^+$ in Ricks *et al.* [196]. For the linear isomer, the most prominent vibrational modes ν_3 , ν_4 , ν_7 and ν_{11} were clearly identified. The ν_5 and ν_6 modes were identified as a blended broader feature, but not determined with high accuracy. The effect of Neon complexation on the IRPD spectra seems to have only a small influence on the vibrational band positions, once more indicating that the use of weakly bound rare gas ligands such as Ne or He in IRPD action spectroscopy is well suited to obtain IR spectra resembling those of the bare ion.

3

The method of saturation depletion, enabled by the available high FELIX FEL power, was used to investigate the isomeric ratio of $[C_3H_3]^+$ produced with different ion source conditions and precursors. Whereas a rather clean production method could be identified for the formation of c- $C_3H_3^+$, but it has proven difficult to form the more reactive $H_2C_3H^+$ isomer preferentially. Nevertheless, the possibility to quantify the isomer ratio in an isomeric mixture offers great potential for reactivity studies of these ions, which are needed as input for astrochemical models. Furthermore, spectroscopic isomer identification and quantification as described here can be employed to probe the outcome of chemical reactions forming the $[C_3H_3]^+$ isomers. Examples are the $CH_3^+ + C_2H_{2,4}$ and $C_3H^+ + H_2$ reactions proposed to lead to $[C_3H_3]^+$ in interstellar clouds and planetary atmospheres [164, 155].

The accurate spectral characterisation on $[C_3H_3]^+$ and $[C_3D_3]^+$ isomers is very important because their fundamental vibrational modes can be used for astronomical searches in the IR region for these ions, e.g. with the upcoming JWST telescope. With a robust experimental methodology and theoretical description now at hand, it would be interesting to extend these studies to the singly and doubly deuterated forms of these species. Whereas the c- $C_3H_3^+$ and c- $C_3D_3^+$ ions belong to the dihedral D_{3h} point group, and do not possess a permanent dipole moment, an effective permanent dipole moment is created upon mono/di D-substitution, because the center of mass is displaced from the center of charge [225]. This makes these partly deuterated isomers amenable for direct rotational spectroscopy, e.g. using novel action spectroscopic methods that have been developed recently to obtain rotational spectra of reactive ionic species [99, 3, 97, 110]. Rotational transition frequencies of these species, as well as for the likewise polar $H_2C_3H^+$ isomer, will enable searches for them in space using sensitive radio telescope, thereby allowing to elucidate their role in interstellar carbon chemistry [177, 175].

4

INFRARED PREDISSOCIATION SPECTROSCOPY OF PROTONATED METHYL CYANIDE, CH_3CNH^+

This chapter is adapted from : Marimuthu, A. N.; Huis in't Veld, F; Thorwirth, S.; Redlich, B.; Brünken, S. Journal of Molecular Spectroscopy 2021, 379, 111477.

ABSTRACT

The gas phase vibrational spectrum of CH₃CNH⁺ is recorded using a messenger infrared predissociation (IRPD) action spectroscopic method. Vibrational bands were recorded in the 300 – 1700 cm⁻¹ and 2000 – 3300 cm⁻¹ regions making use of the widely tunable free electron laser for infrared experiments, FELIX, coupled to a cryogenic ion trap instrument. Band assignments were aided by high-level quantum-chemical calculations, which showed excellent agreement with the experimental data. Effects of the neon atom used as messenger in the IRPD method are investigated in detail. The data presented here will support astronomical searches for the CH₃CNH⁺ ion in space, and provides a basis for high-resolution ro-vibrational and pure rotational studies in vibrationally excited states.

4.1. INTRODUCTION

Methyl cyanide (CH_3CN , also known as acetonitrile) was among the first polyatomic molecules detected during radio-astronomical observations of the interstellar medium (ISM) [226]. It has since been detected in a variety of galactic sources, covering most evolutionary stages from dense cold cores [227, 228], via low- and high-mass star-forming regions [229, 230] and protoplanetary disks [231] to photodissociation regions [232] and circumstellar envelopes [233]. CH_3CN has also been detected in the atmosphere of Saturn's moon Titan [234, 235, 236].

As methyl cyanide has a proton affinity of $788(8)$ kJ/mol [237], much larger than that of H_2 , its protonated version (CH_3CNH^+) might form effectively via exothermic proton transfer from H_3^+ to CH_3CN in the interstellar medium [238]. Another effective formation pathway of protonated methyl cyanide is via radiative association of CH_3^+ and HCN. The latter pathway, followed by dissociative recombination, was suggested to be the major gas-phase route for the interstellar synthesis of methyl cyanide (and its isocyanide isomer) [239, 240, 241]. Despite its dominant role in the formation of the ubiquitous methyl cyanide molecule, previous searches for CH_3CNH^+ in the interstellar medium were unsuccessful [242]. Protonated methyl cyanide, as well as other protonated nitriles, have, however, been detected in Titan's upper atmosphere by the Ion Neutral Mass Spectrometer (INMS) on board the Cassini spacecraft [243]. It is dominantly formed by protonation of CH_3CN via reactions with the highly abundant ions HCNH^+ and C_2H_5^+ , whose deprotonated variants have a lower proton affinity than methyl cyanide [183].

The pure rotational spectrum of protonated methyl cyanide has been studied extensively in the microwave [244] and submillimeter-wave region [245]. Several infrared studies on CH_3CNH^+ exist, including matrix-isolation FT-IR [246] of its CH and NH stretching bands, infrared-predissociation (IRPD) action spectroscopy of its complex with H_2 in the H₂ and NH stretching region [247], and high-resolution gas-phase absorption spectroscopy on the ν_1 NH stretching fundamental band of the bare ion [248, 249]. All these studies focus on the stretching bands located at wavelengths below $3.4\ \mu\text{m}$, or at wavenumbers above $2900\ \text{cm}^{-1}$, respectively, and to date no spectroscopic data on its low-lying vibrational modes existed.

In this study we recorded the vibrational spectrum of gas-phase CH_3CNH^+ over a broad frequency range ($300 - 1700$ and $2000 - 3300\ \text{cm}^{-1}$) covering all fundamental modes except the previously studied NH stretching band. Experiments were performed using Ne-tagging infrared-predissociation spectroscopy in a cryogenic ion trap coupled to the powerful and widely tunable FELIX (Free Electron Lasers for Infrared eXperiments, [115]) free-electron IR lasers. These data can serve as reference data for future laboratory infrared studies at high

spectral resolution as well as astronomical searches for this important ion in space, e.g., with the upcoming James Webb Space Telescope (JWST).

4.2. METHODS

4.2.1. EXPERIMENTAL DETAILS

4

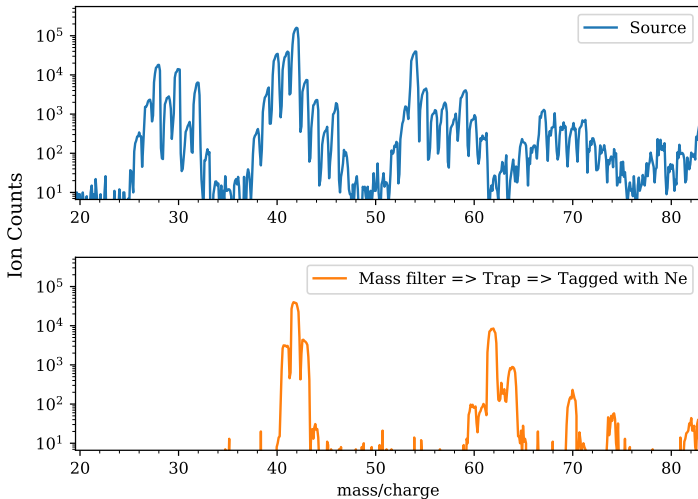


Figure 4.1.: Upper panel: Mass spectra of ions produced from electron impact ionization (~30eV) in a storage ion source. See text for discussion of the main peaks Lower panel: Mass filtered CH_3CNH^+ ($m/z = 42$, < 10 % contribution at $m/z = 41$ and 43) together with tagged $\text{CH}_3\text{CNH}^+ \text{-Ne}$ ($m/z = 62$, also $\text{CH}_3\text{CNH}^+ \text{-}^{22}\text{Ne}$ at $m/z = 64$) species produced in the cryogenic ion trap. Additional weaker contributions at $m/z = 60$, 70 , and 74 stem from tagging with residual H_2O , N_2 , and O_2 , respectively.

The vibrational spectrum of CH_3CNH^+ was recorded using the FELion cryogenic 22-pole ion trap instrument. A detailed account of the FELion instrument is provided in Section 2.1 and the infrared-predissociation (IRPD) of in-situ rare gas tagged cold molecular ions in Section 1.5.1.1. Here we only give a brief account of details specific to the CH_3CNH^+ ion.

Protonated methyl cyanide ($m/z = 42$) was produced by electron impact ionization (EI, electron energy 30 eV) from neutral methyl cyanide (Sigma Aldrich, > 99.9%) in a Gerlich-type storage ion source (SIS) [201], where primary ions pro-

duced by EI are accumulated for the duration of an experimental cycle (of the order of seconds). The precursor gas was admitted either pure or diluted with He at a ratio of 1:3 to the ion source chamber at a pressure of $\sim 10^{-5}$ mbar. Self-protonation of the primarily formed methyl cyanide radical cations with neutral methyl cyanide [250], led to effective production of CH_3CNH^+ (see Figure 4.1). Additional prominent mass-peaks in the mass-spectrum are due to the radical methyl cyanide cation ($m/z = 41$) and the hydrogen loss fragment CH_2CN^+ with $m/z = 40$. Interestingly, we observe the appearance of a mass-peak at $m/z = 54$, which is likely caused by a reaction of CH_2CN^+ with neutral methyl cyanide in the storage source [251]. Fragment ions, including their protonated forms are apparent in the range $m/z = 26 - 32$, contamination from water and air leads to additional contributions at $m/z = 18$ (not shown), 28, and 32.

For spectroscopic IRPD experiments a few 10 ms long pulse of ions is extracted from the respective source and filtered for the mass of interest, $m/z = 42$ in the case of CH_3CNH^+ by a quadrupole mass filter before entering the 22-pole ion trap which is held at a fixed temperature in the range 6.1-7 K for experiments using Ne as tagging gas. Around 10-20 ms before the ions enter the trap, an intense 80-150 ms long Ne:He pulse (1:3 mixing ratio and number density of $\sim 10^{15} \text{ cm}^{-3}$) is admitted to the trap, leading to efficient collisional cooling of the ions to the ambient temperature. Under these conditions, around 20 % of the CH_3CNH^+ ions form weakly bound complexes with Ne, see Figure 4.1. The ions are stored for several seconds in the ion trap and are exposed to several laser pulses before extraction. An IR-PD spectrum is recorded by mass-selecting and counting the CH_3CNH^+ -Ne complex ions while tuning the laser frequency ν . A relative depletion $D = 1 - \frac{N_{ON}(\nu)}{N_{OFF}}$ in the number of complex ions $N_{ON}(\nu)$ from the baseline value N_{OFF} is observed upon resonant vibrational excitation. To account for varying laser pulse energy P , pulse number n , and for saturation effects, the signal is normalized prior to averaging using $I = \frac{-\ln(N_{ON}(\nu)/N_{OFF})}{n \cdot P / (\hbar\nu)}$, giving the intensity I in units of relative cross-section per photon. After normalizing each measurement in this way, the final spectrum is then obtained by averaging using statistical binning with a typical bin size of 2.5 cm^{-1} . Line parameters such as band positions, intensities, and line widths (fwhm) are then obtained by fitting a multi-component Gaussian function to the experimental data, also providing statistical errors of the line parameters.

The vibrational IRPD spectra were recorded using the IR radiation of FEL-2 of the FELIX Laboratory in the frequency region $300-1700 \text{ cm}^{-1}$, and in the range $2000-3300 \text{ cm}^{-1}$ employing the 3rd harmonic mode of the FEL. The laser was operated at 10 Hz with macro pulse energies in the interaction region between 1.5-60 mJ, and for each datapoint $n = 3-66$ pulses were admitted depending on the signal strength. The FEL was optimized for narrow bandwidth with a full width

at half-maximum (fwhm) of 0.3 – 1 % of the center wavelength.

4.2.2. COMPUTATIONAL DETAILS

4

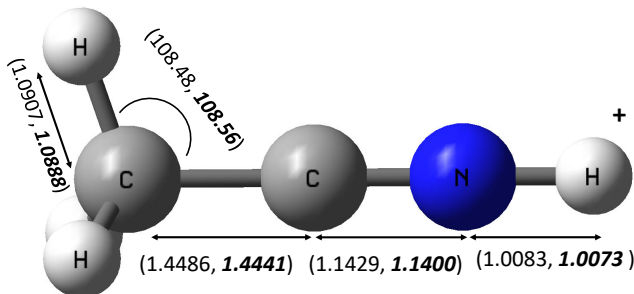


Figure 4.2.: Computed equilibrium geometry (C_{3v} symmetry) for CH₃CNH⁺ based on (fc-CCSD(T)/ANO2, ***ae-CCSD(T)/cc-pwCV5Z***) level of theory. Bond lengths and angles are in Å and deg° respectively.

The stability and relative energies of the [C₂H₄N]⁺ isomeric family have been extensively studied previously at various levels of theory, showing N-protonated acetonitrile (CH₃CNH⁺, ¹A₁, C_{3v} symmetry) to be the global minimum structure [252, 253]. In the present study we have investigated CH₃CNH⁺ at the coupled-cluster singles and doubles (CCSD) level augmented by a perturbative treatment of triple excitations, CCSD(T) [203], in combination with atomic natural orbital (ANO0, ANO1, and ANO2) basis sets from Almlöf and Taylor [204] as well as the correlation-consistent valence basis set cc-pVDZ [130] in the frozen core (fc) approximation. A best estimate equilibrium structure has been calculated using the cc-pwCV5Z basis set [254] using all electrons in the correlation treatment. Equilibrium geometries of CH₃CNH⁺ have been calculated using analytic gradient techniques [205] and our results for the bare ion (Figure 4.2) match well with an earlier report by Botschwina [255] who employed ab initio methods up to the CCSD(T)/cc-pCVQZ level. Harmonic frequencies were subsequently computed by numerical differentiation of gradients [132, 133]. For anharmonic calculations, second-order vibrational perturbation theory (VPT2) [208] has been employed. All calculations have been carried out using the CFOUR program

package [210, 136]. The CCSD(T) method in combination with ANO basis sets has been shown previously to provide vibrational wavenumbers of high quality [211, 212], and we have recently applied it successfully for a vibrational study of $[C_3H_3]^+$ isomers and isotopologues [256].

Additionally, we have performed potential energy scans to find the lowest energy structure of CH_3CNH^+ complexed with Ne, as outlined in Section 4.3.3. These studies were conducted at the CCSD(T)/cc-pVDZ and CCSD(T)/ANO0 level of theory using the PSI4 program package [257]. The potential energy surface as a function of H-Ne distance of the lowest energy conformer was then further investigated to account for Basis Set Superposition Errors [138] using i) the counter-poise (CP) method introduced by Boys and Bernardi [139], i.e. by calculating CP-corrected CCSD(T) interaction energies at each geometry, and ii) higher-order symmetry-adapted perturbation theory, SAPT2+3/cc-pVDZ [140, 141]. In all PES calculations the geometry of the bare ion was kept fixed to its equilibrium structure calculated at the same level of theory. No zero-point vibrational energy (ZPE) corrections were applied to the derived binding energies.

4.3. RESULTS AND DISCUSSIONS

4.3.1. VIBRATIONAL SPECTROSCOPY OF CH_3CNH^+

The measured IRPD spectra for $[C_2H_4N]^+$ with Ne as a tagging agent are displayed in Figures 4.3 and 4.4, compared to the calculated spectrum of the energetically lowest lying isomer, CH_3CNH^+ . Based on these results we can infer that only the most stable isomer CH_3CNH^+ , i.e. N-protonated methyl cyanide, is produced via self-protonation in our storage ion-source. By exposing the complexes to > 100 FEL shots on resonance with the strong band at 898 cm^{-1} we could verify that $> 95\%$ of the complexes dissociate, i.e. that only one isomeric variant absorbing at this specific frequency is present in the ion trap. The CH_3CNH^+ structure with C_{3v} symmetry has 10 IR active fundamental modes of E and A_1 symmetry. As can be clearly seen in Figure 4.3 and 4.4, we have covered and assigned all fundamental modes, except the high-lying NH-stretching mode that was out of the range of the FEL. Four remaining weak to moderately strong features could be assigned to combination and overtone modes predicted by the anharmonic force field calculations. The fitted band positions and assignments are summarized in Table 4.1. Several remaining, weak features, e.g., between $600 - 700\text{ cm}^{-1}$ are likely due to combination bands of the bare ions fundamental modes and those involving the weakly bound Ne atom. The observed transitions for CH_3CNH^+ -Ne are in very good agreement with the computed values of the bare ion CH_3CNH^+ (see Table 4.1). For most bands the deviation is less than 10 cm^{-1} , except for the CNH bending mode, and the overtone and combi-

4

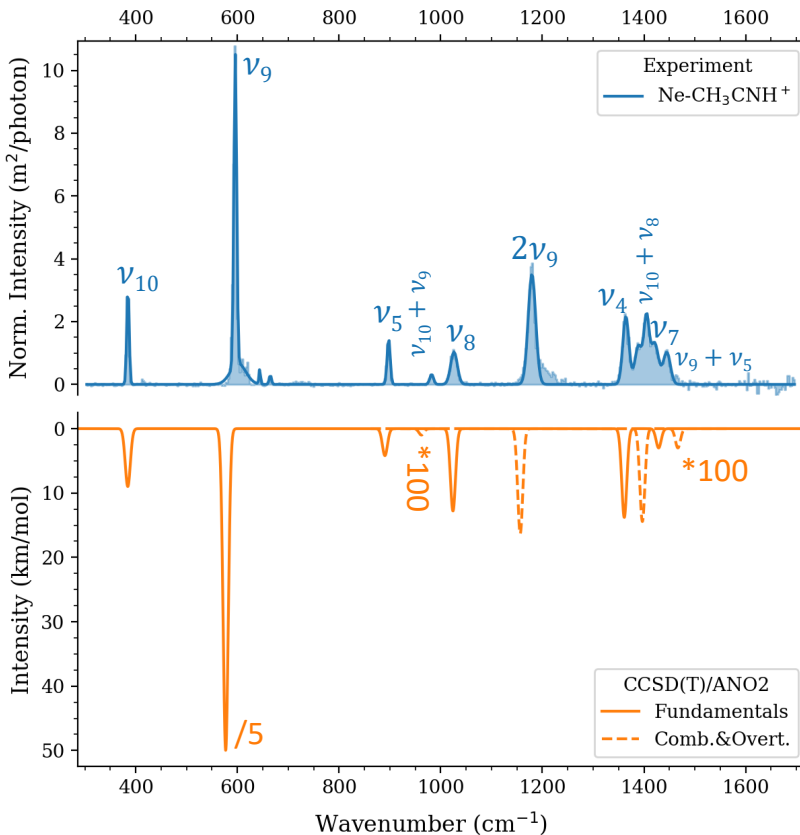


Figure 4.3.: The experimental and fitted FELIX IRPD spectrum of CH_3CNH^+ -Ne (upper panel) compared to the computed anharmonic (VPT2) frequency values (lower panel) of CH_3CNH^+ at the fc-CCSD(T)/ANO2 level of theory showing fundamental (orange, solid line), combination and overtone (orange, dashed line) bands. NOTE: $/n$ and $*n$ indicates that the computed intensities are divided or multiplied, respectively, by a factor n for better visualisation

nation modes, as will be discussed below. The influence of the neon-tag on the vibrational band positions is discussed in more detail in section 4.3.3.

The lowest energy CCN bending mode ν_{10} is clearly observed at 385 cm^{-1} with excellent agreement to the anharmonic predicted value at 384 cm^{-1} . The

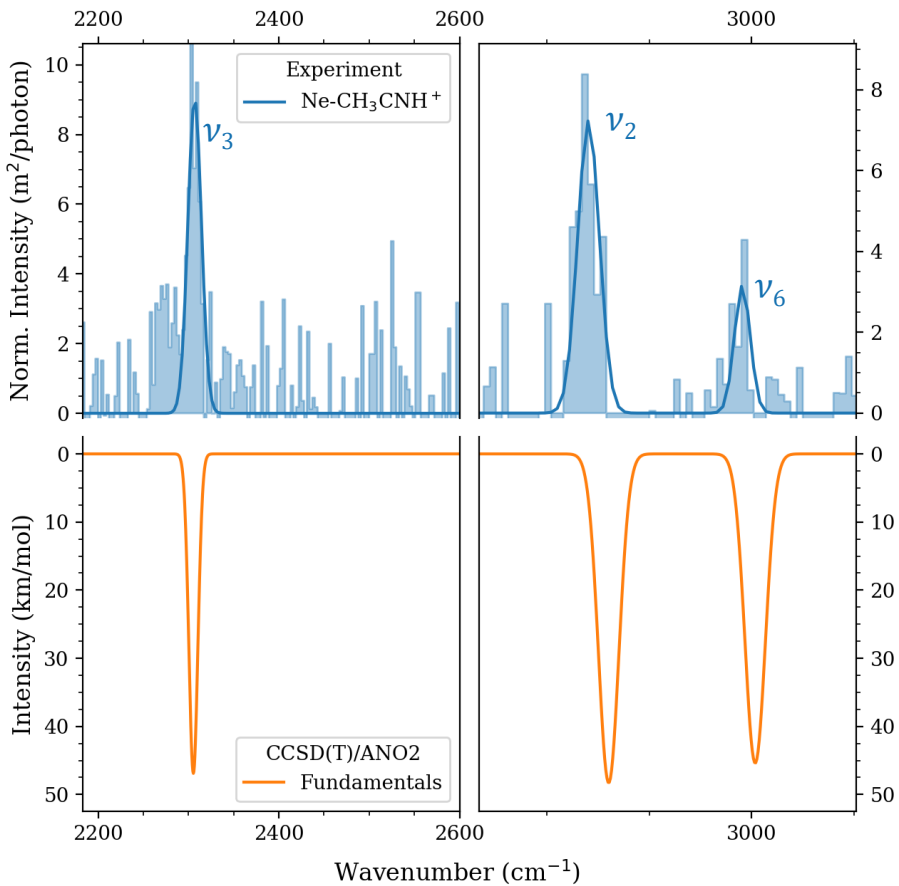


Figure 4.4.: The experimental and fitted FELIX IRPD spectrum of CH_3CNH^+ -Ne (upper panel) but using FELIX in 3rd harmonic mode, compared to the computed anharmonic (VPT2) frequency values (lower panel) of CH_3CNH^+ at the (fc)-CCSD(T)/ANO2 level of theory.

most prominent feature, the ν_9 CNH bending mode, is observed at 596 cm^{-1} , almost 20 cm^{-1} blue-shifted from the predicted band position of the bare ion. This shift is likely caused by the attached neon atom, that binds to the proton involved in this bending mode (see section 4.3.3). The combination band of these two bending modes (CCN and CNH) was also observed at 982 cm^{-1} as a weak feature. Also a very clear feature of the CNH first overtone appears at 1179 cm^{-1} . In general the computed values for the combination and overtone modes are

10 – 20 cm⁻¹ shifted with respect to the experimentally observed bands. The CC stretching frequency ν_5 is measured at 898 cm⁻¹ with a ~ 7 cm⁻¹ blue-shift from the predicted value 890 cm⁻¹. The weak combination mode of the CC stretching with the CNH bending mode also appears with sizable intensity at 1445 cm⁻¹. We could also clearly observe the CH₃ vibrations, i.e. the ν_8 wagging and ν_7 scissoring, at 1026 and 1421 cm⁻¹ respectively (see vibrational displacement vectors given in the Supplementary Information Figure B.2). The former also forms a combination mode with the CCN bending at 1405 cm⁻¹ which matches well with the predicted value at 1397 cm⁻¹ (intensity over 14 km/mol). The ν_4 CH₃ umbrella like bending mode appears at 1364 cm⁻¹ very close to the predicted value at 1361 cm⁻¹. The ν_3 CN stretching, CH₃ ν_2 symmetric and ν_6 asymmetric stretching bands were measured with FELIX 3rd harmonic mode (see Figure 4.4) resulting in lower resolution and signal-to-noise spectra, reflected in the larger experimental error of these lines. In addition, measurements of the two CH stretching bands suffered from calibration issues of the grating spectrometer used to determine the FEL frequency, reflected in their large systematic errors of 10 cm⁻¹.

Table 4.1.: Summary of IRPD experimental vibrational band position of CH_3CNH^+ -Ne and comparison to computed values. Vibrational frequencies are in cm^{-1} [calc. intensities in km/mol]

Vibrational symmetry and mode (CH_3CNH^+ , C_{3v} , 1A_1 ground state)		CCSD(T)/ANO2 (VPT2, anh.)	Ne corrected ^a (this work)	Ne-IRPD ^b (this work)	prev. work
<hr/>					
Fundamental bands					
ν_{10}	E	CCN bend	384 [4.5]	386	385 (1)
ν_9	E	CNH bend	577 [132.3]	595	596 (1)
ν_5	A_1	CC str.	890 [4.2]	891	898 (1)
ν_8	E	CH ₃ wagging	1024 [6.4]	1025	1026 (1)
ν_4	A_1	CH ₃ umbrella	1361 [13.8]	1362	1364 (1)
ν_7	E	CH ₃ scissoring	1429 [1.5]	1429	1421 (1)
ν_3	A_1	CN str.	2305 [46.9]	2305	2307 (2)
ν_2	A_1	CH ₃ sym. str.	2930 [48.3]	2930	2924 (10)
ν_6	E	CH ₃ asym. str.	3002 [22.7]	3002	2996 (10)
					2946.5 [53] ^c

^a CH_3CNH^+ & CH_3CNH^+ -Ne (C_{3v} symmetry isomer) harmonic frequencies were computed at the CCSD(T)/ANO0 level of theory and their differences were added as Neon contribution to CH_3CNH^+ frequencies computed at CCSD(T)/AN02 (see section 4.3.3).

^b Frequencies (error in parentheses). nc indicates not covered.

^c Ne-matrix, Ref [246]

^d Gas-phase, Ref [249]

Table 4.1 – continued on next page

Table 4.1 – continued from previous page

Vibrational symmetry and mode (CH ₃ CNH ⁺ , C _{3v} , ¹ A ₁ ground state)	CCSD(T)/ANO2 (VPT2, anh.)	Ne corrected ^a (this work)	Ne-IRPD ^b (this work)	prev. work
<hr/>				
Fundamental bands				
<hr/>				
ν_1	A ₁	NH str.	3525 [654.7]	3516
				nc
<hr/>				
Overtones and Combination bands				
<hr/>				
$\nu_{10} + \nu_9$	A ₁	CCN bend + CNH bend	962 [0.01]	982 (2)
2 ν_9	A ₁	CNH bend (2)	1157 [16.3]	1179 (1)
$\nu_{10} + \nu_8$	A ₁	CCN bend + CH ₃ wag	1397 [14.4]	1405 (1)
$\nu_9 + \nu_5$	E	CC str. + CNH bend	1467 [0.03]	1445 (1)

4.3.2. PREDICTION OF ROTATIONAL SPECTROSCOPIC PARAMETERS

The above discussion clearly shows that anharmonic calculations at the CCSD(T)/ANO2 level provide a reliable means to predict vibrational band positions for CH_3CNH^+ . In addition we present in Table 4.2 the calculated equilibrium and ground state rotational constants and compare the latter to experimentally derived values [244, 245] and a previous calculations using the aug-cc-pVQZ basis set [253]. From the relative deviations of the calculated spectroscopic constants to the experimental values, it is obvious that the fc-CCSD(T)/ANO2 calculation of B_0 (from the equilibrium rotational constant B_e complemented by the zero point vibrational contribution ΔB_0 , see below) are slightly further off than the CCSD(T)/aug-cc-pVQZ values reported earlier [253], whereas centrifugal distortion constants show a similar accuracy. Best estimate ground state rotational constants have been calculated here using a hybrid approach with the equilibrium structure calculated at the ae-CCSD(T)/cc-pwCV5Z and the zero-point vibrational corrections $\Delta B_0 = \frac{1}{2} \sum \alpha_i^B$ (analogous for A) from rotation-vibration interaction constants α_i calculated at the fc-CCSD(T)/ANO2 level of theory (see Table B.4 in the Supplementary Information), showing excellent agreement (to within 0.05%) with the experimentally obtained B_0 value. CH_3CNH^+ has two energetically low-lying, degenerate bending vibrations, the CCN bending mode at 385 cm^{-1} , and the CNH bending mode at 596 cm^{-1} . These modes should be readily excited in discharge experiments used previously to record the rotational spectrum of the vibrational ground state [244, 245], and in warmer regions of the ISM, i.e. hot cores in star-forming regions. In order to guide future micro-/millimeter-wave studies of the vibrational satellite spectrum, estimates of the rotational constants within these states are provided in the following based on the calculated rotation-vibration interaction constants α_i (at the CCSD(T)/ANO2 level of theory), applied to the experimentally determined B_0 value, i.e. $B_i = B_0 - \alpha_i$, and the calculated A_0 values (see Table 4.2). In this way we obtain for the ν_{10} CCN bending mode (with $\alpha_{10}^A = 91.3 \text{ MHz}$, $\alpha_{10}^B = -20.2 \text{ MHz}$) $A_{10} = 154929 \text{ MHz}$, $B_{10} = 8610.8 \text{ MHz}$ and $q_{10} = 14.8 \text{ MHz}$ for the l -type doubling parameter, and for the CNH bending mode ($\alpha_9^A = 31.1 \text{ MHz}$, $\alpha_9^B = -8.3 \text{ MHz}$) $A_9 = 154989 \text{ MHz}$, $B_9 = 8598.9 \text{ MHz}$ and $q_9 = 8.9 \text{ MHz}$, respectively. Direct comparison of the calculated values with experiment are possible for the ν_1 NH stretching mode studied by Amano [249]. The calculated value for $B_1 = 8569.1 \text{ MHz}$ agrees to within 0.005 % with the experimental one of 8568.6 MHz . The deviation for A is larger, Amano gives $A_0 - A_1 = 49.394 \text{ MHz}$, which is about twice our calculated value of $-\alpha_9 = 23.4 \text{ MHz}$.

Table 4.2.: Comparison of calculated (all using CCSD(T)) and experimental spectroscopic constants for the vibrational ground state of CH₃CNH⁺, with relative deviations to the experimental values [244] given in parentheses (in %). The last two columns give scaled spectroscopic constants for the two lowest vibrational state

	Exp. [244]	Exp. [245]	ANO2 this work	aug-cc-pVQZ [253]	cc-pCVQZ [255]	cc-pwCV5Z best estimate ^a
A_e (MHz)			156213		156734	156897
B_e (MHz)			8569		8600	8614
A_0 (MHz)	-	-	154336	157166		155020
B_0 (MHz)	8590.557	8590.559	8541(-0.58)	8600 (0.11)		8587(-0.045)
D_J (kHz)	3.125	3.141	3.06(-2.1)	2.93 (-6.5)		
D_K (MHz)	-	-	2.50	2.52		
D_{JK} (MHz)	0.1568	0.1633	0.161(2.7)	0.172 (2.0)		

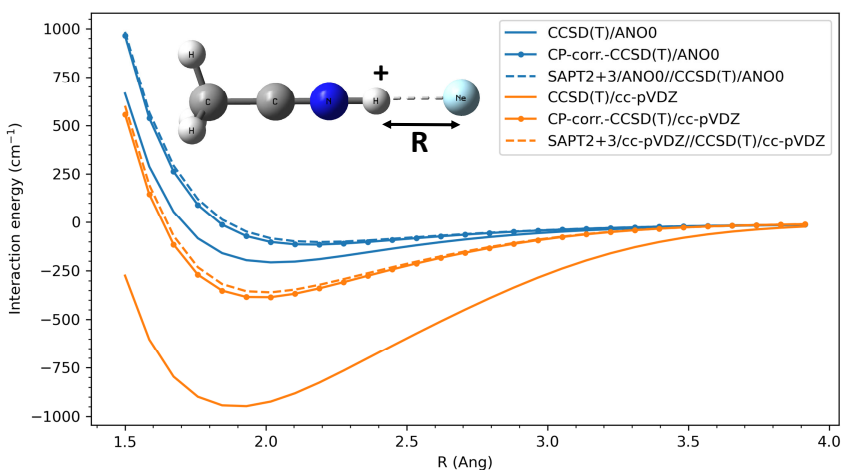
^a This work. A_0 and B_0 values were obtained by using the corresponding equilibrium values from ae-CCSD(T)/cc-pwCV5Z and rotation-vibration constants α_i from fc-CCSD(T)/ANO2 (see Table B.4 in the Supplementary Information for details).

Table 4.3.: Computed binding energies E_{int} or D_e , respectively, for the lowest energy CH₃CNH⁺-Ne complex (C_{3v} structure) using different BSSE corrections methods. All values are in cm⁻¹.

Method	D_e	CP-corrected: D_e (BSSE)	SAPT2+3: E_{int}
CCSD(T)/ANO0	-207	-105 (-102)	-86
CCSD(T)/cc-pVDZ	-950	-378 (-572)	-348

4.3.3. INFLUENCE OF THE NEON ATOM ON VIBRATIONAL BAND POSITIONS

Usually, the impact of neon-tagging on vibrational spectra is rather small [see, e.g., Ref. 258, 256, 259]. To determine the influence of the neon atom tag on the observed IRPD spectra of CH₃CNH⁺, we first searched for the global minimum structure of the CH₃CNH⁺-Ne complex. In a first step the geometry of the bare ion was optimized at the CCSD(T)/cc-pVDZ level of theory, and then kept rigid



4

Figure 4.5.: Computed potential energy surface as a function of H-Ne distance R for the minimum energy C_{3v} structure of the CH_3CNH^+ -Ne complex at various levels of theory.

at its equilibrium structure in the following calculations. Potential energy scans were performed at the same level of theory as a function of the distance of the neon ligand from the CH_3CNH^+ ion along three trajectories: i) along the molecular symmetry axis, starting from the protonation site, ii) along the CH coordinate of the methyl group, and iii) starting from the nitrogen atom and moving perpendicular to the molecular symmetry axis. The resulting PESs are shown in the Supplementary Information, Figure B.1, revealing the C_{3v} structure, with the neon atom bound to the proton, to be the global minimum.

The global minimum structure of the complex was further investigated to account for the Basis Set Superposition Error (BSSE) problem which is a mathematical artefact present in all molecular electronic structure calculations. It is due to the fact that the practical quantum chemical calculations are restricted to the use of finite basis sets [260]. This means that in a complex, the basis sets of the monomers are going to overlap and a situation arises where each atom borrows basis set functions of the other atom, effectively increasing its basis set and therefore stabilizing its energy, i.e. leading to an artificially too deep potential well,

as was first observed for the helium-helium dimer interaction[261, 138]. Since BSSE is strongly geometry dependent, the corresponding PES can substantially differ from the BSSE-free ones [262]. The usual way to correct for BSSE is based on the counterpoise (CP) scheme introduced by Boys and Bernardi [139]. This effect can be clearly noticed in the computed PES as shown in Figure 4.5. The BSSE for comparably sized basis sets, cc-pVDZ and ANO0, are -572 cm^{-1} and -102 cm^{-1} , respectively (see Table 4.3). Additionally, symmetry-adapted perturbation theory (SAPT) which was developed specifically to describe non-covalent interactions between atoms and/or molecules [140, 141], was also computed on the optimized geometry of CH₃CNH⁺ using the CCSD(T) method with cc-pVDZ and ANO0 basis sets. Since the SAPT computes the interaction energy directly via a perturbative approach, it is inherently BSSE-free as we can also clearly see in Figure 4.5. Interestingly the SAPT interaction energy results are very similar to the CP-corrected CCSD(T) (see Figure 4.5) while being computationally much more efficient as was also noted in previous studies [263]. Therefore, to conclude, the ANO0 basis set removes BSSE relatively more efficiently than the corresponding cc-pVDZ (see Figure 4.5) and also performs better for frequency calculation (see Table B.3 in the Supplementary Information). This is in agreement with previous studies [211] where several small poly-atomic molecule's fundamental frequencies were computed at CCSD(T) using both cc-pVXZ(X=D,T,Q) and ANOX(X=0,1,2) basis sets, and compared with experimental results. Here the authors stated that the ANO0 outperforms the similarly sized cc-pVDZ basis sets at least for frequency calculations.

Concluding that CCSD(T) in combination with ANO basis sets provides reliable results for structural calculations of the weakly bound CH₃CNH⁺-Ne complex, we calculated its harmonic vibrational frequencies and compared them to those obtained for the bare CH₃CNH⁺ ion at the CCSD(T)/ANO0 level of theory. The calculated differences in band positions were added to the anharmonic fundamental mode positions of the bare ion obtained at the CCSD(T)/ANO2 level of theory, and are summarized in Table 4.1. For most modes the complexation with neon leads to band shifts of below 1 cm⁻¹, within the uncertainty of the experimental data. An exception are the CNH bending and NH stretching modes, with calculated differences of +18 and -9 cm^{-1} , respectively. This is not surprising, since the binding site of the neon atom is at the NH-proton, which is involved in those two vibrational modes, causing a blue and red-shift, respectively, of the bending and stretching bands. Similar but more pronounced effects have been seen for other smaller molecular ions tagged with neon, e.g., HCO⁺ [264] and CH₃⁺ [265]. It is interesting to note that the corrected frequency for the CNH bending mode now matches the experimental IRPD band position to within its uncertainty. Apart from inducing bandshifts, the IRPD messenger-

tagging method can lead to additional bands in the recorded vibrational spectrum caused by combination modes of fundamental modes of the ion core with intramolecular modes involving the neon atom. For the CH_3CNH^+ -Ne complex harmonic calculations predict a degenerate bending mode (E) at 32 cm^{-1} and a stretching mode (A_1) at 68 cm^{-1} due to vibrations of the neon atom (See Table B.3 in the Supplementary Information). The low-lying bending mode frequency matches well with the frequency difference of weak satellite features observed to the blue of the CCN bending mode (at 414 cm^{-1}), the CNH bending mode (at $611, 620, 644, 664 \text{ cm}^{-1}$), and the CH_3 umbrella mode (1388 cm^{-1}). These combination modes might also be responsible for the observed shoulder towards higher frequencies of the CCN bending overtone at 1157 cm^{-1} . The long progression of combination bands with multiple excitation of the Ne bending mode seen for the CNH bending mode might be explained by effective dissociation of the CH_3CNH^+ -Ne complex upon excitation along the Ne dissociation coordinate, similar effects have been observed previously for other ion ligand complexes [68, 266, 65].

4.4. CONCLUSIONS

In this work, we present a comprehensive experimental and quantum-chemical study of the vibrational spectrum of CH_3CNH^+ , a potential interstellar molecular ion. Experimental band positions were measured for all fundamental bands, with the exception of the NH stretching band that was studied previously [247, 249]. The assignment of the corresponding vibrational modes was straightforward based on anharmonic frequency calculations of the bare ion performed at the CCSD(T)/ANO2 level of theory. We could demonstrate that quantum-chemical calculations using the comparatively low-cost ANO0 basis set provide accurate estimates on the influence of the weakly-bound neon atom, used as tag in the IRPD experiments, on the vibrational band positions.

The experimental vibrational frequencies obtained in this work provide reliable reference data for infrared astronomical observations to search for protonated methyl cyanide in warmer regions of the ISM or within (exo-)planetary atmospheres, such as that of Titan, where CH_3CNH^+ has been mass spectroscopically detected [243]. The present results also provide a basis for further laboratory studies of CH_3CNH^+ at higher resolution in the infrared, e.g., via action spectroscopic schemes like LIICG pioneered in the Schlemmer group [63, 267], and for measurements of rotational transitions in its energetically low-lying vibrational states, for which spectroscopic constants are predicted based on high-level quantum-chemical calculations.

This work demonstrates once more the versatility of IRPD using weakly bound rare gas atoms as tags, providing vibrational spectra very closely resembling those of the bare ion. However, the proverbial "innocence" of the neon atom needs to be taken with a grain of salt. For the rather small CH₃CNH⁺ molecular ion quite substantial shifts > 10 cm⁻¹ were observed for those vibrational modes that involve the binding site of the neon atom, as also verified by our quantum-chemical calculations. Experiments using helium as tag might be better suited, due to its even lower polarizability and binding energy, as has been demonstrated previously [268, 269, 270, 65]. However, for the same reason, i.e. its lower polarizability, He-ion complexes have smaller binding energies, and thus show lower complexation yields, which in turn results in lower signal-to-noise spectra. Using neon as tagging agent in IRPD is thus a reasonable compromise, and allows in combination with the widely tunable FELIX FELs to uncover broad range vibrational spectra of a large class of molecular ions.

5

A VIBRATIONAL ACTION SPECTROSCOPIC STUDY OF THE RENNER-TELLER AND SPIN-ORBIT AFFECTED CYANOACETYLENE RADICAL CATION HC_3N^+

This chapter is adapted from : Steenbakkers, K., Marimuthu, A.N., Redlich, B., Groenenboom, G.C., Brünken, S.. J. Chem. Phys. 2023, (in press).

This work is an equal contribution of Steenbakkers, K. and Marimuthu, A.N. I would like to thank Steenbakkers, K for her vital contribution to this study, especially the theoretical part.

ABSTRACT

The linear radical cation of cyanoacetylene, $\text{HC}_3\text{N}^+({}^2\Pi)$, is not only of astro-physical interest, being the, so far undetected, cationic counterpart of the abundant cyanoacetylene, but is also of fundamental spectroscopic interest due to its strong spin-orbit and Renner-Teller interactions. Here, we present the first broadband vibrational action spectroscopic investigation of this ion through the infrared pre-dissociation (IRPD) method using a Ne tag. Experiments have been performed using the FELion cryogenic ion-trap instrument in combination with the FELIX free-electron lasers and a Laservision OPO/OPA system. The vibronic splitting patterns of the three interacting bending modes (ν_5, ν_6, ν_7), ranging from $180 - 1600 \text{ cm}^{-1}$, could be fully resolved revealing several bands that were previously unobserved. The associated Renner-Teller and intermode coupling constants have been determined by fitting an effective Hamiltonian to the experimental data, and the obtained spectroscopic constants are in reasonable agreement with previous photoelectron spectroscopy (PES) studies and *ab initio* calculations on the HC_3N^+ ion. The influence of the attached Ne atom on the infrared spectrum has been investigated by *ab initio* calculations at the RCCSD(T)-F12a level of theory, which strongly indicates that the discrepancies between the IRPD and PES data are a result of the effects of the Ne attachment.

5.1. INTRODUCTION

The simplest cyanopolyyne, cyanoacetylene (HC_3N), is one of the most widespread polyatomic species in the interstellar medium (ISM) and has been observed in a variety of astronomical sources in the Milky Way and in external galaxies[271, 272, 273]. It also plays an important role in the complex nitrogen chemistry of Titan, Saturn's largest moon, being one of the most abundant nitrogen bearing species detected in its atmosphere. [274, 235]. Its highly reactive cationic counterpart, HC_3N^+ , is efficiently produced by ionization of the neutral cyanoacetylene by solar vacuum-ultraviolet (VUV) radiation and may participate in Titan's thiolin formation [243]. In the ISM, neutral HC_3N is readily ionized by cosmic rays or UV photons to form HC_3N^+ [275]. However, this cation has yet to be detected in the ISM, which is likely a result of lack of reference data.

Besides being astrochemically relevant, the cyanoacetylene radical cation (${}^2\Pi$) is interesting on a fundamental spectroscopic level due its open-shell linear character. The vibronic coupling effects that occur as a result of this character, such as Renner-Teller (RT) [276] coupling, cause a breakdown of the Born-Oppenheimer (BO) approximation. Subsequent analysis of the complex splitting pattern then requires methods that go beyond the BO approximation, such as effective Hamiltonian analysis (for small couplings)[277] or a full nonadiabatic description of the molecule.[278, 279]

Previous work on HC_3N^+ includes several low- and high-resolution photoelectron spectroscopy (PES) studies [4, 280, 281, 282]. The high-resolution pulsed-field ionization zero kinetic energy (PFI-ZEKE) study by Dai *et al.* [4] presented sufficient experimental resolution to reveal an intricate RT and spin-orbit (SO) splitting pattern in the observed vibronic spectrum, which was analyzed on the basis of diabatic calculations. The observed medium to weak coupling strengths make this ion an excellent candidate for an effective Hamiltonian analysis rendering experimental spectroscopic constants that can be used to benchmark *ab initio* calculations.

Vibrational spectroscopic work on HC_3N^+ is limited to a Ne-matrix assisted absorption spectroscopy study in the C-H stretching region[283], which does not contain any information on the three RT affected vibrational bending modes. Gaining information on these modes through vibrational spectroscopy would be complementary to the earlier PES work due to the different selection rules at hand and would aid to a full understanding of this complex ion. Furthermore, this data could serve as a reference for future high-resolution studies and for astronomical searches (e.g., with the James Webb Space Telescope operating in the infrared region).

Infrared pre-dissociation spectroscopy (IRPD) is an excellent method to obtain gas-phase vibrational spectra of molecular ions. Here a messenger (usu-

ally a rare-gas atom) is weakly bound to the target ion at cryogenic temperatures and its subsequent on-resonant dissociation is monitored by mass spectrometry. This messenger atom, also called tag, acts as a spectator and in the case of rare-gas atoms like He or Ne its influence on the vibrational structure is generally rather small [256, 284, 258]. This method is especially suited for small reactive cations, since other (tag-free) action spectroscopic methods are not suitable [47] (e.g.infrared multi-photon dissociation is limited due to the small size of the ion [285, 286], laser induced reactions [91] require a suitable endothermic reaction, and laser inhibition of complex growth [287, 288] does work only with cw lasers).

The goal of the present study is to obtain the first broad-band gas-phase vibrational spectrum of the HC_3N^+ cation covering all fundamental vibrational modes including the RT perturbed bending modes, in order to complement and extend the earlier PES studies. The spectrum was recorded by means of infrared predissociation spectroscopy (IRPD) using Ne as a rare-gas (RG) messenger atom carried out in a cryogenic ion trap interfaced with the widely tunable FELIX (Free Electron Laser for Infrared eXperiments) [115] free electron laser [65]. The recorded spectrum is fitted with an effective Hamiltonian and compared to *ab initio* calculation of Dai *et al.* [4], and the results are discussed with an emphasis on the influence of the Ne atom used as a tag in the IRPD scheme.

5.2. METHODS

5.2.1. EXPERIMENTAL METHODS

The vibrational spectrum of the cyanoacetylene cation (HC_3N^+) was recorded using the FELion cryogenic 22-pole ion trap instrument. A detailed account of the FELion instrument is provided in Section 2.1 and the infrared-predissociation (IRPD) of in-situ rare gas tagged cold molecular ions in Section 1.5.1.1, and here we only give a brief account of details specific to the HC_3N^+ ion. The ion is produced by direct electron impact ionization [28(2) eV] from the neutral precursor acrylonitrile (CH_2CHCN , $\geq 99\%$ purity, Sigma-Aldrich). The liquid precursor was evaporated into the ion source and diluted with helium in a 5:1 (He: CH_2CHCN) mixing ratio. An about 100 ms long pulse of ions is extracted from the source and the ions of interest, *i.e.*, HC_3N^+ with m/z 51, are mass selected by a quadrupole mass filter before entering the 22-pole ion trap which is held at a fixed temperature in the range 8 – 9 K. Around 10 – 15 ms before the ions enter the trap, an intense ~ 80 ms long Ne:He pulse (1:3 mixing ratio and number density of $\sim 10^{15} \text{ cm}^{-3}$) is admitted to the trap, leading to efficient collisional cooling of the ions close to the trap ambient temperature and the formation of Ne-ion complexes by termolecular collisions. Under these conditions, around $\sim 10\%$ of the

primary ions form weakly bound complexes with Ne, see Fig. 5.1.

The ions are stored for several seconds in the ion trap (typically 1 – 3 s) and are exposed to several FELIX IR laser pulses before extraction. An IRPD spectrum is recorded by mass-selecting and detecting the $\text{Ne}-\text{HC}_3\text{N}^+$ complex ions as a function of wavenumber. The following wavenumber ranges were covered in this study: (a) $130 - 270 \text{ cm}^{-1}$, (b) $310 - 2500 \text{ cm}^{-1}$, and (c) $3110 - 3270 \text{ cm}^{-1}$, using the free-electron IR lasers FEL-1 (a) and FEL-2 (b) of the FELIX Laboratory¹ with macropulse repetition rate of 10 Hz, maximum pulse energy in the trap region of $< 35 \text{ mJ}$ (at 1100 cm^{-1}), and linewidths (fwhm) of around 0.5 % of the center wavenumber. Region (c) was covered using a Laservision OPO/OPA system ($\sim 1 \text{ cm}^{-1}$ fwhm, 10 Hz repetition rate) with typical output power of $< 20 \text{ mJ}$.

A relative depletion $D = 1 - \frac{N_{\text{ON}}(\nu)}{N_{\text{OFF}}}$ in the number of complex ions $N_{\text{ON}}(\nu)$ from the baseline value N_{OFF} is observed upon resonant vibrational excitation. To account for varying laser pulse energy E , pulse number n , and for saturation effects, the signal is normalized prior to averaging using $I = \frac{-\ln[N_{\text{ON}}(\nu)/N_{\text{OFF}}]}{E(\text{in J})}$, giving the intensity I in units of cross-section per Joule. After normalizing each individual spectrum in this way, the final spectrum is then obtained by averaging using statistical binning with a typical bin size of 2 cm^{-1} . Line parameters such as band positions, intensities, and line widths (fwhm) are then obtained by fitting a multi-component Gaussian function to the experimental data, also providing statistical errors of the line parameters.

¹<https://www.ru.nl/felix/about-felix/about-felix/felix-laboratory/>

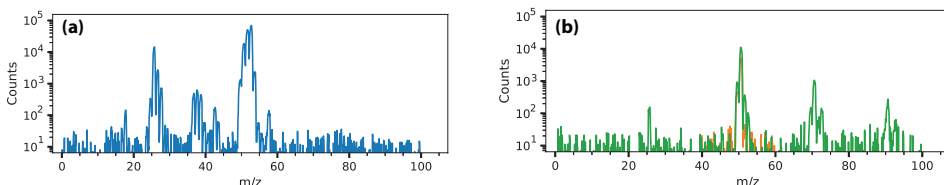


Figure 5.1.: (a) Mass spectrum of ions produced from electron impact ionization ($\sim 28 \text{ eV}$) of acrylonitrile (blue). (b) Mass-selected (orange) HC_3N^+ (m/z 51) together with tagged (green) $\text{Ne}-\text{HC}_3\text{N}^+$ (m/z 71) complexes produced in the cryogenic ion trap at temperature $8.5(2) \text{ K}$ and He:Ne gas mixture number density of $9(1) \cdot 10^{14} \text{ cm}^{-3}$. The attachment of isotopic ^{22}Ne can also be seen in panel (b). A small contamination from C_3N^+ (m/z 50) can be seen in the mass-selected spectrum, resulting from insufficient mass-filtering of the primary ions.

5.2.2. THEORETICAL APPROACH

5.2.2.1. AB INITIO

To understand and describe the vibrational IRPD spectra and the influence of the attached Ne atom on the observed band positions we performed *ab initio* quantum chemical calculations on the HC_3N^+ cation and the Ne– HC_3N^+ complex. Geometry optimization and subsequent harmonic wavenumber calculations on the bare ion were performed at the partially spin-restricted, explicitly correlated, coupled cluster level of theory, with single, double, and perturbative triple excitations, RCCSD(T)-F12a [289] using cc-pVXZ-F12 (X=D,T,Q) [290] basis sets, and for the Ne– HC_3N^+ using the cc-pVTZ-F12 basis set. Information on the perpendicular component of the dipole moment of the bare ion was obtained by the use of finite-field perturbation theory, where a finite dipole field ($F = 0.005$ a.u.) is added to the core energy and the one-electron Hamiltonian. The dipole moment μ is then obtained as

5

$$\mu = -\frac{E(+F) - E(-F)}{2F}, \quad (5.1)$$

where $E(F)$ is the energy as a function of the field.

To investigate the interaction of HC_3N^+ with the Ne atom a one-dimensional cut of the potential energy surface was made by attaching the Ne atom to the middle carbon atom for fixed Ne-C-H angles, while optimizing all other geometry parameters. All quantum chemical calculations were performed using the MOLPRO suite, version 2015.1.[291]

5.2.2.2. EFFECTIVE HAMILTONIAN

The spin-vibronic energy levels of HC_3N^+ were calculated with an effective Hamiltonian approach similar to the model of He and Clouthier [277] following the nomenclature employed by Dai *et al.* [4]. We ignore the effects of molecular rotation since its effects are too small to be seen with the experimental resolution of approximately 0.5% of the center wavenumber: for Ne– HC_3N^+ complex $B_e \approx 0.033 \text{ cm}^{-1}$, calculated at the RCCSD(T)-F12a/cc-pVTZ-F12 level of theory.

A Hund's case (a) basis, $|\mathbf{n}\rangle$, was chosen with:

$$|\mathbf{n}\rangle = |\Lambda\rangle|\Sigma\rangle \prod_{k=5}^7 |\nu_k, l_k\rangle|K\rangle|P\rangle. \quad (5.2)$$

Here, quantum numbers $\Lambda = \pm 1$ and $\Sigma = \pm 1/2$ are the projection of the orbital and spin angular momenta on the molecular axis, respectively, $\nu_k = 0, 1, \dots$ is the vibrational quantum number of mode ν_k and l_k is the projection of the vibrational angular momentum ($l_k = -\nu_k, -\nu_k + 2, \dots, \nu_k$). We only include the three

bend normal modes $v_5 - v_7$. Quantum number $K = \Lambda + \sum_k l_k$ is the projection of the total angular momentum excluding electron spin and $P = K + \Sigma$ is the projection of the total angular momentum onto the molecular axis. In the case of strong vibronic coupling, such as RT coupling, Λ and l_k are ill-defined, but P is a good quantum number since we neglect overall rotation. Furthermore, we only include diagonal spin-orbit coupling and first order RT, see below, and hence K is also a good quantum number. For a basis truncated at $v_{\text{tot}} = v_5 + v_6 + v_7 = 8$ we find that energy levels are converged up to $v_{\text{tot}} = 3$.

We approximate the total effective Hamiltonian by:

$$\hat{H} = \hat{H}_{\text{vib}} + \hat{H}_{\text{SO}} + \hat{H}_{\text{RT}}, \quad (5.3)$$

where \hat{H}_{vib} represents the harmonic vibrational energy,

$$\hat{H}_{\text{vib}} = \sum_{k=5}^7 \omega_k (v_k + 1) |v_k\rangle\langle v_k|, \quad (5.4)$$

5

with ω_k the harmonic frequencies of the bending modes $v_5 - v_7$. The spin-orbit Hamiltonian is given by [292]

$$\hat{H}_{\text{SO}} = A_{\text{SO}} \hat{L}_z \hat{S}_z, \quad (5.5)$$

where we take the SO constant $A_{\text{SO}} = -44 \text{ cm}^{-1}$ independent of the vibrational mode [4] and \hat{L}_z and \hat{S}_z are the molecule fixed components of the electronic orbital and spin angular momenta operators, respectively. The effective RT Hamiltonian is [293]

$$\hat{H}_{\text{RT}} = \left[\frac{1}{2} \sum_{k=5}^7 g_k q_{k,+}^2 + g_{56} q_{5,+} q_{6,+} + g_{57} q_{5,+} q_{7,+} + g_{67} q_{6,+} q_{7,+} \right] |\Lambda = -1\rangle\langle\Lambda = 1| + \text{h.c.}, \quad (5.6)$$

where h.c. stands for Hermitian conjugate and the operator $|\Lambda = -1\rangle\langle\Lambda = 1|$ couples the two diabatic electronic states. The constants g_k are related to the dimensionless RT constants ϵ_k as

$$g_k = \epsilon_k \omega_k \quad (5.7)$$

and the coupling parameters g_{kl} are related to the dimensionless intermode RT couplings ϵ_{kl} by

$$g_{kl} = \epsilon_{kl} \sqrt{\omega_k \omega_l}. \quad (5.8)$$

The spherical normal mode operators $q_{k,\pm}$ are related to the Cartesian normal modes $q_{k,x}$ and $q_{k,y}$ by

$$q_{k,\pm} = q_{k,x} \pm i q_{k,y}. \quad (5.9)$$

The wave function is expanded in the basis

$$|\Psi_i\rangle = \sum_{\mathbf{n}} |\mathbf{n}\rangle u_{\mathbf{n},i} \quad (5.10)$$

and the expansion coefficients $u_{\mathbf{n},i}$ are determined variationally by solving the matrix eigenvalue problem given below, using the free and open source numerical software SCILAB version 6.1.1. [294].

$$\mathbf{H}\mathbf{u}_i = E_i \mathbf{u}_i, \quad (5.11)$$

Here E_i are the eigenvalues and \mathbf{H} the Hamiltonian matrix of which the matrix elements are given in Ref [277]. All parameters, excluding A_{SO} and the g_{57} intermode RT coupling parameter, were obtained from a nonlinear least-squares fit to 14 lines of the experimental spectrum. We use the `lsqrssolve` Levenberg-Marquardt algorithm implemented in SCILAB, starting from the calculated spectroscopic parameters of Dai *et al.* [4]. For this purpose we write the Hamiltonian matrix \mathbf{H} as

$$\mathbf{H} = \mathbf{H}_0 + \sum_{j=1}^8 p_j \mathbf{H}_j, \quad (5.12)$$

where the p_j 's are the parameters to be fitted $\{\omega_5, \omega_5, \omega_7, g_5, g_6, g_7, g_{56}, g_{67}\}$ and \mathbf{H}_0 contains the spin-orbit Hamiltonian and $v_5 - v_7$ intermode RT coupling which are kept constant. The fitting algorithm employs the Jacobian matrix \mathbf{J} of the derivatives of the transition energies $E_i - E_0$ with respect to the parameters

$$J_{ij} = \frac{\partial(E_i - E_0)}{\partial p_j}. \quad (5.13)$$

We obtain the derivatives of the energies with respect to the parameters as expectation values of the Hamiltonian matrices \mathbf{H}_j for the normalized eigenvectors \mathbf{u}_i

$$\frac{\partial E_i}{\partial p_j} = \mathbf{u}_i^T \mathbf{H}_j \mathbf{u}_i. \quad (5.14)$$

where the T indicates the transpose of the column vector \mathbf{u}_i .

The fitting error (σ_j) in parameter p_j is approximated by:

$$\sigma_j = \sqrt{\mathbf{C}_{j,j}}, \quad (5.15)$$

where the covariance matrix \mathbf{C} is related to the Jacobian matrix \mathbf{J} and the root-mean-squares (RMS) error in the transition energies (r) by

$$\mathbf{C} = (\mathbf{J}^T \mathbf{J})^{-1} r^2. \quad (5.16)$$

Finally, the intensities are computed by

$$I_k(i' \leftarrow i) = |\langle \Psi_{i'} | \hat{\mu}_{\pm} | \Psi_i \rangle|^2, \quad (5.17)$$

where the dipole operator $\hat{\mu}_{\pm}$ is approximated by

$$\hat{\mu}_{\pm} = \sum_{k=5}^7 \mu_k^{\perp} q_{k,\pm}. \quad (5.18)$$

The perpendicular dipole moments μ_k^{\perp} are given in Sec. 5.3.2.

5.2.2.3. THE HC_3N^+ ION

The linear HC_3N^+ ion exhibits a ${}^2\Pi_{3/2}$ electronic ground state known from experimental PES work and calculations [280, 281, 4]. As discussed in earlier work [282, 4, 280, 281] the v_1 - v_4 modes represent the C—H, C≡N, C≡C, and C—C stretches (of a_1 symmetry), and the v_5 - v_7 H—C≡C, C—C≡N, and C≡C—C in- (b_1) and out-of-plane (b_2) bendings, respectively. Here the plane is defined with respect to the molecular orbitals. For closed-shell species these bending modes are degenerate, but since this ion is open-shell and linear they are RT perturbed.

Already within the Born-Oppenheimer approximation the degeneracy is lifted and the RT coupling causes a complicated splitting pattern in the vibrational structure. *Ab initio* spectroscopic parameters and experimental results from the earlier PFI-ZEKE work of Dai *et al.* [4] show that v_5 has the largest RT perturbation ($\epsilon_5 \approx 0.18$), while v_6 ($\epsilon_6 \approx -0.05$) and v_7 ($\epsilon_7 \approx -0.06$) are only minimally affected. Some differences between the vibrational IRPD spectrum and the PES work may, however, be expected because of the different selection rules at hand; photo-electron spectroscopy is subjected to Franck-Condon overlap and vibrational spectroscopy to the $\Delta K = \pm 1$ and $\Delta P = \pm 1$ selection rules for the RT perturbed bending modes and $\Delta P = 0$ for the stretching modes. Furthermore, the HC_3N^+ is cooled to its vibrational and SO ground state ($P = 3/2$, $A_{\text{SO}} = -44 \text{ cm}^{-1}$), so that one of the two SO components is predominantly observed ($P = 3/2$ for the stretching modes and $P = 1/2$ or $P = 5/2$ for the bending modes). The population of the other SO level should be limited to approximately $\sim 4.5\%$, based on a Boltzmann distribution calculated with 44 cm^{-1} energy level separation and an estimated ion temperature of 20 K.

5.3. RESULTS AND DISCUSSION

Harmonic vibrational calculations were performed on RCCSD(T)-F12a/cc-pVQZ-F12 (X=D,T,Q) level of theory both for the bare ion as well as the ion-Ne complex

(see Sec. 5.3.3). The calculated equilibrium geometries are in good agreement with previous calculations [4, 280, 282] and are shown for the sake of completeness in Table 5.1.

Table 5.1.: Calculated equilibrium bond lengths (in Å) of the bare ion for linear geometry.

	H — C	C ≡ C	C — C	C ≡ N
RCCSD(T)-F12a/cc-pVQZ-F12	1.078	1.244	1.339	1.186
RCCSD(T)-F12a/cc-pVTZ-F12	1.078	1.244	1.339	1.186
RCCSD(T)-F12a/cc-pVDZ-F12	1.078	1.245	1.340	1.187
RCCSD(T)-F12a/cc-p(c)VTZ-F12 ¹	1.078	1.244	1.339	1.180
CASPT2/AVTZ ²	1.067	1.237	1.328	1.188
CCSD(T)/AVTZ ³	1.072	1.213	1.352	1.155
PBE0/AVTZ ³	1.079	1.233	1.333	1.179

¹ From Ref. [4] ² From Ref. [280] ³ From Ref. [282]

5

Figure 5.2 shows the recorded IRPD spectrum of HC_3N^+ using Ne as a messenger atom in the range $130 - 250 \text{ cm}^{-1}$ (FEL-1), $350 - 2500 \text{ cm}^{-1}$ (FEL-2), and $3110 - 3270 \text{ cm}^{-1}$ (OPO). The obtained line positions are shown in Table 5.2 together with previous experimental [4, 282, 280, 281, 283] and computational [4, 281] work. To gain accurate line positions of the weaker bands the relative depletion spectrum (not power corrected) was fitted with a Gaussian profile as described above (Sec. 5.2.1). A full list of the obtained frequencies, relative intensities and their uncertainties is given in Appendix Table C.1. The provided relative intensities were estimated from the power normalized spectrum. For clarity we treat the assignment of the well behaved stretching modes (Sec. 5.3.1) separately from the analysis of the RT and SO splitting patterns of the bending modes (see Sec. 5.3.2).

5.3.1. STRETCHING MODES

The bands at 3184, 2170, and 1846 cm^{-1} can be readily assigned to the ν_1 , ν_2 , and ν_3 modes representing the C — H, C ≡ N, and C ≡ C stretches, respectively, and they are in good agreement with *ab initio* calculations and earlier experimental work presented in Table 5.2. It is noteworthy that the ν_1 mode is approximately 60 cm^{-1} blue-shifted compared to earlier PES works, which is likely a direct consequence of the Ne attachment (see Sec. 5.3.3). This hypothesis is strengthened by comparing our experimentally derived wavenumber to the earlier Ne-matrix assisted vibrational spectroscopic measurements by Smith-Gicklhorn *et al.* [283] exhibiting a similar blue-shift.

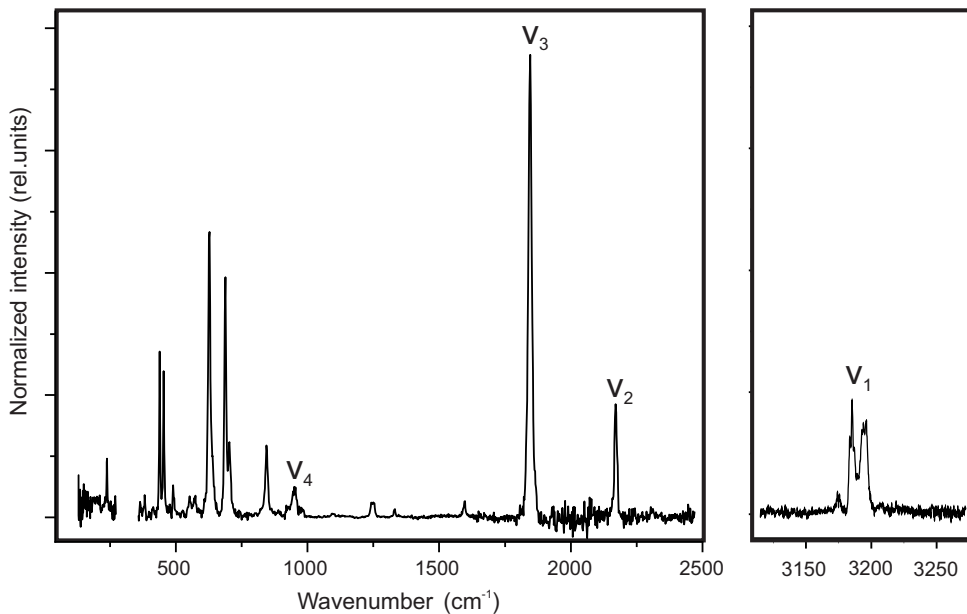


Figure 5.2.: Measured IRPD spectrum of the HC_3N^+ ion in the range $130\text{--}270\text{ }\text{cm}^{-1}$ (FEL1) $310\text{--}2500\text{ }\text{cm}^{-1}$ (FEL2), and $3110\text{--}3270\text{ }\text{cm}^{-1}$ (OPO) using Ne as a messenger atom. The $\nu_1\text{--}\nu_4$ labels represent the four stretching modes of HC_3N^+ and $\nu_5\text{--}\nu_7$ the RT-affected bending modes. A full list of the obtained frequencies, relative intensities and their uncertainties is given in Appendix Table C.1.

In the ν_1 mode a clear substructure is observed with peaks at 3174.0 , 3182.9 , 3184.7 , 3185.7 , 3192.9 , and $3195.2\text{ }\text{cm}^{-1}$. The predicted rotational structure (calculated with PGOPHER [122] at 20 K and using $B = 0.033\text{ }\text{cm}^{-1}$ for the Ne– HC_3N^+ , see Appendix Figure 1) has a FWHM due to unresolved rotational structure of approximately $4\text{ }\text{cm}^{-1}$ and cannot explain all observed peaks. We hypothesize that the 3183 , 3184 , and $3185\text{ }\text{cm}^{-1}$ peaks are the P, Q, and R branches of the C—H stretch, though the observed strong Q-band intensity remains a mystery. The 3192 and $3195\text{ }\text{cm}^{-1}$ bands may be attributed to the P-R branches of a combination band of the C—H stretch with one of the low-lying modes involving the Ne atom, which is linearly attached to the hydrogen atom (see Sec. 5.3.3).

Table 5.2.: Comparison of experimental and calculated harmonic frequencies (in cm^{-1}). If the bands are split due to vibronic interaction the lowest and highest observed components are given.

	ν_1	ν_2	ν_3	ν_4	ν_5	ν_6	ν_7
IRPD (This work)	3184(1)	2171(1)	1845(1)	957(1)	626(1)-846(1)	439(1)-490(1)	189(1)-238(1)
PFI-ZEKE ¹	...	2176(4)	445(5)	198(5)
TPES ²	3123(20)	2177(20)	1855(30)	829(30)	648(40)	422(20)	203(40)
IR-matrix ³	3196.47	2175.79	1852.82
SPES ⁴	3105	2185	1830	411	...
PFI-ZEKE ⁵	3121	2171	628-873	438-488	190-236
RCCSD(T)-F12a ⁶	3318	2224	1870	910	[767,646]	[427,410]	[183,179]
RCCSD(T)-F12a ⁷	3317	2222	1868	908	[771,644]	[462,444]	[196,186]
RCCSD(T)-F12a ⁸	3316	2217	1864	907	[763,638]	[452,436]	[194,186]
RCCSD(T)-F12a ⁹	3322	2228	1872	912	[843,699]	[474,449]	[204,198]
CASPT2 ¹⁰	3467	2270	1881	951	[853,687]	[501,468]	[222,215]

¹ From Ref. [281]

² Threshold Photoelectron Spectroscopy (TPES) from Ref. [280]

³ From Ref. [283]

⁴ Slow Photoelectron Spectroscopy (SPES) from Ref. [282]

⁵ From Ref. [4]

⁶ Using cc-pVQZ-F12 (this work)

⁷ Using cc-pVTZ-F12 (this work)

⁸ Using cc-pVDZ-F12 (this work)

⁹ Using cc-p(c)VQZ-F12 basis from Ref. [4]

¹⁰ Using CASPT2//AVTZ/CAS(9,9) from Ref. [280]

Less trivial is the assignment of the ν_4 C — C stretching mode, which we attribute to the band observed at 950 cm^{-1} . This value agrees with harmonic vibrational wavenumber calculations that predict a band between $908\text{-}951\text{ cm}^{-1}$, depending on the level of theory, but is significantly different from the 829 cm^{-1} reported in the earlier Threshold PES (TPES) work of Desrier *et al.* [280]. The authors speculated that this red-shift is a result of anharmonic coupling of the polyad involving the ν_4 , ν_6 , and ν_7 vibrational modes. No other works claim to have detected the ν_4 stretching mode and in the high-resolution ZEKE work of Dai *et al.* [4] it was not mentioned in their analysis. They, however, do observe two bands at 873 and 920 cm^{-1} , which they attribute to the $5^1\kappa\Sigma$ fundamental and the $5^17^2\Pi_{1/2}$ combination band of the RT and SO affected ν_5 and ν_7 vibrational modes. We propose that the bands at 873 and 920 cm^{-1} observed in the ZEKE study are in fact the two SO components of the ν_4 stretching mode and the band at 829 cm^{-1} observed in the TPES work to be one of the vibronic splitting components (also observed by Dai *et al.* [4]). In our work, however, only one of the two SO components is observed for all bands, which is a direct result of the cooling of the ions to their vibrational and SO ground state ($P = \frac{3}{2}$, with a population of 96 % based on the Boltzmann distribution at 20 K). Since only $\Delta P = \pm 1$ transitions are allowed for the bending modes and $\Delta P = 0$ for the stretching modes we indeed expect to observe only one of the two SO components. The relative blue-shift of the ν_4 stretching observed here may be a result of the Ne attachment similar to the effect on the ν_1 C — H stretching mode (see Sec. 5.3.3).

5.3.2. VIBRONIC COUPLING EFFECTS

To test our effective Hamiltonian model we first computed the energy levels of the bending modes based on the *ab initio* spectroscopic parameters of Dai *et al.* [4] (see Appendix Table C.2) and the obtained energies fully agree with the earlier work.

Based on our calculations we assign the energy level at 739.9 cm^{-1} to $5^1\kappa\Sigma$ and the level at 875.4 cm^{-1} to $5^1\Pi_{3/2}$. Note that in Table 3 of Dai *et al.* [4] these assignments were reversed. We also computed the vibrational transition intensities, where we may expect the selection rules $\Delta K = \pm 1$ and $\Delta P = \pm 1$ since the employed Hamiltonian does not include any mixing terms with stretching modes or between the P and K levels. The dipole moments were approximated by finite-field calculations in the xy -plane (perpendicular to the molecular z -axis) at normal mode displacement of each of the three bending modes: $\mu_5^\perp = 0.21\text{ a.u.}$, $\mu_6^\perp = -0.016\text{ a.u.}$, and $\mu_7^\perp = -0.0087\text{ a.u.}$.

Based on the calculated wavenumber positions, intensities, and the proposed selection rules, we could safely assign nine bands corresponding to the $\mu\Sigma$, $\Delta_{5/2}$,

and $\kappa\Sigma$ fundamentals of each mode (see Table 5.3). These fundamentals explain the most intense peaks of the spectrum, but several weaker bands remain unassigned. Based on the *ab initio* calculations these unassigned bands could be attributed to combination bands, overtones or transitions that violate the selection rules of our model. Since the density of states in the higher wavenumber region ($>800 \text{ cm}^{-1}$) is rather large and all transitions are of very low or zero predicted intensity their assignment is nontrivial. To gain more clarity regarding the assignment of the weak features we performed a nonlinear least squares fit of the fundamental bands to the effective Hamiltonian and iteratively included newly assigned bands. The final fit included the 14 bands marked with a star in Table 5.3. In order to check the validity of this fitting routine as well as the quality of the *ab initio* parameters, the experimental results of Dai *et al.* [4] were also fitted using this model. The resulting spectroscopic parameters are compared in Table 5.4.

5

We found that the g_{57} intermode RT coupling parameter was ill-defined for both fits, likely because of its large covariance with the g_{67} and g_{56} intermode RT coupling terms. Therefore, we decided to exclude the g_{57} parameter in the fit and kept it fixed at the *ab initio* value, which drastically improved the errors on the estimated parameters. Overall, a reasonable agreement was found between both fits and the *ab initio* values and the RMSs are close to the respective experimental uncertainties (3 cm^{-1} for PES and 1 cm^{-1} for IRPD). We note, however, that the g_{67} intermode parameter has a large error for both fits, indicating that it is not well defined within our parameter space, which is likely caused by the interdependence with the g_{57} term. Furthermore, we notice that the ω_5 , g_{55} , and g_{56} parameters are significantly lower for the IRPD work compared to the PES values. A possible explanation of this is the effect of the rare-gas attachment, which is discussed in Sec. 5.3.3.

The fitted spectroscopic parameters were in turn used to predict vibrational band positions and intensities. Figure 5.3 shows the predicted spectrum overlaid with the experimental one and the predicted line positions with their (scaled) intensities are given in Appendix Table C.3. By iteratively including new assignments in the fit, we could assign several more bands with reasonable certainty (e.g. bands at 384 , 572 , 630 , 1097 , and 1331 cm^{-1}), though the large density of states $>800 \text{ cm}^{-1}$ leads to only tentative assignments of the bands at 1243 , 1246 , and 1595 cm^{-1} . Table 5.3 summarizes the observed bands together with the *ab initio* values and the predictions based on the final fit including the 14 assigned bands (marked with a star).

All of the newly assigned bands are, however, of zero or very low predicted intensity. We suggest three reasons why this may be happening: First, the employed model excludes coupling between stretching and bending modes, but

Table 5.3.: Observed and calculated transition frequencies in wavenumbers together with their normalized calculated intensity.

Obs. [int]	<i>Ab initio</i> [int]	Calc. fit [int]	Assignment
189(1)* [0.1]	191 [0.042]	190 [0.040]	$7^1\mu\Sigma$
200(3)* [0.1]	196 [0.044]	195 [0.017]	$7^1\Delta_{5/2}$
208(2) [0.1]	$7^1\Delta_{5/2} + \nu_{\text{Ne}}?$
231(1) [0.1]
238(1)* [0.224]	237 [0.132]	240 [0.130]	$7^1\kappa\Sigma$
384(1)* [0.057]	382 [0.000]	381 [0.000]	$7^2\Pi_{1/2}$
439(1)* [0.786]	446 [0.073]	440 [0.073]	$6^1\mu\Sigma$
454(1)* [0.645]	458 [0.081]	452 [0.079]	$6^1\Delta_{5/2}$
490(1)* [0.164]	497 [0.385]	491 [0.354]	$6^1\kappa\Sigma$
552(2) [0.040]
572(1)* [0.048]	577 [0.005]	574 [0.006]	$7^3\Delta_{5/2}$
626(1)* [0.861]	630 [0.717]	627 [0.735]	$5^1\mu\Sigma$
630(1)* [0.367]	627 [0.0088]	633 [0.013]	$7^3\Delta_{5/2}$
688(1)* [1]	698 [1]	687 [1]	$5^1\Delta_{5/2}$
704(1) [0.326]	$5^1\Delta_{5/2} + \nu_{\text{Ne}}?$
846(1)* [0.322]	875 [0.547]	847 [0.563]	$5^1\kappa\Sigma$
926(1) [0.041]	ν_4 stretch
957(1) [0.147]	ν_4 stretch
981(1) [0.035]	ν_4 stretch
1097(1)* [0.013]	1105 [0.003]	1097 [0.002]	$6^27^1\Delta_{5/2}$
1243(1) [0.072]	1257 [0.004]	1256 [0.000]	$5^2\Pi_{3/2}?$
1253(1) [0.067]	1259 [0.001]	1256 [0.000]	$5^2\Pi_{3/2}?$
1331(1)* [0.039]	1339 [0.001]	1331 [0.001]	$6^3\Sigma$
1595(1) [0.072]	1616 [0.001]	1594 [0.000]	$5^2\Pi_{3/2}?$

¹ Bands marked with * were included in the fit.

² Tentatively assigned bands are marked with ?.

mixing of these terms could potentially result in intensity gain of these low-intensity bending modes. Secondly, mode ν_5 has a reasonably large RT parameter that may necessitate the inclusion of higher order terms in the effective Hamiltonian, which would in turn result in a mixing of the K states and with it relax the selection rule $\Delta K = \pm 1$. Finally, by attaching the Ne atom another RT-affected bending mode is generated (see 5.3.3), which could couple to the bending modes of the HC_3N^+ , affecting their intensity and line positions.

Table 5.4.: *Ab initio* and fitted spectroscopic parameters. The fitted parameters are determined based on the bands marked with a * in Appendix Table C.4

	<i>ab initio</i> ¹	Fit PES ²	Fit IRPD (this work)
ω_5 (cm ⁻¹)	713.25	705(2)	699(1)
g_{55}	129.50	132(4)	115(2)
g_{56}	-54.13	-63(4)	-50(3)
ω_6 (cm ⁻¹)	462.05	460(2)	455(1)
g_{66}	-24.77	-26(4)	-23(2)
g_{57}^3	-34.72	[-34.72]	[-34.72]
ω_7 (cm ⁻¹)	198.18	197(3)	198(2)
g_{77}	-12.14	-14(2)	-14(2)
g_{67}	26.81	29(14)	15(10)
RMS (cm ⁻¹)		2.8	1.8

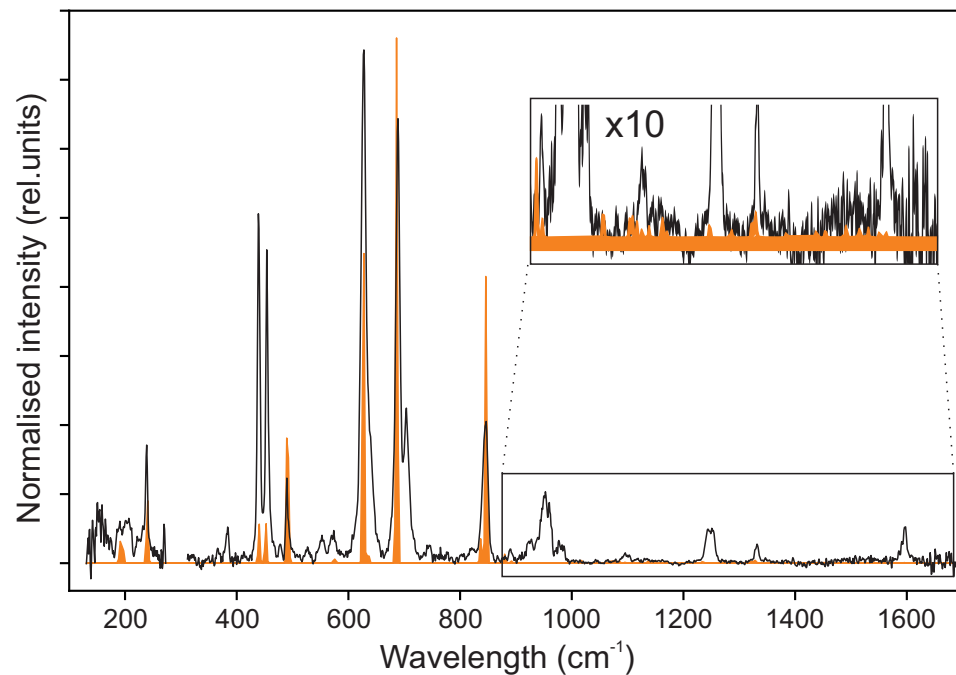
¹ From Dai *et al.* [4]

² Fitted using experimental line positions from Dai *et al.* [4]

³ g_{57} was kept at the *ab initio* value.

5.3.3. INFLUENCE OF THE RARE-GAS TAG

One of the main disadvantages of the IRPD method is that the RG-ion complex is taken as a proxy for the spectrum of the bare ion. For larger, closed-shell molecular ions the attachment or rare-gas atoms like Ne or He typically only results in minimal shifts of the vibrational frequencies [256, 284, 259, 270, 295], but symmetry-breaking effects were observed, e.g., in the case of cyclic C₃H₃⁺ [296, 195]. The influence of the tag on the bending modes of RT-affected open-shell species has, however, not yet been investigated. When comparing the observed splitting pattern of the Ne–HC₃N⁺ to that of the earlier ZEKE work [4] of the bare HC₃N⁺ we note two key differences: First, due to the different selection rules we have on the one hand recorded several features that have not been observed previously, such as the 6¹Δ_{5/2} fundamental, but on the other, we failed to see several combination bands and overtones, such as the bands at 1414 and 1460 cm⁻¹ (see Appendix Table C.4 for a full comparison between the bands observed with ZEKE [4] and IRPD). Secondly, we only see one of the two SO components since the ions are cooled down to their vibrational and SO ground state (Π_{3/2}) and the selection rule ΔP = ±1 for the bending modes must be obeyed. Finally, some of the bands that were observed by both methods are shifted compared to each other. To capture this effect in a reliable way the fitted spectroscopic parameters that were presented before in Table 5.4 were compared. Even though the param-



5

Figure 5.3.: Bending region of the IRPD spectrum of $\text{Ne}-\text{HC}_3\text{N}^+$ (black) overlaid with the bands predicted from the fitted spectroscopic parameters (orange). For the assignment of weaker features please see Table 5.3. A zoom of the $900 - 1600 \text{ cm}^{-1}$ region is presented to show the large density of transitions of weak intensity.

eters agree fairly well, the largest deviation is seen in the RT constant of mode ν_5 (ϵ_5), which represents the C-C-H bending. We hypothesize that this discrepancy is a result of the Ne attachment.

To investigate the influence of the Ne attachment a scan of the $\text{Ne}-\text{HC}_3\text{N}^+$ potential energy surface was made. The Ne atom was attached to the middle C-atom of the HC_3N^+ and moved around the ion, with all geometry parameters relaxed except for the angle Θ , see inlay in Fig. 5.4. For all $\text{Ne}-\text{HC}_3\text{N}^+$ geo-metries the bare ion remained linear so that a symmetry plane for the Ne-ion complex could be defined (here xz). The wavefunction can then be either symmetric, A', or asymmetric, A'', with regard to this plane, where the Π_x orbital is partially filled for the A' state and completely filled for the A'' state.

Figure 5.4 shows the calculated counter-poise corrected interaction energy as a function of the Ne angle for both A' and A'' symmetries. For both symmetries, the global minimum is located at $\Theta = 180^\circ$, which represents linear attachment of

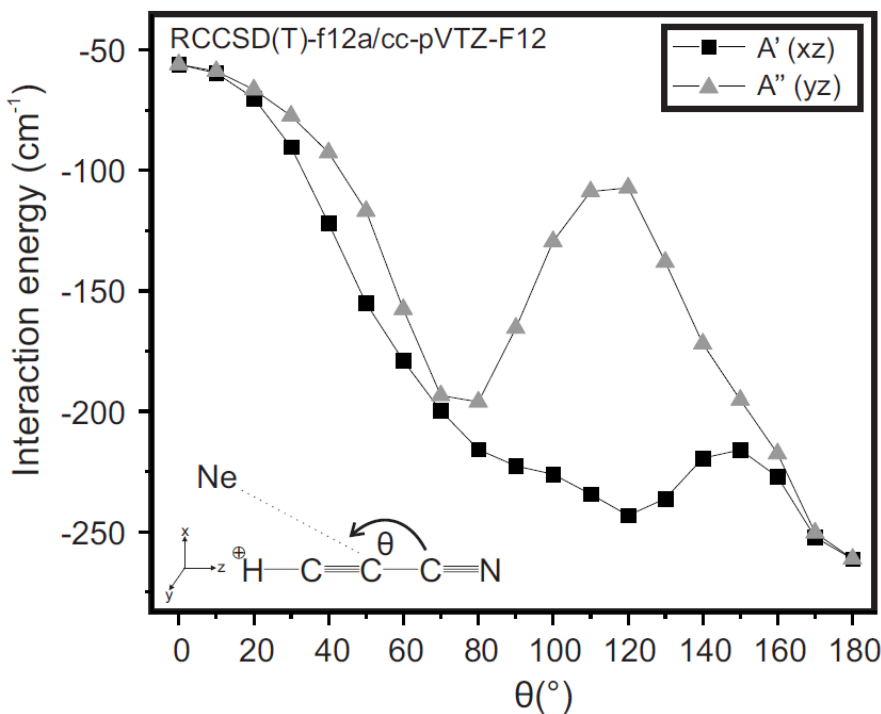
the Ne on the H atom, though both states show fairly different potential energy surfaces. Generally, the A' state is lower in energy than the A'' state, which is likely due to the lower electron density in the xz-plane for A' compared to A''. In order to explain the shape of the curves we can look at the Mulliken charges of the bare HC_3N^+ . The charges on the H, C1, C2, C3, N are +0.37, +0.02, +0.61, +0.09 and -0.08, respectively. Since the binding strength with the Ne is mainly determined by electrostatic interaction the binding will be stronger for a more positive charge. Furthermore, electrostatic repulsion of the Π_x orbital must be taken into account. For the A'' state this orbital is completely filled so that we only see minima at the H ($\Theta = 180^\circ$) and C2 $\Theta = 80^\circ$ positions, where the positive charge is largest. For the A' the Π_x orbital is only partially filled, lowering the electrostatic repulsion and allowing the Ne to come closer to the ion thus increasing its interaction energy. For this state a second minimum can then be distinguished at a bent geometry, with $\Theta = 120^\circ$ and a $\sim 40 \text{ cm}^{-1}$ barrier to linearity.

5

Since the Ne atom attaches on the H atom we expect the largest impact to be on the modes that involve this hydrogen, so the C-H stretch (ν_1) and the C-C-H bend (ν_5). Harmonic wavenumber calculations (see Table 5.5) indeed show that these modes are most affected. Here modes $\nu_1 - \nu_7$ correspond to the vibrations of the bare ion, ν_8 to the Ne-H stretch and ν_9 to the Ne-H bending. The fact that the bending modes ν_9 are not fully degenerate indicates that also this mode is Renner-Teller affected and may couple to the bending modes of the bare HC_3N^+ . Whereas in the IRPD experiment the C-H stretching wavenumber is about 60 cm^{-1} blue-shifted, harmonic wavenumber calculations actually predict a redshift. We hypothesize that this blue shift could be a result of a restriction of the H-stretching amplitude due to the Ne attachment and a subsequent reduction of the anharmonicity of this mode, resulting in a relative blue-shift. Regarding the C-H bending mode, it is beyond the scope of this study to calculate the effect of the Ne attachment on the vibronic splitting patterns: In principle the attachment leads to a six-atom linear open-shell species, introducing an additional degenerate bending mode which likely interacts with the three bending modes of the bare ion discussed above, and is expected to show large-amplitude vibrational characteristics. However, the calculated position of the Ne attachment could explain the relatively large deviation of the RT constant of mode ν_5 with respect to the earlier PES work.

5.4. CONCLUSIONS

In this work, we have investigated the vibrational structure of the HC_3N^+ ion with IRPD. The combination of a cryogenic ion trap with the wide wavenumber coverage of the FEL-1 and FEL-2 free electron lasers allowed to probe the low-



5

Figure 5.4.: Calculated interaction energy as a function of the Ne angle with respect to the molecular axis. A' represents the symmetric electronic wavefunction, where the Π_x orbitals are partially filled. A'' represents the antisymmetric electronic wavefunction, where the Π_x orbitals are completely filled

Table 5.5.: Harmonic vibrational frequencies of HC_3N^+ and $\text{Ne}-\text{HC}_3\text{N}^+$ calculated on RCCSD(T)-F12a/cc-pVTZ-F12 level of theory.

	ν_1	ν_2	ν_3	ν_4	ν_5 ¹	ν_6 ¹	ν_7 ¹	ν_8	ν_9 ¹
HC_3N^+	3317	2222	1868	908	[771,644]	[461,445]	[196,187]
$\text{Ne}-\text{HC}_3\text{N}^+$	3306	2221	1869	910	[785,662]	[463,447]	[203,196]	68	[28,26]

¹ The x- and y- components of the bending frequencies are given between brackets

lying RT disturbed bending modes directly, giving complementary information to earlier PES work [4]. The obtained spectrum was fitted with an effective Hamiltonian and the resulting spectroscopic parameters are in reasonable agreement with the *ab initio* and experimental data of Dai *et al.* [4]. The largest deviations were found in the parameters describing the H — C≡C bending mode ν_5 ,

which has the largest RT coupling of the three bending modes. We hypothesize that this discrepancy is a direct result of the Ne attachment, which was calculated to bind linearly on the H atom. This hypothesis is strengthened by the large blue shift (60 cm^{-1}) we observe for the C — H (ν_1) stretching mode compared to the other stretches.

This relatively large impact of the Ne on the HC_3N^+ raises the question of whether the IRPD method may be suitable to investigate these RT-affected ions, but currently, no alternative tag-free methods are available. To overcome the problems of the rare-gas attachment one might look into a way to elucidate the rare-gas effect on these complex open-shell species systematically by using different rare-gas tags (e.g. Ar, or N_2) or attaching multiple tags to the same ion. This would not only help to extrapolate to the bare-ion spectrum but also gives insight into weakly-bound system interactions. Furthermore, this data might act as a theory benchmark for future research combining the large-amplitude motion of the tag with the vibronic coupling effects of the ion.

III

ROTATIONAL SPECTROSCOPY

6

KINETICS OF CD^+ ION WITH HE BUFFER GAS

6.1. MOTIVATION

This chapter will discuss the kinetics of the CD⁺ molecular ion with neutral helium atoms. The formation rate coefficient (k_e) for He_{*n*}CD⁺ (*n* indicates the number of He atoms attached to CD⁺ ion) complexes are derived, and their temperature dependence will be discussed. These kinetics measurements are performed with and without the presence of radiation resonant with the CD⁺ $J = 0 - 1$ pure rotational transition via the ROSAA action spectroscopic technique (see Section 2.3.1 for more detail). The main motivation of these studies is to understand the ROSAA process and its signal intensities in detail with the support of numerical simulation results. The CD⁺ ion is best suited for this purpose since at lower collisional temperature (< 7 K), one can assume a two-level quantum system (Section 6.8) and state-dependent formation rate coefficient $k_{e(J)}$ can be derived from measured, k_e , (Section 6.7.3 and 6.8) which can provide us with an experimental comparison to the developed ROSAA numerical model.

6.2. KINETIC MEASUREMENT

6

The experiments were carried out using the 22-pole cryogenic ion trap instrument (FELion). A detailed account of the FELion instrument has been provided in Section 2.1. The CD⁺ ions were produced by electron impact ionization (EI, electron energy 30 – 35 eV) from neutral CD₄ precursor (99 atoms % D, Sigma-Aldrich). A short pulse, ~50ms, of mass-selected CD⁺ (typically ~ 10⁴ counts) is injected into the trap and stored for a specified time, typically ~ 600 – 900 ms for spectroscopic experiments, and varied between 0 and 6500 ms in 30 – 40 steps for kinetic measurements, with continuous inflow of He buffer gas for collisional cooling and complex formation. By counting the primary CD⁺ and He_{*n*}CD⁺ complexes, and possibly other product ions formed by reactions with neutral contaminants, as a function of trap time, the association and collision-induced dissociation rate constants can be determined, which is discussed in Section 6.3. For measuring rotational transitions of CD⁺ the ROSAA action spectroscopic technique is employed as described in Section 2.3.1. The pure-rotational spectra are measured in 10~ kHz steps and are averaged over ~ 20 iterations.

At low temperatures and high enough He number densities (typically < 10 K and > 1 · 10¹⁴ cm⁻³, respectively), the He_{*n*}CD⁺ complexes are readily formed by three-body collision processes and dissociated as well by collision-induced dissociation due to their low binding energies. The formation and collisional dissociation processes of CD⁺ + He are characterized by the formation (k_e) and dissociation (k_{CID}) rate coefficients, discussed in Sections 6.3 and 6.4.

Figure 6.1 shows the mass spectrum of filtered and trapped CD⁺ at a nominal temperature 4.7(3) K. After storing CD⁺ for about 600 ms, a 14(1) % yield to at-

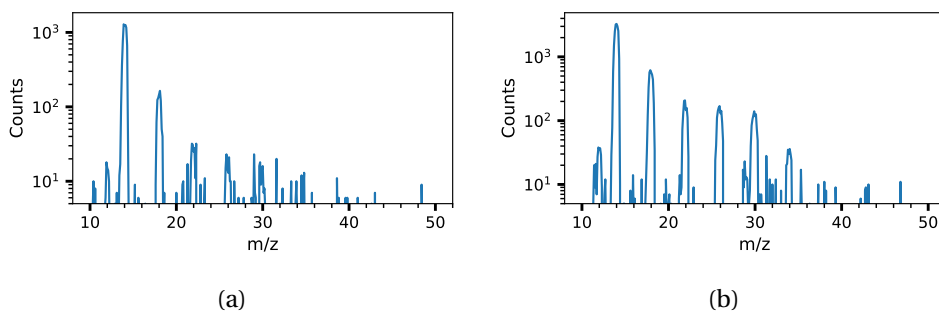


Figure 6.1.: Measured mass spectrum after storing CD^+ ions (m/z 14) for ~ 600 ms in the cryogenic ion trap using He buffer gas (a): $1.97(7) \cdot 10^{14} \text{ cm}^{-3}$; (b): $3.07(12) \cdot 10^{14} \text{ cm}^{-3}$ number density at $T=4.8(3)\text{K}$, showing the CD^+ ion and the subsequent formation of ion-He complexes with up to (a): four; (b): five He atoms attached.

tach the first He atom is achieved and up to two He atoms ([6.1a](#)) are attached at $1.97(7) \cdot 10^{14} \text{ cm}^{-3}$. Higher order complexes are formed by increasing the He number density as shown in Figure [6.1b](#), which also increases the HeCD^+ yield. In this study, the $\text{CD}^+ + 2\text{He}$ kinetics measurements were performed for helium number density range of $1 - 7 \times 10^{14} \text{ cm}^{-3}$ and 5 – 7 K temperature range.

6

6.3. THEORY OF ASSOCIATION REACTIONS

The helium complex formation process is an association reaction treated here as an independent “two-step” process. In this section, the equation for the overall effective binary association rate constant as described by Gerlich and Horning [54], and Bates and Herbst [297] are simplified and derived as follows.

Initially as the first step, the ion and neutral come together to form an excited intermediate complex:



where k_c is a bi-molecular rate constant for complex formation. The term complex indicates that it is a long-lived intermediate molecular ion with total internal energy above its dissociation limit and a lifetime of τ_{dis} towards dissociation::



where $k_{dis} = \frac{1}{\tau_{dis}}$ is a first-order rate for this back-dissociation process. Under

most experimental conditions Eq. 6.2 dominates but a fraction of complexes are stabilized either via emitting a photon:



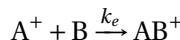
where k_{rad} is a radiative rate

or via stabilizing collision with a neutral reactant molecule B



where k_B is collisional stabilization rate constant with a neutral third body B and its rate is given by $\frac{1}{\tau_B} = k_B [B]$.

The overall association reaction can be summarised as



where k_e is an overall second-order effective rate constant for the formation of AB⁺ stable complex which can be described as follows (while substituting B = He, i.e., helium which is the neutral reaction partner used in this study)

$$k_e = k_c \cdot \frac{k_{He}[He] + k_{rad}}{k_{dis} + k_{He}[He] + k_{rad}} \quad (6.5)$$

where [He] indicates helium number density [in cm⁻³].

Since as discussed in eq. 6.2, k_{dis} dominates over radiative and collisional stabilisation rates i.e., $k_{dis} \gg k_{He}[He] + k_{rad}$, Eq. 6.5 can be simplified into the form of

$$k_e = k_c \cdot \frac{k_{He}[He] + k_{rad}}{k_{dis}}$$

which can be expressed in terms of ternary association (k_3) and bi-molecular radiative (k_r) rate constants

$$k_3 = k_c \cdot \frac{k_{He}}{k_{dis}} \quad (6.6)$$

$$k_r = k_c \cdot \frac{k_{rad}}{k_{dis}} \quad (6.7)$$

The final simplified overall effective binary rate constant (k_e) and rate (R_e) is expressed as:

$$k_e = k_3[He] + k_r \quad (6.8)$$

$$R_e = k_e [He] \quad (6.9)$$

Langevin rate coefficient:

For ion-neutral reactions, the Langevin rate coefficient, k_L , is a classical theoretical reaction rate coefficient given by Langevin [298]. The final equation for k_L , with an ion of charge q [in C], ion-neutral reduced mass μ [in amu] and polarizability of the neutral α [in \AA^3], summarised by Asvany and Schlemmer [299] Appendix A, is given below

$$\begin{aligned} k_L [\text{cm}^3/\text{s}] &= q \sqrt{\frac{\pi \alpha}{\epsilon_0 \mu}} \\ &= 2.342 \cdot \sqrt{\frac{\alpha}{\mu}} \cdot 10^{-9} \end{aligned} \quad (6.10)$$

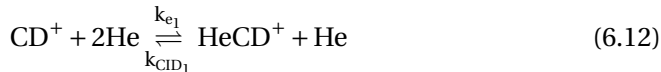
The Langevin rate coefficient, k_L , for the $\text{CD}^+ + \text{He}$ reaction can be calculated from Eq. 6.10 by substituting helium polarizability, $\alpha = 0.208 \text{\AA}^3$ [300] and HeCD^+ pair reduced mass $\mu = 3.11$ amu:

$$k_L = 6 \cdot 10^{-10} \text{ cm}^3/\text{s}. \quad (6.11)$$

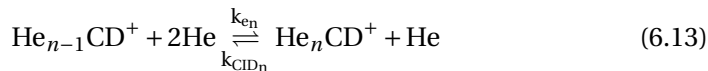
NOTE: The computed binding energy of HeCD^+ , $D_e = 491 \text{ cm}^{-1}$ at CCSD(T) /aug-cc-pVTZ level of theory. The binding energy is counterpoise corrected for the basis set superposition error [139].

6.4. RATE EQUATIONS

Following the theory of ternary association processes as discussed in Section 6.3. The pathway for the three-body reaction $\text{CD}^+ + 2\text{He}$ is expressed as shown below:



the first complex *i.e.* HeCD^+ acts as the source for the formation of higher-order complexes ($n > 1$). The pathway for higher-order complexes is expressed as:



The effective binary complex formation and collision-induced dissociation rates (in s⁻¹) are labelled as R_{e_n} and R_{CID} , respectively. The R_e is given by eq. 6.9 and R_{CID_n} can be expressed in terms of rate constants k_{CID_n} and number density [He] as below:

$$R_{CID} = k_{CID} \cdot [He] \quad (6.14)$$

The corresponding rate equation for Eq. 6.12 and 6.13 are then given as:

$$\frac{d\text{CD}^+}{dt} = -R_{e_1} \cdot \text{CD}^+ + R_{CID_1} \cdot \text{HeCD}^+ \quad (6.15)$$

$$\begin{aligned} \frac{d\text{HeCD}^+}{dt} = & +R_{e_1} \cdot \text{CD}^+ - R_{CID_1} \cdot \text{HeCD}^+ \\ & - R_{e_2} \cdot \text{HeCD}^+ + R_{CID_2} \cdot \text{He}_2\text{CD}^+ \end{aligned}$$

A general equation for all $(n - 1)^{th}$ complex can be expressed as:

$$\begin{aligned} \frac{d\text{He}_{n-1}\text{CD}^+}{dt} = & +R_{e_{n-1}} \cdot \text{He}_{n-2}\text{CD}^+ - R_{CID_{n-1}} \cdot \text{He}_{n-1}\text{CD}^+ \\ & - R_{e_n} \cdot \text{He}_{n-1}\text{CD}^+ + R_{CID_n} \cdot \text{He}_n\text{CD}^+ \end{aligned} \quad (6.16)$$

The complex with the highest observed number n of attached He, i.e., He _{n} CD⁺ in this system is treated as a reservoir for all possible higher order complexes, and its rate equation is given as:

$$\frac{d\text{He}_n\text{CD}^+}{dt} = R_{e_n} \cdot \text{He}_{n-1}\text{CD}^+ - R_{CID_n} \cdot \text{He}_n\text{CD}^+ \quad (6.17)$$

6.5. RATE LOSS CHANNELS

The ions are stored up to a maximum of 6 seconds, often this leads to a trap loss of stored ions [301, 302]. To include this loss channel, Eq. 6.15, 6.16 and 6.17 are modified into the following:

$$\frac{d\text{CD}^+}{dt} = \text{Eq. 6.15} - R_{loss} \cdot \text{CD}^+ \quad (6.18)$$

$$\frac{d\text{He}_{n-1}\text{CD}^+}{dt} = \text{Eq. 6.16} - R_{loss} \cdot \text{He}_{n-1}\text{CD}^+ \quad (6.19)$$

$$\frac{d\text{He}_n\text{CD}^+}{dt} = \text{Eq. 6.17} - R_{loss} \cdot \text{He}_n\text{CD}^+ \quad (6.20)$$

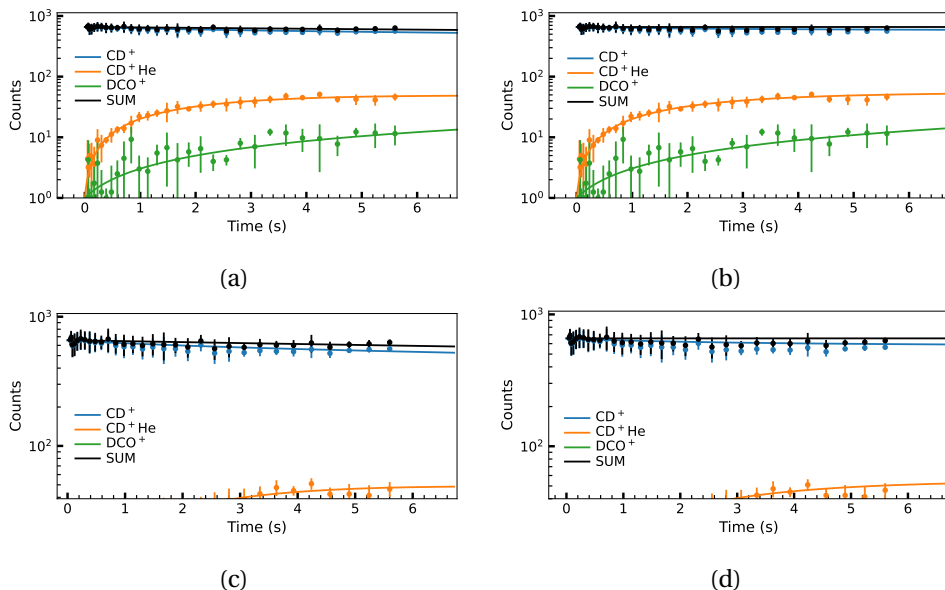


Figure 6.2.: Comparing loss channels additions: (a) is with both R_{loss} and R_{loss30} channels included while (b) is only with R_{loss30} . The (c) and (d) are zoomed-in regions for (a) and (b), respectively. The measurements were carried out at 6.9(3) K and $1.770(45) \cdot 10^{14} \text{ cm}^{-3}$ helium number density. No higher order complexes were formed other than mass 30, which most probably could be DCO⁺ as described in Eq. 6.22 and 6.23

where R_{loss} indicates the trap loss rate [in s^{-1}]. In addition to the R_{loss} channel, we have noticed a growth of m/z=30, which has been seen even at a very low pressure where no higher order complexes except HeCD⁺ as shown in Figure 6.2. Therefore, this channel is accounted for by adding an additional loss channel, as shown below:

$$\frac{d\text{CD}^+}{dt} = \text{Eq. 6.18} - R_{loss30} \cdot \text{CD}^+ \quad (6.21)$$

The most probable candidate for m/z 30 is DCO⁺, which could potentially form at low temperatures by the following reaction with CO₂ or H₂O neutrals (as shown for CH⁺ isotope in KIDA database [303]):



$$\frac{d\text{DCO}^+}{dt} = R_{loss30} \cdot \text{CD}^+ \quad (6.24)$$

Since the m/z 30 also corresponds to the He₄CD⁺ complex, Eq. 6.19 is modified only when $n - 1 = 4$ (or Eq. 6.20 when $n = 4$) by adding the corresponding loss channel $R_{loss30} \cdot \text{CD}^+$ as shown below:

$$\frac{d(\text{He}_4\text{CD}^+ + \text{DCO}^+)}{dt} = (\text{Eq. 6.19 or 6.20}) + R_{loss30} \cdot \text{CD}^+ \quad (6.25)$$

The coupled ordinary differential equations for parent ion CD⁺ (Eq. 6.15, 6.18 or 6.21) and the formed complexes (Eq. 6.16, 6.17 or 6.25) are used to numerically simulate and fit the experimentally observed data to determine the rate constants, which is discussed in more detail in the next section in different aspects. This process is vital for understanding the ROSAA spectroscopic technique employed in this work.

6

6.6. DERIVING RATE CONSTANTS

In the experiment, the parent ion CD⁺ and He _{n} CD⁺ complexes count are monitored as a function of trap time (in the following, it will be referred to as “kinetics scan”) where all ions are monitored for a duration of up to 6 s, with 4-5 iterations per data point, as shown in Figure 6.3. The coupled ordinary differential (ODE) rate equations, as discussed in section 6.4 and 6.5, are solved using the implicit Runge-Kutta method of the Radau IIA family of order 5 [124], and the solution is numerically fitted to the measured data using Levenberg-Marquardt algorithm also known as damped least-squares (DLS) method (as shown as solid lines in Figure 6.3) to derive the rates [s⁻¹] R_e and R_{CID} . These computations are carried out using the SciPy library [125]. The corresponding rate coefficients are derived from the rates as described in equations 6.9 and 6.14.

Figure 6.4a shows the exemplary derived effective binary rate constant k_e plotted against the Helium number density [He] to determine the ternary association rate constant (k_3) and radiative rate (k_r) using Eq. 6.8 at 4.8(3) K temperature. The radiative rate, $k_r = 1.2(1.9) \cdot 10^{-17}$ could not be determined, and the derived error margin can be viewed as an upper limit to this value. . Thus, one can simplify the equation 6.9 such that $k_3[\text{He}] >> k_r$ then:

$$R_e = k_e[\text{He}] = k_3[\text{He}]^2 \quad (6.26)$$

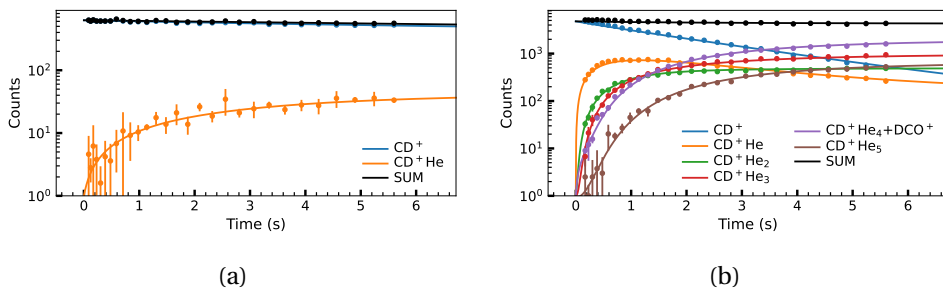


Figure 6.3.: (a) and (b) shows the counts of primary and complex ions monitored as a function of trap time at $1.16(2) \cdot 10^{14} \text{ cm}^{-3}$ and $6.0(2) \cdot 10^{14} \text{ cm}^{-3}$ respectively at $4.8(3) \text{ K}$. The circle marker and the solid line represent measured and numerically fitted data, respectively.

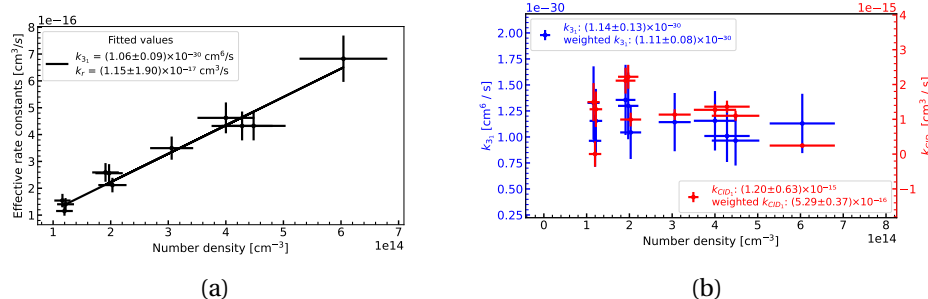


Figure 6.4.: The effective binary rate constant (k_e), the ternary association (k_{31}) and collision-induced dissociation (k_{CID_1}) rate constants are plotted as a function of helium number density. (a) The effective binary rate constant (k_e) is plotted as a function of number density to derive k_{31} (ternary association) and k_r (radiative) rate constants. The solid line indicates the linear fit where the slope and intercept correspond to k_3 and k_r , respectively. (b) shows the k_{31} as a function of number density under $k_3[He] \gg k_r$ assumption (see text). The weighted average values are shown in the legend box.

Table 6.1.: Comparing derived k_{3n} rate coefficients [in $\text{cm}^6 \text{s}^{-1}$] in this work to previous results from Brünken *et al.* [3]

$T_{trap} [\text{K}]$	$T_{ion} [\text{K}]$	$k_{31} \times 10^{-30}$	$k_{32} \times 10^{-30}$	$k_{33} \times 10^{-30}$	$k_{34} \times 10^{-30}$
-----------------------	----------------------	--------------------------	--------------------------	--------------------------	--------------------------

this work	4.8(3)	15(3)	1.1(1)	3.6(4)	13(2)	10(1)
Ref [3]	5	12(1)	1.2(1)	3.7(3)	13(2)	19(2)

Table 6.2.: Comparing derived k_{CID_n} rate constants [in cm^3s^{-1}] in this work to previous results from Brünken *et al.* [3]

	$T_{trap}[K]$	$T_{ion}[K]$	$k_{CID_1} \times 10^{-16}$	$k_{CID_2} \times 10^{-15}$	$k_{CID_3} \times 10^{-15}$	$k_{CID_4} \times 10^{-15}$
this work	4.8(3)	15(3)	5.3(4)	1.2(1)	4.3(4)	2.4(3)
Ref [3]	5	12(1)	9(2)	1.9(2)	6.5(9)	11(3)

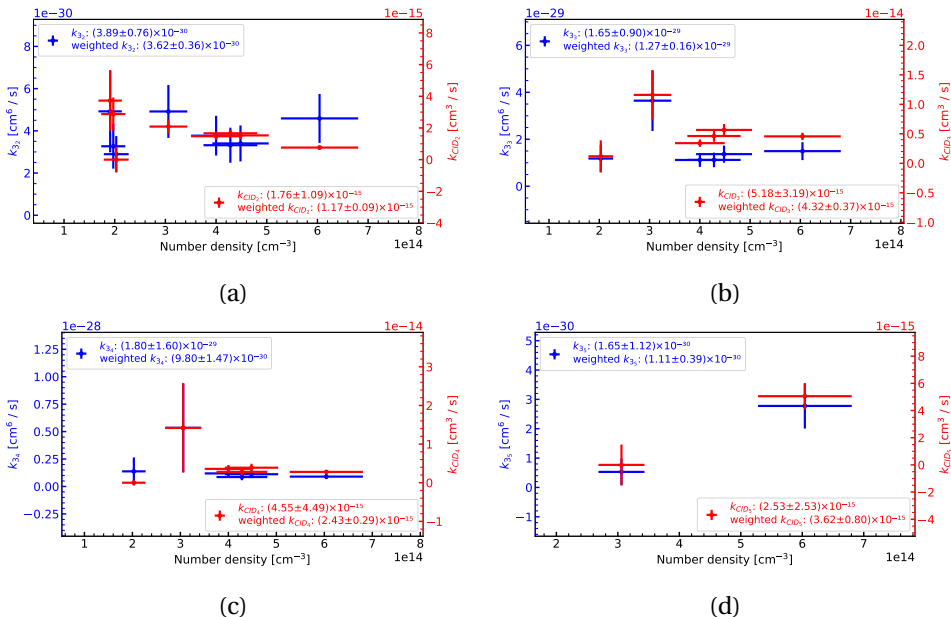


Figure 6.5.: The numerically derived formation and dissociation rate constants for higher order of complexes ($n > 1$) plotted as a function of number density at 4.8(3) K temperature.

Figure 6.4b and 6.5 shows the derived ternary association rate constant (k_3) at a nominal trap temperature of 4.8(3) K using equation 6.26. Each data point results from a single kinetics scan (as shown in Figure 6.3) at a given number density. Since the rate constants are defined to be independent (only when $k_3[\text{He}] \gg k_r$)

of number density, one can compute a weighted mean value as reported in Table 6.1 and 6.2. It should be noted that if the trap loss channel is not included (see Section 6.5), then the formation rate (k_3) does not vary within the given error bar, but the dissociation rate (k_{CID}) increases by 20 – 25%. This is also evidently seen as shown in Table 6.1 and 6.2, i.e., the previously reported values [3] for k_{CID} , disagree within the uncertainties due to lack of not considering the loss channels. However, the trap loss channel is required to fit the total sum (indicated as a black line in Figure 6.2). Hence all the derived rate constants include the trap loss and other loss channels as described in Section 6.5.

6.7. INFLUENCE OF RADIATION

Following the main motivation of this chapter (Section 6.1), in this section, the $\text{CD}^+ + \text{He}$ reaction kinetics under the influence of radiation ($\text{CD}^+, J = 0 - 1$ transition) will be discussed.

The measurement of the pure rotational, $J = 0 - 1$ line of CD^+ has been previously studied by employing the ROSAA action spectroscopic method and numerical simulations [116, 3]. In this study, an improved numerical simulation model has been implemented (see Section 2.3.5) that employs the numerically stable implicit Runge-Kutta ODE solver for stiff equations instead of explicit Euler approach, $\text{CD}^+ + \text{He}$ collisional rate coefficients [304] instead of derived rate coefficients from the $\text{CH}^+ + \text{He}$ reaction, and that includes spontaneous emission on all involved energy states. As a result, a more adaptable program has been developed for the general-purpose numerical kinetic model with an easy-to-use graphical user interface. Additionally, the $\text{CD}^+, J = 0 - 1$ rotational transition is measured using neon atoms as collision and association partner, allowing the use of a higher temperature range (up to 14 K) which shows us the possibility of using Ne atoms for ROSAA measurement of energetically higher-lying rotational transitions.

6

6.7.1. CD^+ ROTATIONAL TRANSITION ($J = 0 - 1$)

Figure 6.6 shows the measured CD^+ rotational spectrum using both He- and Ne- for the ROSAA method fitted with various lineshapes such as Gaussian, Lorentz and Voigt. The experiment is repeated with various temperatures and over large pressure ranges as summarized in Table 6.3 and 6.4 with fitted parameters such as central transition frequency, signal intensity (He CD^+ depletion %) and full-width half maxima (FWHM). The measured $J = 0 - 1$ transition frequency fitted with a Voigt profile line shape is 453521.852(5) MHz via He-ROSAA and 453521.853(5) MHz via Ne-ROSAA, respectively, and agrees well within the respective error bars, with each other and with the previous literature value 453521.8509(7) and 453521.8530(6)

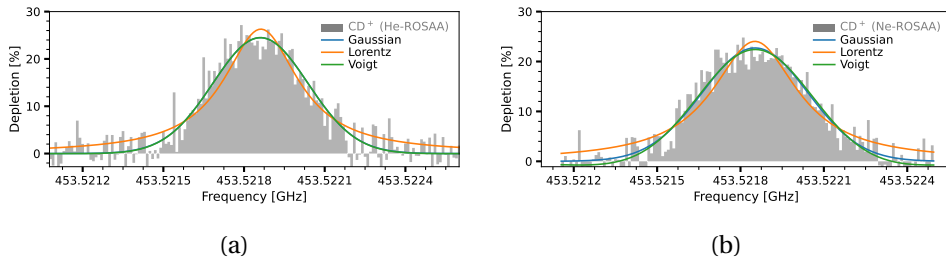


Figure 6.6.: CD^+ measured $J = 0 - 1$ rotational transition using ROSAA technique (see Section 2.3.1). The coloured solid lines indicate the fitted line profile as labelled. The experiment performed at $35(12) \sim \mu\text{W}$ power - (a) with He tag, $T_{trap} = 4.7(3) \text{ K}$ [$2.7(4) \cdot 10^{14} \text{ cm}^{-3}$] with He tag and derived $T_{ion} = 14(5) \text{ K}$ and $T_{coll} = 7(1) \text{ K}$; (b): with Ne tag , $T_{trap} = 8.7(3) \text{ K}$ [$1.8(2) \cdot 10^{14} \text{ cm}^{-3}$] and derived $T_{ion} = 23(5) \text{ K}$ and $T_{coll} = 19(3) \text{ K}$.

Table 6.3.: Pure-rotational $J = 0 - 1$ transition frequency of CD^+ ion using ROSAA action spectroscopy with He tag at 4.5(3) and 5.6(2) K temperature, and $35 \sim \mu\text{W}$ power.

T_{trap} K	Number density $\times 10^{14} \text{ cm}^{-3}$	Frequency MHz	Depletion %	FWHM kHz
4.5(3)	2.2(3)	453521.852(05)	25.56(60)	420(11)
4.5(3)	2.7(4)	453521.856(05)	24.79(61)	406(12)
4.5(3)	5.7(7)	453521.849(05)	24.49(66)	397(12)
5.6(2)	6.3(9)	453521.849(13)	13.19(90)	384(30)

MHz via He-ROSAA by Brünken *et al.* [3] and Doménech *et al.* [94], respectively; and via glow discharge experiment 453521.851(20) MHz by Amano [305].

6.7.2. DETERMINING ION TEMPERATURE

The ion temperature (T_{ion}) can be determined from a measured line profile fitted with a Voigt lineshape (see Section 2.3.4 for detail). Figure 6.7 shows the plot comparing measured nominal trap temperature, T_{trap} and derived T_{ion} for CD^+

Table 6.4.: Pure-rotational $J = 0 - 1$ transition frequency of CD^+ ion using ROSAA action spectroscopy with Ne tag for temperature range 5–14 K, and $35 \sim \mu\text{W}$ power.

T_{trap} K	Number density $\times 10^{14} \text{ cm}^{-3}$	Frequency MHz	Depletion %	FWHM kHz
16	1.9(2)	453521.908(35)	11(2)	455(083)
16	1.9(2)	453521.845(63)	6(1)	563(148)
14	1.5(2)	453521.872(26)	14(1)	610(060)
8.7	1.2(2)	453521.843(33)	19(4)	355(078)
8.7	1.8(2)	453521.848(6)	22(1)	446(014)
8.7	1.5(2)	453521.847(9)	24(1)	448(022)
9	3.8(5)	453521.828(26)	14(3)	253(060)
9	2.0(3)	453521.858(9)	19(1)	390(021)
5.5	8(1)	453521.852(26)	12(3)	204(061)
6	1.0(1)	453521.845(28)	19(2)	414(065)

, from Table 6.3 and 6.4. The plot is compared with the previously determined values in the FELion instrument by Kluge [116]. This confirms that the ion temperature is higher than the nominal trap temperatures, as observed previously in the 22-pole ion trap [299, 306, 119]. For $T_{trap} < 5$ and > 5 K, the corresponding T_{ion} are derived from He-ROSAA and Ne-ROSAA measurements, respectively.

Our measured T_{ion} data lies higher than the previous literature data (see Figure 6.7). However, different experimental conditions could explain this difference. Since, as discussed by Endres *et al.* [119], various factors such as RF heating, buffer gas thermalisation with trap walls, black-body radiation from surrounding room temperature vacuum chamber, and collision with warm residual gas that enter the cryogenic trap, in principle, can influence the ion temperature.

The measurements are performed at $\sim 35 \mu\text{W}$ for $\text{CD}^+ J = 0 - 1$ transition. The T_{ion} dependency for CD^+ ion, of ion-to-buffer gas mass ratio, i.e., for He and Ne, could not be determined in this study. However, Endres *et al.* [119] showed that for OH^- , the T_{ion} is independent of the ion-to-buffer gas mass ratio using He and HD. The number density investigated in the range $(2 - 6) \cdot 10^{14} \text{ cm}^{-3}$ around 5 K temperature for helium (see Table 6.3) did not influence the derived T_{ion} within

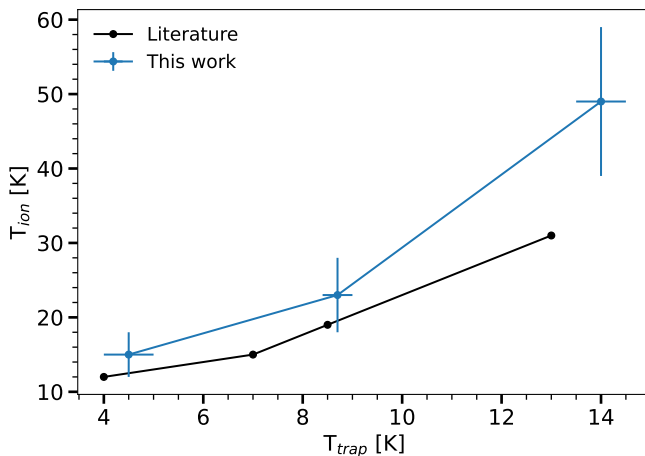


Figure 6.7.: Comparing nominal trap temperature (T_{trap}) and derived ion temperature (T_{ion}) from rotational spectrum. The solid (black) line corresponds to Ref. [116], and the solid (blue) represents derived data in this work (see text).

6

the error limits.

The effective collisional temperature, i.e., T_{coll} , is derived from T_{trap} and T_{ion} using equation 2.3. In detail, the following sections investigate the kinetic measurement in the presence of radiation and ROSAA simulations at a given collisional temperature.

6.7.3. KINETICS

The measured formation rate constants (k_3) in kinetic experiments are a weighted averaged rate coefficient over the thermal population of rotational levels (J) at a given collisional temperature (T_{coll}). The rotational state-specific ternary rate constants (k_{3_1}) for the first attachment process can be written as

$$k_{3_1}(T_{coll}) = \frac{\sum_J k_{3_1}(J, T_{coll}) \cdot N_{CD^+(J)}}{N_{CD^+}} \quad (6.27)$$

where $N_{CD^+(J)}$ and N_{CD^+} indicates the fraction of thermal population at specific rotational J level and total population of CD⁺ ion, respectively.

Figure 6.8 shows the HeCD⁺ formation rate coefficient as described in equation 6.27. The formation rate coefficients (k_{3_1}) for the first complex (HeCD⁺) at $T_{coll} = 7(1)$ K, measured with and without the presence of radiation resonant

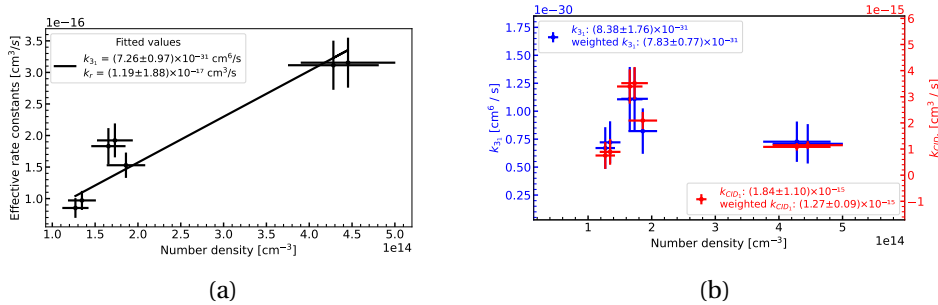


Figure 6.8.: Deriving rate coefficients in the presence of radiation resonant with $J = 0 - 1$ transition of CD^+ . (a) The effective binary rate constant (k_e) is plotted as a function of number density to derive k_{3_1} (ternary association) and k_r (radiative) rate constants. The solid line indicates the linear fit where the slope and intercept correspond to k_3 and k_r , respectively. While (b) shows the ternary association (k_{3_1}) and collision-induced dissociation (k_{CID_1}) rate constants are plotted as a function of helium number density under the assumption: $k_3[\text{He}] \gg k_r$ (see text). The weighted average values are shown in the legend box.

with $J = 0 - 1$ transition of CD^+ ion. It is denoted by $k_{3_1}(\text{ON})$ and $k_{3_1}(\text{OFF})$, respectively and as shown in Figure 6.4b and 6.8b, they are derived and given by:

$$\begin{aligned} k_{3_1}(\text{OFF}) &= 1.1(1) \cdot 10^{-30} \text{ cm}^6/\text{s} \\ k_{3_1}(\text{ON}) &= 8.4(1.8) \cdot 10^{-31} \text{ cm}^6/\text{s} \end{aligned} \quad (6.28)$$

Following the discussion from Section 2.3.5, the state-dependent formation rate constant is the key factor in understanding the ROSAA process and, subsequently, its signal intensity (referred to as depletion counts [%] in Figure 6.6). The next section discusses this relationship in detail with numerical simulations.

6.8. ROSAA NUMERICAL SIMULATION

In this section, we shall discuss the results from the numerical simulation of the ROSAA processes described in detail in Section 2.3.5.

6.8.1. COLLISIONAL PROCESS

As the hot CD^+ ions from the ion source ($T_{coll} = 300$ K) enter the 22-pole ion trap ($T_{trap} = 4.8(3)$ K), they are collisionally cooled down by He buffer gas atoms

and, at equilibrium, reach the effective collision temperature ($T_{coll} = 7(1)$ K). The T_{coll} is derived using T_{ion} and T_{trap} temperature as described in Eq. 2.3 (see Section 6.7.2). In the absence of radiation and attachment processes, the collisional process reaches an equilibrium of the relative population of rotational quantum states, which is given by the Boltzmann distribution (at T_{coll}), as shown in Figure 6.9 (see Section 2.3.5.1). The collisional rate coefficient values are derived from Werfelli *et al.* [304], for $T_{coll} = 7$ K, the rate constants for $J = 0 - 5$ are given in Appendix Table D.2. The rates are in the order of $> 10^4 \text{ s}^{-1}$ for $2.2 \cdot 10^{14} \text{ cm}^{-3}$ helium number density. As can be seen in Fig. 6.9, thermalization of the initially hot ions to the Boltzmann distribution at the collisional temperature happens within 0.3 ms under typical experimental conditions.

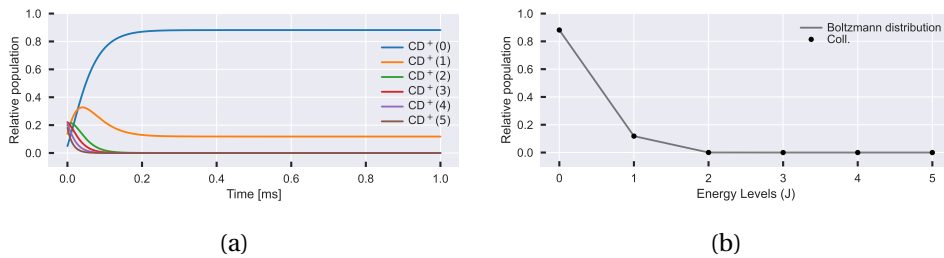


Figure 6.9.: (a) Collisional process for CD^+ ion up to $J = 5$ with He buffer gas ($2.2 \cdot 10^{14} \text{ cm}^{-3}$). The coloured label indicates the corresponding CD^+ (J) state. At $t = 0$, $T_{coll} = 300$ K, at which the relative population corresponds to Boltzmann distribution at 300 K. The relative population evolves as collisions with He with rate constants for $T_{coll} = 7$ K (derived from [304]), subsequently reaching equilibrium at < 0.5 ms. (b) Comparison of the Boltzmann distribution at 7 K with the relative population involving only collisional process (Coll.) at $t = 1$ ms.

The spontaneous emission rates (A) are also included in this process, as discussed in section 2.3.5.2. However, the collision process dominates it by 8 orders of magnitude (see Table D.2 and D.3). Therefore, in the following sections, spontaneous emission rates will not be mentioned specifically, although it is included in all the cases during simulation.

6.8.2. RADIATIVE PROCESSES

As discussed above, when including only the collisional process, the relative population re-distributed from room temperature (300 K) to Boltzmann distribution ($T_{coll} = 7$ K) at equilibrium within < 0.5 ms. Furthermore, in the presence of radi-

ation resonant with $J = 0 - 1$ of CD^+ , the population can be further re-distributed due to a competing radiative process as shown in Figure 6.10. The simulation of the evolution of the relative population of the $\text{CD}^+(J)$ rotational levels is shown in Figure 6.10a for a duration of 1 ms. The derivation of radiative rates is described in detail in section 2.3.5.3. The radiative rates for power $35 \mu\text{W}$ are in the same order of magnitude as collisional rates, i.e., $> 10^4 \text{ s}^{-1}$ (see Table D.3).

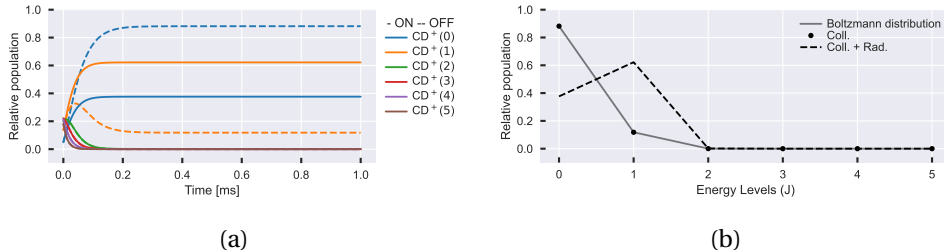


Figure 6.10.: (a) Simulated relative rotational level populations for CD^+ as labelled in parenthesis. The population evolves from $t = 0$ ($T_{coll} = 300$ K) to reach equilibrium at $t < 0.5$ ms. The solid and dashed line-shapes correspond with (ON) and without (OFF) the presence of radiation for $\text{CD}^+ J = 0 - 1$ transition. The radiation power is $35 \mu\text{W}$. (b) Compares the Boltzmann distribution at 7 K with the relative population involving only collisional process (Coll.) and, collision and radiative process (Coll. + Rad.) at $t = 1$ ms.

As depicted in Figure 6.10b, the distribution no longer follow a Boltzmann distribution. Furthermore, if the radiative rates dominate the collisional rates (Coll. \ll Rad), say for power 10^5 higher, i.e., 3.5 W , we get rates in the order of $> 10^7 \text{ s}^{-1}$. The resulting population on $J = 0$ and $J = 1$ quantum levels should then reach their statistical weights ($g(J) = 2J + 1$). The simulated relative population evolution and equilibrium population under the condition Coll. \ll Rad. is shown in Figure 6.11, for a duration of 1 ms. And Figure 6.11b also clearly shows the $J = 0$ and $J = 1$ rotational states reaching their statistical weight of 0.25 and 0.75, respectively.

The next section investigates the helium attachment process, vital in understanding the ROSAA signal, i.e., the measured rotational spectrum intensity.

6.8.3. ATTACHMENT PROCESSES

As the CD^+ ion collides with the He buffer gas at low temperature and high number density, it forms He complexes, i.e., He_nCD^+ . The formation and subsequent

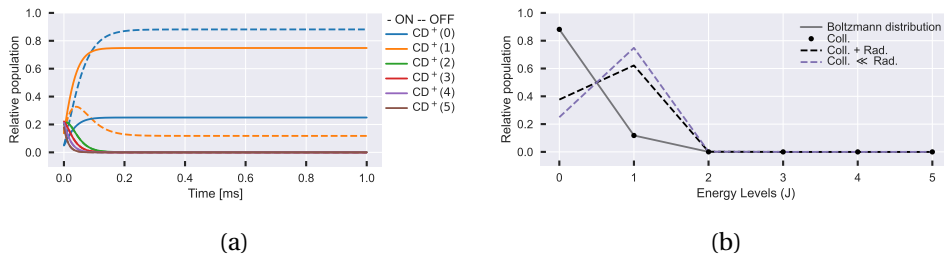


Figure 6.11.: (a) Simulated relative rotational level populations for CD^+ and corresponding number J levels as labelled in parenthesis. The population evolves from $t = 0$ ($T_{\text{coll}} = 300$ K) to reach equilibrium at $t < 0.5$ ms. The solid and dashed lineshapes correspond with (ON) and without (OFF) the presence of radiation for CD^+ $J = 0 - 1$ transition. The radiation power is 3.5 W. (b) Compares the Boltzmann distribution at 7 K with the relative population involving only collisional process (Coll.) and, collision and radiative process for power 3.5 μW (Coll. + Rad.), collision and radiative process for power 3.5 W (Coll. \ll Rad.), at $t = 1$ ms.

6

dissociation rate coefficients of He_nCD^+ are discussed in section 6.6. The numerical simulation method for the attachment process is described in detail in Section 2.3.5.4.

The ROSAA action spectroscopic technique method utilises the rotation-specific rate coefficients for the helium attachment process to observe the change in helium-complex formed at resonant frequency (see Section 2.3). Since, as discussed above, involving radiative processes re-distributes the population of rotational quantum states. They subsequently result in different numbers of complexes formed, thus a ROSAA-signal, i.e., depletion counts [%] of HeCD^+ as shown in Figure 6.6a.

A complete simulation involving the radiation, collisional, and attachment processes is vital to investigate the experimentally measured rotational spectrum, i.e., ROSAA-signal intensity. However, a rotational state-specific rate coefficient is required to include the attachment process, which is not straightforward to measure directly. Nevertheless, as discussed in section 6.2, the weighted rate coefficient was measured for $\text{CD}^+ + \text{He}$ kinetic reaction, with and without the presence of radiation resonant with $J = 0 - 1$ transition for CD^+ ion, and this allows to obtain the ratio between the rate-coefficients in the two rotational levels.

Since the relative population of $\text{CD}^+(0) + \text{CD}^+(1) \geq 0.97$ at $T_{\text{coll}} = 7$ K (see

Figure 6.9a), we can assume a 2-level quantum system to determine the rotational state-specific ternary rate constants ($k_{3_1}(J)$) from the measured, weighted ternary rate coefficients (k_{3_1}) using Equation 6.27. The k_{3_1} ratio (also referred to as “ a ”) is given by:

$$\begin{aligned} a &= \frac{k_{3_1}(J=1)}{k_{3_1}(J=0)} \\ &= \frac{X \cdot CD^+(0) - CD^+(0)_{on}}{CD^+(1)_{on} - X \cdot CD^+(1)} \end{aligned} \quad (6.29)$$

where X is the ratio of measured weighted rate constant with (ON) and without (OFF) radiation, i.e., $X = k_{3_1}(ON)/k_{3_1}(OFF)$, $CD^+(0)$ and $CD^+(1)$ represents CD^+ rotational population ratio at $J = 0$ and $J = 1$, respectively. The subscript on indicates the relative population in the presence of radiation; otherwise no radiation was admitted.

Using $k_{3_1}(ON)$ and $k_{3_1}(OFF)$ value from equation 6.28, we get X as:

$$X = 0.76 \quad (6.30)$$

6

and for the following condition ¹,

$$\begin{aligned} T_{coll} &= 7 \text{ K} \\ [He] &= 2.2 \cdot 10^{14} \text{ cm}^{-3} \\ P &= 3.5 \cdot 10^{-5} \text{ W} \end{aligned}$$

the relative population for $CD^+(J)$ is given as (see Figure 6.9a and 6.10a):

$$CD^+(0) = 0.9 \quad (6.31)$$

$$CD^+(1) = 0.1 \quad (6.32)$$

$$CD^+(0)_{on} = 0.4 \quad (6.33)$$

$$CD^+(1)_{on} = 0.6 \quad (6.34)$$

Substituting equations 6.30 through 6.34 in Eq. 6.29, we can get experimentally derived k_{3_1} ratio as:

$$a = 0.5 \quad (6.35)$$

¹ refer Section 2.3.3 for power derivation, Section 2.3.4 and Figure 2.3 for T_{coll} derivation

The derived k_{3_1} ratio value, $a = 0.5$, agrees well with the previously estimated value $a = 0.55(5)$ from Brünken *et al.* [3]. In the previous study, [3], the “ a ” value is estimated by measuring $J = 0 - 1$ transition of CD^+ at different number density and radiation power and fitting the measured ROSAA depletion signal intensity to the numerical model. However, in this study, the “ a ” is experimentally derived from kinetic measurement in the presence and absence of radiation resonant with $J = 0 - 1$ of CD^+ molecular ion. This approach also directly validates the equation 6.27, thereby, the rotational state-dependent attachment of rare gas atoms to molecular ions. In addition, this systematically supports our investigation of various processes involved in the ROSAA technique. And as described in Section 6.1, the main motivation is to develop a robust general-purpose ROSSA numerical model and be adaptable to systematically add various processes.

In the following section, the derived “ a ” is used to analyse the full model, including collisional, radiation and attachment process to the measured pure rotational transition intensity of CD^+ ion.

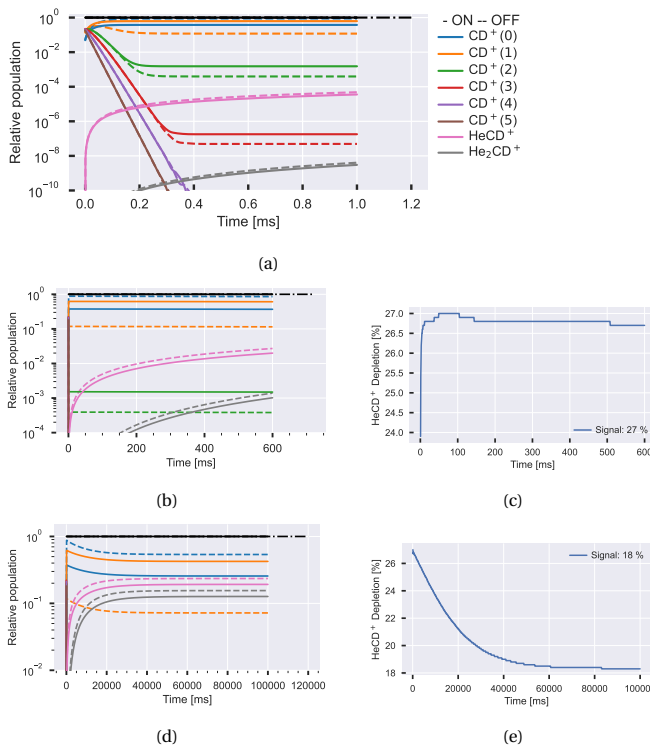
6.8.4. ANALYSING NUMERICAL RESULTS

6

The full model simulation, i.e., including collisional, radiation and attachment process for CD^+ molecular ion up to 5 rotational quantum states ($J = 0 - 5$), is shown in Figure 6.12a for 7 K temperature, $2.2 \cdot 10^{14} \text{ cm}^{-3}$ helium number density, k_{3_1} ratio, $a = 0.5$ and $3.5 \mu\text{W}$ power. The $\text{CD}^+(J)$ ion for $J > 3$ becomes insignificant within $< 0.5 \text{ ms}$, i.e., reaches $\ll 10^{-10}$ in relative population ratio while $\text{CD}^+(2)$ and $\text{CD}^+(3)$ equilibrates to $< 10^{-2}$ and $< 10^{-6}$, respectively in relative population ratio. Therefore, in this simulation under 2-level system assumption, the ternary attachment rate coefficients $k_{3_1}(J \geq 2) = 0$, i.e., only the $\text{CD}^+(J = 0)$ and $\text{CD}^+(J = 1)$ participates in the cluster formation. However, the $\text{CD}^+(J \geq 2)$ is included in the simulation to monitor its relative population evolution.

The attachment and dissociation rates timescale are in the order of 10^{-1} s^{-1} (see Table D.1). Thus, the first complex (HeCD^+) population is very small, i.e., $< 10^{-4}$ in relative population, during the first 1 ms; however, it tends to increase. Therefore, when the simulation is extended for a longer duration, i.e., for 600 ms (see Figure 6.12b) and 100 s (see Figure 6.12d), the HeCD^+ relative population reaches 0.03 and attains equilibrium at 0.2 after 40 s, respectively. Also, as our initial consideration of a 2-level quantum system, the former and latter figures supports this assumption, i.e., only $\text{CD}^+(0)$ and $\text{CD}^+(1)$ are relatively significant (> 0.1 relative population) at 7 (K) temperature.

As expected, and shown in Figure 6.12b and 6.12d, a significant difference in population is observed in the first HeCD^+ complex with (-ON) and without (-OFF) the presence of radiation resonant with the $J = 0 - 1$ transition of CD^+ . This difference is indeed the measured ROSAA depletion signal of HeCD^+ at



6

Figure 6.12.: (a) Simulated relative rotational level populations for CD^+ and corresponding number of He_nCD^+ clusters ($n=1, 2$) where $\text{CD}^+(J)$ indicates CD^+ in J rotational state. The simulation conditions are as follows: k_{31} ratio, $a = 0.5$, collisional rates for $T_{coll} = 7 \text{ K}$ (at $t = 0$, $T_{coll} = 300 \text{ K}$), Helium number density $2.2 \cdot 10^{14} \text{ cm}^{-3}$ and radiation power $3.5 \cdot 10^{-5} \text{ W}$. The solid and dashed lines correspond to, with (-ON) and without (-OFF), the presence of radiation on the $\text{CD}^+ J = 0 - 1$ transition frequency. The simulation duration for (a) 1 ms, (b) 600 ms and (d) 100 s. Figures (c) and (e) correspond to signal intensity, i.e., HeCD^+ depletion % as a function of time for (b) and (d), respectively.

resonance. Figure 6.12c represent the expected signal intensity of the measured rotational spectrum (as shown in Figure 6.6) for a trap duration of 600 ms. Before analysing further, let us look at approaches to validate our model.

There are three direct ways to verify the validity of the numerical model.

- One is to compare it with the Boltzmann distribution when only collisional processes are considered. Then at equilibrium, the relative population of CD⁺ (J) reaches T_{coll} temperature, which should be equivalent to the Boltzmann distribution at T_{coll} . This has been discussed in Section 6.8.1 and can be verified in Figure 6.9b.
- The other way is when collisional and radiative processes are involved, competing with each other. Under conditions when the radiative process (for $J = 0 - 1$ transition of CD⁺) dominates the collisional process (Coll. \ll Rad.), the equilibrium relative population of CD⁺ ($J = 0$) and CD⁺ ($J = 1$) should reach its statistical weight ($g(J) = 2J + 1$), i.e., 0.25 and 0.75, respectively. This has been discussed in section 6.8.2 and can be verified in Figure 6.11b.
- Another direct approach is to verify the signal intensity is ~ 0 when k_{3_1} ratio $a = 1$. This indicates that the rate constants are not state-dependent but rather the same, thus leading to the absence of ROSAA signal intensity.

6

In addition to validating the third point (3) for the numerical model, similar to the signal intensity plot as shown in Figure 6.12c and 6.12e, a complete overview of signal intensity simulations as a function of power ranging from $10^{-7} - 10^{-2}$ W, number density from $10^{12} - 10^{16}$ cm⁻³ and k_{3_1} ratio, a ranging from 0.3 – 1, is shown in Figure 6.13. The third point can be verified as shown in Figure 6.13e, where the signal intensity is 0 as expected when $a = 1$.

Experimental ROSAA signal strength under the condition of $2.2 \cdot 10^{14}$ cm⁻³ helium number density and 35 μ W power at 600 ms trap time, is 26(1)% (see Table 6.3). With the same condition, Figure 6.12c shows the signal intensity of 27% at $t = 600$ ms. Therefore, there is close agreement with our numerical model simulation results. Figure 6.13c depicts an overview of the achievable signal intensity as a function of number density and power for $a = 5$ and 600 ms duration. They are directly proportional to radiation power and are inversely proportional to number density. We have utilised our THz radiation source to full power without attenuation (see Section 2.2.2), with the number density adjusted for optimal 700 – 1000 counts of HeCD⁺ complexes formed for spectroscopy measurement (see Figure 6.1). As shown in Table 6.3, we have measured at different number densities, and $2.2 \cdot 10^{14}$ cm⁻³ at $T_{trap} = 4.8(3)$ K ($T_{coll} = 7(1)$ K) appears to be an optimal condition to achieve a signal of 27(1)% which is not far from the maximum achievable signal, i.e., $\approx 33\%$ as shown in Figure 6.13c.

The Ne-ROSAA measurement is shown in Figure 6.6b and Table 6.4. Since pure Ne kinetics measurement was very challenging at low temperatures due to

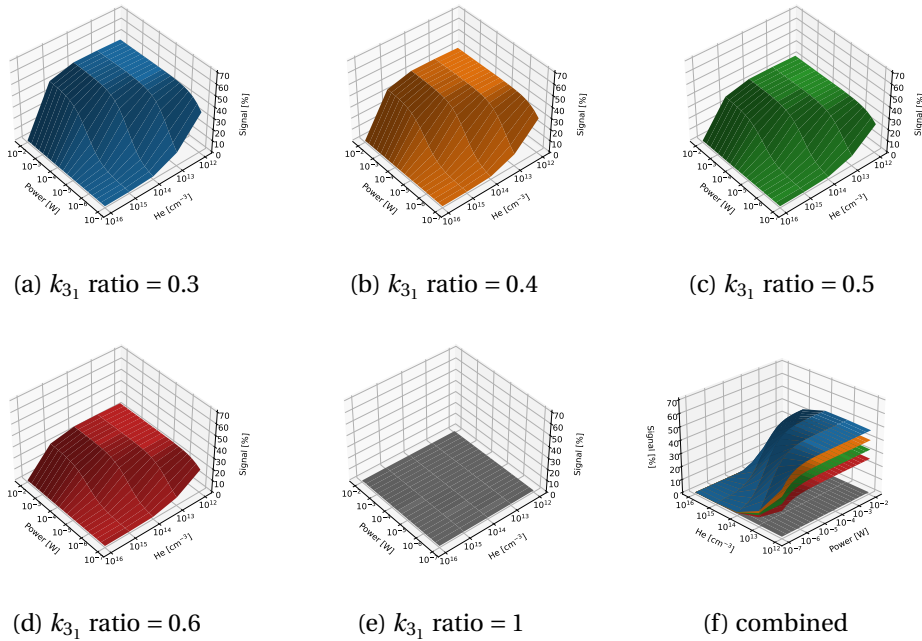


Figure 6.13.: Numerical simulation of ROSAA process with computed signal intensities as a function of radiation power, $10^{-7} - 10^{-2}$ W, He number density, $10^{12} - 10^{16}$ cm $^{-3}$, and function of k_{31} ratio, 0.3 – 1, at 600 ms trap duration and $T_{coll} = 7(1)$ K temperature. The captions of subplots (a)-(e) indicate the respective k_{31} ratio value. (f) as captioned, shows the combined plots of (a)-(e).

freeze-out , it will be explored in detail in future studies, and here we assume the same attachment and dissociation rate coefficients as for helium. We run simulations under the following condition:

$$[Ne] = 1.5 \cdot 10^{14} \text{ cm}^{-3}$$

$$P = 35 \mu\text{W}$$

$$t = 600 \text{ ms}$$

$$T_{trap} = 8.7 \text{ K}$$

$$T_{coll} = 18.2 \text{ K}$$

The experimentally measured Ne-ROSAA signal 24(1)% best fits with the sim-

ulation result (24%) but with the reduced $\alpha = 0.25$ rather than $\alpha = 0.5$, at $T_{coll} = 18.2$ K. As also discussed in Brünken *et al.* [3], $k_{3_1}(J = 1)$ likely shows a steeper decreasing temperature dependence than $k_{3_1}(j = 0)$.

Nevertheless, our initial goal was to develop an adaptable and robust numerical simulation model (with an easy-to-use graphical user interface). In addition to investigating He-CD⁺ and Ne-CD⁺ ROSAA model, it is extended to investigate the CO⁺ molecular ion (Chapter 7), which is an open-shell species hence the rotational quantum states split into fine structure levels due to non-zero net electron spin. Therefore, we have shown that extending this model to different systems is possible and will be used to predict the ROSAA signal intensity for rotational transition measurements when given energy level information (from the calculation) and rate coefficients from kinetic measurements.

The next section briefly discusses an interesting observation on the temperature dependence of ternary attachment rate coefficients.

6.9. TEMPERATURE DEPENDENCE OF RATE COEFFICIENTS

6

This section briefly discusses the temperature dependence of the ternary association and collision-induced dissociation of CD⁺ ion with He buffer gas. As discussed in Section 6.6, Figure 6.14 shows the experimentally measured formation (k_{3_1}) and collision dissociation (k_{CID_1}) rate coefficient plotted as a function of temperature (T_{trap}). The subscript 1 corresponds to the first complex, i.e., HeCD⁺. As depicted in the figure, the k_{3_1} and k_{CID_1} increase as the temperature increases.

The dissociation rates are collision-induced. The reaction cross-section gives the probability of ion and neutral collision. Thus, the rate coefficients are derived by multiplying the cross-section with a relative velocity of reactants followed by averaging over a Maxwell-Boltzmann distribution. So, as the temperature increases, the collisional velocity and energy increase, which increases k_{CID} rate coefficients.

However, the formation rates, especially for the ternary association reactions between ions and neutrals at a low temperature, possess an inverse temperature dependence because of a decrease in the effective probability of forming a stable complex with a single collision [307] (see Section 6.3 for two-step process). This contrasts our observation as shown in Figure 6.14. The ternary rate temperature dependence of $k_3(T) \propto T^{-3/4}$ was obtained back in the 1960s by Smirnov [308] for ion-neutral three-body association reactions at temperatures > 100 K. The same dependence was also shown in recent studies based on the classical trajectory approach [309, 310].

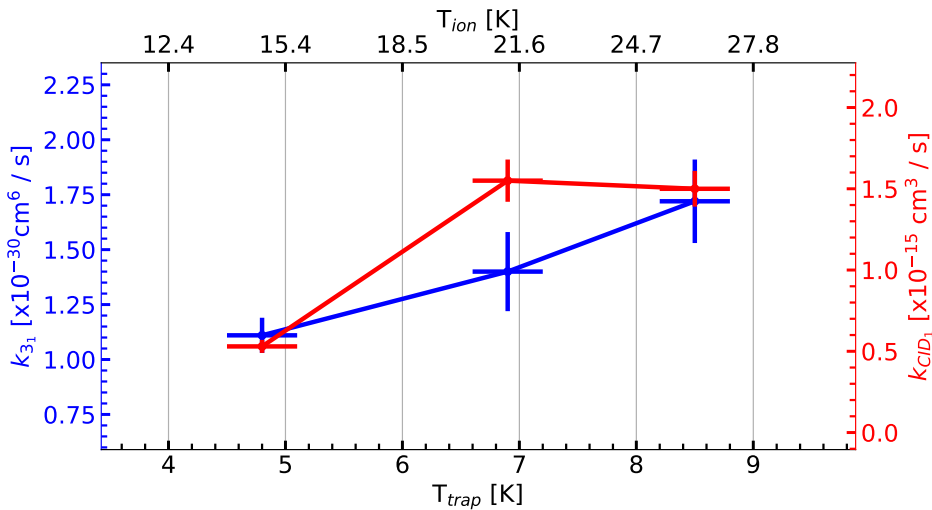


Figure 6.14.: HeCD⁺ The formation (k_{31}) and dissociation (k_{CID_1}) rate constants (weighted) are plotted as a function of nominal trap temperature (T_{trap}) and ion temperature (T_{ion}). The x-axis error bar corresponds to T_{trap} .

6

Bohringer *et al.* [311] experimentally investigated the temperature dependence (30 – 300 K) of He₂⁺ formation via ternary association using a cryogenic selected ion drift tube, i.e., similar a ion-neutral reaction, but He⁺ ion is investigated instead of molecular CD⁺, as shown below:



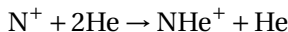
They observed an inverse temperature dependence and derived a relation for Eq. 6.36, such as:

$$k_3(T) = 1.4 \times 10^{-31} (300 \text{ K}/T)^{0.6} \text{ cm}^6 \text{s}^{-1} \quad (6.37)$$

Gerlich [312] and Plašil, et al. [313] performed the same He₂⁺ experiment but using a ring electrode trap and 22-pole cryogenic ion trap, respectively. They showed the inverse temperature dependence for k_3 at $T_{trap} > 10$ K that agrees with the equation 6.37.

In order to investigate if the discrepancy stems from the fact that we use a molecular ion, or if the observed increase might stem from a reaction-specific

resonance in the attachment process, we repeated the measurement but now with N^+ , i.e.,



The N^+ ion has the same m/z 14 as CD^+ . The experimental procedure is similar to the one described in Section 6.2. The derived formation and dissociative rate coefficients are shown in Figure D.1 (in appendix) for a temperature $T_{trap} = 5 - 10$ K and a pressure range from $(1 - 9) \cdot 10^{14} \text{ cm}^{-3}$. The temperature dependence plot for k_3 and k_{CID} for $\text{N}^+ + 2\text{He}$ reaction is shown in Figure 6.15.

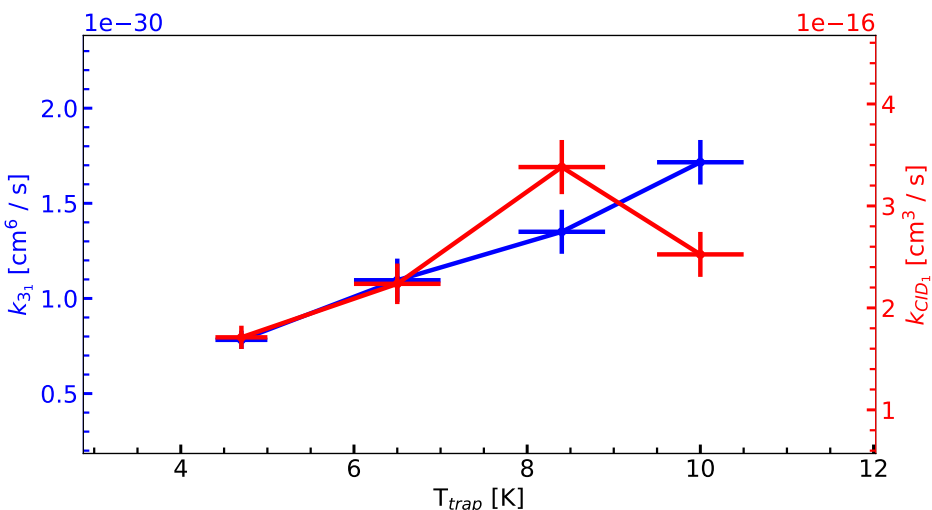


Figure 6.15.: HeN^+ formation (k_{3_i}) and dissociation (k_{CID_i}) rate constants (weighted) are plotted as a function of nominal trap temperature

Surprisingly, similar to CD^+ ion, the N^+ molecular ion also shows the same increasing trend for ternary association reaction. The measured ternary association and collision-induced dissociation rate coefficients are summarised in Table 6.5.

However, most experiments previously performed, including the study on He^+ previously discussed above are performed at temperatures > 10 K. Interestingly, Gerlich [77] again investigated the He_2^+ formation (see Eq. 6.36) using a 22-pole cryogenic ion trap but at $T_{trap} = 4$ K temperature. But unlike the experiments at > 10 K (see above), this disagrees (i.e., k_3 is lower at a lower temperature) with the relation as shown in equation 6.37.

Xie *et al.* [314] performed a quantum dynamical study for the same He_2^+ formation reaction via three-body association (Eq. 6.36). They reported that the

Table 6.5.: Formation (k_{3_1}) and dissociation (k_{CID_1}) rate constants for N^+ and CD^+ reactions with helium at different nominal trap temperature

T_{trap} [K]	k_{3_1} [cm^6s^{-1}] $\times 10^{-30}$		k_{CID_1} [cm^3s^{-1}] $\times 10^{-16}$	
	N^+	CD^+	N^+	CD^+
4.7(3)	0.80(1)	1.1(1)	1.7(1)	5.3(0.4)
6.5(5)	1.1(1)	1.4(2)	2.2(2)	15.5(1.3)
8.4(5)	1.4(1)	1.7(2)	3.4(3)	15.0(1.1)
10.0(5)	1.7(1)	-	2.5(2)	-

ternary association rate coefficient dramatically increases with temperature, i.e., $k_3(T) \propto T$, but only at temperatures below < 30 K, then they drop down after reaching a maximum value. They argued that this behaviour is because, up to a certain low temperature, the population of quantum states of ions contributing to a resonance state promoting complex formation increases with temperature, thus increasing in k_3 . This also indicates that the particular ion-neutral reaction proceeds via a two-step mechanism as discussed in Section 6.3.

In order to verify if the complex formation for HeCD^+ and HeN^+ also proceeds via a resonance state, theoretical calculations need to be performed. First quasi-classical scattering calculations cannot reproduce the observed temperature dependence (J. Perez-Rios, private communication), so full quantum scattering calculations are likely needed. The fact that both temperature curves (for N^+ and CD^+) show the same behaviour, might also indicate an experimental artefact, e.g., periodic freezing out of He to the trap walls due to the 1s duty cycle of the cryostat. In the future, we would like to repeat the He_2^+ reaction at low temperatures in our apparatus and compare the results to literature values [311, 313, 77].

6.10. CONCLUSION

We have reported a detailed systematic analysis on the ternary attachment reaction of CD^+ with He atoms.. A kinetic measurement in the presence of resonant radiation to derive a rotational-state-specific k_3 is illustrated. All together this

helps us to investigate the ROSAA signal intensity of pure rotational spectra via a numerical simulation model. A complete simulation overview of the model, i.e., function of time, number density, power and k_3 ratio is reported and analysed for the $J = 0 - 1$ rotational transition of the CD^+ molecular ion. Furthermore, reaction of the N^+ ion with helium atoms is investigated. The temperature dependence of k_3 and k_{CID} are discussed in detail for CD^+ , and N^+ reactions with He at low temperatures, i.e., $T_{trap} < 10 \text{ K}$.

7

THE ZEEMAN EFFECT IN CO⁺ OBSERVED WITH ROTATIONAL ACTION SPECTROSCOPY

This chapter is adapted from : Marimuthu, A. N.; Steenbakkers, K.; Redlich, B.; Brünken, S. Molecular Physics 2022, 120, 15 – 16, e2067089.

ABSTRACT

We discuss newly measured rotational transitions of CO⁺ ($X^2\Sigma^+$) in its vibrational ground state $v = 0$, in particular the fine-structure components of the $N = 0 - 1$ and $N = 1 - 2$ transitions. We employed a rotational action spectroscopic technique in a cryogenic ion trap for the measurements. The recorded low-temperature and high-resolution spectra of CO⁺ show resolved Zeeman splittings caused by the Earth's magnetic field. The highly accurate experimental transition frequencies and derived molecular constants agree with previous measurements and improve the spectroscopic parameters for this known interstellar molecular ion.

7.1. INTRODUCTION

Carbon monoxide, CO, is the second most abundant molecule in the interstellar medium (after H₂). In its ionic form, CO⁺, it was first detected in interstellar photo-dissociation regions (PDRs) and planetary nebulae (PNs) by Latter *et al.* [315]. Later studies confirmed the presence of CO⁺ in several other dense PDRs, PNs and reflection nebulae [316, 317, 318, 319, 320], and also in an external galaxy [321]. A search for CO⁺ in the diffuse interstellar medium has been unsuccessful so far, but the obtained upper limits on its abundance provide crucial information on the origin of CO in these regions [322].

The rotational spectrum of the CO⁺ (X²Σ⁺, $v=0$) molecular ion has been rather extensively studied previously. The pure rotational spectrum of its two lowest fine-structure components $N = 0 - 1$ was first measured by Dixon and Woods [323] by a direct absorption experiment through a CO discharge. The spectral coverage was later extended to higher frequencies by Sastry *et al.* [324] covering the $N = 1 - 2$ through $N = 3 - 4$ transitions, and Heuvel and Dymanus [325] measured the first far-infrared (supra THz) $N = 8 - 9$ transition of CO⁺. A recent study from Spezzano *et al.* [326] extended the range up to 1.3 THz (up to $N = 10 - 11$) and also provides the to date most accurate spectroscopic parameters for CO⁺ and its isotopologues based on an isotopically invariant fit.

Interestingly, so far the astronomically observed CO⁺ emission lines indicate that the rotational excitation temperatures are typically around 10 K [315], which is much lower than the surrounding PDR. This anomaly is yet to be clearly understood; Stäuber and Bruderer [327] suggested this may be due to CO⁺ being excited upon formation. On the other hand, this suggests the need of accurate laboratory measurements at low temperatures for astronomical detections of molecular ions.

7

The previous laboratory measurements of the CO⁺ molecular ion as discussed above were based on direct absorption experiments through liquid-nitrogen cooled DC glow discharges. This approach poses some challenging limitations for achieving very high spectral resolution, mainly due to the high kinetic and excitation temperatures in the discharge, leading to large Doppler linewidths and partition functions, and due to difficulties in producing the reactive ions with sufficient number density, leading to low signal-to-noise spectra. Another complication arises from background contamination from other species that are formed in the discharge. These limitations can be avoided by employing action spectroscopic methods based on sensitive mass-spectrometric techniques, which measure the change in chemical composition of ions when they interact with res-

onant radiation light. This can offer several advantages such as mass selection and storage in a cold ion-trap, which leads to uncontaminated spectra and narrow linewidths. The first realization of pure rotational action spectroscopy in a cryogenic trap was shown by Schlemmer and coworkers [100] using a direct rotational laser induced reaction (LIR) method. Further action spectroscopic techniques were later developed to generalise the scheme for a wide range of molecular ions, such as rotation-vibration double resonance - via LIR [101, 102], via predissociation [104], or via laser induced inhibition of complex growth (LIICG) [97]. Another direct method for high-resolution rotational action spectroscopy is rotational state-dependent attachment of rare gas atoms (ROSAA) [99, 3], which is used in the present study. A detailed review of these techniques was recently provided by Asvany and Schlemmer [48].

In this study, we used the ROSAA action spectroscopic method [3] to record several low N rotational transitions of CO⁺ in a 4K-cryogenic ion trap instrument. The open shell CO⁺ molecular ion in its ground electronic and vibrational state has $^2\Sigma^+$ symmetry. Each rotational quantum state N splits into two fine-structure components ($N_J = N \pm 1/2$) due to the presence of the uncoupled electron spin $S = 1/2$. The allowed transitions are $\Delta N = 1$ and $\Delta J = 0, \pm 1$. In the presence of a magnetic field each N_J levels splits further into $2J + 1$ Zeeman components, thereby lifting the angular momentum degeneracy. In fact, the CO⁺ ground state $N = 0 - 1$ rotational transition was already targeted by us using this technique in an earlier study [3]. Interestingly, only the $\Delta J = 1$, $N_J = 0_{1/2} - 1_{3/2}$ transition was observed at the time (without any observable sub-structure due to Zeeman splitting), with a signal strength ten times higher than the 3σ noise level at the position of the $\Delta J = 0$, $N_J = 0_{1/2} - 1_{1/2}$ transition. At the time it was speculated whether this non-detection is related to intrinsic quantum-mechanical state-dependent effects during the formation of the He-CO⁺ complex. This puzzling finding partly motivated the current study. In this work we present and discuss the measured high-resolution pure rotational transitions of CO⁺ ($X^2\Sigma^+$, $v = 0$), namely the $N_J=0_{1/2} - 1_{1/2}$, $0_{1/2} - 1_{3/2}$, $1_{3/2} - 2_{3/2}$ and $1_{1/2} - 2_{3/2}$ transitions. We observe clearly resolved Zeeman splittings for the $0_{1/2} - 1_{1/2}$ transition caused by the Earth's magnetic field.

7.2. EXPERIMENT

The rotational spectra of CO⁺ were recorded with a novel action spectroscopic scheme ROSAA using the FELion cryogenic 22-pole ion trap instrument. A detailed account of the FELion instrument is provided in Section 2.1 and the ROSAA technique in Section 2.3. Here we only give a brief account of details specific to

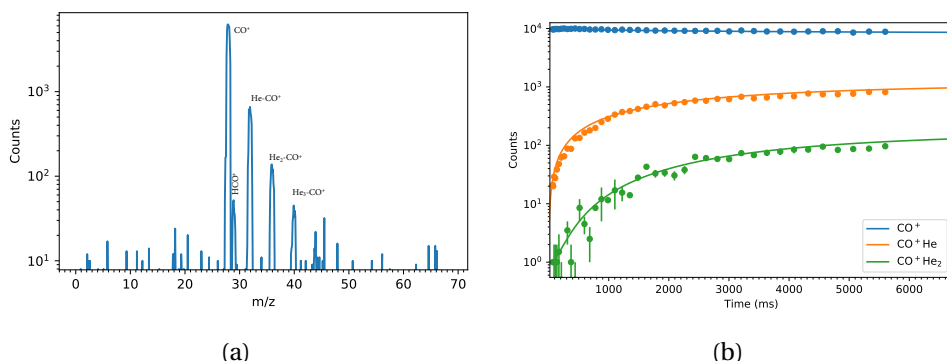
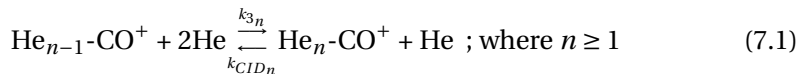


Figure 7.1.: (a): Measured mass spectrum after storing CO^+ ions (m/z 28) for ~ 600 ms in the cryogenic ion trap using He buffer gas ($\sim 4 \cdot 10^{14}$ cm $^{-3}$ number density, $T=4.7(3)$ K), showing the CO^+ ion and the subsequent formation of ion-He complexes with up to three He atoms attached. A small contamination from HCO^+ can be seen, resulting from insufficient mass-filtering of the primary ions. (b): The counts of primary and complex ions are monitored as a function of trap time ($\sim 1.5 \cdot 10^{14}$ cm $^{-3}$, $T=4.7(3)$ K). The formation (k_{3_1}) and dissociation rate (k_{CID_1}) constants as described in Eq. 7.1 are derived by numerical fitting.

the CO^+ ion.

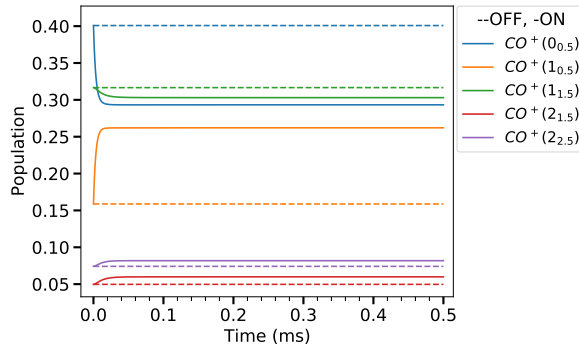
7

The ions were produced by electron impact ionization (EI, electron energy 25 eV) from neutral CO precursor. A short pulse (~ 50 ms) of mass-selected (using quadrupole mass filter) CO^+ is injected into the trap and stored for a specified time, typically ~ 600 ms for spectroscopic experiments, with continuous inflow of He buffer gas for collisional cooling and complex formation. At low temperature (around $\sim 4.7(3)$ K ambient temperature in the present experiments) and high number density $\sim 10^{14}$ cm $^{-3}$ of gas inflow, helium gas will readily attach to CO^+ by ternary association and can dissociate by collision induced dissociation (CID):



The efficient formation of complexes can be clearly seen in the mass spectrum shown in Figure 7.1a. The formed complex is mass filtered with a second quadrupole mass-filter and detected with a single ion counting Daly detector[120].

By measuring the primary CO⁺ and He-CO⁺ complex ion counts as a function of trap time, we measured the ternary association and collision induced dissociation rate coefficients as shown in Figure 7.1b. At a nominal trap temperature of $\sim 4.7(3)$ K, translating to a collisional temperature of ~ 6 K caused by the higher kinetic energy (~ 15 K) of the ions in the radio-frequency trap, we obtained $k_{31} = 1.74(1) \cdot 10^{-30}$ cm⁶s⁻¹, and $k_{CID_1} = 2.01(4) \cdot 10^{-15}$ cm³s⁻¹.



7 Figure 7.2.: CO⁺ ($X^2\Sigma^+$, $v = 0$): Numerical simulation of rotational population distribution of N_J states with (-ON) and without (-OFF) radiation for the $N_J = 0_{1/2} - 1_{1/2}$ transition. At $t=0$, the initial population is given by a Boltzmann distribution (at collisional temperature $T=6(1)$ K) and the collisional rates (with He number density $[He]=4 \cdot 10^{14}$ cm⁻³) are derived from He-CO⁺ collisional rate constants values [328]. The radiation rates (Einstein B coefficients for stimulated emission and absorption) are derived from Einstein A coefficients for spontaneous emission (PGOPHER simulation [122]).

For measuring rotational transitions of CO⁺ we employed the ROSAA technique, which utilises the change in the helium attachment rate to molecular ions depending on their internal excitation, i.e., ions with certain quantum number N_J have different attachment rate coefficients for forming He-CO⁺ clusters with Helium. The measured k_3 rate coefficient given above is actually a weighted averaged rate coefficient over the thermal population of rotational levels, i.e., the Boltzmann distribution close to the nominal trap temperature, reached by He collisions with a rate of $\sim 10^4$ s⁻¹ at the typical number densities used in the experiments. Upon resonant excitation the thermal equilibrium distribution is disturbed by competing radiative processes (typically with comparable rates of $\sim 10^5$ s⁻¹ for the CO⁺ ground state transitions), leading to a change in the attach-

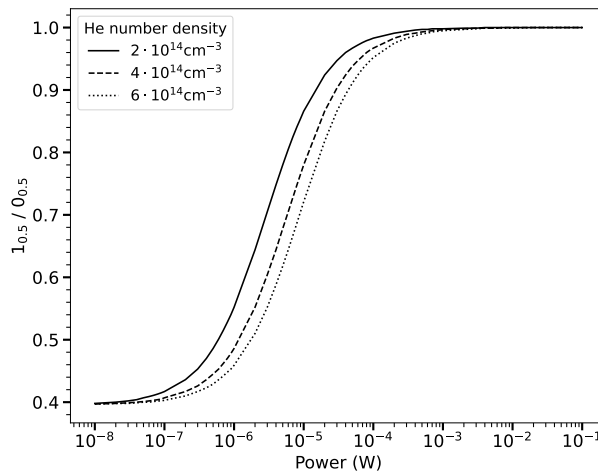


Figure 7.3.: Simulated population ratio (N_J : up/down) of the CO^+ $N_J = 0_{1/2} - 1_{1/2}$ transition as a function of excitation power, at different He number densities, after storing for 600 ms in the trap. Lower He number densities lead to saturation of the transition at lower excitation power.

ment rate and thus number of formed complexes. Hence, the measured signal intensity (S) is given as the observed change (in %) of the number of He- CO^+ complexes formed between the set frequency (I_{ON}) and a fixed reference frequency (I_{OFF} , offset about 3 GHz from scanning range), and scaled by I_{OFF} , i.e., $S = (I_{OFF} - I_{ON}) / I_{OFF}$, after storing for a fixed time of 600 ms in the trap at each data point. The spectra are measured in 10 kHz steps and are averaged over 70 iterations.

The temporal changes in rotational level population, neglecting Zeeman splitting, without and with radiation (switched on at $t = 0$) are shown exemplary for excitation of the $N''_{J''} - N'_{J'} = 0_{1/2} - 1_{1/2}$ transition and typical experimental conditions (radiation power $\sim 25 \mu\text{W}$, He number density $4 \cdot 10^{14} \text{ cm}^{-3}$) in Figure 7.2. We used collisional rate coefficients for the He- CO^+ system that were recently calculated [328] and Einstein coefficients determined using the PGopher program suite [122]. The dependence of the ratio of the upper-to-lower level population $N'_{J'}/N''_{J''} = 1_{1/2}/0_{1/2}$ on the radiation power in the trap at different He number densities is shown in Figure 7.3. The actual power of $25 \mu\text{W}$ used in the experiments to minimize power broadening is only slightly below the saturation power for the used He number density of $4 \cdot 10^{14} \text{ cm}^{-3}$. Without radiation the ra-

tio is 0.4, with a total population of $P_{tot} = (16 + 40)\% = 56\%$ in both states, given by the Boltzmann distribution. The maximum achievable population change upon radiation leads to a ratio corresponding to the statistical weight ratio of $(2J' + 1)/(2J'' + 1) = 1$, with the same total population of 56 % in both states, i.e., the percentage of molecular ions addressed directly by the applied radiation. An upper limit on the observable depletion signal can be estimated by, albeit unrealistically, assuming that all states except the excited one form complexes with the same rate, and the excited one does not form complexes at all: $S_{max} \approx 14\%$. In reality the depletion signal will be lower depending on the actual change in the attachment rate coefficient for different rotational levels, and by the Zeeman splitting of the lower state levels, leading to an equal partitioning of the overall population over the two Zeeman states. Numerical simulations for other rotational transitions are shown in the Supplementary Information.

As radiation source we used a continuous wave Signal Generator Extension (SGX) Module (VDI - Virginia Diode, Inc. WR9.0-SGX) to cover the $N_J=0_{1/2}-1_{1/2}$, $0_{1/2}-1_{3/2}$ transitions at frequencies around 117 and 118 GHz, respectively. For the $N_J=1_{1/2}-2_{3/2}$ and $1_{3/2}-2_{3/2}$ transitions we used an additional frequency doubler (WR9.0SGX + WR4.3X2) to reach approximately 235 GHz. The SGX is driven by a muwave signal generator (R&S® SMB100A) disciplined by an atomic clock (Stanford Research Systems - FS740). Intrinsic radiation linewidths are better than 1 kHz and the relative frequency accuracy is specified to be better than $1 \cdot 10^{-13}$. The radiation is directed into the trap through a 0.6 mm thick CVD diamond window (Diamond Materials GmbH) with a conical horn antenna. The maximum output power of this radiation source setup is ~ 20 mW (~ 3 mW when using the doubler), which can be regulated. Considering the geometrical aspect and distance of the trap from the source, around $\sim 5\%$ of the output is reaching the trap center. We did not attempt to compensate for the Earth magnetic field, as was done in earlier absorption measurements [329].

7

7.3. RESULTS AND DISCUSSIONS

We targeted four fine-structure lines of CO⁺, of which three were detected as shown in Figure 7.5. The signal-to-noise ratio of the $1_{3/2}-2_{3/2}$ transition is very low, thus no transition frequencies were extracted in this case. As shown in Figure 7.4, each N_J levels splits further into $2J+1$ Zeeman components in the presence of a magnetic field. The splitting energy, i.e, magnetic interaction energy (ΔE_J) of each N_J state at low magnetic-field strengths is defined as:

$$\Delta E_J = g_J \cdot M_J \cdot \mu_B \cdot B \quad (7.2)$$

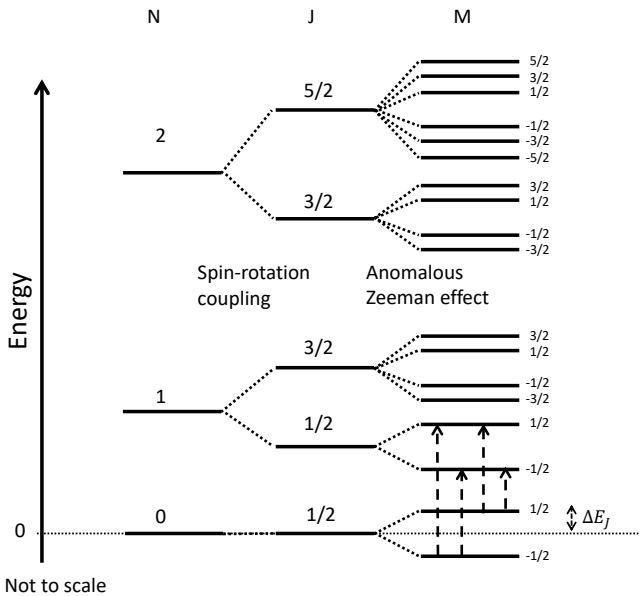
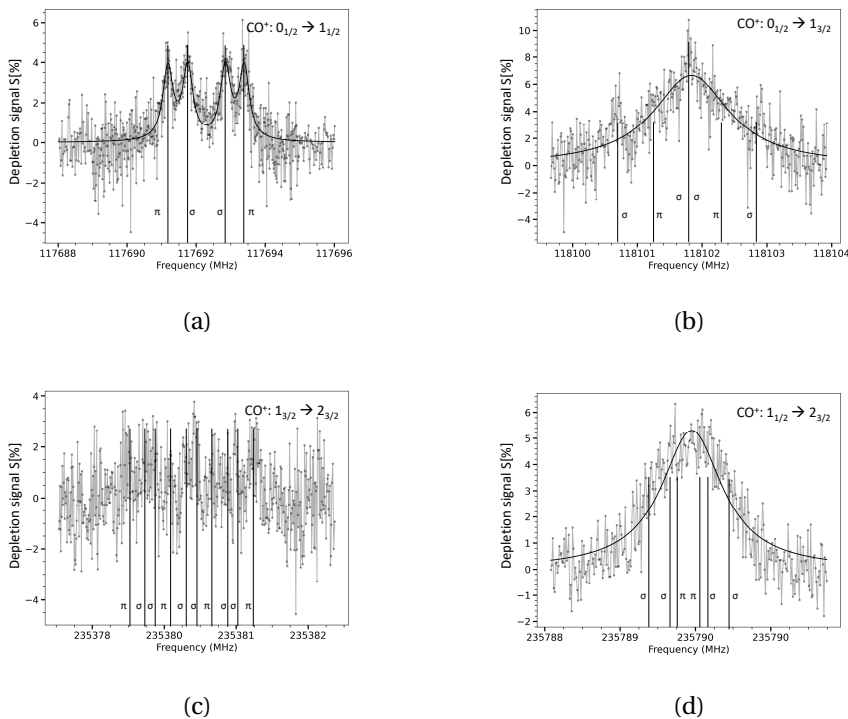


Figure 7.4.: Rotational energy level diagram for CO^+ ($X\ 2\Sigma^+$, $\nu = 0$) showing fine-structure and Zeeman splittings (not to scale). The dashed arrow lines show the expected Zeeman components of the $N_J = 0_{1/2} - 1_{1/2}$ transition. ΔE_J , the magnetic interaction energy is given by Equation 7.2.

where

$$g_J = g_S \cdot \frac{S(S+1) + J(J+1) - N(N+1)}{2J(J+1)} \quad (7.3)$$

is the effective Landé g-factor [330] for the Zeeman effect due to a weak magnetic field in the presence of net non-zero electron spin, $g_S = 2.002318$ is the electron spin g-factor, M_J is the magnetic quantum number, and μ_B and h are Bohr magneton and Planck's constants, respectively. B corresponds to the magnetic field strength, which can be derived from a fit to an effective Hamiltonian using PGOPHER [122]. The allowed transitions follow $\Delta N = 1 = \pm 1$, $\Delta J = (0, \pm 1)$ and $\Delta M = (0, \pm 1)$. From our measurements we determined the total magnetic field as $B = \sim 60(1)\ \mu\text{T}$, which closely corresponds to the total Earth magnetic field (EMF) of $\sim 49\ \mu\text{T}$ at the location Nijmegen (The Netherlands). The small difference of the measured B field from EMF is likely due to the nearby magnetic bearings of a high vacuum pump. Further, as shown in Figure 7.5a a), we see both σ ($\Delta M = \pm 1$) and π ($\Delta M = 0$) transitions of comparable strength, which



7 Figure 7.5.: Measured rotational transitions of the CO⁺ molecular ion in the presence of Earth magnetic field causing anomalous Zeeman splitting. The σ and π correspond to perpendicular ($\Delta M = \pm 1$) and parallel ($\Delta M = 0$) magnetic field, respectively, w.r.t electric field.

indicates that the magnetic field is oriented under nearly 45° relative to our vertically polarised radiation. However, due to the action spectroscopic method used, we would expect the same depletion signal for each of the Zeeman components once we saturate the transition.

Figure 7.5a shows the $N_J=0_{1/2} - 1_{1/2}$ transition with clearly resolved Zeeman splitting (see Table 7.1 for line positions). The Zeeman effect on the other two transitions $N_J = 0_{1/2} - 1_{3/2}$ and $1_{1/2} - 2_{3/2}$ could not be clearly resolved (Figure 7.5). Since we are measuring at low kinetic ion temperature $T_{ion} \approx 15$ K, we minimise the Doppler broadening (Doppler FWHM, $f_D = \sim 60$ kHz for $N_J = 0_{1/2} - 1_{1/2}$ and ~ 110 kHz for $N_J = 1_{1/2} - 2_{3/2}$, compared to values of ~ 270 and ~ 550 kHz at room temperature, for the above transitions respectively). The Doppler width

Table 7.1.: Resolved Zeeman splitting for $N_J = 0_{1/2} - 1_{1/2}$ transition
 $M'' \rightarrow M'$ Frequencies (MHz)

M''	\rightarrow	M'	Frequencies (MHz)
+1/2	→	+1/2	117691.183 (14)
-1/2	→	+1/2	117691.759 (14)
+1/2	→	-1/2	117692.849 (14)
-1/2	→	-1/2	117693.395 (14)

increases proportionally with \sqrt{T} and frequency. We could also minimise the Lorentz contribution (f_L) caused by power broadening by reducing the radiation power ($f_L = 350$ kHz for the $N_J = 0_{1/2} - 1_{3/2}$ transition corresponds to < 0.5 W/m² or 25 μ W total power inside the trap). Since the power broadening effect is dominating over Doppler, the transition frequencies are derived from the measured line profile by analytically fitting the spectra with a Lorentzian line shape (given in Table 7.2). The FWHM obtained for the resolved $J_N = 0_{1/2} - 1_{1/2}$ Zeeman components is 360(20) kHz. For this fine-structure component the actual (un-split) transition frequency was obtained from a weighted average of the four Zeeman components. For the unresolved transitions, with combined FWHM of ~ 1.4 MHz and ~ 0.8 MHz for the $J_N = 0_{1/2} - 1_{3/2}$ and $J_N = 1_{1/2} - 2_{3/2}$, respectively, a single Lorentzian line shape was used for fitting. Therefore, as a result, we can obtain accurate measurements of line frequencies with small experimental uncertainties. Compensating for the Earth magnetic field might yield even better accuracies, but was not attempted here.

The measured frequencies were fitted with an open-shell effective Hamiltonian approach using the PGOPHER program [122]. The B_0 and γ_0 constants as determined from a partial fit, i.e., just including data from this work (using D_0 fixed to that obtained from previous measurements) agree well with previous measurements (Table 7.3) [323, 324, 325, 326]. The measured transitions from this work combined with all available previous measurements (global fit), see Table 7.2, yield spectroscopic constants $B_0 = 58983.029(1)$ MHz, $\gamma_0 = 273.008(5)$ MHz and $D_0 = 189.150(12)$ kHz with reduced uncertainties compared to those obtained from previous work alone, as shown in Table 7.3. Therefore, our high-resolution narrow-linewidth measurements allow us to provide more accurate spectroscopic parameters for the CO⁺ molecular ion. The sextic centrifugal distortion parameter H_0 could not be determined ($H_0 = -2.1(3.6) \cdot 10^{-7}$ MHz) and

Table 7.2.: Rotational transition frequencies of CO⁺ ($X^2\Sigma^+$)

$N'' J''$	\rightarrow	$N' J'$	Frequencies (MHz)	$O - C$ (kHz)	Prev. work
-----------	---------------	---------	-------------------	---------------	------------

$0_{1/2}$	\rightarrow	$1_{1/2}^{**}$	117692.296 (007) *	2.5	117692.360(030) ^d
$0_{1/2}$	\rightarrow	$1_{3/2}$	118101.835 (023) *	29.3	118101.812(050) ^d
$1_{3/2}$	\rightarrow	$2_{3/2}$	235380.046 (150) ^a	2.6	
$1_{1/2}$	\rightarrow	$2_{3/2}$	235789.555 (011) *	-4.6	235789.641(030) ^b
$1_{3/2}$	\rightarrow	$2_{5/2}$	236062.553 (020) ^a	-14.7	
$2_{3/2}$	\rightarrow	$3_{5/2}$	353741.223 (030) ^b	-19.4	
$2_{5/2}$	\rightarrow	$3_{7/2}$	354014.257 (020) ^b	6.5	
$3_{5/2}$	\rightarrow	$4_{7/2}$	471679.213 (120) ^b	-96.4	
$3_{7/2}$	\rightarrow	$4_{9/2}$	471952.343 (100) ^b	25.5	
$4_{7/2}$	\rightarrow	$5_{9/2}$	589599.236 (100) ^b	28	
$4_{9/2}$	\rightarrow	$5_{11/2}$	589872.224 (100) ^b	-0.1	
$5_{9/2}$	\rightarrow	$6_{11/2}$	707496.506 (100) ^b	90.4	
$5_{11/2}$	\rightarrow	$6_{13/2}$	707769.401 (100) ^b	-27.7	
$6_{11/2}$	\rightarrow	$7_{13/2}$	825366.363 (200) ^b	-29.6	
$6_{13/2}$	\rightarrow	$7_{15/2}$	825639.665 (200) ^b	262.3	
$7_{13/2}$	\rightarrow	$8_{15/2}$	943204.603 (250) ^b	17.5	
$7_{15/2}$	\rightarrow	$8_{17/2}$	943477.836 (200) ^b	249.4	
$8_{15/2}$	\rightarrow	$9_{17/2}$	1061005.900 (1.0) ^c	-558.5	
$9_{17/2}$	\rightarrow	$10_{19/2}$	1178767.451 (200) ^b	-28.2	
$9_{19/2}$	\rightarrow	$10_{21/2}$	1179040.392 (100) ^b	-96.3	
$10_{19/2}$	\rightarrow	$11_{21/2}$	1296756.174 (100) ^b	60	
$10_{21/2}$	\rightarrow	$11_{23/2}$	1296483.005 (200) ^b	-101.9	

* this work. ** Derived from Table 7.1.

^a Sastry et. al., [324]. ^b Spezzano et. al., [326]. ^c Heuvel and Dymanus [325].

^d Bogey et. al., [329]

did not change the rotational and quartic centrifugal distortion constant within their respective error limits; it was thus not included in the fit.

In contrast to our earlier work [3], where the $N_J = 0_{1/2} - 1_{1/2}$ $\Delta J = 0$ transition was not observed down to a depletion signal $S < 1\%$, we clearly observe it here with $S \approx 5\%$ for each Zeeman component, comparable to that of individual (only

Table 7.3.: Derived molecular constants

Constants (MHz)	Partial fit ^a	Global Fit ^b	Previous work ^c
B_0	58983.030 (5)	58983.029 (1)	58983.032 (2)
γ_0	273.009 (14)	273.008 (5)	272.971 (15)
$D_0 \times 10^3$	[189.162] ^c	189.150 (12)	189.162 (15)

^a The fit includes data from this work exclusively, but uses D_0 from a fit to previous work^(c).

^b The final global fit including all available data^(a+c)

^c Constants derived from previous measurements alone [323, 324, 325, 326]

partly resolved) Zeeman transitions of the $N_J = 0_{1/2} - 1_{3/2}$ transition. The non-resolved FWHM of 1.4 MHz of the latter transition observed here is larger than the 420 kHz measured earlier, which points to a smaller Zeeman splitting in the earlier investigation (since the used radiation power and thus power broadening is comparable), and thus the depletion signal should have been even larger and detectable. In the present study, we used a lower radiation power of 25 μW compared to 80 μW used earlier, and a higher He number density of $\sim 4 \cdot 10^{14} \text{ cm}^{-3}$ compared to $\sim 2 \cdot 10^{14} \text{ cm}^{-3}$, respectively, for both $N = 0-1$ fine-structure components. Judging from Figures 7.3, demonstrating that radiative pumping is more efficient at lower He number densities (collisions acting to maintain the thermal Boltzmann population), the earlier study should have achieved a comparable population change and thus observable depletion signal for the $N_J = 0_{1/2} - 1_{1/2}$ fine-structure component. Our numerical simulations can thus not explain the earlier results. As a consequence, the earlier non-detection seems not to be related to the different change in J quantum number of the two transitions, $\Delta J = 0$ vs. $\Delta J = 1$ for the $N_J = 0_{1/2} - 1_{1/2}$ and $N_J = 0_{1/2} - 1_{3/2}$ transitions, respectively. Instead it is likely an energetic effect, i.e., molecular ions in higher-lying rotational states (the $N_J = 1_{1/2}$ and $1_{3/2}$ rotational states have a comparable rotational energy) are less likely to form stable He-ion complexes.

The around two-fold weaker signal observed for the $N_J = 1_{3/2} - 2_{3/2}$ over the $N_J = 1_{1/2} - 2_{3/2}$ transition can however easily be explained by a) the presence of ten over six magnetic Zeeman levels, respectively, leading to a dilution of the signal strength and b) the lower absorption cross-section for the $\Delta J = 0$ over the $\Delta J = 1$ transition, leading to only partial population change in the former case

when using the same radiation power of 20 μW , see Figures E.2 and E.3 (Supplementary Information) for the respective simulations).

7.4. CONCLUSIONS

In summary, we measured several fine-structure components of the two lowest rotational transitions of CO⁺ at low temperature in a cryogenic ion trap with (partly) resolved Zeeman splittings. The rotational action spectroscopic method used in this study can provide accurate transition frequencies of pure rotational transitions of this open-shell molecular ion, as was shown for closed-shell species in earlier studies [99, 107, 110, 112]. Interestingly, earlier attempts to use this method for open-shell systems had failed [73, 331]. Including the new rotational data to a global dataset and fitting to an effective Hamiltonian including spin-rotation provides accurate spectroscopic parameters for CO⁺ in its vibrational ground state, important data for its astronomical observation.

The work presented here is also vital for our understanding of the state-dependent action spectroscopic method (ROSAA) applied to systems with uncoupled electron spin and non-degenerate Zeeman transitions. Our results show that the change in ternary rate attachment for different rotational fine-structure states in CO⁺ is mainly due to energetic effects. A qualitative discussion on the observed signal intensities was provided on the example of the $N_J = 0_{1/2} - 1_{1/2}$ and $N_J = 1_{3/2} - 2_{3/2}$ transitions, paving the way for a more elaborate study to extract rotational and fine-structure state-dependent ternary attachments rate coefficients of rare gas atoms to CO⁺. The overall attachment rate with and without resonant excitation is a weighted averaged value over all quantum states involved. Since several rotational and fine-structure states are populated initially even at the low temperatures used in the experiments, and rotational excitation resonant on one transition influences the population of neighbouring levels, see Figure 7.2, this would involve measurements of additional higher-lying rotational transitions. This might be possible by heating the ion trap to higher temperatures, and using other more strongly bound rare gas atoms, e.g., neon or argon, for complex formation.

APPENDICES

A

CHAPTER 3

A

A.1. INTERNAL COORDINATES OF C-C₃H₃⁺**A.1.1. FC-CCSD(T)/ANO0**

```

X
X 1 rd
C 2 r1 1 a90
C 2 r1 1 a90 3 d120
C 2 r1 1 a90 4 d120
H 2 r2 1 a90 3 d0
H 2 r2 1 a90 4 d0
H 2 r2 1 a90 5 d0

rd    =      1.000000613972272
r1    =      0.795954871089489
a90   =      90.000000000000000
d120  =      120.000000000000043
r2    =      1.882733950537102
d0    =      0.000000000000000

```

A.1.2. FC-CCSD(T)/ANO1

```

X
X 1 rd
C 2 r1 1 a90
C 2 r1 1 a90 3 d120
C 2 r1 1 a90 4 d120
H 2 r2 1 a90 3 d0
H 2 r2 1 a90 4 d0
H 2 r2 1 a90 5 d0

rd    =      1.000000409314806
r1    =      0.789085470855492
a90   =      90.000000000000000
d120  =      120.000000000000014
r2    =      1.869030138645467
d0    =      0.000000000000000

```

A.1.3. FC-CCSD(T)/ANO2

```

X
X 1 rd

```

C 2 r1 1 a90
 C 2 r1 1 a90 3 d120
 C 2 r1 1 a90 4 d120
 H 2 r2 1 a90 3 d0
 H 2 r2 1 a90 4 d0
 H 2 r2 1 a90 5 d0

rd = 1.000000613972272
 r1 = 0.787249651644386
 a90 = 90.0000000000000000
 d120 = 119.99999999999986
 r2 = 1.866721530420376
 d0 = 0.0000000000000000

A.2. INTERNAL COORDINATES OF H₂C₃H⁺

A.2.1. FC-CCSD(T)/ANO0

H
 C 1 r1
 X 2 rd 1 a90
 C 2 r2 3 a90 1 d180
 X 4 rd 2 a90 3 d0
 C 4 r3 5 a90 2 d180
 H 6 r4 4 a1 5 d0
 H 6 r4 4 a1 5 d180

r1 = 1.081884877618416
 rd = 1.000000409314806
 a90 = 90.0000000000000000
 r2 = 1.246343011416748
 d180 = 180.0000000000000000
 d0 = 0.0000000000000000
 r3 = 1.361798271600899
 r4 = 1.094590581296569
 a1 = 120.284642603942274

A.2.2. FC-CCSD(T)/ANO1

H
 C 1 r1
 X 2 rd 1 a90

A

```
C 2 r2 3 a90 1 d180
X 4 rd 2 a90 3 d0
C 4 r3 5 a90 2 d180
H 6 r4 4 a1* 5 d0
H 6 r4 4 a1* 5 d180
```

```
r1      =      1.074705266639338
rd     =      1.000000204657382
a90    =      90.000000000000000
r2      =      1.234261558515133
d180   =      180.000000000000000
d0      =      0.000000000000000
r3      =      1.351397370372584
r4      =      1.088292080166718
a1      =      120.373581553220575
```

A.2.3. FC-CCSD(T)/ANO2

```
H
C 1 r1
X 2 rd 1 a90
C 2 r2 3 a90 1 d180
X 4 rd 2 a90 3 d0
C 4 r3 5 a90 2 d180
H 6 r4 4 a1* 5 d0
H 6 r4 4 a1* 5 d180
```

```
r1      =      1.074153711426225
rd     =      1.000000409314806
a90    =      90.000000000000000
r2      =      1.231322876212024
d180   =      180.000000000000000
d0      =      0.000000000000000
r3      =      1.349557181907095
r4      =      1.087405908293182
a1      =      120.356533501538024
```

Table A.1.: Vibrational wavenumbers and IR intensities of c-C₃H₃⁺ (cm⁻¹ and km/mol, respectively).

Mode	Harm. ^a	Anharm. ^a	Harm. ^b	Anharm. ^c	Int. ^a
$\nu_1(a'_1)$	3325	3194	3310	3179	0
$\nu_2(a'_1)$	1629	1596	1642	1610	0
$\nu_3(a'_2)$	1028	1004	1048	1024	0
$\nu_4(e')$	3276	3142	3260	3127	189
$\nu_5(e')$	1301	1266	1318	1284	88
$\nu_6(e')$	940	920	944	925	60
$\nu_7(a''_2)$	763	754	764	754	69
$\nu_8(e'')$	1007	989	1017	1000	0

^a fc-CCSD(T)/ANO0. IR intensity obtained via VPT2.

^b fc-CCSD(T)/ANO2

^c From fc-CCSD(T)/ANO2 harmonic wavenumbers and fc-CCSD(T)/ANO0 anharmonic corrections.

Table A.2.: Vibrational wavenumbers and IR intensities of c-C₃D₃⁺ (cm⁻¹ and km/mol, respectively); CCSD(T)/ANO1 anharmonic force field.

Mode	Harm. ^a	Anharm. ^a	Harm. ^b	Anharm. ^c	Int. ^a
$\nu_1(a'_1)$	2552	2475	2552	2474	0
$\nu_2(a'_1)$	1501	1472	1507	1478	0
$\nu_3(a'_2)$	845	831	852	838	0
$\nu_4(e')$	2420	2341	2419	2340	64
$\nu_5(e')$	1266	1236	1273	1244	66
$\nu_6(e')$	684	673	684	673	28
$\nu_7(a''_2)$	561	556	561	556	29
$\nu_8(e'')$	823	813	827	817	0

^a fc-CCSD(T)/ANO1. IR intensity obtained via VPT2.

^b fc-CCSD(T)/ANO2

^c From fc-CCSD(T)/ANO2 harmonic wavenumbers and fc-CCSD(T)/ANO1 anharmonic corrections.

A

Table A.3.: Vibrational wavenumbers and IR intensities of c-C₃D₃⁺ (cm⁻¹ and km/mol, respectively); CCSD(T)/ANO0 anharmonic force field.

Mode	Harm. ^a	Anharm. ^a	Harm. ^b	Anharm. ^c	Int. ^a
$\nu_1(a'_1)$	2560	2481	2552	2473	0
$\nu_2(a'_1)$	1497	1466	1507	1477	0
$\nu_3(a'_2)$	835	818	852	835	0
$\nu_4(e')$	2430	2346	2419	2336	52
$\nu_5(e')$	1256	1225	1273	1243	62
$\nu_6(e')$	681	670	684	672	26
$\nu_7(a''_2)$	560	554	561	555	27
$\nu_8(e'')$	818	806	827	815	0

^a fc-CCSD(T)/ANO0. IR intensity obtained via VPT2.

^b fc-CCSD(T)/ANO2

^c From fc-CCSD(T)/ANO2 harmonic wavenumbers and fc-CCSD(T)/ANO0 anharmonic corrections.

Table A.4.: Vibrational wavenumbers and IR intensities of H₂C₃H⁺ (cm⁻¹ and km/mol, respectively); CCSD(T)/ANO1 anharmonic force field.

Mode	Harm. ^a	Anharm. ^a	Harm. ^b	Anharm. ^c	Int. ^a
$\nu_1(a_1)$	3365	3233	3362	3230	103
$\nu_2(a_1)$	3119	2998	3118	2997	26
$\nu_3(a_1)$	2123	2077	2123	2078	348
$\nu_4(a_1)$	1477	1442	1480	1444	13
$\nu_5(a_1)$	1131	1106	1133	1109	2
$\nu_6(b_1)$	1125	1104	1120	1100	13
$\nu_7(b_1)$	877	873	878	875	8
$\nu_8(b_1)$	259	266	256	263	27
$\nu_9(b_2)$	3227	3086	3228	3087	37
$\nu_{10}(b_2)$	1037	1015	1037	1016	2
$\nu_{11}(b_2)$	619	612	624	618	59
$\nu_{12}(b_2)$	286	296	289	299	15

^a fc-CCSD(T)/ANO1. IR intensity obtained via VPT2.

^b fc-CCSD(T)/ANO2

^c From fc-CCSD(T)/ANO2 harmonic wavenumbers and fc-CCSD(T)/ANO1 anharmonic corrections.

Table A.5.: Vibrational wavenumbers and IR intensities of H₂C₃H⁺ (cm⁻¹ and km/mol, respectively); CCSD(T)/ANO0 anharmonic force field.

Mode	Harm. ^a	Anharm. ^a	Harm. ^b	Anharm. ^c	Int. ^a
$\nu_1(a_1)$	3372	3239	3362	3229	104
$\nu_2(a_1)$	3131	3005	3118	2992	24
$\nu_3(a_1)$	2118	2070	2123	2076	325
$\nu_4(a_1)$	1473	1437	1480	1443	12
$\nu_5(a_1)$	1124	1121	1133	1130	7
$\nu_6(b_1)$	1112	1091	1120	1100	11
$\nu_7(b_1)$	865	858	878	872	7
$\nu_8(b_1)$	249	257	256	264	26
$\nu_9(b_2)$	3250	3103	3228	3082	37
$\nu_{10}(b_2)$	1034	1012	1037	1015	2
$\nu_{11}(b_2)$	598	587	624	612	57
$\nu_{12}(b_2)$	267	276	289	298	13

^a fc-CCSD(T)/ANO0. IR intensity obtained via VPT2.

^b fc-CCSD(T)/ANO2

^c From fc-CCSD(T)/ANO2 harmonic wavenumbers and fc-CCSD(T)/ANO0 anharmonic corrections.

A

Table A.6.: Vibrational wavenumbers and IR intensities of $\text{D}_2\text{C}_3\text{D}^+$ (cm^{-1} and km/mol , respectively).

Mode	Harm. ^a	Anharm. ^a	Harm. ^b	Anharm. ^c	Int. ^a
$\nu_1(a_1)$	2609	2531	2605	2527	0
$\nu_2(a_1)$	2288	2210	2278	2200	2
$\nu_3(a_1)$	1987	1949	1990	1951	329
$\nu_4(a_1)$	1209	1192	1218	1201	0.02
$\nu_5(a_1)$	949	942	953	946	12
$\nu_6(b_1)$	887	874	895	882	1
$\nu_7(b_1)$	693	688	706	700	0.3
$\nu_8(b_1)$	225	228	230	233	16
$\nu_9(b_2)$	2424	2341	2408	2324	13
$\nu_{10}(b_2)$	830	817	835	822	4
$\nu_{11}(b_2)$	457	447	481	471	22
$\nu_{12}(b_2)$	241	245	257	262	9

^a fc-CCSD(T)/ANO0. IR intensity obtained via VPT2.

^b fc-CCSD(T)/ANO2

^c From fc-CCSD(T)/ANO2 harmonic wavenumbers and fc-CCSD(T)/ANO0 anharmonic corrections.

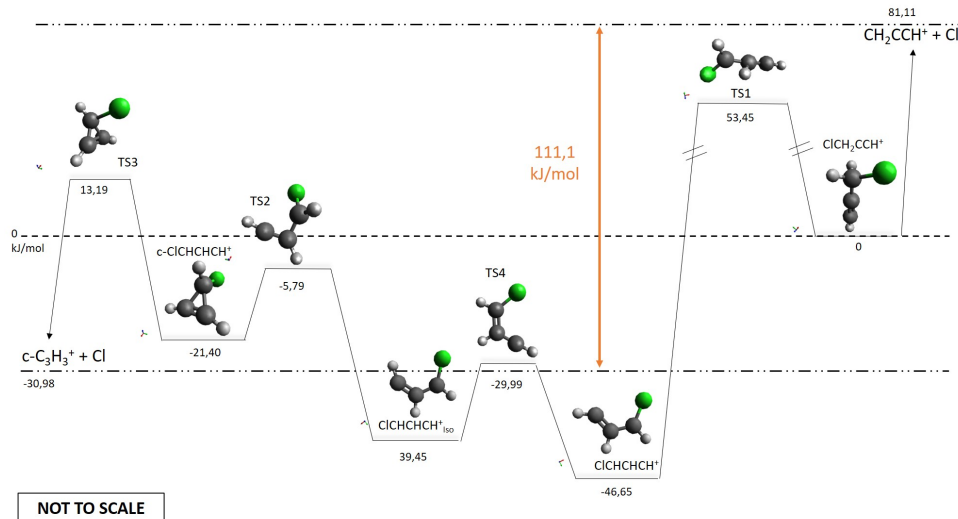


Figure A.1.: Potential energy pathway for c-C₃H₃⁺ and H₂C₃H⁺ formation from ionization of propargyl chloride (ClCH₂CCH). The calculations are done at the CCSD(T)/cc-pVTZ level with zero-point energy corrections from MP2/cc-pVTZ level. The ClCH₂CCH⁺ ion (propargyl chloride cation, relative energy arbitrarily set to 0 ~kJ/mol) can undergo hydrogen migration to the linear ClCHCHCH⁺ ion ($E_{\text{rel}} = -46.56 \sim \text{kJ/mol}$) via transition state TS1 ($E_{\text{rel}} = 53.45 \sim \text{kJ/mol}$). This isomer can then convert to ClCHCHCH⁺ (iso) ($E_{\text{rel}} = -30.98 \sim \text{kJ/mol}$) via TS4 ($E_{\text{rel}} = -39.45 \sim \text{kJ/mol}$). The latter species can subsequently cyclise via a submerged transition state TS2 ($E_{\text{rel}} = -5.79 \sim \text{kJ/mol}$) to the cyclic c-ClCHCHCH⁺ ($E_{\text{rel}} = -21.40 \sim \text{kJ/mol}$). This means that the highest barrier for the isomerisation of ClCH₂CCH⁺ to c-ClCHCHCH⁺ is 53.45~kJ/mol, i.e. only 0.55~eV. Also the dissociation energy barrier to c-C₃H₃⁺ and Cl ($E_{\text{rel}} = -29.99 \sim \text{kJ/mol}$) is only at 13.19~kJ/mol (TS3).

B

CHAPTER 4

B.1. INTERNAL COORDINATES OF CH₃CNH⁺

B.1.1. FC-CCSD(T)/ANO0

B

```
H
C 1 r1
C 2 r2 1 a1
X 3 rd 2 a90 1 d0
N 3 r3 4 a90 2 d180
X 5 rd 3 a90 4 d0
H 5 r4 6 a90 3 d180
H 2 r1 3 a1 1 d120
H 2 r1 3 a1 8 d120
```

```
r1      =      1.097234034575213
r2      =      1.461586511773973
a1      =      108.354029317585457
rd      =      1.000000409314806
a90     =      89.999999999999972
d0      =      0.000000000000000
r3      =      1.153699023716097
d180    =      180.000000000000000
r4      =      1.013272030286403
d120    =      120.000000000000114
```

B.1.2. FC-CCSD(T)/ANO1

```
H
C 1 r1
C 2 r2 1 a1
X 3 rd 2 a90 1 d0
N 3 r3 4 a90 2 d180
X 5 rd 3 a90 4 d0
H 5 r4 6 a90 3 d180
H 2 r1 3 a1 1 d120
H 2 r1 3 a1 8 d120
```

```
r1      =      1.091588568955683
r2      =      1.450334012198720
```

```

a1      =      108.507798899076860
rd      =      1.000000613972271
a90     =      89.999999999999986
d0      =      0.000000000000000
r3      =      1.145583771122200
d180    =      180.000000000000000
r4      =      1.008294043229717
d120    =      119.99999999999972

```

B.1.3. FC-CCSD(T)/ANO2

```

H
C 1 r1
C 2 r2 1 a1
X 3 rd 2 a90 1 d0
N 3 r3 4 a90 2 d180
X 5 rd 3 a90 4 d0
H 5 r4 6 a90 3 d180
H 2 r1 3 a1 1 d120
H 2 r1 3 a1 8 d120

```

```

r1      =      1.090663342780039
r2      =      1.448609574844010
a1      =      108.480759568085148
rd      =      1.000001227944922
a90     =      90.000000000000028
d0      =      0.000000000000000
r3      =      1.142864353443497
d180    =      180.000000000000000
r4      =      1.008334309784723
d120    =      120.000000000000327

```

B.1.4. FC-CCSD(T)/cc-PVDZ

```

H
C 1 r1
C 2 r2 1 a1

```

B

```
X 3 rd 2 a90 1 d0
N 3 r3 4 a90 2 d180
X 5 rd 3 a90 4 d0
H 5 r4 6 a90 3 d180
H 2 r1 3 a1 1 d120
H 2 r1 3 a1 8 d120
```

```
r1 = 1.104421287381395
r2 = 1.467855029147642
a1 = 108.258731223153745
rd = 1.000000409314806
a90 = 89.999999999999957
d0 = 0.000000000000000
r3 = 1.160263599078930
d180 = 180.000000000000000
r4 = 1.020376191984162
d120 = 120.000000000000171
```

B.1.5. FC-CCSD(T)/CC-PVTZ

```
H
C 1 r1
C 2 r2 1 a1
X 3 rd 2 a90 1 d0
N 3 r3 4 a90 2 d180
X 5 rd 3 a90 4 d0
H 5 r4 6 a90 3 d180
H 2 r1 3 a1 1 d120
H 2 r1 3 a1 8 d120
```

```
r1 = 1.091362895166567
r2 = 1.453075807535473
a1 = 108.438787022956490
rd = 1.000000204657382
a90 = 89.999999999999986
d0 = 0.000000000000000
r3 = 1.146078556823367
d180 = 180.000000000000000
r4 = 1.009021121407080
```

d120 = 120.0000000000000099

B.1.6. AE-CCSD(T)/CC-PWCV5Z

B

```

H
N 1 r1*
X 2 rd 1 a90
C 2 r2* 3 a90 1 d180
X 4 rd 2 a90 3 d0
C 4 r3* 5 a90 2 d180
H 6 r4* 4 a1* 5 d0
H 6 r4* 4 a1* 7 d120
H 6 r4* 4 a1* 8 d120

r1      =      1.0073314907
rd      =      1.0
a90     =      90.0
r2      =      1.1399556988
d180    =      180.0000000000000000
d0      =      0.0000000000000000
r3      =      1.4440897526
r4      =      1.0887809197
a1      =      108.5586585536
d120    =      120.0

```

B.2. INTERNAL COORDINATES OF CH₃CNH⁺ -NE

B.2.1. FC-CCSD(T)/ANO0

```

H
C 1 r1
C 2 r2 1 a1
X 3 rd 2 a90 1 d0
N 3 r3 4 a90 2 d180
X 5 rd 3 a90 4 d0
H 5 r4 6 a90 3 d180
H 2 r1 3 a1 1 d120
H 2 r1 3 a1 8 d120

```

X 7 rd 5 a90 6 d0
 NE 7 r5 10 a90 5 d180

B

```
r1      =      1.097234259132258
r2      =      1.461586810898442
a1      =      108.354029317585457
rd      =      1.000000613972271
a90     =      89.999999999999972
d0      =      0.000000000000000
r3      =      1.153699259829119
d180    =      180.000000000000000
r4      =      1.013272237660004
d120    =      119.999999999999758
r5      =      2.117272059249112
```

B.2.2. FC-CCSD(T)/CC-PVDZ

```
H
C 1 r1
C 2 r2 1 a1
X 3 rd 2 a90 1 d0
N 3 r3 4 a90 2 d180
X 5 rd 3 a90 4 d0
H 5 r4 6 a90 3 d180
H 2 r1 3 a1 1 d120
H 2 r1 3 a1 8 d120
X 7 rd 5 a90 6 d0
NE 7 r5 10 a90 5 d180
```

```
r1      =      1.097234483689349
r2      =      1.461587110022973
a1      =      108.354029317585457
rd      =      1.000000818629779
a90     =      89.999999999999972
d0      =      0.000000000000000
r3      =      1.153699495942189
d180    =      180.000000000000000
r4      =      1.013272445033648
d120    =      119.999999999999758
```

r5 = 1.990534530346215

Table B.1.: Computed fc-CCSD(T) vibrational frequencies (in cm^{-1}) using ANO basis sets for CH_3CNH^+ .

mode	sym C_{3v}	exp. ^a	harmonic ^b			anharmonic (VPT2) ^b	
			ANO0	ANO1	ANO2	ANO0	ANO1
ν_{10}	E	385	374 (-11)	381 (-4)	382 (-3)	376 (-9)	384 (-1)
ν_9	E	596	581 (-15)	580 (-16)	585 (-11)	570 (-26)	579 (-17)
ν_5	A ₁	898	889 (-9)	897 (-1)	900 (2)	878 (-20)	887 (-11)
ν_8	E	1026	1051 (25)	1048 (22)	1050 (24)	1025 (-1)	1023 (-3)
ν_4	A ₁	1364	1395 (31)	1393 (29)	1398 (34)	1358 (-6)	1358 (-6)
ν_7	E	1421	1444 (23)	1442 (21)	1447 (26)	1422 (1)	1428 (7)
ν_3	A ₁	2307	2336 (29)	2345 (38)	2350 (43)	2290 (-17)	2300 (-7)
ν_2	A ₁	2924	3060 (136)	3049 (125)	3051 (127)	2934 (10)	2927 (3)
ν_6	E	2996	3174 (178)	3149 (153)	3152 (156)	3019 (23)	2999 (3)
ν_1	A ₁	nc	3688 (-)	3699 (-)	3687 (-)	3528 (-)	3534 (-)

^a This work, Ne-IRPD experiment.^b Shift from Ne-IRPD experiment is given in parenthesis.

Table B.2.: Computed harmonic CCSD(T) vibrational frequencies (in cm⁻¹) using Dunning's basis sets for CH₃CNH⁺.

mode	sym.	exp. ^a	cc-pVDZ ^b	cc-pVTZ ^b
ν_{10}	E	385	362 (-23)	380 (-5)
ν_9	E	596	564 (-32)	586 (-10)
ν_5	A ₁	898	893 (-5)	895 (-3)
ν_8	E	1026	1042 (15)	1052 (25)
ν_4	A ₁	1364	1381 (16)	1398 (34)
ν_7	E	1421	1433 (12)	1450 (29)
ν_3	A ₁	2307	2331 (24)	2343 (36)
ν_2	A ₁	2924	3066 (142)	3052 (128)
ν_6	E	2996	3181 (185)	3151 (154)
ν_1	A ₁	nc	3663 (-)	3684 (-)

^a This work, Ne-IRPD experiment.

^b Shift from Ne-IRPD experiment is given in parenthesis.

Table B.3.: Computed harmonic CCSD(T) vibrational frequencies (in cm^{-1}) comparing both CH_3CNH^+ (bare ion) and $\text{CH}_3\text{CNH}^+ \text{-Ne}$ (complex) using ANO0 and cc-pVDZ basis sets.

B

mode	sym. C_{3v}	exp. ^a	ANO0 ^b		cc-pVDZ ^b	
			CH_3CNH^+	$\text{CH}_3\text{CNH}^+ \text{-Ne}$	CH_3CNH^+	$\text{CH}_3\text{CNH}^+ \text{-Ne}$
$\nu_{\text{Ne-bend}}$	E			32		26
$\nu_{\text{Ne-str.}}$	A ₁			68		102
ν_{10}	E	385	374 (-11)	375 (-10)	362 (-23)	322 (-63)
ν_9	E	596	581 (-15)	599 (3)	564 (-32)	551 (-45)
ν_5	A ₁	898	889 (-9)	890 (-8)	893 (-5)	913 (15)
ν_8	E	1026	1051 (25)	1052 (26)	1042 (15)	1024 (-2)
ν_4	A ₁	1364	1395 (31)	1395 (31)	1381 (16)	1370 (6)
ν_7	E	1421	1444 (23)	1445 (24)	1433 (12)	1425 (4)
ν_3	A ₁	2307	2336 (29)	2336 (29)	2331 (24)	2380 (73)
ν_2	A ₁	2924	3060 (136)	3060 (136)	3066 (142)	3129 (205)
ν_6	E	2996	3174 (178)	3173 (177)	3181 (185)	3247 (251)
ν_1	A ₁	nc	3688 (-)	3679 (-)	3663 (-)	3730 (-)

^a This work, Ne-IRPD experiment.

^b Shift from Ne-IRPD experiment is given in parenthesis.

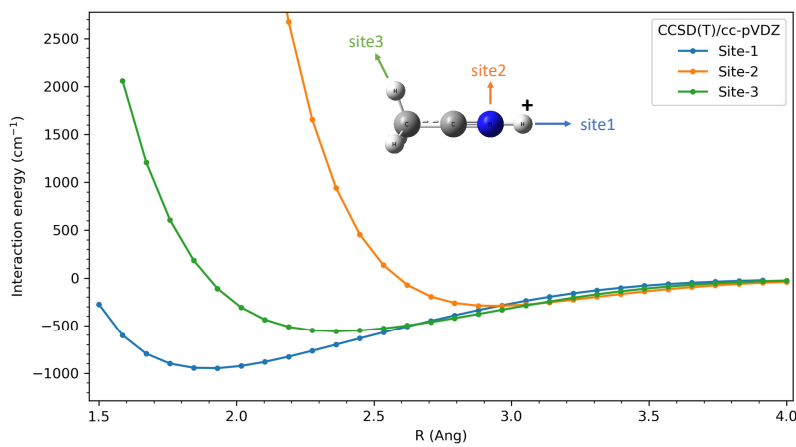


Figure B.1.: Computed potential energy surface as a function of Ne distance R for CH_3CNH^+ -Ne from various sites neon atom placed.

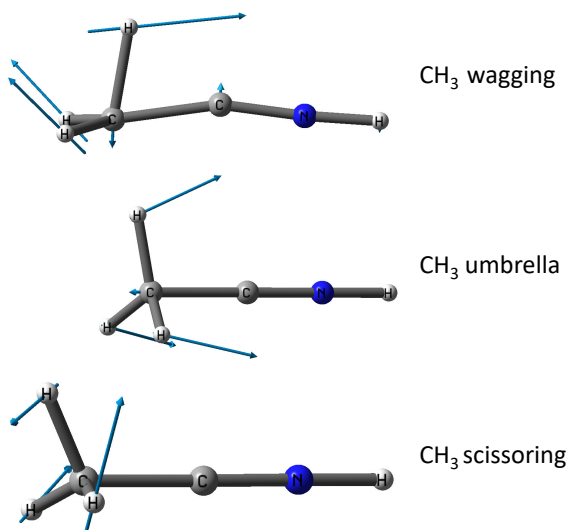
B

Figure B.2.: Vibrational displacement vectors for CH_3 modes.

Table B.4.: Calculated spectroscopic parameters of CH₃CNH⁺ at the CCSD(T)/ANO2 level of theory. Rotational constants B_e , B_0 , $\Delta B_0 = 1/2\sum \alpha_i^B$ (ΔA_0 analogous), and α_i^A and α_i^B . All values are in MHz.

A_e	A_0	ΔA_0	B_e	B_0	ΔB_0
156213.5	154336.7	1876.8	8659.2	8541.5	27.8
<hr/>					
mode		α_i^A	α_i^B	q_i	
ν_{10}	CCN bend	91.3	-20.2	14.8	
ν_9	CNH bend	31.1	-8.3	8.9	
ν_5	CC stretch	251	50.6		
ν_8	CH ₃ wagging	-883	-0.09	3.6	
ν_4	CH ₃ umbrella	-912	68.0		
ν_7	CH ₃ scissoring	902	-37.7	60.2	
ν_3	CN stretch	103	44.0		
ν_2	CH ₃ sym. stretch	1645	2.2		
ν_6	CH ₃ asym. stretch	1204	0.99	0.634	
ν_1	NH stretch	-23.4	21.5		

C

CHAPTER 5

Table C.1.: Observed band centers and intensities in the IRPD spectrum of HC_3N^+ tagged with Ne obtained from fitting Gaussian functions to the experimental data in both relative depletion and power normalized intensity units (see main text). The frequency error is dominated by the calibration method using either a grating spectrometer (FEL) or a wavemeter (OPO).

Freq. (cm^{-1}) ^a	Freq. err. (cm^{-1})	Norm. Int. (rel.u) ^b	Norm. Int. err. (rel.u) ^b
189	2	1.6 ^c	-
200	3	1.6 ^c	-
208	3	1.6 ^c	-
231	2	1.4 ^c	-
238	1	3.4	0.5
384	1	0.9	0.3
439	1	12.1	0.3
454	1	9.9	0.3
489	1	2.5	0.3
552	2	0.6	0.2
572	2	0.7	0.2
626	1	13.2	0.5
631	1	5.7	0.4
688	1	15.4	0.2
704	1	5.0	0.2
846	1	4.9	0.2
926	1	0.6	0.2
957	1	2.2	0.2
981	2	0.5	0.2
1097	1	0.2	0.2
1243	1	1.1	0.3
1253	1	1.0	0.5
1331	1	0.6	0.3
1595	1	1.1	0.2

^a Taken from Gaussian fit of relative depletion spectrum (not power normalized).

^b Taken from Gaussian fit of power normalized spectrum.

^c Estimated from power normalized spectrum: fitting was problematic in the power normalized spectrum in this region due to the high noise level as a result of the relatively low power.

Table C.1 – continued from previous page

Freq. (cm⁻¹)^a	Freq. err. (cm⁻¹)	Norm. Int. (rel.u)^b	Norm. Int. err. (rel.u)^b
1845	1	35.9	0.2
2171	1	8.8	0.2
3174.0	1	5.4	0.4
3182.9	0.5	16	2
3184.7	0.5	19	2
3185.7	0.5	22	1
3191.9	0.5	20	4
3195.2	0.5	28	3

^a Taken from Gaussian fit of relative depletion spectrum (not power normalized).

^b Taken from Gaussian fit of power normalized spectrum.

^c Estimated from power normalized spectrum: fitting was problematic in the power normalized spectrum in this region due to the high noise level as a result of the relatively low power.

C

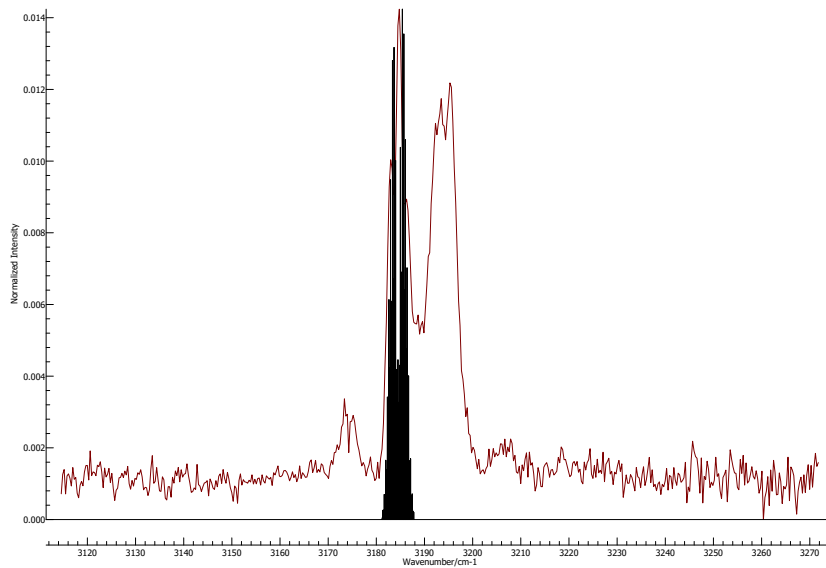


Figure C.1.: IRPD spectrum of the HC_3N^+ ion tagged with Ne in the range $3120\text{-}3260\text{ cm}^{-1}$ recorded with an OPO (red) overlayed with a prediction of the ν_1 ro-vibrational structure using the PGOPHER program package [122] (black, $T=20\text{ K}$ and $B = 0.033\text{ cm}^{-1}$, calculated at RCCSD(T)/cc-PVTZ level of theory).

Table C.2.: Calculated frequencies and intensities based on *ab initio* parameters of Dai *et al.* [4] together with the assigned P and K quantum numbers and the population in the ν_5 , ν_6 and ν_7 bending modes

Freq (cm^{-1})	Rel. (a.u.)	Int	K	P	pop ν_5	pop ν_6	pop ν_7	pop tot
190.77	0.0423		0	0.5	0.02	0.01	0.99	1.02
195.46	0.0443		2	2.5	0.01	0.01	1.01	1.03
237.33	0.132		0	0.5	0.02	0.02	0.98	1.02
238.17	0		2	1.5	0.02	0.01	1.01	1.04
382.26	0		1	0.5	0.02	0.02	1.98	2.02
383.77	0		1	1.5	0.02	0.01	2	2.03
431.86	0		1	1.5	0.03	0.04	1.96	2.03

continued on next page

Table C.2 – continued from previous page

Freq (cm ⁻¹)	Rel. (a.u.)	Int	K	P	pop <i>v</i> ₅	pop <i>v</i> ₆	pop <i>v</i> ₇	pop tot
434.43	0		1	0.5	0.03	0.02	1.98	2.03
446.02	0.0727		0	0.5	0.04	0.97	0.02	1.03
457.8	0.081		2	2.5	0.01	1.01	0.01	1.03
496.53	0.3849		0	0.5	0.17	0.83	0.02	1.02
500.45	0.0084		2	1.5	0.02	1.01	0.01	1.04
573.56	0.0051		0	0.5	0.02	0.02	2.99	3.03
574.26	0.0004		2	1.5	0.02	0.02	2.97	3.01
576.7	0.0046		2	2.5	0.02	0.02	3	3.04
626.58	0.0088		2	2.5	0.04	0.05	2.94	3.03
629.6	0.7167		0	0.5	0.84	0.17	0.02	1.03
630.58	0.0514		0	0.5	0.04	0.04	2.94	3.02
631.05	0		2	1.5	0.03	0.03	2.98	3.04
639.03	0		1	0.5	0.04	0.97	1.01	2.02
640.54	0		1	1.5	0.03	0.99	1.01	2.03
649.84	0		1	1.5	0.03	0.99	1	2.02
688.74	0		1	0.5	0.05	1	0.98	2.03
694.18	0		1	1.5	0.16	0.85	1.01	2.02
696.79	0		1	0.5	0.14	0.87	1.02	2.03
697.87	1		2	2.5	1.03	0.01	0.01	1.05
739.89	0		2	1.5	1.04	0.01	0.01	1.06
823.55	0		1	1.5	0.85	0.18	0.99	2.02
824.04	0		1	0.5	0.85	0.17	1	2.02
830.01	0.0027		0	0.5	0.03	1	2	3.03
832.29	0.0006		2	1.5	0.04	0.98	2	3.02
833.64	0.003		2	2.5	0.03	1	2.01	3.04
840.86	0.0132		0	0.5	0.04	1	1.99	3.03
847.01	0.0105		2	2.5	0.04	0.98	2.02	3.04
875.36	0.5467		0	0.5	0.93	0.09	0.14	1.16
880.22	0.1438		0	0.5	0.11	0.98	1.81	2.9
883.97	0		2	1.5	0.05	1.01	1.99	3.05
887.72	0		1	1.5	0.94	0.22	0.89	2.05
891.73	0		2	2.5	0.15	0.87	2	3.02
895.48	0.0012		0	0.5	0.15	0.87	2.01	3.03
895.59	0		1	0.5	0.06	1.93	0.03	2.02
895.62	0		2	1.5	0.14	0.86	2.03	3.03
897.55	0		1	1.5	0.13	1.78	0.12	2.03

continued on next page

Table C.2 – continued from previous page

Freq (cm ⁻¹)	Rel. (a.u.)	Int	K	P	pop <i>v</i> ₅	pop <i>v</i> ₆	pop <i>v</i> ₇	pop tot
927.01	0		1	0.5	1	0.14	0.9	2.04
952.36	0		1	1.5	0.26	1.72	0.05	2.03
959.59	0		1	0.5	0.26	1.67	0.11	2.04
1016.86	0.0031		0	0.5	0.86	0.17	1.99	3.02
1017.8	0.0044		2	2.5	0.87	0.18	1.99	3.04
1018.63	0		2	1.5	0.86	0.17	2	3.03
1065.54	0		1	1.5	0.94	0.17	1.06	2.17
1069.42	0		1	0.5	0.96	0.09	1.05	2.1
1077.95	0.003		0	0.5	0.85	0.43	1.76	3.04
1083.01	0.0032		2	2.5	0.98	0.14	1.94	3.06
1088.09	0.0052		0	0.5	0.23	1.6	1.2	3.03
1089.7	0		2	1.5	0.06	1.94	1.02	3.02
1090.94	0.0013		2	2.5	0.09	1.87	1.07	3.03
1094.39	0		1	0.5	0.77	1.17	0.23	2.17
1097.24	0		1	1.5	0.79	1.22	0.02	2.03
1097.4	0.0045		0	0.5	0.08	1.89	1.06	3.03
1104.7	0.0025		2	2.5	0.04	2	1	3.04
1116.79	0.0025		0	0.5	1	0.18	1.86	3.04
1121.83	0		2	1.5	1.02	0.12	1.93	3.07
1142.98	0		2	1.5	0.05	2.03	0.97	3.05
1144.64	0		1	1.5	1.14	0.79	0.11	2.04
1150.29	0.0057		0	0.5	0.25	1.7	1.08	3.03
1151.33	0.0037		2	2.5	0.25	1.74	1.04	3.03
1157.74	0		2	1.5	0.23	1.73	1.09	3.05
1158.66	0.0013		0	0.5	0.25	1.71	1.08	3.04
1171.57	0		1	0.5	1.26	0.73	0.06	2.05
1256.75	0.0037		2	2.5	0.96	0.21	1.99	3.16
1259.34	0.0012		0	0.5	0.98	0.18	1.93	3.09
1263.41	0		2	1.5	0.98	0.11	2	3.09
1270.56	0		1	1.5	1.72	0.29	0.05	2.06
1285.89	0.0004		0	0.5	0.83	1.2	1	3.03
1287.75	0		1	0.5	1.62	0.39	0.04	2.05
1287.92	0		2	1.5	0.82	1.19	1.05	3.06
1289.36	0.0027		2	2.5	0.81	1.23	0.99	3.03
1291.39	0.0008		0	0.5	0.82	1.21	1.02	3.05
1337.46	0.0064		0	0.5	0.83	1.39	0.81	3.03

continued on next page

Table C.2 – continued from previous page

C

Freq (cm ⁻¹)	Rel. (a.u.)	Int	K	P	pop <i>v</i> ₅	pop <i>v</i> ₆	pop <i>v</i> ₇	pop tot
1339.32	0.0013	2		2.5	0.9	1.3	0.85	3.05
1344.8	0.005	0		0.5	0.38	2.31	0.34	3.03
1346.92	0		2	1.5	0.07	2.91	0.05	3.03
1346.99	0.0033		2	2.5	1.02	0.97	1.06	3.05
1349.2	0.0001		2	2.5	0.28	2.48	0.27	3.03
1350.4	0		1	0.5	1.11	0.91	0.03	2.05
1353.66	0		1	1.5	1.09	0.93	0.09	2.11
1366.31	0.0014		0	0.5	1.18	0.84	1.02	3.04
1370.89	0		2	1.5	1.23	0.74	1.09	3.06
1377.57	0		2	1.5	1.02	1.15	0.89	3.06
1409.08	0.0012		2	2.5	0.32	2.64	0.07	3.03
1415.93	0.0003		0	0.5	0.36	2.59	0.09	3.04
1420.3	0		2	1.5	0.3	2.61	0.14	3.05
1464.62	0.001		0	0.5	1.58	0.38	1.35	3.31
1467.83	0.0003		2	2.5	1.41	0.53	1.56	3.5
1483.97	0		2	1.5	1.42	0.6	1.34	3.36
1485.88	0.0017		0	0.5	1.61	0.44	1.03	3.08
1529.41	0.0009		0	0.5	1.13	1.2	0.76	3.09
1539.79	0.0013		0	0.5	1.11	1.1	0.89	3.1
1539.97	0.0015		2	2.5	1.1	1.09	0.97	3.16
1542.3	0		2	1.5	1.11	0.98	0.99	3.08
1558.24	0		2	1.5	0.76	2.16	0.24	3.16
1562.27	0.0015		2	2.5	0.8	2.16	0.07	3.03
1562.55	0.0019		0	0.5	0.8	2.01	0.26	3.07
1578.58	0.0026		2	2.5	2	0.13	0.94	3.07
1596.91	0		0	0.5	1.17	1.62	0.26	3.05
1606.17	0.0019		2	2.5	1.18	1.69	0.19	3.06
1612.81	0		2	1.5	1.89	0.45	0.74	3.08
1615.51	0.0014		0	0.5	1.33	1.59	0.13	3.05

Table C.3.: Same as Table C.2, but calculated based on fitted spectroscopic parameters of the IRPD spectrum, all given in cm^{-1} : $\omega_5 = 699$, $g_{55} = 115$, $g_{56} = -50$, $\omega_6 = 455$, $g_{66} = -23$, $g_{57} = -34.72$, $\omega_7 = 198$, $g_{77} = -14$, $g_{67} = 15$, $A_{SO} = -44$.

Freq (cm^{-1})	Rel. (a.u.)	Int	K	P	pop ν_5	pop ν_6	pop ν_7	pop tot
190.26	0.0399	0	0.5	0.01	0.01	1	1.02	
195.14	0.0138	2	2.5	0.01	0	1.01	1.02	
238.09	0.0399	2	1.5	0.01	0	1.01	1.02	
240.07	0.1296	0	0.5	0.02	0.01	0.99	1.02	
381.43	0	1	0.5	0.02	0.01	1.99	2.02	
382.02	0	1	1.5	0.01	0.01	2	2.02	
436.77	0	1	1.5	0.03	0.02	1.97	2.02	
437.94	0	1	0.5	0.03	0.01	1.99	2.03	
439.59	0.0727	0	0.5	0.03	0.98	0.01	1.02	
452.45	0.0789	2	2.5	0.01	1.01	0	1.02	
490.94	0.3548	0	0.5	0.14	0.86	0.01	1.01	
495.41	0.0099	2	1.5	0.01	1.01	0.01	1.03	
570.88	0.0068	0	0.5	0.02	0.01	3	3.03	
573.24	0	2	1.5	0.02	0.01	2.99	3.02	
573.91	0.0061	2	2.5	0.02	0.01	3	3.03	
626.7	0.7345	0	0.5	0.87	0.14	0.01	1.02	
631.6	0	1	0.5	0.03	0.98	1	2.01	
632.92	0	1	1.5	0.03	0.99	1.01	2.03	
633.33	0.0127	2	2.5	0.04	0.02	2.96	3.02	
635.16	0	2	1.5	0.03	0.01	2.99	3.03	
636.84	0.0192	0	0.5	0.04	0.02	2.97	3.03	
645.02	0	1	1.5	0.03	0.99	1	2.02	
684.3	0	1	0.5	0.08	0.93	1.01	2.02	
686.69	1	2	2.5	1.03	0.01	0.01	1.05	
689.14	0	1	1.5	0.13	0.88	1	2.01	
692.86	0	1	0.5	0.08	0.95	0.99	2.02	
729.03	0	2	1.5	1.03	0.01	0.01	1.05	
821.32	0	1	1.5	0.88	0.14	1.01	2.03	
821.47	0	1	0.5	0.87	0.14	1.01	2.02	
821.75	0.0037	0	0.5	0.03	0.99	2	3.02	
824.05	0.0008	2	1.5	0.04	0.98	2	3.02	
825.56	0.0012	2	2.5	0.03	0.99	2.01	3.03	

continued on next page

Table C.3 – continued from previous page

Freq (cm⁻¹)	Rel. (a.u.)	Int	K	P	pop <i>v</i>₅	pop <i>v</i>₆	pop <i>v</i>₇	pop tot
836.16	0.0387	0	0.5	0.04	0.99	1.98	3.01	
840.33	0.0083	2	2.5	0.03	0.98	2.01	3.02	
846.54	0.5631	0	0.5	0.98	0.03	0.02	1.03	
878.37	0	1	1.5	0.98	0.12	0.94	2.04	
879.26	0	2	1.5	0.08	0.94	2.02	3.04	
880.88	0.0163	0	0.5	0.06	0.99	1.97	3.02	
882.64	0	1	0.5	0.05	1.95	0.01	2.01	
885.21	0	1	1.5	0.08	1.88	0.06	2.02	
886.98	0.0014	2	2.5	0.13	0.9	1.99	3.02	
890.93	0	2	1.5	0.08	0.95	2	3.03	
891.72	0.0052	0	0.5	0.11	0.92	1.99	3.02	
918.98	0	1	0.5	1.03	0.06	0.96	2.05	
940.47	0	1	1.5	0.22	1.78	0.02	2.02	
946.85	0	1	0.5	0.2	1.78	0.05	2.03	
1014.15	0.0036	0	0.5	0.88	0.14	2.01	3.03	
1016.01	0.0042	2	2.5	0.88	0.14	2.01	3.03	
1016.35	0	2	1.5	0.88	0.13	2.01	3.02	
1040.55	0	1	1.5	1	0.05	0.98	2.03	
1042.23	0	1	0.5	0.98	0.04	1.02	2.04	
1069.81	0.0049	0	0.5	0.78	0.53	1.72	3.03	
1073.23	0.0022	2	2.5	1	0.07	1.97	3.04	
1074.13	0.0037	0	0.5	0.29	1.48	1.25	3.02	
1075.53	0	2	1.5	0.05	1.96	1.01	3.02	
1077.85	0.0007	2	2.5	0.06	1.92	1.04	3.02	
1083.16	0	1	0.5	0.83	1.17	0.04	2.04	
1083.64	0.0033	0	0.5	0.06	1.93	1.03	3.02	
1085.87	0	1	1.5	0.82	1.19	0.02	2.03	
1096.72	0.0019	2	2.5	0.03	2	1	3.03	
1110.16	0.0025	0	0.5	1.03	0.08	1.93	3.04	
1113.19	0	2	1.5	1.03	0.05	1.98	3.06	
1126.29	0	1	1.5	1.11	0.87	0.05	2.03	
1135.28	0.0037	0	0.5	0.21	1.78	1.04	3.03	
1136.8	0	2	1.5	0.07	1.95	1.01	3.03	
1139.19	0.0018	2	2.5	0.21	1.79	1.02	3.02	
1145.99	0	2	1.5	0.15	1.87	1.02	3.04	
1146.25	0.0013	0	0.5	0.2	1.79	1.03	3.02	

continued on next page

Table C.3 – continued from previous page

Freq (cm ⁻¹)	Rel. (a.u.)	Int	K	P	pop <i>v</i> ₅	pop <i>v</i> ₆	pop <i>v</i> ₇	pop tot
1157.14	0		1	0.5	1.22	0.79	0.03	2.04
1234.44	0.0038		2	2.5	1.01	0.08	1.95	3.04
1236.07	0.0006		0	0.5	1	0.08	1.95	3.03
1237.54	0		2	1.5	0.98	0.06	2.02	3.06
1256.04	0		1	1.5	1.65	0.36	0.02	2.03
1271.64	0		1	0.5	1.54	0.46	0.02	2.02
1275.18	0.0008		0	0.5	0.83	1.17	1.07	3.07
1277.29	0		2	1.5	0.8	1.15	1.18	3.13
1279.09	0.0011		2	2.5	0.84	1.18	1.02	3.04
1281.57	0.0002		0	0.5	0.85	1.16	1.01	3.02
1319.08	0		1	0.5	1.22	0.8	0.07	2.09
1319.78	0.0043		0	0.5	0.92	1.23	0.87	3.02
1322.17	0		1	1.5	1.23	0.79	0.02	2.04
1322.77	0.0015		2	2.5	1.05	0.98	1.02	3.05
1325.64	0.0032		0	0.5	0.23	2.6	0.2	3.03
1327.4	0		2	1.5	0.07	2.93	0.02	3.02
1328.4	0.0025		2	2.5	0.86	1.36	0.82	3.04
1331.24	0.0014		2	2.5	0.27	2.51	0.24	3.02
1351.38	0.0005		0	0.5	1.19	0.84	1.01	3.04
1353.43	0		2	1.5	1.2	0.8	1.05	3.05
1367.33	0		2	1.5	1.03	1.08	0.94	3.05
1390.86	0.0009		2	2.5	0.28	2.71	0.04	3.03
1397.54	0.0005		0	0.5	0.32	2.57	0.23	3.12
1401.23	0		2	1.5	0.24	2.72	0.08	3.04
1449.53	0.0014		0	0.5	1.66	0.35	1.05	3.06
1453.17	0.0008		2	2.5	1.62	0.38	1.06	3.06
1468.25	0		2	1.5	1.56	0.45	1.02	3.03
1471.2	0.0014		0	0.5	1.43	0.6	1.11	3.14
1508.58	0.0002		0	0.5	1.28	0.85	0.94	3.07
1512.92	0		2	1.5	1.21	0.83	1.06	3.1
1514.27	0.0011		2	2.5	1.24	0.83	0.98	3.05
1514.62	0.002		0	0.5	1.23	0.84	1	3.07
1538.77	0.0016		0	0.5	0.81	2.15	0.07	3.03
1538.92	0		2	1.5	0.82	2.18	0.04	3.04
1542.34	0.0011		2	2.5	0.82	2.18	0.07	3.07
1558.55	0.002		2	2.5	2.03	0.06	0.97	3.06

continued on next page

Table C.3 – continued from previous page

C

Freq (cm⁻¹)	Rel. (a.u.)	Int	K	P	pop <i>v</i>₅	pop <i>v</i>₆	pop <i>v</i>₇	pop tot
1569.7	0		0	0.5	1.14	1.78	0.12	3.04
1581.14	0.0014		2	2.5	1.12	1.84	0.08	3.04
1589.09	0		1	0.5	1.48	0.81	0.37	2.66
1592.68	0		1	0.5	0.74	1.93	0.84	3.51
1593.52	0		1	1.5	1.9	0.16	0.08	2.14
1596.32	0		2	1.5	1.93	0.26	0.94	3.13
1611.11	0		2	1.5	1.33	1.55	0.17	3.05

Table C.4.: Comparison between the derived band center frequencies of the PFI-ZEKE work [4] and those obtained in our work.

Obs IRPD	Obs ZEKE	Assignment
189*	190*	$7^1\mu\Sigma$
200*	190*	$7^1\Delta_{5/2}$
...	236*	$7^1\Delta_{3/2}$
238*	236*	$7^1\kappa\Sigma$
384*	380*	$7^2\Pi_{1/2}$
...	380*	$7^2\Pi_{1/2}$
439*	438*	$6^1\mu\Sigma$
454*	...	$7^3\Delta_{5/2}$
490*	488*	$6^1\kappa\Sigma$
572	...	$7^3\mu\Sigma$
626*	628*	$5^1\mu\Sigma$
630*	...	$7^3\Delta_{5/2}$
688*	683*	$5^1\Delta_{5/2}$
...	727*	$5^1\Delta_{3/2}$
...	817*	$5^17^1\Pi_{3/2}$
...	817*	$5^17^1\Pi_{1/2}$
...	833	$6^17^2\Sigma$
846*	873*	$5^1\kappa\Sigma$
957	920	ν_4 stretch
1097*	...	$6^27^1\Delta_{5/2}$
1243	1262*	$5^2\Pi_{3/2}?$
1253	1262	$5^2\Pi_{3/2}?$
...	1322	$5^16^17^1\Sigma?$
1331*	...	$6^3\mu\Sigma$
...	1414	$6^3\Delta_{5/2}?$
...	1460	$5^16^17^1\Sigma?$
...	1586	$5^16^2\Sigma?$
1595	...	$5^2\Pi_{3/2}$

¹ Tentatively assigned bands are marked with ?.

² Bands that were included in the respective fits are marked with a *.

D

CHAPTER 6

D.1. CD⁺+ HE RATE COEFFICIENTS

Table D.1.: Derived attachment and dissociation rate coefficients (k_3 & k_{CID}) and rates (R_3 & R_{CID}), for CD⁺ molecular ion collision with helium buffer gas at $2.2 \cdot 10^{14} \text{ cm}^{-3}$ number density. The rates are given for up to two complexes, i.e., HeCD⁺ and He₂CD⁺.

	k_3 [cm ³ /s]	R_3 [s ⁻¹]	k_{CID} [cm ⁶ /s]	R_{CID} [s ⁻¹]
HeCD ⁺	$1.1 \cdot 10^{-30}$	0.053	$5.9 \cdot 10^{-16}$	0.130
He ₂ CD ⁺	$3.6 \cdot 10^{-30}$	0.174	$1.2 \cdot 10^{-15}$	0.264

D

Table D.2.: Derived collisional rates at $T = 7 \text{ K}$ (derived from [304]), CD⁺ collision with He [$2.2 \cdot 10^{14} \text{ cm}^{-3}$ number density] for an initial $|i\rangle$ state transitions into final $|j\rangle$ state via k_{ij} rate coefficients [in cm³/s] and R_{ij} rate [in s⁻¹].

i	j	k_{ij}	R_{ij}
0	→	1	$9.9 \cdot 10^{-11}$ $2.2 \cdot 10^4$
0	→	2	$6.3 \cdot 10^{-11}$ $1.4 \cdot 10^4$
1	→	2	$1.6 \cdot 10^{-10}$ $3.4 \cdot 10^4$
0	→	3	$4.3 \cdot 10^{-11}$ $9.4 \cdot 10^3$
1	→	3	$6.1 \cdot 10^{-11}$ $1.3 \cdot 10^4$
2	→	3	$1.5 \cdot 10^{-10}$ $3.2 \cdot 10^4$
0	→	4	$5.5 \cdot 10^{-12}$ $1.2 \cdot 10^3$
1	→	4	$5.8 \cdot 10^{-11}$ $1.3 \cdot 10^4$
2	→	4	$8.7 \cdot 10^{-11}$ $1.9 \cdot 10^4$
3	→	4	$1.3 \cdot 10^{-10}$ $2.9 \cdot 10^4$
0	→	5	$1.4 \cdot 10^{-11}$ $3.1 \cdot 10^3$
1	→	5	$2.0 \cdot 10^{-11}$ $4.4 \cdot 10^3$
2	→	5	$5.7 \cdot 10^{-11}$ $1.3 \cdot 10^4$
3	→	5	$1.0 \cdot 10^{-10}$ $2.3 \cdot 10^4$
4	→	5	$1.2 \cdot 10^{-10}$ $2.7 \cdot 10^4$
1	→	0	$1.3 \cdot 10^{-11}$ $2.9 \cdot 10^3$
2	→	0	$2.8 \cdot 10^{-14}$ $6.2 \cdot 10^0$

2	→	1	$5.2 \cdot 10^{-13}$	$1.1 \cdot 10^2$
3	→	0	$2.4 \cdot 10^{-18}$	$5.2 \cdot 10^{-4}$
3	→	1	$2.5 \cdot 10^{-17}$	$5.6 \cdot 10^{-3}$
3	→	2	$1.8 \cdot 10^{-14}$	$4.1 \cdot 10^0$
4	→	0	$1.6 \cdot 10^{-24}$	$3.5 \cdot 10^{-10}$
4	→	1	$1.3 \cdot 10^{-22}$	$2.8 \cdot 10^{-8}$
4	→	2	$5.7 \cdot 10^{-20}$	$1.3 \cdot 10^{-5}$
4	→	3	$6.8 \cdot 10^{-16}$	$1.5 \cdot 10^{-1}$
5	→	0	$9.4 \cdot 10^{-31}$	$2.1 \cdot 10^{-16}$
5	→	1	$9.9 \cdot 10^{-30}$	$2.2 \cdot 10^{-15}$
5	→	2	$8.4 \cdot 10^{-27}$	$1.8 \cdot 10^{-12}$
5	→	3	$1.2 \cdot 10^{-22}$	$2.7 \cdot 10^{-8}$
5	→	4	$2.8 \cdot 10^{-17}$	$6.1 \cdot 10^{-3}$

Table D.3.: Derived radiative rates at $P=3.5 \cdot 10^{-5}$ W, for an initial $|i\rangle$ state transitions into final $|j\rangle$ state with A_{ij} spontaneous emission, B_{ij} stimulated absorption and B_{ji} stimulated emission. The spontaneous emission rates are derived from the effective Hamiltonian fitting of CD⁺ ion using the Pgopher program [122]. Subsequently, the stimulated emissions are computed from spontaneous emission rates (see Section 2.3.5.3). All A_{ij} , B_{ij} and B_{ji} are in units of s⁻¹.

i	j	A_{ij}	B_{ij}	B_{ji}
1	0	$3.6 \cdot 10^{-4}$	$2.5 \cdot 10^4$	$7.4 \cdot 10^4$
2	1	$3.5 \cdot 10^{-3}$	$3.0 \cdot 10^4$	$4.9 \cdot 10^4$
3	2	$1.3 \cdot 10^{-2}$	$3.2 \cdot 10^4$	$4.4 \cdot 10^4$
4	3	$3.1 \cdot 10^{-2}$	$3.3 \cdot 10^4$	$4.2 \cdot 10^4$
5	4	$6.1 \cdot 10^{-2}$	$3.4 \cdot 10^4$	$4.1 \cdot 10^4$

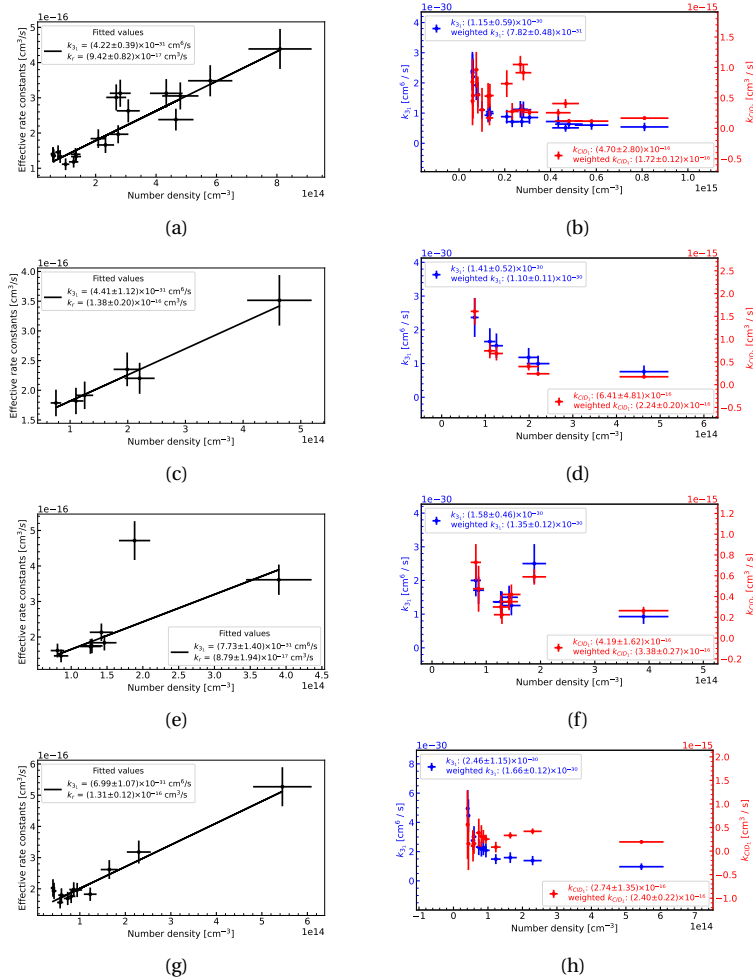


Figure D.1.: $\text{N}^+ + \text{He}$ reaction rate constants at (a)&(b) $\Rightarrow 4.8(3)$ K, (c)&(d) $\Rightarrow 6.5(3)$ K, (e)&(f) $\Rightarrow 8.4(3)$ K and (g)&(h) $\Rightarrow 10.0(4)$ K: The ternary association (k_{31}) and collision-induced dissociation (k_{CID_1}) rate constants are plotted as a function of helium number density. (a, c, e, g) - represents: Effective binary rate constants are plotted as a function of number density to derive k_{31} (ternary association) and k_r (radiative) rate coefficients. The solid line indicates the linear fit where the slope and intercept correspond to k_3 and k_r , respectively. (b, d, f, h) corresponds to formation rate without k_r , the weighted average values are shown in the legend box (see Section 6.6).

E

CHAPTER 7

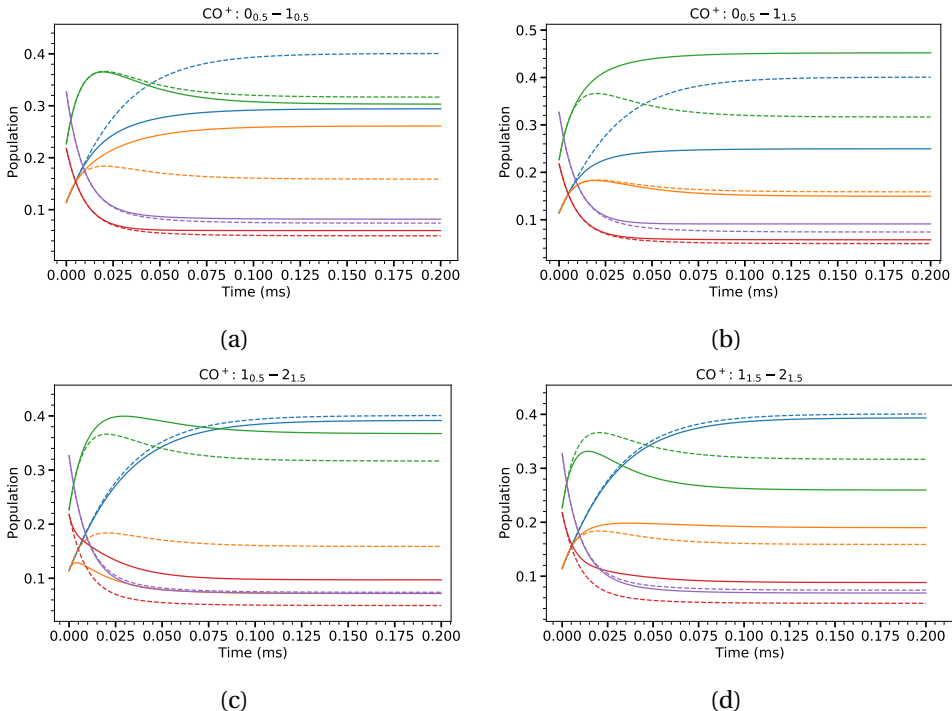


Figure E.1.: Numerical simulations of the rotational state population distribution of N_J states with (solid line) and without (dashed line) radiation upon excitation of the transitions indicated in the title of each figure. The color code represents N_J states as follows: $\text{CO}^+ (0_{0.5})$, $\text{CO}^+ (1_{0.5})$, $\text{CO}^+ (1_{1.5})$, $\text{CO}^+ (2_{1.5})$ and $\text{CO}^+ (2_{2.5})$. At $t=0$, the initial population is given by the Boltzmann distribution at $T=300$ K which undergoes collisional cooling to reach collisional temperature $T=6(1)$ K. The collisional rates are computed from collisional rate constants and He number density $[\text{He}] \sim 4 \cdot 10^{14} \text{ cm}^{-3}$. The radiative rates (Einstein B coefficients for stimulated emission and absorption) are derived from Einstein A coefficients for spontaneous emission (PGOPHER simulation) with radiation power for (a) & (b) $25\mu\text{W}$ and (c) & (d) $20\mu\text{W}$.

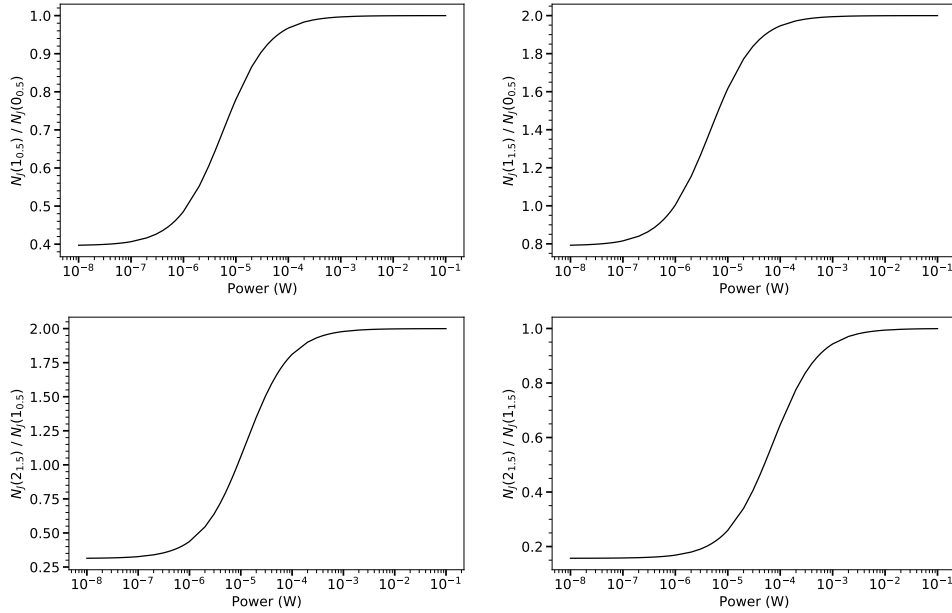


Figure E.2.: Simulated population ratio (N_J : up/down) of CO⁺ fine-structure transitions as a function of continuous excitation power on the respective transition after storing for 600ms in the trap with a constant He number density of [He]~ $4 \cdot 10^{14}$ cm⁻³.

E

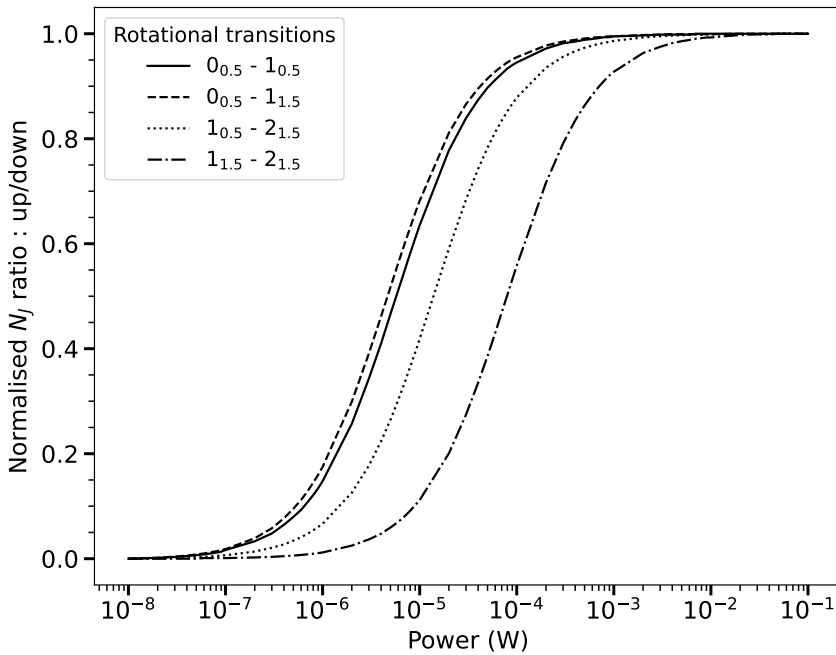


Figure E.3.: Comparison of the normalized simulated population ratio (N_j : up/down) of the respective CO^+ fine-structure transitions as a function of continuous excitation power on the respective transition after storing for 600ms in a trap with a constant He number density of $[\text{He}] \sim 4 \cdot 10^{14} \text{ cm}^{-3}$. Transitions with higher transition strength reach saturation at lower excitation power.

BIBLIOGRAPHY

- [1] J. v. Fraunhofer, Denkschriften der Münch. Akademie der Wissenschaften **5**, 193 (1817).
- [2] B. J. McCall, Proceedings of the International Astronomical Union **1**, 165–174 (2005). doi:[10.1017/S1743921306007162](https://doi.org/10.1017/S1743921306007162)
- [3] S. Brünken, L. Kluge, A. Stoffels, J. Pérez-Ríos, and S. Schlemmer, Journal of Molecular Spectroscopy **332**, 67–78 (2017). doi:[10.1016/j.jms.2016.10.018](https://doi.org/10.1016/j.jms.2016.10.018)
- [4] Z. Dai, W. Sun, J. Wang, and Y. Mo, J. Chem. Phys. **143**, 054301 (2015). doi:[10.1063/1.4927005](https://doi.org/10.1063/1.4927005)
- [5] F. W. Bessel, Monthly Notices of the Royal Astronomical Society **4**, 152–161 (1838). doi:[10.1093/mnras/4.17.152](https://doi.org/10.1093/mnras/4.17.152)
- [6] T. Henderson, Memoirs of the Royal Astronomical Society **11**, 61 (1840).
- [7] F. G. W. Struve, *Stellarum duplicitum et multiplicitum mensurae micrometricae per magnum fraunhoferi tubum annis a 1824 ad 1837 in specula dorpatensi institutae...* (1, 1837).
- [8] M. J. Reid and K. M. Menten, Astronomische Nachrichten **341**, 860–869 (2020). doi:[10.1002/asna.202013833](https://doi.org/10.1002/asna.202013833)
- [9] I. Newton, American Journal of Physics **61**, 108–112 (1993). doi:[10.1119/1.17323](https://doi.org/10.1119/1.17323)
- [10] G. Kirchhoff and R. Bunsen, Annalen der Physik und der Chemie **110**, 161–189 (1860).
- [11] J. Harju, M. Juvela, S. Schlemmer, L. K. Haikala, K. Lehtinen, and K. Mattila, Astronomy & Astrophysics **482**, 535–539 (2008). doi:[10.1051/0004-6361:20079259](https://doi.org/10.1051/0004-6361:20079259)
- [12] A. S. Eddington, Proceedings of the Royal Society of London. Series A, Containing Papers of a Mathematical and Physical Character **111**, 424–456 (1926). doi:[10.1098/rspa.1926.0076](https://doi.org/10.1098/rspa.1926.0076)
- [13] J. Hartmann, The Astrophysical Journal **19**, 268–286 (1904). doi:[10.1086/141112](https://doi.org/10.1086/141112)

- [14] M. L. Heger, Lick Observatory Bulletin **326**, 59–63 (1919). doi:[10.5479/ADS/bib/1919LicOB.10.59H](https://doi.org/10.5479/ADS/bib/1919LicOB.10.59H)
- [15] J. S. Plaskett, Monthly Notices of the Royal Astronomical Society **84**, 80–93 (1923). doi:[10.1093/mnras/84.2.80](https://doi.org/10.1093/mnras/84.2.80)
- [16] P. W. Merrill, Publications of the Astronomical Society of the Pacific **46**, 206 (1934). doi:[10.1086/124460](https://doi.org/10.1086/124460)
- [17] H. N. Russell, Monthly Notices of the Royal Astronomical Society **95**, 610–636 (1935). doi:[10.1093/mnras/95.8.610](https://doi.org/10.1093/mnras/95.8.610)
- [18] P. W. Merrill, The Astrophysical Journal **83**, 126 (1936). doi:[10.1086/143707](https://doi.org/10.1086/143707)
- [19] E. K. Campbell, M. Holz, D. Gerlich, and J. P. Maier, Nature **523**, 322–323 (2015). doi:[10.1038/nature14566](https://doi.org/10.1038/nature14566)
- [20] T. Dunham Jr, Publications of the Astronomical Society of the Pacific **49**, 26 (1937). doi:[10.1086/124759](https://doi.org/10.1086/124759)
- [21] W. S. Adams, *Quoted in "dunham, t., publ. astron. soc. pac. 49, 26–8 (1937)" unpublished* (1937).
- [22] A. McKellar, Publications of the Astronomical Society of the Pacific **52**, 187–192 (1940).
- [23] A. McKellar, Publications of the Astronomical Society of the Pacific **52**, 312 (1940). doi:[10.1086/125205](https://doi.org/10.1086/125205)
- [24] F. A. Jenkins and D. E. Wooldridge, Physical Review **53**, 137–140 (1938). doi:[10.1103/PhysRev.53.137](https://doi.org/10.1103/PhysRev.53.137)
- [25] A. E. Douglas and G. Herzberg, The Astrophysical Journal **94**, 381 (1941). doi:[10.1086/144342](https://doi.org/10.1086/144342)
- [26] A. E. Douglas and G. Herzberg, Canadian Journal of Research **20a**, 71–82 (1942). doi:[10.1139/cjr42a-008](https://doi.org/10.1139/cjr42a-008)
- [27] D. R. Bates and L. Spitzer Jr., The Astrophysical Journal **113**, 441 (1951). doi:[10.1086/145415](https://doi.org/10.1086/145415)
- [28] P. M. Solomon and W. Klemperer, The Astrophysical Journal **178**, 389–422 (1972). doi:[10.1086/151799](https://doi.org/10.1086/151799)
- [29] E. Herbst and W. Klemperer, The Astrophysical Journal **185**, 505–534 (1973). doi:[10.1086/152436](https://doi.org/10.1086/152436)
- [30] S. Weinreb, A. H. Barrett, M. L. Meeks, and J. C. Henry, Nature **200**, 829–831 (1963). doi:[10.1038/200829a0](https://doi.org/10.1038/200829a0)

- [31] A. C. Cheung, D. M. Rank, C. H. Townes, D. D. Thornton, and W. J. Welch, *Physical Review Letters* **21**, 1701–1705 (1968). doi:[10.1103/PhysRevLett.21.1701](https://doi.org/10.1103/PhysRevLett.21.1701)
- [32] A. C. Cheung, D. M. Rank, C. H. Townes, D. D. Thornton, and W. J. Welch, *Nature* **221**, 626–628 (1969). doi:[10.1038/221626a0](https://doi.org/10.1038/221626a0)
- [33] L. E. Snyder, D. Buhl, B. Zuckerman, and P. Palmer, *Physical Review Letters* **22**, 679–681 (1969). doi:[10.1103/PhysRevLett.22.679](https://doi.org/10.1103/PhysRevLett.22.679)
- [34] B. A. McGuire, *The Astrophysical Journal Supplement Series* **259**, 30 (2021). doi:[10.3847/1538-4365/ac2a48](https://doi.org/10.3847/1538-4365/ac2a48)
- [35] F. C. Gillett, W. J. Forrest, and K. M. Merrill, *The Astrophysical Journal* **183**, 87 (1973). doi:[10.1086/152211](https://doi.org/10.1086/152211)
- [36] K. M. Merrill, B. T. Soifer, and R. W. Russell, *The Astrophysical Journal* **200**, L37 (1975). doi:[10.1086/181891](https://doi.org/10.1086/181891)
- [37] R. W. Russell, B. T. Soifer, and S. P. Willner, *The Astrophysical Journal* **217**, L149 (1977). doi:[10.1086/182559](https://doi.org/10.1086/182559)
- [38] S. P. Willner, B. T. Soifer, R. W. Russell, R. R. Joyce, and F. C. Gillett, *The Astrophysical Journal* **217**, L121–L124 (1977). doi:[10.1086/182553](https://doi.org/10.1086/182553)
- [39] A. Leger and J. L. Puget, *Astronomy and Astrophysics* **137**, L5–L8 (1984).
- [40] L. J. Allamandola, A. G. G. M. Tielens, and J. R. Barker, *The Astrophysical Journal* **290**, L25–L28 (1985). doi:[10.1086/184435](https://doi.org/10.1086/184435)
- [41] B. A. McGuire and Mcguiregroup, doi:[10.5281/ZENODO.5541828](https://doi.org/10.5281/ZENODO.5541828) (2021).
- [42] T. Oka, *Science* **347**, 1313–1314 (2015). doi:[10.1126/science.aaa6935](https://doi.org/10.1126/science.aaa6935)
- [43] O. Asvany, P. K. P. B. Redlich, I. Hegemann, S. Schlemmer, and D. Marx, *Science* **309**, 1219–1222 (2005). doi:[10.1126/science.1113729](https://doi.org/10.1126/science.1113729)
- [44] W. Paul, O. Osberghaus, and E. Fischer, *Forschungsberichte des Verkehrs- und Wirtschaftsministeriums Nordrhein-Westfalen* **415**, 1–42 (1955).
- [45] W. Paul and M. Raether, *Zeitschrift für Physik* **140**, 262–273 (1955). doi:[10.1007/BF01328923](https://doi.org/10.1007/BF01328923)
- [46] H. Schwarz and K. R. Asmis, *Chem.: Eur. J.* **25**, 2112–2126 (2019). doi:[{10.1002/chem.201805836}](https://doi.org/10.1002/chem.201805836)
- [47] A. Pereversev and J. Roithová, *J. Mass Spectrom.* **57**, e4826 (2022). doi:[10.1002/jms.4826](https://doi.org/10.1002/jms.4826)
- [48] O. Asvany and S. Schlemmer, *Physical Chemistry Chemical Physics* **23**, 26602–26622 (2021). doi:[10.1039/dlcp03975j](https://doi.org/10.1039/dlcp03975j)

- E**
- [49] H. G. Dehmelt, *Advances in atomic and molecular physics*, Vol. 3, edited by D. R. Bates and I. Estermann (Academic Press, 1, 1968), pp. 53–72, doi:[10.1016/S0065-2199\(08\)60170-0](https://doi.org/10.1016/S0065-2199(08)60170-0)
 - [50] R. Wester, Journal of Physics B: Atomic, Molecular and Optical Physics **42**, 154001 (2009). doi:[10.1088/0953-4075/42/15/154001](https://doi.org/10.1088/0953-4075/42/15/154001)
 - [51] D. Gerlich, Physica Scripta **T59**, 256–263 (1995). doi:[10.1088/0031-8949/1995/T59/035](https://doi.org/10.1088/0031-8949/1995/T59/035)
 - [52] O. Asvany, F. Bielau, D. Moratschke, J. Krause, and S. Schlemmer, Review of Scientific Instruments **81**, 076102 (2010). doi:[10.1063/1.3460265](https://doi.org/10.1063/1.3460265)
 - [53] D. Smith, Chemical Reviews **92**, 1473–1485 (1992). doi:[10.1021/cr00015a001](https://doi.org/10.1021/cr00015a001)
 - [54] D. Gerlich and S. Horning, Chemical Reviews **92**, 1509–1539 (1992). doi:[10.1021/cr00015a003](https://doi.org/10.1021/cr00015a003)
 - [55] D. Gerlich, *Advances in chemical physics* (John Wiley & Sons, Ltd, 1992), pp. 1–176.
 - [56] F. C. Fehsenfeld, A. L. Schmeltekopf, and E. E. Ferguson, The Journal of Chemical Physics **46**, 2802–2808 (1967). doi:[10.1063/1.1841117](https://doi.org/10.1063/1.1841117)
 - [57] J. K. Kim, L. P. Theard, and W. T. Huntress, The Journal of Chemical Physics **62**, 45–52 (1975). doi:[10.1063/1.430236](https://doi.org/10.1063/1.430236)
 - [58] D. Smith, N. G. Adams, and T. M. Miller, The Journal of Chemical Physics **69**, 308–318 (1978). doi:[10.1063/1.436354](https://doi.org/10.1063/1.436354)
 - [59] W. Paul, B. Lücke, S. Schlemmer, and D. Gerlich, International Journal of Mass Spectrometry and Ion Processes **149-150**, 373–387 (1995). doi:[10.1016/0168-1176\(95\)04269-Q](https://doi.org/10.1016/0168-1176(95)04269-Q)
 - [60] W. Paul, S. Schlemmer, B. Lücke, and D. Gerlich, Chemical Physics **209**, 265–274 (1996). doi:[10.1016/0301-0104\(96\)00160-7](https://doi.org/10.1016/0301-0104(96)00160-7)
 - [61] S. Chakrabarty, M. Holz, E. K. Campbell, A. Banerjee, D. Gerlich, and J. P. Maier, The Journal of Physical Chemistry Letters **4**, 4051–4054 (2013). doi:[10.1021/jz402264n](https://doi.org/10.1021/jz402264n)
 - [62] J. G. Redwine, Z. A. Davis, N. L. Burke, R. A. Oglesbee, S. A. McLuckey, and T. S. Zwier, International Journal of Mass Spectrometry **348**, 9–14 (2013). doi:[10.1016/j.ijms.2013.04.002](https://doi.org/10.1016/j.ijms.2013.04.002)
 - [63] O. Asvany, S. Brünken, L. Kluge, and S. Schlemmer, English, Applied Physics B **114**, 203–211 (2014). doi:[10.1007/s00340-013-5684-y](https://doi.org/10.1007/s00340-013-5684-y)
 - [64] A. Günther, P. Nieto, D. Müller, A. Sheldrick, D. Gerlich, and O. Dopfer, Journal of Molecular Spectroscopy **332**, 8–15 (2017). doi:[10.1016/j.jms.2016.08.017](https://doi.org/10.1016/j.jms.2016.08.017)

- [65] P. Jusko, S. Brünken, B. Brünken, O. Asvany, S. Thorwirth, A. Stoffels, L. Van Der Meer, G. Berden, B. Redlich, J. Oomens, and S. Schlemmer, *Faraday Discuss.* **217**, 172 (2019). doi:[10.1039/c8fd00225h](https://doi.org/10.1039/c8fd00225h)
- [66] D. B. Rap, J. G. M. Schrauwen, A. N. Marimuthu, B. Redlich, and S. Brünken, *Nature Astronomy* **6**, 1059–1067 (2022). doi:[10.1038/s41550-022-01713-z](https://doi.org/10.1038/s41550-022-01713-z)
- [67] R. C. Dunbar, *Journal of the American Chemical Society* **95**, 472–476 (1973). doi:[10.1021/ja00783a028](https://doi.org/10.1021/ja00783a028)
- [68] M. Okumura, L. I. Yeh, and Y. T. Lee, *The Journal of Chemical Physics* **83**, 3705–3706 (1985). doi:[10.1063/1.449127](https://doi.org/10.1063/1.449127)
- [69] E. J. Bieske and J. P. Maier, *Chemical Reviews* **93**, 2603–2621 (1993). doi:[10.1021/cr00024a002](https://doi.org/10.1021/cr00024a002)
- [70] M. A. Duncan, *International Reviews in Physical Chemistry* **22**, 407–435 (2003). doi:[10.1080/0144235031000095201](https://doi.org/10.1080/0144235031000095201)
- [71] J. M. Lisý, *The Journal of Chemical Physics* **125**, 132302 (2006). doi:[10.1063/1.2338317](https://doi.org/10.1063/1.2338317)
- [72] K. R. Asmis, M. Brümmer, C. Kaposta, G. Santambrogio, G. v. Helden, G. Meijer, K. Rademann, and L. Wöste, *Physical Chemistry Chemical Physics* **4**, 1101–1104 (2002). doi:[10.1039/B111056](https://doi.org/10.1039/B111056)
- [73] H. Kohguchi, P. Jusko, K. M. T. Yamada, S. Schlemmer, and O. Asvany, *The Journal of Chemical Physics* **148**, 144303 (2018). doi:[10.1063/1.5023633](https://doi.org/10.1063/1.5023633)
- [74] M. Töpfer, A. Jensen, K. Nagamori, H. Kohguchi, T. Szidarovszky, A. G. Császár, S. Schlemmer, and O. Asvany, *Physical Chemistry Chemical Physics* **22**, 22885–22888 (2020). doi:[10.1039/D0CP04649C](https://doi.org/10.1039/D0CP04649C)
- [75] F. Dahlmann, P. Jusko, M. Lara-Moreno, P. Halvick, A. N. Marimuthu, T. Michaelsen, R. Wild, K. Geistlinger, S. Schlemmer, T. Stoecklin, R. Wester, and S. Brünken, *Molecular Physics*, e2085204 (2022). doi:[10.1080/00268976.2022.2085204](https://doi.org/10.1080/00268976.2022.2085204)
- [76] J. Roithová, A. Gray, E. Andris, J. Jašík, and D. Gerlich, *Accounts of Chemical Research* **49**, 223–230 (2016). doi:[10.1021/acs.accounts.5b00489](https://doi.org/10.1021/acs.accounts.5b00489)
- [77] D. Gerlich, *Journal of the Chinese Chemical Society* **65**, 637–653 (2018). doi:[10.1002/jccs.201800122](https://doi.org/10.1002/jccs.201800122)
- [78] N. R. Isenor, V. Merchant, R. S. Hallsworth, and M. C. Richardson, *Canadian Journal of Physics* **51**, 1281–1287 (1973). doi:[10.1139/p73-169](https://doi.org/10.1139/p73-169)
- [79] C. A. Wight and J. L. Beauchamp, *Journal of the American Chemical Society* **103**, 6499–6501 (1981). doi:[10.1021/ja00411a042](https://doi.org/10.1021/ja00411a042)

- [80] T. G  umann, J. M. Riveros, and Z. Zhu, Helvetica Chimica Acta **73**, 1215–1218 (1990). doi:[10.1002/hlca.19900730510](https://doi.org/10.1002/hlca.19900730510)
- [81] D. M. Peiris, M. A. Cheeseman, R. Ramanathan, and J. R. Eyler, The Journal of Physical Chemistry **97**, 7839–7843 (1993). doi:[10.1021/j100132a009](https://doi.org/10.1021/j100132a009)
- [82] J. Oomens, A. J. A. v. Roij, G. Meijer, and G. v. Helden, The Astrophysical Journal **542**, 404–410 (2000). doi:[10.1086/309545](https://doi.org/10.1086/309545)
- [83] J. Lemaire, P. Boissel, M. Heninger, G. Mauclaire, G. Bellec, H. Mestdagh, A. Simon, S. L. Caer, J. M. Ortega, F. Glotin, and P. Maitre, Physical Review Letters **89**, 273002 (2002). doi:[10.1103/PhysRevLett.89.273002](https://doi.org/10.1103/PhysRevLett.89.273002)
- [84] N. C. Polfer, Chemical Society Reviews **40**, 2211–2221 (2011). doi:[10.1039/C0CS00171F](https://doi.org/10.1039/C0CS00171F)
- [85] J. G. Black, E. Yablonovitch, N. Bloembergen, and S. Mukamel, Physical Review Letters **38**, 1131–1134 (1977). doi:[10.1103/PhysRevLett.38.1131](https://doi.org/10.1103/PhysRevLett.38.1131)
- [86] A. A. Makarov, I. Y. Petrova, E. A. Ryabov, and V. S. Letokhov, The Journal of Physical Chemistry A **102**, 1438–1449 (1998). doi:[10.1021/jp972487c](https://doi.org/10.1021/jp972487c)
- [87] J. Oomens, B. G. Sartakov, G. Meijer, and G. von Helden, International Journal of Mass Spectrometry **254**, 1–19 (2006). doi:[10.1016/j.ijms.2006.05.009](https://doi.org/10.1016/j.ijms.2006.05.009)
- [88] P. Parneix, M. Basire, and F. Calvo, The Journal of Physical Chemistry A **117**, 3954–3959 (2013). doi:[10.1021/jp402459f](https://doi.org/10.1021/jp402459f)
- [89] J. I. Steinfeld, *Molecules and radiation: an introduction to modern molecular spectroscopy*, 2nd ed (MIT Press, Cambridge, Mass, 1985).
- [90] S. Schlemmer, T. Kuhn, E. Lescop, and D. Gerlich, International Journal of Mass Spectrometry **185–187**, 589–602 (1999). doi:[10.1016/S1387-3806\(98\)14141-6](https://doi.org/10.1016/S1387-3806(98)14141-6)
- [91] S. Schlemmer, E. Lescop, J. von Richthofen, D. Gerlich, and M. A. Smith, The Journal of Chemical Physics **117**, 2068–2075 (2002). doi:[10.1063/1.1487373](https://doi.org/10.1063/1.1487373)
- [92] O. Asvany, T. Giesen, B. Redlich, and S. Schlemmer, Physical Review Letters **94**, 073001 (2005). doi:[10.1103/PhysRevLett.94.073001](https://doi.org/10.1103/PhysRevLett.94.073001)
- [93] S. Schlemmer, O. Asvany, and T. Giesen, Physical Chemistry Chemical Physics **7**, 1592–1600 (2005). doi:[10.1039/B418495P](https://doi.org/10.1039/B418495P)
- [94] J. L. Dom  enech, P. Jusko, S. Schlemmer, and O. Asvany, The Astrophysical Journal **857**, 61 (2018). doi:[10.3847/1538-4357/aab36a](https://doi.org/10.3847/1538-4357/aab36a)
- [95] P. Jusko, C. Konietzko, S. Schlemmer, and O. Asvany, Journal of Molecular Spectroscopy **319**, 55–58 (2016). doi:[10.1016/j.jms.2015.12.002](https://doi.org/10.1016/j.jms.2015.12.002)

- [96] P. Jusko, A. Stoffels, S. Thorwirth, S. Brünken, S. Schlemmer, and O. Asvany, *Journal of Molecular Spectroscopy* **332**, 59–66 (2017). doi:[10.1016/j.jms.2016.10.017](https://doi.org/10.1016/j.jms.2016.10.017)
- [97] C. R. Markus, S. Thorwirth, O. Asvany, and S. Schlemmer, *Physical Chemistry Chemical Physics* **21**, 26406–26412 (2019). doi:[10.1039/c9cp05487a](https://doi.org/10.1039/c9cp05487a)
- [98] J. L. Doménech, O. Asvany, C. R. Markus, S. Schlemmer, and S. Thorwirth, *Journal of Molecular Spectroscopy* **374**, 111375 (2020). doi:[10.1016/j.jms.2020.111375](https://doi.org/10.1016/j.jms.2020.111375)
- [99] S. Brünken, L. Kluge, A. Stoffels, O. Asvany, and S. Schlemmer, *The Astrophysical Journal* **783**, L4, L4 (2014). doi:[10.1088/2041-8205/783/1/L4](https://doi.org/10.1088/2041-8205/783/1/L4)
- [100] O. Asvany, O. Ricken, H. S. Müller, M. C. Wiedner, T. F. Giesen, and S. Schlemmer, *Physical Review Letters* **100**, 13–16 (2008). doi:[10.1103/PhysRevLett.100.233004](https://doi.org/10.1103/PhysRevLett.100.233004)
- [101] S. Gärtner, J. Krieg, A. Klemann, O. Asvany, S. Brünken, and S. Schlemmer, *Journal of Physical Chemistry A* **117**, 9975–9984 (2013). doi:[10.1021/jp400258e](https://doi.org/10.1021/jp400258e)
- [102] P. Jusko, O. Asvany, A. C. Wallerstein, S. Brünken, and S. Schlemmer, *Physical Review Letters* **112**, 253005, 2–5 (2014). doi:[10.1103/PhysRevLett.112.253005](https://doi.org/10.1103/PhysRevLett.112.253005)
- [103] R. V. Olkhov, S. A. Nizkorodov, and O. Dopfer, *The Journal of Chemical Physics* **110**, 9527–9535 (1999). doi:[10.1063/1.478917](https://doi.org/10.1063/1.478917)
- [104] M. Töpfer, T. Salomon, H. Kohguchi, O. Dopfer, K. M. Yamada, S. Schlemmer, and O. Asvany, *Physical Review Letters* **121**, 143001 (2018). doi:[10.1103/PhysRevLett.121.143001](https://doi.org/10.1103/PhysRevLett.121.143001)
- [105] S. Lee, D. Hauser, O. Lakhmanskaya, S. Spieler, E. S. Endres, K. Geistlinger, S. S. Kumar, and R. Wester, *Physical Review A* **93**, 032513 (2016). doi:[10.1103/PhysRevA.93.032513](https://doi.org/10.1103/PhysRevA.93.032513)
- [106] A. Stoffels, L. Kluge, S. Schlemmer, and S. Brünken, *Astronomy & Astrophysics* **593**, A56 (2016). doi:[10.1051/0004-6361/201629101](https://doi.org/10.1051/0004-6361/201629101)
- [107] J. L. Doménech, S. Schlemmer, and O. Asvany, *The Astrophysical Journal* **849**, 60 (2017). doi:[10.3847/1538-4357/aa8fca](https://doi.org/10.3847/1538-4357/aa8fca)
- [108] T. Salomon, M. Töpfer, P. Schreier, S. Schlemmer, H. Kohguchi, L. Surin, and O. Asvany, *Physical Chemistry Chemical Physics* **21**, 3440–3445 (2019). doi:[10.1039/C8CP04532A](https://doi.org/10.1039/C8CP04532A)
- [109] J. L. Doménech, S. Schlemmer, and O. Asvany, *The Astrophysical Journal* **866**, 158 (2018). doi:[10.3847/1538-4357/aadf83](https://doi.org/10.3847/1538-4357/aadf83)

- [110] S. Thorwirth, P. Schreier, T. Salomon, S. Schlemmer, and O. Asvany, *Astrophys. J. Lett.* **882**, L6 (2019). doi:[10.3847/2041-8213/ab3927](https://doi.org/10.3847/2041-8213/ab3927)
- [111] P. C. Schmid, S. Thorwirth, C. P. Endres, M. Töpfer, Á. Sánchez-Monge, A. Schwörer, P. Schilke, S. Schlemmer, and O. Asvany, *Frontiers in Astronomy and Space Sciences* **8**, doi:[10.3389/fspas.2021.805162](https://doi.org/10.3389/fspas.2021.805162) (2022).
- [112] O. Asvany, C. R. Markus, A. Roucou, S. Schlemmer, S. Thorwirth, and C. Lauzin, *Journal of Molecular Spectroscopy* **378**, 111447 (2021). doi:[10.1016/j.jms.2021.111447](https://doi.org/10.1016/j.jms.2021.111447)
- [113] O. Asvany, C. R. Markus, K. Nagamori, H. Kohguchi, J. Furuta, K. Kobayashi, S. Schlemmer, and S. Thorwirth, *The Astrophysical Journal* **910**, 15 (2021). doi:[10.3847/1538-4357/abe536](https://doi.org/10.3847/1538-4357/abe536)
- [114] A. N. Marimuthu, K. Steenbakkers, B. Redlich, and S. Brünken, *Molecular Physics*, e2067089 (2022). doi:[10.1080/00268976.2022.2067089](https://doi.org/10.1080/00268976.2022.2067089)
- [115] D. Oepts, A. F. van der Meer, and P. W. van Amersfoort, *Infrared Phys. Technol.* **36**, 297–308 (1995). doi:[10.1016/1350-4495\(94\)00074-U](https://doi.org/10.1016/1350-4495(94)00074-U)
- [116] L. A. Kluge, “State-selective attachment of helium to molecular ions in a new cryogenic ion trap”, PhD thesis (Universität zu Köln, Köln, 2016), 171 pp.
- [117] A. J. Dempster, *Physical Review* **11**, 316–325 (1918). doi:[10.1103/PhysRev.11.316](https://doi.org/10.1103/PhysRev.11.316)
- [118] W. Bleakney, *Physical Review* **34**, 157–160 (1929). doi:[10.1103/PhysRev.34.157](https://doi.org/10.1103/PhysRev.34.157)
- [119] E. S. Endres, G. Egger, S. Lee, O. Lakhmanskaya, M. Simpson, and R. Wester, *Journal of Molecular Spectroscopy* **332**, 134–138 (2017). doi:[10.1016/j.jms.2016.12.006](https://doi.org/10.1016/j.jms.2016.12.006)
- [120] N. R. Daly, *Review of Scientific Instruments* **31**, 264–267 (1960). doi:[10.1063/1.1716953](https://doi.org/10.1063/1.1716953)
- [121] J. J. Olivero and R. L. Longbothum, *Journal of Quantitative Spectroscopy and Radiative Transfer* **17**, 233–236 (1977). doi:[10.1016/0022-4073\(77\)90161-3](https://doi.org/10.1016/0022-4073(77)90161-3)
- [122] C. M. Western, *J. Quant. Spectrosc. Radiat. Transf.* **186**, 221–242 (2017). doi:[10.1016/j.jqsrt.2016.04.010](https://doi.org/10.1016/j.jqsrt.2016.04.010)
- [123] E. Hairer and G. Wanner, *Solving ordinary differential equations II*, Vol. 14 (Springer Berlin Heidelberg, Berlin, Heidelberg, 1991), doi:[10.1007/978-3-662-09947-6](https://doi.org/10.1007/978-3-662-09947-6)

- [124] E. Hairer and G. Wanner, *Solving ordinary differential equations II: stiff and differential-algebraic problems*, edited by E. Hairer and G. Wanner (Springer, Berlin, Heidelberg, 1996), pp. 118–130, doi:[10.1007/978-3-642-05221-7_8](https://doi.org/10.1007/978-3-642-05221-7_8)
- [125] P. Virtanen, R. Gommers, T. E. Oliphant, M. Haberland, T. Reddy, D. Cournapeau, E. Burovski, P. Peterson, W. Weckesser, J. Bright, S. J. van der Walt, M. Brett, J. Wilson, K. J. Millman, N. Mayorov, A. R. Nelson, E. Jones, R. Kern, E. Larson, C. J. Carey, İ. Polat, Y. Feng, E. W. Moore, J. VanderPlas, D. Laxalde, J. Perktold, R. Cimrman, I. Henriksen, E. A. Quintero, C. R. Harris, A. M. Archibald, A. H. Ribeiro, F. Pedregosa, P. van Mulbregt, A. Vijaykumar, A. P. Bardelli, A. Rothberg, A. Hilboll, A. Kloeckner, A. Scopatz, A. Lee, A. Rokem, C. N. Woods, C. Fulton, C. Masson, C. Häggström, C. Fitzgerald, D. A. Nicholson, D. R. Hagen, D. V. Pasechnik, E. Olivetti, E. Martin, E. Wieser, F. Silva, F. Lenders, F. Wilhelm, G. Young, G. A. Price, G. L. Ingold, G. E. Allen, G. R. Lee, H. Audren, I. Probst, J. P. Dietrich, J. Silterra, J. T. Webber, J. Slavič, J. Nothman, J. Buchner, J. Kulick, J. L. Schönberger, J. V. de Miranda Cardoso, J. Reimer, J. Harrington, J. L. C. Rodríguez, J. Nunez-Iglesias, J. Kuczynski, K. Tritz, M. Thoma, M. Newville, M. Kümmerer, M. Bolingbroke, M. Tartre, M. Pak, N. J. Smith, N. Nowaczyk, N. Shebanov, O. Pavlyk, P. A. Brodtkorb, P. Lee, R. T. McGibbon, R. Feldbauer, S. Lewis, S. Tygier, S. Sievert, S. Vigna, S. Peterson, S. More, T. Pudlik, *et al.*, *Nature Methods* 2020 **17**: 261–272 (2020). doi:[10.1038/s41592-019-0686-2](https://doi.org/10.1038/s41592-019-0686-2)
- [126] M. Born and R. Oppenheimer, *Annalen der Physik* **389**, 457–484 (1927). doi:[10.1002/andp.19273892002](https://doi.org/10.1002/andp.19273892002)
- [127] K. Raghavachari, G. W. Trucks, J. A. Pople, and M. Head-Gordon, *Chemical Physics Letters* **157**, 479–483 (1989). doi:[10.1016/S0009-2614\(89\)87395-6](https://doi.org/10.1016/S0009-2614(89)87395-6)
- [128] J. Almlöf and P. R. Taylor, *The Journal of Chemical Physics* **86**, 4070–4077 (1987). doi:[10.1063/1.451917](https://doi.org/10.1063/1.451917)
- [129] J. Almlöf and P. R. Taylor, *Advances in quantum chemistry*, Vol. 22, edited by P.-O. Löwdin, J. R. Sabin, and M. C. Zerner (Academic Press, 1, 1991), pp. 301–373, doi:[10.1016/S0065-3276\(08\)60366-4](https://doi.org/10.1016/S0065-3276(08)60366-4)
- [130] T. H. Dunning, *The Journal of Chemical Physics* **90**, 1007–1023 (1989). doi:[10.1063/1.456153](https://doi.org/10.1063/1.456153)
- [131] J. D. Watts, J. Gauss, and R. J. Bartlett, *Chemical Physics Letters* **200**, 1–7 (1992). doi:[10.1016/0009-2614\(92\)87036-O](https://doi.org/10.1016/0009-2614(92)87036-O)
- [132] T. J. Lee and A. P. Rendell, *The Journal of Chemical Physics* **94**, 6229–6236 (1991). doi:[10.1063/1.460411](https://doi.org/10.1063/1.460411)

- [133] J. D. Watts, J. Gauss, and R. J. Bartlett, *The Journal of Chemical Physics* **98**, 8718–8733 (1993). doi:[10.1063/1.464480](https://doi.org/10.1063/1.464480)
- [134] I. M. Mills, *Molecular spectroscopy*, edited by K. N. Rao and C. W. Mathews (Academic Press, 1, 1972), pp. 115–140, doi:[10.1016/B978-0-12-580640-4.50013-3](https://doi.org/10.1016/B978-0-12-580640-4.50013-3)
- [135] D. A. Matthews, L. Cheng, M. E. Harding, F. Lipparini, S. Stopkowicz, T.-C. Jagau, P. G. Szalay, J. Gauss, and J. F. Stanton, *The Journal of Chemical Physics* **152**, 214108 (2020). doi:[10.1063/5.0004837](https://doi.org/10.1063/5.0004837)
- [136] M. E. Harding, T. Metzroth, J. Gauss, and A. A. Auer, *Journal of Chemical Theory and Computation* **4**, 64–74 (2008). doi:[10.1021/ct700152c](https://doi.org/10.1021/ct700152c)
- [137] D. G. A. Smith, L. A. Burns, A. C. Simmonett, R. M. Parrish, M. C. Schieber, R. Galvelis, P. Kraus, H. Kruse, R. Di Remigio, A. Alenaizan, A. M. James, S. Lehtola, J. P. Misiewicz, M. Scheurer, R. A. Shaw, J. B. Schriber, Y. Xie, Z. L. Glick, D. A. Sirianni, J. S. O'Brien, J. M. Waldrop, A. Kumar, E. G. Hohenstein, B. P. Pritchard, B. R. Brooks, H. F. Schaefer, A. Y. Sokolov, K. Patkowski, A. E. DePrince, U. Bozkaya, R. A. King, F. A. Evangelista, J. M. Turney, T. D. Crawford, and C. D. Sherrill, *The Journal of Chemical Physics* **152**, 184108 (2020). doi:[10.1063/5.0006002](https://doi.org/10.1063/5.0006002)
- [138] A. D. M. B. Liu, *J. Chem. Phys.* **59**, 4557 (1973). doi:[10.1063/1.1680654](https://doi.org/10.1063/1.1680654)
- [139] S. Boys and F. Bernardi, *Molecular Physics* **19**, 553–566 (1970). doi:[10.1080/00268977000101561](https://doi.org/10.1080/00268977000101561)
- [140] B. Jeziorski, R. Moszynski, and K. Szalewicz, *Chemical Reviews* **94**, 1887–1930 (1994). doi:[10.1021/cr00031a008](https://doi.org/10.1021/cr00031a008)
- [141] E. G. Hohenstein and C. D. Sherrill, *The Journal of Chemical Physics* **133**, 014101 (2010). doi:[10.1063/1.3451077](https://doi.org/10.1063/1.3451077)
- [142] O. Reynolds, *Philosophical Transactions of the Royal Society of London* **170**, 727–845 (1879). doi:[10.1098/rstl.1879.0078](https://doi.org/10.1098/rstl.1879.0078)
- [143] M. Knudsen, *Annalen der Physik* **336**, 633–640 (1910). doi:[10.1002/ANDP.19103360310](https://doi.org/10.1002/ANDP.19103360310)
- [144] T. Takaishi and Y. Sensui, *Transactions of the Faraday Society* **59**, 2503 (1963). doi:[10.1039/tf9635902503](https://doi.org/10.1039/tf9635902503)
- [145] J. Sanderson, H. Tanuma, N. Kobayashi, and Y. Kaneko, *The Journal of Chemical Physics* **103**, 7098–7103 (1995). doi:[10.1063/1.470338](https://doi.org/10.1063/1.470338)
- [146] E. O. LEBIGOT, *Uncertainties: a python package for calculations with uncertainties*.

- [147] J. M. Goodings, D. K. Bohme, and C.-w. Ng, COMBUSTION AND FLAME **43**, 27–43 (1979).
- [148] S. E. Wheeler, K. A. Robertson, W. D. Allen, H. F. S. Iii, Y. J. Bomble, and J. F. Stanton, J. Phys. Chem. A **111**, 3819–3830 (2007). doi:[10.1021/jp0684630](https://doi.org/10.1021/jp0684630)
- [149] J. A. Miller and M. J. Pilling, Proceedings of the Combustion Institute **30**, 43–88 (2005). doi:[10.1016/j.proci.2004.08.281](https://doi.org/10.1016/j.proci.2004.08.281)
- [150] E. Herbst, N. G. Adams, and D. Smith, The Astrophysical Journal **269**, 329 (1983). doi:[10.1086/161046](https://doi.org/10.1086/161046)
- [151] N. G. Adams and D. Smith, Journal of Chemical Information and Modeling **317**, L25–L27 (1987). doi:[10.1086/184906](https://doi.org/10.1086/184906)
- [152] J. Cernicharo, C. Gottlieb, M. Guelin, T. Killian, G. Paubert, P. Thaddeus, and J. Vrtilek, Astrophys. J. **368**, L39–L41 (1991). doi:[10.1086/185943](https://doi.org/10.1086/185943)
- [153] A. Korth, M. L. Marconi, D. A. Mendis, F. R. Krueger, A. K. Richter, R. P. Lin, D. L. Mitchell, K. A. Anderson, C. W. Carlson, H. Rème, J. A. Sauvaud, and C. d'Uston, Nature **337**, 53–55 (1989). doi:[10.1038/337053a0](https://doi.org/10.1038/337053a0)
- [154] V. G. Anicich, D. B. Milligan, D. A. Fairley, and M. J. McEwan, Icarus **146**, 118–124 (2000). doi:[10.1006/icar.2000.6353](https://doi.org/10.1006/icar.2000.6353)
- [155] A. Ali, E. C. Sittler, D. Chornay, B. R. Rowe, and C. Puzzarini, Planetary and Space Science **87**, 96–105 (2013). doi:[10.1016/j.pss.2013.07.007](https://doi.org/10.1016/j.pss.2013.07.007)
- [156] X. Huang, P. R. Taylor, and T. J. Lee, J. Phys. Chem. A **115**, 5005–5016 (2011). doi:[10.1021/jp2019704](https://doi.org/10.1021/jp2019704)
- [157] M. A. Duncan, J. Phys. Chem. A **116**, 11477–11491 (2012). doi:[10.1021/jp309037d](https://doi.org/10.1021/jp309037d)
- [158] T. Baer, C.-Y. Ng, and I. Powis, *The structure, energetics, and dynamics of organic ions* (Wiley, 1996).
- [159] J. L. Holmes, C. Aubry, and P. M. Mayer, *Assigning structures to ions in mass spectrometry* (CRC Press, 2007).
- [160] J. Pety, P. Gratier, V. Guzmán, E. Roueff, M. Gerin, J. R. Goicoechea, S. Bardeau, A. Sievers, F. Le Petit, J. Le Bourlot, A. Belloche, and D. Talbi, Astron. Astrophys. **548**, A68, A68 (2012). doi:[10.1051/0004-6361/201220062](https://doi.org/10.1051/0004-6361/201220062)
- [161] B. A. McGuire, P. B. Carroll, R. A. Loomis, G. A. Blake, J. M. Hollis, F. J. Lovas, P. R. Jewell, and A. J. Remijan, Astrophys. J. **774**, 56, 56 (2013). doi:[10.1088/0004-637X/774/1/56](https://doi.org/10.1088/0004-637X/774/1/56)
- [162] B. A. McGuire, P. B. Carroll, J. L. Sanders III, S. L. W. Weaver, G. A. Blake, and A. J. Remijan, Mon. Not. R. Astron. Soc. **442**, 2901–2908 (2014). doi:[10.1093/mnras/stu1047](https://doi.org/10.1093/mnras/stu1047)

- [163] M. C. McCarthy, K. N. Crabtree, M.-A. Martin-Drumel, O. Martinez Jr., B. A. McGuire, and C. A. Gottlieb, *Astrophys. J. Suppl. S.* **217**, doi:{10.1088/0067-0049/217/1/10} (2015).
- [164] D. Smith and N. Adams, *Int. J. Mass. Spectrom.* **76**, 307–317 (1987). doi:{10.1016/0168-1176(87)83035-5}
- [165] S. Maluendes, A. McLean, K. Yamashita, and E. Herbst, *J. Chem. Phys.* **99**, 2812–2820 (1993). doi:{10.1063/1.465190}
- [166] P. Thaddeus, J. M. VRTILEK, and C. A. GOTTLIEB, *The Astrophysical Journal* **299**, L63–L66 (1985).
- [167] H. Matthews and W. Irvine, *Astrophys. J.* **298**, L61–L65 (1985). doi:{10.1086/184567}
- [168] K. Kawaguchi, N. Kaifu, M. Ohishi, S.-I. Ishikawa, Y. Hirahara, S. Yamamoto, S. Saito, S. Takano, A. Murakami, J. M. Vrtilek, C. A. Gottlieb, P. Thaddeus, and W. M. Irvine, *PASJ* **43**, 607–619 (1991).
- [169] J. Cernicharo, P. Cox, D. Fosse, and R. Güsten, *Astron. Astrophys.* **351**, 341–346 (1999).
- [170] S. Yamamoto, S. Saito, M. Ohishi, H. Suzuki, S. Ishikawa, N. Kaifu, and A. Murakami, *Astrophys. J.* **322**, L55–L58 (1987). doi:{10.1086/185036}
- [171] P. Thaddeus, C. Gottlieb, A. Hjalmarson, L. Johansson, W. Irvine, P. Friberg, and R. Linke, *Astrophys. J.* **294**, L49–L53 (1985). doi:{10.1086/184507}
- [172] S. Maluendes, A. McLean, and E. Herbst, *Astrophys. J.* **417**, 181–186 (1993). doi:{10.1086/173301}
- [173] S. Cuadrado, J. R. Goicoechea, P. Pillera, J. Cernicharo, A. Fuente, and C. Joblin, *ASTRONOMY & ASTROPHYSICS* **575**, doi:{10.1051/0004-6361/201424568} (2015).
- [174] O. Sipilä, S. Spezzano, and P. Caselli, *Astron. Astrophys.* **591**, doi:{10.1051/0004-6361/201628689} (2016).
- [175] J.-C. Loison, M. Agundez, V. Wakelam, E. Roueff, P. Gratier, N. Marcelino, D. N. Reyes, J. Cernicharo, and M. Gerin, *Mon. Not. R. Astron. Soc.* **470**, 4075–4088 (2017). doi:{10.1093/mnras/stx1265}
- [176] M. B. Bell, P. A. Feldman, H. E. Matthews, and L. W. Avery, *ApJ* **311**, L89 (1986). doi:{10.1086/184804}
- [177] S. Spezzano, S. Brünken, P. Schilke, P. Caselli, K. M. Menten, M. C. McCarthy, L. Bizzocchi, S. P. Treviño-Morales, Y. Aikawa, and S. Schlemmer, *ApJ* **769**, L19, L19 (2013). doi:{10.1088/2041-8205/769/2/L19}

- [178] S. Spezzano, H. Gupta, S. Brünken, C. A. Gottlieb, P. Caselli, K. M. Menten, H. S. P. Mueller, L. Bizzocchi, P. Schilke, M. C. McCarthy, and S. Schlemmer, *Astron. Astrophys.* **586**, doi:[10.1051/0004-6361/201527460](https://doi.org/10.1051/0004-6361/201527460) (2016).
- [179] M. Gerin, H. A. Wootten, F. Combes, F. Boulanger, I. Peters W. L., T. B. H. Kuiper, P. J. Encrenaz, and M. Bogey, *A&A* **173**, L1–L4 (1987).
- [180] M. B. Bell, L. W. Avery, H. E. Matthews, P. A. Feldman, J. K. G. Watson, S. C. Madden, and W. M. Irvine, *ApJ* **326**, 924 (1988). doi:[10.1086/166150](https://doi.org/10.1086/166150)
- [181] L. Majumdar, P. Gratier, I. Andron, V. Wakelam, and E. Caux, *MNRAS* **467**, 3525–3532 (2017). doi:[10.1093/mnras/stx259](https://doi.org/10.1093/mnras/stx259)
- [182] I. Savić, S. Schlemmer, and D. Gerlich, *Astrophys. J.* **621**, 1163–1170 (2005). doi:[10.1086/427648](https://doi.org/10.1086/427648)
- [183] V. Vuitton, R. V. Yelle, and M. J. McEwan, *Icarus* **191**, 722–742 (2007). doi:[10.1016/j.icarus.2007.06.023](https://doi.org/10.1016/j.icarus.2007.06.023)
- [184] K. SMYTH, S. LIAS, and P. AUSLOOS, *COMBUSTION SCIENCE AND TECHNOLOGY* **28**, 147–154 (1982). doi:[10.1080/00102208208952550](https://doi.org/10.1080/00102208208952550)
- [185] M. McEwan, C. McConnell, C. Freeman, and V. Anicich, *J. Phys. Chem.* **98**, 5068–5073 (1994). doi:[10.1021/j100070a021](https://doi.org/10.1021/j100070a021)
- [186] V. G. Anicich, *Journal of Physical and Chemical Reference Data* **22**, 1469–1569 (1993). doi:[10.1063/1.555940](https://doi.org/10.1063/1.555940)
- [187] P. Fathi, W. D. Geppert, A. Kaiser, and D. Ascenzi, *MOLECULAR ASTROPHYSICS* **2**, 1–11 (2016). doi:[10.1016/j.molap.2015.09.002](https://doi.org/10.1016/j.molap.2015.09.002)
- [188] R. Breslow and J. T. Groves, *Journal of the American Chemical Society* **92**, 984–987 (1970). doi:[10.1021/ja00707a040](https://doi.org/10.1021/ja00707a040)
- [189] M. Wyss, E. Riaplov, and J. P. Maier, *Journal of Chemical Physics* **114**, 10355 (2001). doi:[10.1063/1.1367394](https://doi.org/10.1063/1.1367394)
- [190] C.-H. Chin, M.-Y. Lin, T.-P. Huang, P.-Z. Wu, and Y.-J. Wu, *Sci. Rep.* **8**, 14392 (2018). doi:[10.1038/s41598-018-32644-3](https://doi.org/10.1038/s41598-018-32644-3)
- [191] D. Roth and O. Dopfer, *Physical Chemistry Chemical Physics* **4**, 4855–4865 (2002). doi:[10.1039/b206170h](https://doi.org/10.1039/b206170h)
- [192] O. Dopfer, D. Roth, and J. Maier, *INTERNATIONAL JOURNAL OF MASS SPECTROMETRY* **218**, 281–297 (2002). doi:[10.1016/S1387-3806\(02\)00737-6](https://doi.org/10.1016/S1387-3806(02)00737-6)
- [193] P. Botschwina, R. Oswald, and G. Rauhut, *PHYSICAL CHEMISTRY CHEMICAL PHYSICS* **13**, 7921–7929 (2011). doi:[10.1039/c1cp20206e](https://doi.org/10.1039/c1cp20206e)

- [194] P. Botschwina and R. Oswald, JOURNAL OF CHEMICAL PHYSICS **134**, doi:[10.1063/1.3525466](https://doi.org/10.1063/1.3525466) (2011).
- [195] P. Botschwina, R. Oswald, and O. Dopfer, Physical Chemistry Chemical Physics **13**, 14163–14175 (2011). doi:[10.1039/c1cp20815b](https://doi.org/10.1039/c1cp20815b)
- [196] A. M. Ricks, G. E. Doublerly, P. v. R. Schleyer, and M. A. Duncan, JOURNAL OF CHEMICAL PHYSICS **132**, doi:[10.1063/1.3298881](https://doi.org/10.1063/1.3298881) (2010).
- [197] D. Zhao, K. D. Doney, and H. Linnartz, Astrophys. J. Lett. **791**, doi:[10.1088/2041-8205/791/2/L28](https://doi.org/10.1088/2041-8205/791/2/L28) (2014).
- [198] H. Gao, Z. Lu, L. Yang, J. Zhou, and C. Y. Ng, JOURNAL OF CHEMICAL PHYSICS **137**, doi:[10.1063/1.4764306](https://doi.org/10.1063/1.4764306) (2012).
- [199] G. A. Garcia, B. Gans, J. Kruger, F. Holzmeier, A. Roder, A. Lopes, C. Fittschen, C. Alcaraz, and J.-C. Loison, Phys. Chem. Chem. Phys. **20**, 8707–8718 (2018). doi:[10.1039/c8cp00510a](https://doi.org/10.1039/c8cp00510a)
- [200] K. J. Catani, J. A. Sanelli, V. Dryza, N. Gilka, P. R. Taylor, and E. J. Bieske, JOURNAL OF CHEMICAL PHYSICS **143**, doi:[10.1063/1.4935169](https://doi.org/10.1063/1.4935169) (2015).
- [201] D. Gerlich, *Adv. chem. phys.: state-selected and state-to-state ion-molecule reaction dynamics*, Vol. LXXXII, edited by C.-Y. Ng and M. Baer (Wiley, New York, 1992), pp. 1–176, doi:[10.1002/9780470141397.ch1](https://doi.org/10.1002/9780470141397.ch1)
- [202] P. Jusko, A. Simon, S. Banhatti, S. Brünken, and C. Joblin, ChemPhysChem **23**, 3182–3185 (2018). doi:[10.1002/cphc.201800744](https://doi.org/10.1002/cphc.201800744)
- [203] K. Raghavachari, G. W. Trucks, J. A. Pople, and M. Head-Gordon, Chem. Phys. Lett. **157**, 479–483 (1989).
- [204] J. Almlöf and P. R. Taylor, J. Chem. Phys. **86**, 4070–4077 (1987).
- [205] J. D. Watts, J. Gauss, and R. J. Bartlett, Chem. Phys. Lett. **200**, 1–7 (1992).
- [206] J. Gauss and J. F. Stanton, Chem. Phys. Lett. **276**, 70–77 (1997).
- [207] J. F. Stanton and J. Gauss, Int. Rev. Phys. Chem. **19**, 61–95 (2000).
- [208] I. M. Mills, “Vibration-Rotation Structure in Asymmetric- and Symmetric-Top Molecules”, *Molecular Spectroscopy: Modern Research*, edited by K. N. Rao and C. W. Mathews (Academic Press, New York, 1972), pp. 115–140.
- [209] J. F. Stanton, C. L. Lopreore, and J. Gauss, J. Chem. Phys. **108**, 7190–7196 (1998).
- [210] D. A. Matthews, L. Cheng, M. E. Harding, F. Lipparini, S. Stopkowicz, T.-C. Jagau, P. G. Szalay, J. Gauss, and J. F. Stanton, J. Chem. Phys. **152**, 214108 (2020).
- [211] L. McCaslin and J. F. Stanton, Molecular Physics **111**, 1492–1496 (2013).

- [212] S. Thorwirth, M. E. Harding, D. Muders, and J. Gauss, *J. Mol. Spectrosc.* **251**, 220–223 (2008).
- [213] N. C. Craig, J. Pranata, S. J. Reinganum, J. R. Sprague, and P. S. Stevens, *Journal of the American Chemical Society* **108**, 4378–4386 (1986). doi:[10.1021/ja00275a025](https://doi.org/10.1021/ja00275a025)
- [214] E. Miliordos and K. L. C. Hunt, *The Journal of Chemical Physics* **149**, 234103 (2018). doi:[10.1063/1.5066308](https://doi.org/10.1063/1.5066308)
- [215] P. Schwerdtfeger and J. K. Nagle, *Molecular Physics* **117**, 1200–1225 (2019). doi:[10.1080/00268976.2018.1535143](https://doi.org/10.1080/00268976.2018.1535143)
- [216] G. Frenking and H. Schwarz, *International Journal of Mass Spectrometry and Ion Physics* **52**, 131–138 (1983). doi:[https://doi.org/10.1016/0020-7381\(83\)85034-7](https://doi.org/10.1016/0020-7381(83)85034-7)
- [217] A. M. Mebel and A. D. Bandrauk, *The Journal of Chemical Physics* **129**, 224311 (2008). doi:[10.1063/1.3037204](https://doi.org/10.1063/1.3037204)
- [218] Z. Yang, L. Wang, Y. Lee, D. Shirley, S. Huang, and W. Lester, *Chemical Physics Letters* **171**, 9–13 (1990). doi:[https://doi.org/10.1016/0009-2614\(90\)80041-B](https://doi.org/10.1016/0009-2614(90)80041-B)
- [219] L. FP, English, CANAD. J. CHEM.; CANADA; DA. 1972; VOL. 50; NO 24; PP. 3973-3981; ABS. FR.; BIBL. 50 REF. (1972).
- [220] B. P. Tsai, A. S. Werner, and T. Baer, *The Journal of Chemical Physics* **63**, 4384–4392 (1975). doi:[10.1063/1.431155](https://doi.org/10.1063/1.431155)
- [221] R. Krailler and D. Russell, *INTERNATIONAL JOURNAL OF MASS SPECTROMETRY AND ION PROCESSES* **66**, 339–351 (1985). doi:[10.1016/0168-1176\(85\)80007-0](https://doi.org/10.1016/0168-1176(85)80007-0)
- [222] D. Won, J. Choe, and M. Kim, English, *Rapid Commun. Mass. Spectrom.* **14**, 1110–1115 (2000).
- [223] D. Y. Kim, J. C. Choe, and M. S. Kim, *The Journal of Physical Chemistry A* **103**, 4602–4608 (1999). doi:[10.1021/jp990526+](https://doi.org/10.1021/jp990526+)
- [224] J. L. Holmes and F. P. Lossing, *Canadian Journal of Chemistry* **57**, 249–252 (1979). doi:[10.1139/v79-041](https://doi.org/10.1139/v79-041)
- [225] X. Huang and T. J. Lee, *The Astrophysical Journal* **33**, 736–745 (2011). doi:[10.1088/0004-637X/736/1/33](https://doi.org/10.1088/0004-637X/736/1/33)
- [226] P. M. Solomon, K. B. Jefferts, A. A. Penzias, and R. W. Wilson, *Astrophys. J.* **168**, L107 (1971). doi:[10.1086/180794](https://doi.org/10.1086/180794)

- [227] P. Gratier, L. Majumdar, M. Ohishi, E. Roueff, J. C. Loison, K. M. Hickson, and V. Wakelam, *Astrophys. J. Supp. Ser.* **225**, 25 (2016). doi:[10.3847/0067-0049/225/2/25](https://doi.org/10.3847/0067-0049/225/2/25)
- [228] Vastel, C., Loison, J. C., Wakelam, V., and Lefloch, B., *Astron. Astrophys.* **625**, A91 (2019). doi:[10.1051/0004-6361/201935010](https://doi.org/10.1051/0004-6361/201935010)
- [229] I. Andron, P. Gratier, L. Majumdar, T. H. G. Vidal, A. Coutens, J.-C. Loison, and V. Wakelam, *Mon. Not. R. Astron. Soc.* **481**, 5651–5659 (2018). doi:[10.1093/mnras/sty2680](https://doi.org/10.1093/mnras/sty2680)
- [230] Fayolle, Edith C., Öberg, Karin I., Garrod, Robin T., van Dishoeck, Ewine F., and Bisschop, Suzanne E., *Astron. Astrophys.* **576**, A45 (2015). doi:[10.1051/0004-6361/201323114](https://doi.org/10.1051/0004-6361/201323114)
- [231] K. I. Öberg, V. V. Guzmán, K. Furuya, C. Qi, Y. Aikawa, S. M. Andrews, R. Loomis, and D. J. Wilner, *Nature* **520**, 198–201 (2015). doi:[10.1038/nature14276](https://doi.org/10.1038/nature14276)
- [232] V. V. Guzman, J. Pety, P. Gratier, J. R. Goicoechea, M. Gerin, E. Roueff, F. Le Petit, and J. Le Bourlot, *FARADAY DISCUSSIONS* **168**, 103–127 (2014). doi:[10.1039/c3fd00114h](https://doi.org/10.1039/c3fd00114h)
- [233] M. Agundez, J. Cernicharo, G. Quintana-Lacaci, L. Velilla Prieto, A. Castro-Carrizo, N. Marcelino, and M. Guelin, *Astrophys. J.* **814**, doi:[10.1088/0004-637X/814/2/143](https://doi.org/10.1088/0004-637X/814/2/143) (2015).
- [234] A. Marten, T. Hidayat, Y. Biraud, and R. Moreno, *Icarus* **158**, 532–544 (2002). doi:[10.1006/icar.2002.6897](https://doi.org/10.1006/icar.2002.6897)
- [235] A. E. Thelen, C. Nixon, N. Chanover, M. Cordiner, E. Molter, N. Teanby, P. Irwin, J. Serigano, and S. Charnley, *Icarus* **319**, 417–432 (2019). doi:<https://doi.org/10.1016/j.icarus.2018.09.023>
- [236] T. Iino, H. Sagawa, and T. Tsukagoshi, *Astrophys. J.* **890**, 95 (2020). doi:[10.3847/1538-4357/ab66b0](https://doi.org/10.3847/1538-4357/ab66b0)
- [237] J. S. Knight, C. G. Freeman, and M. J. McEwan, *J. Am. Chem. Soc.* **108**, 1404–1408 (1986). doi:[10.1021/ja00267a007](https://doi.org/10.1021/ja00267a007)
- [238] A. J. Illies, S. Liu, and M. T. Bowers, *J. Am. Chem. Soc.* **103**, 5674–5676 (1981). doi:[10.1021/ja00409a007](https://doi.org/10.1021/ja00409a007)
- [239] J. Huntress W. T. and G. F. Mitchell, *Astrophys. J.* **231**, 456–467 (1979). doi:[10.1086/157207](https://doi.org/10.1086/157207)
- [240] D. J. Defrees, A. D. McLean, and E. Herbst, *Astrophys. J.* **293**, 236 (1985). doi:[10.1086/163229](https://doi.org/10.1086/163229)

- [241] E. Vigren, M. Kamińska, M. Hamberg, V. Zhaunerchyk, R. D. Thomas, M. Danielsson, J. Semaniak, P. U. Andersson, M. Larsson, and W. D. Geppert, *Phys. Chem. Chem. Phys.* **10**, 4014–4019 (2008). doi:[10.1039/B801566J](https://doi.org/10.1039/B801566J)
- [242] B. E. Turner, T. Amano, and P. A. Feldman, *Astrophys. J.* **349**, 376 (1990). doi:[10.1086/168321](https://doi.org/10.1086/168321)
- [243] V. Vuitton, R. V. Yelle, and V. G. Anicich, *Astrophys. J.* **647**, L175–L178 (2006). doi:[10.1086/507467](https://doi.org/10.1086/507467)
- [244] C. A. Gottlieb, A. J. Apponi, M. C. McCarthy, P. Thaddeus, and H. Linnartz, *J. Chem. Phys.* **113**, 1910–1915 (2000). doi:[10.1063/1.481994](https://doi.org/10.1063/1.481994)
- [245] T. Amano, K. Hashimoto, and T. Hirao, *J. Mol. Struct.* **795**, 190–193 (2006). doi:[10.1016/j.molstruc.2006.02.035](https://doi.org/10.1016/j.molstruc.2006.02.035)
- [246] M. Frankowski, Z. Sun, and A. Smith-Gicklhorn, *PHYSICAL CHEMISTRY CHEMICAL PHYSICS* **7**, 797–805 (2005). doi:[10.1039/b415412f](https://doi.org/10.1039/b415412f)
- [247] O. Dopfer, D. Roth, R. V. Olkhov, and J. P. Maier, *J. Chem. Phys.* **110**, 11911–11917 (1999). doi:[10.1063/1.479176](https://doi.org/10.1063/1.479176)
- [248] T. Amano, *Astrophys. J.* **330**, L137 (1988). doi:[10.1086/185222](https://doi.org/10.1086/185222)
- [249] T. Amano, *J. Mol. Spectrosc.* **153**, 654–665 (1992). doi:[10.1016/0022-2852\(92\)90500-N](https://doi.org/10.1016/0022-2852(92)90500-N)
- [250] H. Tachikawa, T. Fukuzumi, K. Inaoka, and I. Koyano, *Phys. Chem. Chem. Phys.* **12**, 15399 (2010). doi:[10.1039/c004202a](https://doi.org/10.1039/c004202a)
- [251] D. Ascenzi, P. Tosi, P. Franceschi, D. Catone, S. Turchini, and K. C. Prince, *Chemical Physics* **398**, 269–277 (2012). doi:[10.1016/j.chemphys.2011.06.009](https://doi.org/10.1016/j.chemphys.2011.06.009)
- [252] E. U. Wuerthwein, *The Journal of Organic Chemistry* **49**, 2971–2978 (1984). doi:[10.1021/jo00190a023](https://doi.org/10.1021/jo00190a023)
- [253] H. B. Cerqueira, J. C. Santos, F. Fantuzzi, F. D. A. Ribeiro, M. L. M. Rocco, R. R. Oliveira, and A. B. Rocha, *Journal of Physical Chemistry A* **124**, 6845–6855 (2020). doi:[10.1021/acs.jpca.0c03529](https://doi.org/10.1021/acs.jpca.0c03529)
- [254] K. A. Peterson and T. H. Dunning, *J. Chem. Phys.* **117**, 10548–10560 (2002).
- [255] P. Botschwina, *Journal of molecular spectroscopy* **203**, 203–204 (2000). doi:[10.1006/jmsp.2000.8172](https://doi.org/10.1006/jmsp.2000.8172)
- [256] A. N. Marimuthu, D. Sundelin, S. Thorwirth, B. Redlich, W. D. Geppert, and S. Brünken, *J. Mol. Spectrosc.* **374**, 111377 (2020). doi:<https://doi.org/10.1016/j.jms.2020.111377>

- [257] R. M. Parrish, L. A. Burns, D. G. A. Smith, A. C. Simmonett, A. E. DePrince, E. G. Hohenstein, U. Bozkaya, A. Y. Sokolov, R. Di Remigio, R. M. Richard, J. F. Gonthier, A. M. James, H. R. McAlexander, A. Kumar, M. Saitow, X. Wang, B. P. Pritchard, P. Verma, H. F. Schaefer, K. Patkowski, R. A. King, E. F. Valeev, F. A. Evangelista, J. M. Turney, T. D. Crawford, and C. D. Sherrill, *J. Chem. Theory Comput.* **13**, 3185–3197 (2017). doi:[10.1021/acs.jctc.7b00174](https://doi.org/10.1021/acs.jctc.7b00174)
- [258] D. B. Rap, A. N. Marimuthu, B. Redlich, and S. Brünken, *J. Mol. Spectrosc.* **373**, 111357 (2020). doi:[10.1016/j.jms.2020.111357](https://doi.org/10.1016/j.jms.2020.111357)
- [259] S. Thorwirth, M. E. Harding, O. Asvany, S. Bruenken, P. Jusko, K. L. K. Lee, T. Salomon, M. C. McCarthy, and S. Schlemmer, *Mol. Phys.* **118**, 19–20 (2020). doi:[10.1080/00268976.2020.1776409](https://doi.org/10.1080/00268976.2020.1776409)
- [260] J. R. A.-I. Annia Galano, *J. Comput. Chem.* **27**, 1204 (2006). doi:[10.1002/jcc.20438](https://doi.org/10.1002/jcc.20438)
- [261] N. R. Kestner, *J. Chem. Phys.* **48**, 252 (1968). doi:[10.1063/1.1667911](https://doi.org/10.1063/1.1667911)
- [262] P. Salvador, B. Paizs, M. Duran, and S. Suhai, *J. Comput. Chem.* **22**, 765–786 (2001). doi:[10.1002/jcc.1042](https://doi.org/10.1002/jcc.1042)
- [263] K. Szalewicz, *JWIREs Comput Mol Sci* **2**, 254–272 (2012). doi:[10.1002/wcms.86](https://doi.org/10.1002/wcms.86)
- [264] S. A. Nizkorodov, O. Dopfer, M. Meuwly, J. P. Maier, and E. J. Bieske, *J. Chem. Phys.* **105**, 1770–1777 (1996). doi:[10.1063/1.472052](https://doi.org/10.1063/1.472052)
- [265] O. Dopfer, R. V. Olkhov, and J. P. Maier, *J. Chem. Phys.* **112**, 2176–2186 (2000). doi:[10.1063/1.480783](https://doi.org/10.1063/1.480783)
- [266] N. L. Pivonka, C. Kaposta, M. Brümmer, G. von Helden, G. Meijer, L. Wöste, D. M. Neumark, and K. R. Asmis, *J. Chem. Phys.* **118**, 5275–5278 (2003). doi:[10.1063/1.1559478](https://doi.org/10.1063/1.1559478)
- [267] O. Asvany, K. M. T. Yamada, S. Brünken, A. Potapov, and S. Schlemmer, *Science* **347**, 1346–1349 (2015). doi:[10.1126/science.aaa3304](https://doi.org/10.1126/science.aaa3304)
- [268] M. Brümmer, C. Kaposta, G. Santambrogio, and K. R. Asmis, *J. Chem. Phys.* **119**, 12700–12703 (2003). doi:[10.1063/1.1634254](https://doi.org/10.1063/1.1634254)
- [269] O. Dopfer, *Int. Rev. Phys. Chem.* **22**, 437–495 (2003). doi:[10.1080/01442350310001128](https://doi.org/10.1080/01442350310001128)
- [270] J. Jašík, J. Žabka, J. Roithová, and D. Gerlich, *Int. J. Mass Spectrom.* **354–355**, 204–210 (2013). doi:[10.1016/j.ijms.2013.06.007](https://doi.org/10.1016/j.ijms.2013.06.007)
- [271] B. Turner, *Astrophys. J.* **163**, L35 (1971). doi:[10.1086/180662](https://doi.org/10.1086/180662)
- [272] M. Morris, B. E. Turner, P. Palmer, and B. Zuckerman, *Astrophys. J.* **205**, 82–93 (1976). doi:[10.1086/154252](https://doi.org/10.1086/154252)

- [273] R. Mauersberger, C. Henkel, and L. J. Sage, *Astron. Astrophys.* **236**, 63–68 (1990). doi:[10.1051/0004-6361:20030386](https://doi.org/10.1051/0004-6361:20030386)
- [274] M. A. Cordiner, C. A. Nixon, N. A. Teanby, P. G. J. Irwin, J. Serigano, S. B. Charnley, S. N. Milam, M. J. Mumma, D. C. Lis, G. Villanueva, L. Paganini, Y.-J. Kuan, and A. J. Remijan, *Astrophys. J. Lett.* **795**, 30 (2014). doi:[10.1088/2041-8205/795/2/L30](https://doi.org/10.1088/2041-8205/795/2/L30)
- [275] V. Wakelam, E. Herbst, J.-C. Loison, I. W. M. Smith, V. Chandrasekaran, B. Pavone, N. G. Adams, M.-C. Bacchus-Montabonel, A. Bergeat, K. Béroff, V. M. Bierbaum, M. Chabot, A. Dalgarno, E. F. Van Dishoeck, A. Faure, W. D. Geppert, D. Gerlich, D. Galli, E. Hébrard, F. Hersant, K. M. Hickson, P. Honvault, S. J. Klippenstein, S. Le Picard, G. Nyman, P. Pernot, S. Schlemmer, F. Selsis, I. R. Sims, D. Talbi, J. Tennyson, J. Troe, R. Wester, and L. Wiesenfeld, *Astrophys. J. Suppl. Ser.* **199**, 21 (2012). doi:[10.1088/0067-0049/199/1/21](https://doi.org/10.1088/0067-0049/199/1/21)
- [276] R. Renner, *Z. Phys.* **92**, 172–193 (1934). doi:[10.1007/bf01350054](https://doi.org/10.1007/bf01350054)
- [277] S.-G. He and D. J. Clouthier, *J. Chem. Phys.* **123**, 519 (2005). doi:[10.1063/1.1938947](https://doi.org/10.1063/1.1938947)
- [278] M. Perić, *Mol. Phys.* **105**, 59–69 (2007). doi:[10.1080/00268970601129076](https://doi.org/10.1080/00268970601129076)
- [279] H. Köppel, W. Domcke, L. S. Cederbaum, and H. Koppel, *J. Chem. Phys.* **74**, 7367 (1981). doi:[10.1063/1.441417](https://doi.org/10.1063/1.441417)
- [280] A. Desrier, C. Romanzin, N. Lamarre, C. Alcaraz, B. Gans, D. Gauyacq, J. Liévin, and S. Boyé-Péronne, *J. Chem. Phys.* **145**, 234310 (2016). doi:[10.1063/1.4972019](https://doi.org/10.1063/1.4972019)
- [281] B. Gans, N. Lamarre, and M. Broquier, *J. Chem. Phys.* **145**, 234309 (2016). doi:[10.1063/1.4972018](https://doi.org/10.1063/1.4972018)
- [282] S. Leach, G. A. Garcia, A. Mahjoub, Y. Bénilan, N. Fray, M. C. Gazeau, F. Gaie-Levrel, N. Champion, and M. Schwell, *J. Chem. Phys.* **140**, 174305 (2014). doi:[10.1063/1.4871298](https://doi.org/10.1063/1.4871298)
- [283] A. M. Smith-Gicklhorn, M. Lorenz, and R. Kołos, *J. Chem. Phys.* **115**, 7534 (2001). doi:[10.1063/1.1405019](https://doi.org/10.1063/1.1405019)
- [284] A. N. Marimuthu, F. Huis in't Veld, S. Thorwirth, B. Redlich, and S. Brünken, *J. Mol. Spectrosc.* **379**, 111477 (2021). doi:[10.1016/J.JMS.2021.111477](https://doi.org/10.1016/J.JMS.2021.111477)
- [285] L. Jašíková and J. Roithová, *Chem. Eur. J.* **24**, 3374–3390 (2018). doi:[10.1002/chem.201705692](https://doi.org/10.1002/chem.201705692)
- [286] J. S. Brodbelt and J. Wilson, *Mass Spectrom. Rev.* **28**, 390–424 (2009). doi:[10.1002/MAS.20216](https://doi.org/10.1002/MAS.20216)

- [287] S. Chakrabarty, M. Holz, E. K. Campbell, A. Banerjee, D. Gerlich, and J. P. Maier, *J. Phys. Chem. Lett.* **4**, 4051–4054 (2013). doi:[10.1021/JZ402264N/ASSET/IMAGES/LARGE/JZ-2013-02264N_0005.JPG](https://doi.org/10.1021/JZ402264N/ASSET/IMAGES/LARGE/JZ-2013-02264N_0005.JPG)
- [288] O. Avany, K. Yamada, S. Brünken, A. Potapov, and S. Schlemmer, *Science* **347**, 1346–1348 (2015). doi:[10.1126/SCIENCE.AAA3304/SUPPL_FILE/ASVANY.SM.PDF](https://doi.org/10.1126/SCIENCE.AAA3304/SUPPL_FILE/ASVANY.SM.PDF)
- [289] L. Kong, F. A. Bischoff, and E. F. Valeev, *Chem. Rev.* **112**, 75–107 (2012). doi:[10.1021/cr200204r](https://doi.org/10.1021/cr200204r)
- [290] K. A. Peterson, T. B. Adler, and H.-J. Werner, *J. Chem. Phys.* **128**, 84102 (2008). doi:[10.1063/1.2831537](https://doi.org/10.1063/1.2831537)
- [291] H.-J. Werner, P. J. Knowles, and F. R. Manby, *J. Chem. Phys.* **152**, 144107 (2020). doi:[10.1063/5.0005081](https://doi.org/10.1063/5.0005081)
- [292] J. A. Pople, *Mol. Phys.* **3**, 16–22 (1960). doi:[10.1080/00268976000100021](https://doi.org/10.1080/00268976000100021)
- [293] J. M. Brown, *J. Mol. Spectrosc.* **68**, 412–422 (1977). doi:[10.1016/0022-2852\(77\)90245-4](https://doi.org/10.1016/0022-2852(77)90245-4)
- [294] SCILAB *version 6.1.1*. www.scilab.org
- [295] G. E. Doublerly, A. Ricks, P. V. R. Schleyer, and M. A. Duncan, *J. Phys. Chem. A. Lett.*, doi:[10.1021/jp802020n](https://doi.org/10.1021/jp802020n) (2008).
- [296] O. Dopfer, D. Roth, and J. P. Maier, *J. Am. Chem. Soc.*, doi:[10.1021/ja012004p](https://doi.org/10.1021/ja012004p) (2002).
- [297] D. R. Bates and E. Herbst, *Radiative association. in: millar, t.j., williams, d.a. (eds) rate coefficients in astrochemistry. astrophysics and space science library*, Vol. 146 (Springer, Dordrecht, 1988), pp. 17–40, doi:[10.1007/978-94-009-3007-0_2](https://doi.org/10.1007/978-94-009-3007-0_2)
- [298] P. Langevin, *Ann. Chim. Phys.* **5**, 245 (1905).
- [299] O. Asvany and S. Schlemmer, *International Journal of Mass Spectrometry* **279**, 147–155 (2009). doi:[10.1016/J.IJMS.2008.10.022](https://doi.org/10.1016/J.IJMS.2008.10.022)
- [300] T. N. Olney, N. M. Cann, G. Cooper, and C. E. Brion, *Chemical Physics* **223**, 59–98 (1997). doi:[10.1016/S0301-0104\(97\)00145-6](https://doi.org/10.1016/S0301-0104(97)00145-6)
- [301] J. Mikosch, U. Fröhling, S. Trippel, D. Schwalm, M. Weidemüller, and R. Wester, *Physical Review Letters* **98**, 223001 (2007). doi:[10.1103/PhysRevLett.98.223001](https://doi.org/10.1103/PhysRevLett.98.223001)
- [302] J. Mikosch, U. Fröhling, S. Trippel, R. Otto, P. Hlavenka, D. Schwalm, M. Weidemüller, and R. Wester, *Physical Review A* **78**, 023402 (2008). doi:[10.1103/PhysRevA.78.023402](https://doi.org/10.1103/PhysRevA.78.023402)

- [303] V. Wakelam, J.-C. Loison, E. Herbst, B. Pavone, A. Bergeat, K. Béroff, M. Chabot, A. Faure, D. Galli, W. D. Geppert, D. Gerlich, P. Gratier, N. Harada, K. M. Hickson, P. Honvault, S. J. Klippenstein, S. D. L. Picard, G. Nyman, M. Ruaud, S. Schlemmer, I. R. Sims, D. Talbi, J. Tennyson, and R. Wester, *The Astrophysical Journal Supplement Series* **217**, 20 (2015). doi:[10.1088/0067-0049/217/2/20](https://doi.org/10.1088/0067-0049/217/2/20)
- [304] G. Werfelli, C. Balança, T. Stoecklin, B. Kerkeni, and N. Feautrier, *Monthly Notices of the Royal Astronomical Society* **468**, 2582–2589 (2017). doi:[10.1093/mnras/stx675](https://doi.org/10.1093/mnras/stx675)
- [305] T. Amano, *The Astrophysical Journal Letters* **716**, L1 (2010). doi:[10.1088/2041-8205/716/1/L1](https://doi.org/10.1088/2041-8205/716/1/L1)
- [306] R. Otto, A. Von Zastrow, T. Best, and R. Wester, *Physical Chemistry Chemical Physics* **15**, 612–618 (2013). doi:[10.1039/c2cp43186f](https://doi.org/10.1039/c2cp43186f)
- [307] E. Herbst, 239–262 (1988). doi:[10.1007/978-94-009-3007-0_15](https://doi.org/10.1007/978-94-009-3007-0_15)
- [308] B. M. Smirnov, *Soviet Journal of Experimental and Theoretical Physics* **24**, 1180 (1967).
- [309] J. Pérez-Ríos and C. H. Greene, *The Journal of Chemical Physics* **143**, 041105 (2015). doi:[10.1063/1.4927702](https://doi.org/10.1063/1.4927702)
- [310] C. H. Greene, P. Giannakeas, and J. Pérez-Ríos, *Reviews of Modern Physics* **89**, 035006 (2017). doi:[10.1103/RevModPhys.89.035006](https://doi.org/10.1103/RevModPhys.89.035006)
- [311] H. Bohringer, W. Glebe, and F. Arnold, *Journal of Physics B: Atomic and Molecular Physics* **16**, 2619 (1983). doi:[10.1088/0022-3700/16/14/022](https://doi.org/10.1088/0022-3700/16/14/022)
- [312] D. Gerlich, *Journal of the Chemical Society, Faraday Transactions* **89**, 2199–2208 (1993). doi:[10.1039/FT9938902199](https://doi.org/10.1039/FT9938902199)
- [313] R. Plašil, I. Zymak, P. Jusko, D. Mulin, D. Gerlich, and J. Glosík, *Philosophical Transactions of the Royal Society A: Mathematical, Physical and Engineering Sciences* **370**, 5066–5073 (2012). doi:[10.1098/rsta.2012.0098](https://doi.org/10.1098/rsta.2012.0098)
- [314] J. Xie, B. Poirier, and G. I. Gellene, *The Journal of Chemical Physics* **119**, 10678–10686 (2003). doi:[10.1063/1.1621384](https://doi.org/10.1063/1.1621384)
- [315] W. B. Latter, C. K. Walker, and P. R. Maloney, *The Astrophysical Journal* **419**, L97 (1993). doi:[10.1086/187146](https://doi.org/10.1086/187146)
- [316] H. Stoerzer, J. Stutzki, and A. Sternberg, *Astronomy and Astrophysics* **296**, L9–12 (1995).
- [317] A. Fuente and J. Martín-Pintado, *Astrophys. J.* **477**, L107–L109 (1997). doi:[10.1086/310532](https://doi.org/10.1086/310532)

- [318] A. Fuente, A. Rodríguez-Franco, S. García-Burillo, J. Martín-Pintado, and J. H. Black, *Astronomy and Astrophysics* **406**, 899–913 (2003). doi:[10.1051/0004-6361:20030712](https://doi.org/10.1051/0004-6361:20030712)
- [319] S. P. Treviño-Morales, A. Fuente, Á. Sánchez-Monge, P. Pilleri, J. R. Goicoechea, V. Ossenkopf-Okada, E. Roueff, J. R. Rizzo, M. Gerin, O. Berné, J. Cernicharo, M. Gómez-García, C. Kramer, S. García-Burillo, and J. Pety, *Astron. Astrophys.* **593**, L12, L12 (2016). doi:[10.1051/0004-6361/201628899](https://doi.org/10.1051/0004-6361/201628899)
- [320] J. R. Goicoechea, S. Cuadrado, J. Pety, E. Bron, J. H. Black, J. Cernicharo, E. Chapillon, A. Fuente, and M. Gerin, *Astron. Astrophys.* **601**, L9, L9 (2017). doi:[10.1051/0004-6361/201730716](https://doi.org/10.1051/0004-6361/201730716)
- [321] A. Fuente, S. García-Burillo, M. Gerin, J. R. Rizzo, A. Usero, D. Teyssier, E. Roueff, and J. Le Bourlot, *The Astrophysical Journal* **641**, L105–L108 (2006). doi:[10.1086/503605](https://doi.org/10.1086/503605)
- [322] M. Gerin and H. Liszt, *Astron. Astrophys.* **648**, A38, A38 (2021). doi:[10.1051/0004-6361/202039915](https://doi.org/10.1051/0004-6361/202039915)
- [323] T. A. Dixon and R. C. Woods, *Physical Review Letters* **34**, 61–63 (1975). doi:[10.1103/PhysRevLett.34.61](https://doi.org/10.1103/PhysRevLett.34.61)
- [324] K. V. L. N. Sastry, P. Helminger, E. Herbst, and F. C. de Lucia, *The Astrophysical Journal* **250**, L91 (1981). doi:[10.1086/183680](https://doi.org/10.1086/183680)
- [325] F. van den Heuvel and A. Dymanus, *Chem. Phys. Lett.* **92**, 219–222 (1982). doi:[10.1016/0009-2614\(82\)80263-7](https://doi.org/10.1016/0009-2614(82)80263-7)
- [326] S. Spezzano, S. Brünken, H. S. Müller, G. Klapper, F. Lewen, K. M. Menten, and S. Schlemmer, *Journal of Physical Chemistry A* **117**, 9814–9818 (2013). doi:[10.1021/jp312616u](https://doi.org/10.1021/jp312616u)
- [327] P. Stäuber and S. Bruderer, *Astronomy and Astrophysics* **505**, 195–203 (2009). doi:[10.1051/0004-6361/200912381](https://doi.org/10.1051/0004-6361/200912381)
- [328] B. Anusuri, *Comput. Theor. Chem.* **1188**, 112937 (2020). doi:[10.1016/j.comptc.2020.112937](https://doi.org/10.1016/j.comptc.2020.112937)
- [329] M. Bogey, C. Demuynck, and J. L. Destombes, *Mol. Phys.* **46**, 679–681 (1982). doi:[10.1080/00268978200101521](https://doi.org/10.1080/00268978200101521)
- [330] A. Landé, *Zeitschrift für Physik* **5**, 231–241 (1921). doi:[10.1007/BF01335014](https://doi.org/10.1007/BF01335014)
- [331] O. Asvany, C. R. Markus, T. Salomon, P. C. Schmid, S. Banhatti, S. Brünken, F. Lippalini, J. Gauss, and S. Schlemmer, *J. Mol. Struct.* **1214**, 128023 (2020). doi:[10.1016/j.molstruc.2020.128023](https://doi.org/10.1016/j.molstruc.2020.128023)

SUMMARY AND OUTLOOK

1. SUMMARY

Interstellar molecules were once thought to be impossible to exist in space due to the extreme conditions of the interstellar medium (ISM). The extremely low densities and temperatures, as well as the intense radiation and high-energy particles present in space, were believed to prevent the formation and survival of molecules.

However, this understanding began to change in the early 20th century with the discovery of CH, CN and CH^+ molecular species in the ISM based on four sharp absorption lines seen in the optical spectra of several distant stars using Mount Wilson Observatory. The later discovery of other molecules, such as hydroxyl radical, water, ammonia and formaldehyde in the ISM by radio astronomy in the 1960s provided evidence for the existence of a wide variety of molecular species in space.

This revelation was significant because it challenged the prevailing view of the ISM and led to the development of new theoretical models about the chemical processes that occur in space. One such revelation is that ion-neutral reactions are a crucial part of the chemistry in the interstellar medium, driving the formation of complex molecules and influencing the chemistry of the ISM. This also provides new insights into the origins of life in the universe, as the discovery of complex organic molecules in space suggests that these building blocks of life may be prevalent throughout the cosmos.

Spectroscopic methods are crucial in studying interstellar molecules and (exo-)planetary atmospheres as well. These methods have been and will continue to be, crucial in discovering new interstellar molecules and understanding the chemistry of space and (exo-)planetary atmospheres. The introduction chapter 1 gives a much more detailed introduction to molecular ions in space, astrochemistry and the development of spectroscopic methods for studying molecular ions in a cryogenic ion trap.

Cryogenic ion traps are important tools in the field of spectroscopy, particularly in the study of molecular ions. They allow us to perform gas-phase action spectroscopy on cold molecular ions at < 10 K ambient temperature, i.e., simulating ISM conditions. The combination of action spectroscopic methods with

cryogenic ion traps provides several advantages over traditional spectroscopy methods, such as mass selection and storage in a cold ion trap, uncontaminated spectra and narrow line widths. Chapter 2 gives a detailed account of the instrumental setup and various measurement techniques used in this study for the rotational and vibrational transition characterisation of cold molecular ions.

The following chapters 3, 4 and 5 provide a characterisation of the vibrational transitions of potential candidates of interstellar molecular ions. They are experimentally (using IRPD) and theoretically investigated in detail, which is briefly summarised below:

The C_3H_3^+ hydrocarbon molecular ion is an important intermediate in various astrochemical environments such as the interstellar medium, cometary comae, and planetary atmospheres. Therefore, in chapter 3 we characterise $[\text{C}_3\text{H}_3]^+$ and $[\text{C}_3\text{D}_3]^+$ isomers. Since these ions have two stable isomers, the cyclic cyclopropenyl cation, $\text{c-C}_3\text{H}_3^+$, and the linear propargyl cation, $\text{H}_2\text{C}_3\text{H}^+$, isomer quantification with different ion-source conditions and precursors are investigated using kinetic scans, i.e., monitoring target ion-complex depletion as a function of time in the presence of resonant radiation on a chosen vibrational transition specific to one isomeric species.

Methyl cyanide (CH_3CN) was among the first polyatomic molecules detected during radio-astronomical observations of the ISM. As methyl cyanide has a high proton affinity, much larger than that of H_2 , its protonated version (CH_3CNH^+) can form effectively via exothermic proton transfer from H_3^+ to CH_3CN in the interstellar medium. Chapter 4 focuses on CH_3CNH^+ providing a comprehensive experimental and quantum-chemical study of the vibrational spectrum of $\text{Ne-CH}_3\text{CNH}^+$. The influence of the weakly-bound neon atom on the IRPD experiments is investigated in detail using various computational methods.

Cyanopolyyne are a class of molecules consisting of a chain of carbon and nitrogen atoms. The simplest cyanopolyyne is cyanoacetylene (HC_3N), one of the ISM's most widespread polyatomic species. It has been observed in various astronomical environments, including the interstellar medium, comets, and the atmosphere of Titan, one of Saturn's moons. However, its highly reactive cationic counterpart (HC_3N^+), which is postulated to form from the ionisation of HC_3N by cosmic rays or UV photons, has yet to be detected in space. Therefore, in chapter 5 we investigate HC_3N^+ through vibrational studies. Interestingly, the HC_3N^+ molecular ion is an open-shell linear species which results in pronounced Renner-Teller (RT) effects, i.e., vibronic coupling. Therefore, the breakdown of the Born-Oppenheimer approximation due to the RT effect is analysed using an effective Hamiltonian approach. The influence of the tag in IRPD, especially on the RT-affected bending modes, is discussed in detail.

The last two chapters, i.e., 6 and 7 focus on the investigation of high resolu-

tion pure-rotational action spectroscopy. Rotational transitions provide similar or even more distinct molecular fingerprints than vibrational transitions. Due to their low excitation temperature, most interstellar species are identified through their rotational transitions. The rotational high-resolution rotational action spectroscopy technique employed in this thesis is called ROtational State-dependent At-tachment of rare gas Atoms (ROSAA), which utilises a change in rare-gas atom attachment rates for measuring pure rotational transitions of bare ions. The main motivation of the last two chapters is to understand the ROSAA process and its signal intensities in detail with the support of numerical simulation results. Therefore, implementation and investigation of this novel rotational action spectroscopic technique are illustrated for a closed-shell (CD^+ in chapter 6) and, for the first time, an open-shell molecular ion (CO^+ in chapter 7). Chapter 6 experimentally investigates the kinetics of the ion-neutral three-body collisional process, subsequently systematically developing a ROSAA kinetic model, while chapter 7 gives a detailed account of utilising this model for the open-shell species CO^+ which was rotationally characterised with resolved Zeeman splitting due to the Earth's magnetic field.

2. OUTLOOK

In this final section, a brief outlook is provided for continuing further in future studies.

As discussed above, measuring the rotational transition of molecular ions can increase the possibility of its astronomical detection significantly. Therefore, the molecular ions which were vibrationally characterised in this thesis can be investigated further for rotational characterisation, with the support of the developed numerical simulation of the ROSAA model. For example, the propargyl cation $l\text{-C}_3\text{H}_3^+$ (i.e., CH_2CCH^+) is an important candidate to study since its neutral form had been recently (2021) detected in the TMC-1 region as one of the most abundant radicals ever found. Likewise, it would be interesting to study rotational transitions of the singly and doubly deuterated forms of $c\text{-C}_3\text{H}_3^+$ (since $c\text{-C}_3\text{H}_3^+$ does not possess permanent dipole moment).

The carbocations are important molecular ions since they are an important intermediate for many organic molecules which are observed abundantly in ISM. The CH_2^+ molecular ion is one such well-known potential interstellar candidate. Therefore, a study focusing on a CH_2^+ and its deuterated isotopologues is very interesting and vital. The CH_2^+ ion also possesses interesting intramolecular dynamics such as Renner-Teller interactions and quasi-linear structure. Several detailed studies both experimentally and theoretically had been carried out on CH_2^+ molecular ions because of the aforementioned reasons. However, experi-

mental gas-phase pure high-resolution rotation data on a vibronic ground state is not available. Therefore, in future, one can try to utilise the ROSAA technique to study and provide accurate rotational constants for its astronomical detection.

In another scenario, we have tried to measure the rotational transitions for CH_2CN^+ molecular ion but failed to detect any ROSAA signal. This should be further investigated using the developed ROSAA model. Therefore, in future studies, the model reported in this thesis can be readily utilised to first understand the expected signal intensity at a given temperature, number density and power, and decide the possibility of applying the ROSAA technique.

On the other hand, for vibrational characterisation, an interesting study proposal had been submitted for a FELIX beam time, which is yet to be performed is *Spectroscopic and structural characterization of the small carbon clusters C_4^+ and C_7^+ : Transition from linear to cyclic structures ?*. Using the methods developed in our group as reported in this thesis extensively, future studies to disentangle and quantify isomeric mixtures of these smaller carbon cluster cations are vital due to their potential importance in circumstellar and interstellar carbon chemistry.

SAMENVATTING

1. SUMMARY

Summary in dutch...

ACKNOWLEDGEMENTS

This is an optional chapter containing acknowledgements.

LIST OF PUBLICATIONS

CURRICULUM VITÆ

Aravindh Nivas MARIMUTHU

14-03-1879 Born in Ulm, Germany.

EDUCATION

- 1892–1896 Grammar School
 Luitpold Gymnasium, München (1892–1895)
 Aurau, Switzerland (1895–1896)
- 1896–1900 Undergraduate in Mathematics & Physics
 Eidgenössische Polytechnische Schule Zürich
- 1905 PhD. Physics
 Eidgenössische Polytechnische Schule Zürich
Thesis: Eine neue Bestimmung der Moleküldimensionen
Promotor: Prof. dr. A. Kleiner

AWARDS

- 1922 Nobel Prize in Physics
- 1925 Copley Medal
- 1929 Max Planck Medal
- 1999 Time magazine's person of the century